# Modeling sediment transport pathways in the mouth of the Scheldt estuary

**Master Thesis - University of Twente, Faculty of Engineering and Technology, Civil Engineering and Management**

**Stefan de Vries**
**20/01/2016**

UNIVERSITY OF TWENTE.

Deltares
Enabling Delta Life

Front cover: Aerial view of the mouth of the Scheldt estuary (near Breskens)
Source: https://beeldbank.rws.nl, Rijkswaterstaat / Joop van Houdt

# Modelling sediment transport pathways in the mouth of the Scheldt estuary

**Master Thesis - University of Twente, Faculty of Engineering and Technology, Civil Engineering and Management**

Stefan (S.B.) de Vries
Student number: s1009907

20/01/2016

Supervising committee:
Dr. Ir. J.S. Ribberink (University of Twente)
Dr. K.M. Wijnberg (University of Twente)
Dr. Ir. J.J. van der Werf (Deltares and University of Twente)
Ir. P.K. Tonnon (Deltares)

# Preface

This thesis concludes the Master Water Engineering and Management at the University of Twente. The Thesis was conducted at Deltares (unit: ZKS, department: AMO) in Delft, within the context of Deltares project “Modellen en verkenningen Schelde Estuarium” (project number 1210301).

After years of following courses at the university, it has been a valuable opportunity to finally apply my knowledge and skills during an in-depth research. The experiences I gained during the last couple of months will be useful for my next graduation project and future work.

I would like to thank all the members of my graduation committee for their commitment and valuable feedback during the processes. A special thanks to my daily supervisors Jebbe van der Werf and Kathelijne Wijnberg for the meetings and advice, as well as the time invested in me. Next, I am greatly thankful to Deltares for providing me all the resources, knowledge and expertise to conduct the graduation project. Furthermore, a special thanks to all the fellow students at Deltares for their help, suggestions and coffee and lunch breaks. They made my staying enjoyable.

Last but not least, I would like to thank my parents for providing me the possibility to study, the encouragements and the unconditional support. Although I still have to graduate for my Master Business Administration, my life as a student almost comes to an end. Finally, I would like to thank Lotte for being my inspiration during the struggles I had while writing the thesis.

Stefan de Vries,
Delft, January 2016

# Abstract

The tide-dominated Scheldt estuary is located in the southwest of the Netherlands. Recent research on the estuary mainly focused on the inner estuary: the Western Scheldt. The renewed interest of the Flemish government to explore the feasibility of large-scale morphological interventions in the mouth of the estuary addresses the need to develop knowledge and prediction tools for this area.

Engineers often use advanced computer models to understand and predict the behaviour of a morphological system. The standard morphodynamic calculations are able to quantify the bed level changes, but cannot provide clear overviews of the sediment flows and link the sink and source locations. This information can be extracted from the sediment transport pathways of tracers and be useful for effective sediment management strategies. Instead of using physical tracer experiments, the study that is presented in this thesis applies numerically modelling to derive the pathways and analyse the sediment transports in the mouth of the Scheldt estuary. For this research, the hydrodynamics and sediment transports are simulated with the existing Delft3D-NeVla model.

Traditionally, the numerical modelling of tracer dispersals is based on the graded sediment approach. This approach follows the concentrations of different sediment fractions over time. It mimics the processes that are also found in the physical experiments; the dispersal of tracers is influenced by the decay in tracer availability due to bed mixing and lag effects due to the burial and resurfacing of sediment. These processes result in tracer dispersal rates that quickly decrease after the tracers have been released and can eventually even become negligible. Although it depends on the model settings, the approach generally requires a long computational time to get an impression of the transport pathways in a large area with a single tracer deposit.

To solve this, one could use the newly developed visualisation tool. It is a post-processing tool that visualizes the maps of the time-varying sediment transports (computed by the Delft3D model). The pathways are visualized by following the movements of numerical tracer particles step by step through the vector fields. Particles are displaced according to the directions and the magnitudes of the sediment transports. The tool is based on an important assumption: the particles do not interact with the bed. Because the numerical particles are continuously moving and are not slowed down by bed mixing, burial and resurfacing; the dispersal rates of tracers are overestimated compared to what is seen in physical tracer experiments and the graded sediment approach. However, the assumption makes it possible to obtain large-scale transport pathways with minimum computational efforts. Before running the simulations, the user has to define 4 parameter values. The most important one is the acceleration coefficient that is used to convert sediment transports into the velocities that are applied for particle movement calculations. As the tool has not been fully documented nor thoroughly tested, this study proposes some guidelines to choose appropriate values for the different parameters. The mouth of the Scheldt estuary forms a useful real-life case to test the tool and the developed guidelines.

By releasing the numerical particles at various locations within the mouth, the tool was able to visualize the dominant sediment transport pathways. The results demonstrated that many of the tracer particles are transported through the various channels in the longitudinal direction. Moreover, the tool is able to reproduce the circulation cell of sediment that is found in front of Walcheren and the cross-channel imbalance at the inlet. The different simulations have shown that many of the numerical particles eventually end up at the Vlakte van de Raan. At the Vlakte van de Raan itself, the visualisation tool revealed that the different flows of

sediment converge into one pathway that is directed towards the northern end of the Deurloo West channel. The study also demonstrated the added value of the visualisation tool in evaluating and comparing the behaviour of disposal locations. Finally, the analysis of various the transport pathways helped to get a better understanding of the modelled erosion and sedimentation patterns in the current bathymetry.

The visualisation tool has also been applied to study the effect of two large-scale human interventions: an island in front of the Knokke-Heist and the construction of a new navigation channel by deepening and extending the Geul van de Walvischstaart and Deurloo West channels. The pathways are able to visualize the changing sediment transports and are helpful when trying to analysing the erosion sedimentation patterns. The island mainly changes the interaction between the alongshore sediment transport and the residual transports within the Scheur. The new navigation channel becomes an important discharge channel for filling and emptying of the Western Scheldt. As a result of the increased velocities, a lot of transport pathways in the mouth are reorienting and are eventually located in the new channel. The visualisation tool also revealed a reorientation of the transport pathways on the Vlakte van de Raan. The reoriented residual sediment transports at the Vlakte van de Raan are directed perpendicular to the Vlakte van de Raan.

Based on the results of this study, it is concluded that the transport pathways computed with the visualisation tool can be a useful additional source of information that can support the findings of the standard morphodynamic calculations.

# Contents

# 1 Introduction

## 1.1 Relevance of this study

1.1.1 Mouth of the Scheldt estuary

The tide-dominated Scheldt estuary is “one of the last relatively natural estuaries with a dynamic multi-channel system and exceptionally valuable eco-system” (Meersschaut et al., 2004, p.10). The estuary forms the meeting point of the North Sea and the river Scheldt and is situated at the border of the Netherlands and Belgium. The mouth is the area seaward of Vlissingen and Breskens (Figure 1.1). Further upstream, one can find the Western Scheldt (the inner estuary) and the Sea Scheldt (river part).

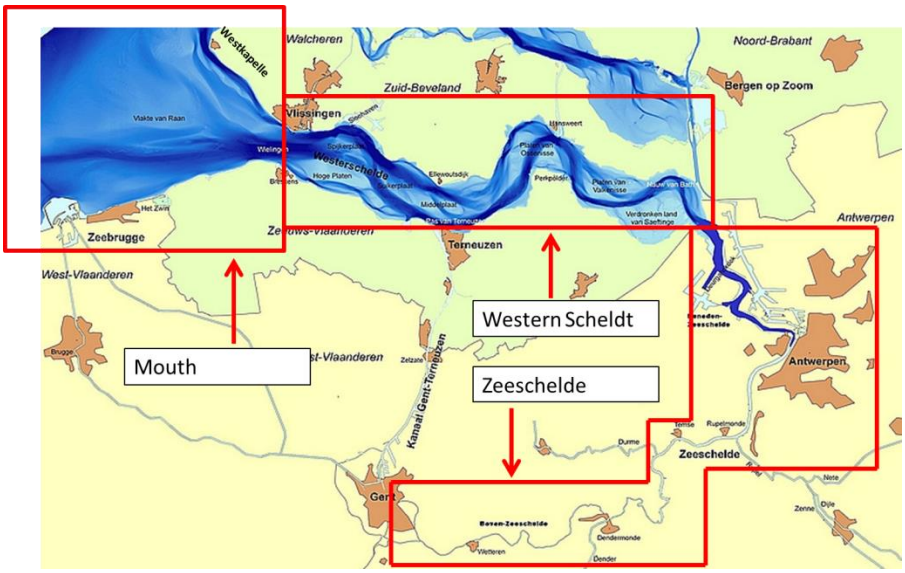


*Figure 1.1 Overview of the Scheldt estuary (Schroevers, 2013).*

The estuary is of vital importance for the Netherlands and Belgium. The unique landscape provides a habitat for various types of ecological valuable flora and fauna. In addition, the estuary is of large economic importance as it provides navigation routes to the ports of Antwerp, Gent, Terneuzen and Vlissingen. At last, the estuary plays an important role in ensuring the safety against flooding. Unlike the other sea arms in the Southwest of the Netherlands, the Western Scheldt is not (semi-)closed as a part of the Delta Works. Dikes around the estuary prevent cities like Middelburg, Vlissingen, Terneuzen and Antwerp from being flooded. Changes in the hydrodynamics (e.g. sea level rise) and bathymetry of Scheldt estuary may affect for instance tidal amplification, and could endanger the functions of the estuary (Consortium Deltares-IMDC-Svasek-Arcadis, 2013c). A thorough understanding of the observed developments and impact of human interventions is required for the preservation of the three functions (nature, accessibility and safety against flooding).

The authorities considered that the preservation of the functions was most critical for the inner estuary. Here, issues like the tidal amplification, navigability and effect of dredging and disposal operations were considered most urgent. Therefore, previous studies mainly focused on the Western Scheldt (e.g. Wang, et al., 1999; Wang, et al., 2002; Consortium Deltares-IMDC-Svasek-Arcadis, 2013c). The Flemish government recently launched the Masterplan Flanders Bays (2014). It describes first explorative ideas about large-scale interventions along the Flemish coastline and in the mouth of the Scheldt estuary to protect the coast against sea level rise and super-storms, and to improve navigability at the same time. This requires new knowledge and prediction tools for the mouth, because the morphodynamics in

the mouth are different from the Western Scheldt. The effect of waves on sediment transport is expected to be more important, there is an interaction with coastal morphodynamics and the influence of dredging and dumping activities is expected to be less pronounced (van der Werf, et al., 2015).

First of all, the improved insights should lead to a better understanding of the interaction between the various channels and shoals within the mouth. This helps to better understand the morphological developments and can be used for the integral management of the different functions of the estuary. Furthermore, improved insights about the sediment transport patterns are useful for more effective dredging and disposal operations. By predicting and steering how the disposed sediment is dispersed within the mouth, the need for dredging operations can be lowered. To come back to the Masterplan Flanders Bays, a thorough understanding of the impact of the designed interventions is necessary to make sure that the state of the estuary, in terms of the three functions, is not negatively affected.

### 1.1.2 Transport pathways

Advanced process-based numerical modelling is a generally recognized method to better understand morphological developments (Lesser et al., 2004). The standard morphodynamic calculations compute the bed level changes and the underlying sediment transports magnitudes and directions. This Eulerian approach does not directly link sediment sinks and sources. A Lagrangian approach does resolve sediment transport pathways, providing information about the direction of the sediment flows and linking sinks and sources. The pathways are not a replacement of the traditional sediment transport modelling; they do not show the erosion-sedimentation rates, but just provide extra qualitative information about the sediment transport patterns. This knowledge can be used helpful for coastal and estuarine management, in particular for the design and assessment of human interventions.

Looking back at the Scheldt estuary, the pathways can be helpful when analysing the sediment transport patterns at the various channels and shoals that cannot be (easily) extracted from the standard erosion-sedimentation maps. In addition, the pathways can explain which areas contribute to the sedimentation in the channels, and help to understand why certain areas constantly have to be dredged. Moreover, one can analyse the pathways for the sediment from the different dump areas and use this knowledge to optimize the disposal strategy. In addition, the pathways can also demonstrate the response of a morphological system on the construction of other large human interventions (e.g. new channel or jetties).

One could derive these transport pathways with physical tracer experiments. As an example, Hordijk (2002) studied how nourished sediment in the mouth of the Scheldt estuary was dispersed over time. Because these field experiments have certain limitations (e.g. expensive, low recovery rate, time consuming), numerical modelling of tracer dispersals and transport pathways is a useful alternative. The pathways can be quickly computed for various hydrodynamic forcing conditions (e.g. different wave conditions) and different designs of the human interventions. Elias et al. (2011), for example, used the dispersal of tracer particles in their Delf3D model to explain the exchange of sediment at the mouth of the Columbia River during a spring-neap cycle and with storm conditions.

Traditionally, the numerical modelling of tracer dispersals is based on the graded sediment approach. This approach follows the concentrations of different sediment fractions over time. It mimics the processes that are also seen in the physical experiments; sediment grains are allowed to interact with the bed by mixing, burial and resurfacing. Similar to the experiments, these processes result in tracer dispersals that quickly decrease after the tracers have been released and can eventually even become negligible. As result, the approach requires a long computational time to get an impression of the transport pathways in a large area.

To compute transport pathways, one could also use the recently developed visualisation tool. It is a post-processing method that uses the maps of the time varying sediment transports that are generated by another numerical model (e.g. Delft3D) that is able to simulate the hydrological and morphological conditions in a certain system. The tool follows numerical tracer particles as they move according to the direction and magnitude of the sediment transports. As the particles are not slowed down by any interactions with the bed, the tool is able to compute large-scale transport pathways (e.g. several kilometres) with a short computational time (e.g. several minutes). The visualisation tool has not been fully documented nor thoroughly tested. Therefore, there is uncertainty about the physical interpretation, usage and the added value of the transport pathways generated by the visualisation tool.

## 1.2 Objective and research questions

To solve this problem, this research will compare the visualisation tool with the graded sediment approach and use the mouth the Scheldt estuary as a proof of concept. The overall research objective is: *To assess the added value of transport pathways generated by the visualisation tool to better understand the natural and human-induced morphodynamics of the mouth of the Scheldt estuary.*

To reach this objective, three research questions are formulated:

- RQ1: How should the visualisation tool be used and its output be interpreted compared to the more traditional graded sediment approach?
- RQ2: What are the sediment transport patterns controlling the morphological developments in the mouth of the Scheldt estuary currently and in the case of large-scale morphological human interventions?
- RQ3: What are the characteristic sediment transport pathways in the mouth of the Scheldt estuary following the visualisation tool, currently and in the case of large-scale morphological human interventions?

To limit the scope, this study will focus only on the movement of fine sand. Multiple other studies have studied the morphological developments in the Scheldt estuary by using this same single grain size (e.g. Consortium Deltares-IMDC-Svasek-Arcadis, 2013c; Damen, 2014; Van der Werf et al., 2015). The behaviour of silt is different and should be studied in a separate research. To limit to scope of the second and third research question, this study focusses on two interventions: the construction of an island in front of Knokke-Heist and the repositioning of the main navigation channel (Section 2.2.1.4).

## 1.3 Methodology

To answer these questions, the research is divided in 5 phases. In phase 1, a literature study is performed on the relevant physical processes and the characteristics of the Scheldt estuary. Gathering this information is essential for understanding the principles behind the graded sediment approach and visualisation tool (hereafter referred to as the transport pathway methodologies) and the sediment transports that are computed for the mouth of the Scheldt estuary. Subsequently (phase 2), there is an in-depth study of the concepts behind the pathway methodologies. The analysis discusses the assumptions that are being made, the underlying equations and the various parameters that affect the model results.

For this study, the graded sediment approach (embedded in the model itself) and the visualisation tool (using of the model output) are based on the process-based Delf3D model. Various studies have proven the reliability of Delft3D model in describing complex coastal systems (Lesser et al., 2004). Furthermore, there is already a Delft3D schematization available for the Scheldt estuary (Delft3D-NeVla). In this study, the model is based on a 2DH approach and assumes a homogeneous distribution of the flow velocity over depth. The 2DH approach is chosen because of the reduced calculation time (compared to the 3D model) and

the fact that 3D effects are expected to be limited for calculations of sand transport in the mouth of the estuary (Vroom et al., 2015a). Moreover, the 2DH Delft3D-NeVla model has been successfully calibrated, validated and used in multiple morphological studies (e.g. Damen, 2014; Tonnon & van der Werf, 2014; Van der Werf et al., 2015).

For both pathway methodologies, the Delft3D simulations are morphostatic. By fixing the bed level, the computational time can be reduced. Moreover, the temporal variations of the transport pathways can be traced back to varying hydraulic conditions as there is no feedback of morphological changes on the flow velocities and water level. The assumption is that significant bed level changes happen on longer time scales than the periods of interest.

The time spans of the simulations differ. For the graded sediment approach, tracer dispersals are often followed for a period of months/years. After this, the dispersal becomes negligible as the initial tracer deposits are spread and mixed within the bed over a large area. The visualisation tool overestimates the tracer movements and its time scale is therefore less realistic. Depending on the different model settings and sediment transport conditions, the tool is able to compute large-scale transport pathways for much shorter periods (e.g. weeks).

For phase 3, the transport pathway methodologies are applied in a simplified environment. This schematic test case helps to get a better understanding the methods and their conceptual differences. Based on phases 2 and 3, one can determine how the visualisation tool should be used and how its output should be interpreted (RQ1).

The last two phases describe an analysis of the mouth of the Scheldt estuary. Both phases discuss three cases: the current situation, the impact of an island in front of Knokke-Heist and the repositioning of the navigation channel. This last intervention is implemented by extending and deepening the Geul van de Walvischstaart and Deurloo West channels. The interventions are designed based on some initial ideas that were provided in the Masterplan Flanders Bays as inspiration for future efforts. Phase 4 describes the hydrodynamics and sediment transport patterns for the three different cases, based on the regular/standard Delft3D model output. This analysis makes use of the literature review about the Scheldt estuary (phase 1). The findings of phase 4 lead to an answer on RQ2. In phase 5, the mouth of the Scheldt estuary is analysed with the transport pathways generated by the visualisation tool. This analysis utilizes all the gathered knowledge from previous phases. This last phase shows the usage and added value of the visualisation tool for a real-life case. The findings lead to an answer on RQ3.

## 1.4 Outline of the report

In Chapter 2, the relevant physical processes and the characteristics of the Scheldt estuary are described. Chapters 3 and 4 discuss respectively the theories behind transport pathway methodologies and the application on the schematic case. Subsequently, Chapter 5 discusses the Delf3D-NeVla model set up for the three different cases that are analysed for the mouth of the Scheldt estuary. Moreover, Chapter 5 describes the standard model output of Delft3D about the hydrodynamics, sediment transports and erosion-sedimentation patterns. The proof of concept of the visualisation tool for the mouth of the Scheldt estuary is discussed in Chapter 6. The chapter discusses the characteristic transport pathways in the current situation and the response of the pathways on the two large-scale interventions. The discussion of uncertainties and assumptions in the study is included in Chapter 7, followed by the conclusions and recommendations in Chapter 8.

The dispersal of tracers in a system can best be illustrated with a few images that demonstrate changes over time. For this study, the series of images are visualized in a number of movies. These movies are delivered to the reader as separate files.

# 2 Literature review

The chapter starts with a summary of the relevant theories about the hydrodynamics and morphological processes in estuaries. Subsequently, the characteristics of the Scheldt estuary are explained.

## 2.1 Theoretical background

### 2.1.1 Hydrodynamics

#### *2.1.1.1 Tides*

Tides are generated due to a combination of gravitational forces between the earth, moon and sun and the centrifugal forces as a result of the motion of the earth around the centre of gravity of the earth-moon and earth-sun system. The tidal wave caused by the $M_2$ constituent (period of 12 hours and 25 minutes) and the interaction between the $M_2$ and $S_2$ constituents (spring-neap cycle, 14.8 days) are important contributors for this study. While the vertical tide describes the rise and fall of the water level, the horizontal tide refers to the discharges and flow velocities. The relationship between the two depends on the cross-section's shape.

Tidal asymmetry

Tides are distorted while propagating through the oceans, seas and into the confinement of estuaries. When the offshore tidal wave propagates in the shallow southern North Sea, it becomes distorted through its interaction with the bed. Here, tidal waves behave as shallow-water waves for which the propagation is governed by the water depth $\left(c = \sqrt{gh}\right)$ (Wright et al., 1999). Due to the larger water depths at the wave crest, they will move faster than the troughs. Subsequently, the rising part of the tidal wave becomes increasingly steeper and the falling part steadily flattens. The distortion is also affected by friction, convergence, shoaling, partial reflections and interactions of tidal components (Wang et al., 2002).

Vertical tidal asymmetry refers to the distortion between the flood and ebb period. As the tidal wave propagates faster during high water with respect to the propagation during low water, the water level rise is shorter than the period of water fall and the system is flood-dominant. Ebb-dominance describes the opposite case. Horizontal tidal asymmetry is generated when there is a residual sediment transport (Wang et al., 1999). This could be caused by the difference in magnitude between ebb and flood velocities and the non-linear response of sediment transport. When the rising period is shorter than the falling period, the flood velocities are relatively larger and the transport is flood-dominated. Horizontal tidal asymmetry also emerges with the differences in the duration of slack water after ebb and flood.

The tidal distortions can be represented by the non-linear growth of compound constituents and harmonics of the principal astronomical tidal components (van der Spek, 1997). The super position of constituents can be used to define the tidal elevation, discharge en velocity. Eq. (2.1) illustrates the super position principle for the flow velocity u based on the $M_2$ tidal wave and its constituents. $\omega_i$ and $\varphi_i$ express the frequency and phase of the constituent. The $M_0$ component represents the cross-section-averaged residual velocity.

$$u(t) = u_{M_0} + \hat{u}_{M_2} \cos\left(\omega_{M_2} t - \varphi_{M_2}\right) + \sum_i \left(u_i \cos(\omega_i t - \varphi_i)\right) \qquad \text{Eq. (2.1)}$$

The tidal asymmetry introduces a net mass transport into the propagation direction, the Stokes drift. Because there can be no mass-transport through the closed upstream boundary,

this Stokes drift needs to be compensated. Therefore, the water level gradient drives a return flow: the compensation of the Stokes drift.

Tide induced horizontal circulation

There are two types tide induced horizontal circulation: geometry-induced and bathymetry induced circulation (Wang et al., 1999). This first type is caused by for example irregular shorelines (e.g. headland). Bathymetry induced circulation implies that flow concentrates in certain channels at certain times and the residual flow differs for the shallower and deeper parts of the cross-section. Within the (often meandering) ebb channels, the total volume of ebb-flow is larger than the volume during flood. The maximum ebb discharge often occurs near the average water level, when the shoals are not inundated and flow is concentrated in the ebb channel. In a flood channel, the total volume of flood-flow is larger than the volume during ebb. Typically, the maximum discharge for flood is reached when shoals are inundated and flow is more diverged. The water tries to find the shortest route, moves over the intertidal areas and concentrates in straight channels that emerge in the bends of the ebb channel (van Veen et al., 2005). The presence of these channels results in isolated residual eddies.

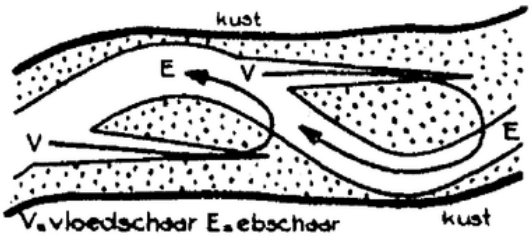


*Figure 2.1 Sketch of the circulating residual flows for situations with ebb and flood channels* (van Veen et al., 2005)

#### *2.1.1.2 Wind and waves*

Wind and short waves can be important factors governing the sand transport in an outer delta and the shallow areas further into an estuary (Elias et al., 2006). Wind-driven currents emerge directly through wind-induced shear stress on the water surface and indirectly via the set-up of water. The waves originate from the wind stress exerted upon a water surface. Wave characteristics (wave height, period and direction) are a function of the prevailing wind (speed, fetch) and water depth.

### 2.1.2 Sediment transport

#### *2.1.2.1 Sediment transport formulation*

The movement of sediment depends on the interaction between the hydrodynamics and sediment properties such as grain size and fall velocity. Moreover, the transport of sediment also depends on the fact whether it is cohesive or non-cohesive. In line with the subsequent chapters, this section only focuses on non-cohesive sediment with a $D_{50}$ of 0.2 mm. For this grain size, there are two important sediment transport modes: bed load and suspended load. Bed load occurs at close proximity to the bed and is directly influenced by instantaneous changes in flow. Here, particles roll, shift or make small jumps over the bed. If the flow velocities exceed some critical value, particles can be lifted up from the bed en be transported within the water column (suspended transport). Suspended load also depends on the relaxation effect. Previous conditions determine the transports at later times.

The sediment transport can schematically be described as function of the velocity (u) with a factor f and power n (Eq. 2.5). Whereas f depends on the sediment and flow properties, n depends on the transport mode (roughly between 1 and 5). Wang et al. (1999) for example used n=3. As result, the relation between sediment transport and flow velocity is non-linear.

$$\vec{s}(t) = f\,\vec{u}^{n}(t) \qquad \text{Eq. (2.5)}$$

Instead of this simple formulation, this study makes uses of the Rijn et al. (2004) sediment transport formulation. The approach makes a distinction between bed load and suspended load based on a reference height “a” (Figure 2.2) and is usually in the order of 1 centimetre. Below the reference height, sediment transport is treated as bed load. Bed load transport depends on the instantaneous bed shear stress, instantaneous velocity, sediment characteristics and a number of other coefficients. Similarly, the suspended load transport (above the reference height) depends (among others) on the effective settling velocity, bed shear stress and turbulence. Generally, the transport rate of suspended sediment in horizontal direction is defined as the integration of the product of velocity (u) and concentration (c) from the edge of the bed-load layer (z=a) to the water surface (z=h).

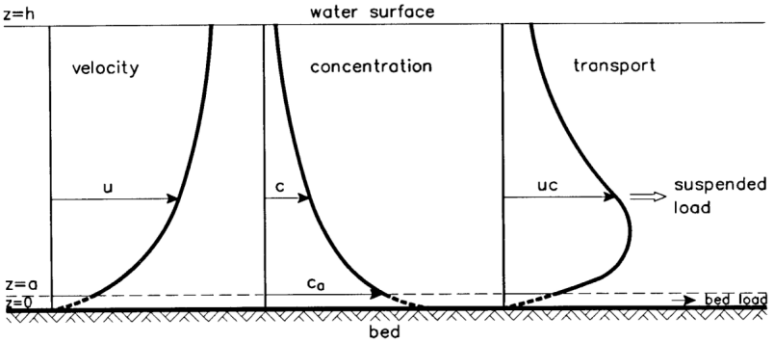


*Figure 2.2 Distinguish bed and suspended load transport based on the reference height a* (van Rijn, 1993)

Usually, the velocity profile is assumed to follow a logarithmic pattern, with the velocities increasing in upward direction. Based on the downward transport of sediment by gravity (settling) and upward directed transport by turbulence processes (mixing), the sediment concentration profile is commonly based on a Rouse distribution. With this, the highest concentrations can be found near the bed. To calculate the concentrations in the water column, the distribution has to be linked with the concentration $c_a$ at the reference height. This concentration is a function of the density of sediment, median grain size, non-dimensional bed-shear and non-dimensional particle diameter. The exact expressions of the reference height, the concentration $c_a$ and other parameters can be found in van Rijn et al. (2001; 2004). As result of the integration, the suspended load is not uniform over the depth. The main part of the suspended transport occurs in the lower section of the water column.

#### *2.1.2.2 Residual sediment transport*

As shown above, sediment transport directly depends on the flow velocities. In this way, residual flow caused by river discharges, tidal induced circulations, stratified flows, Stokes drift and wind; influence the residual sediment transports. Because of the non-linear relation between flow velocity and sediment transport, tidal asymmetry will also lead to residual sediment transport. The short waves that emerge through wind stress can contribute to sediment transports due to wave asymmetry, Stokes drift, currents generated by radiation stresses of breaking (obliquely incident ) waves and the stirring up of sediment (Elias et al., 2006; Verduin, 2009). As stated Section 1.3, the effect of waves and wind in the mouth area of the Scheldt estuary will be neglected.

Van de Kreeke & Robaczewska (1993) expressed the tide-driven net bed load transport based on Eq. (2.4) (with n=3). By describing the flow velocity with Eq. (2.5) and including $K_1$, $S_2$, $N_2$, $M_4$, $M_6$ and $MS_4$ constituents, they showed that the long-term mean bed load transport depends on the residual flow velocity $(u_0)$ and the $M_2$-overtides (Eq. 2.7). In this expression, the phases ($\varphi$) are relative to the $M_2$ tide. They demonstrated (neglecting $M_8$ and higher) that the net bed load is in the direction of the largest flow velocity.

$$\frac{\bar{s}}{f\hat{u}^3} = \frac{3}{2}\frac{u_0}{\hat{u}_{M_2}} + \frac{3}{4}\frac{\hat{u}_{M_4}}{\hat{u}_{M_2}}\cos\left(\varphi_{M_4} - 2\varphi_{M_2}\right) + \frac{3}{2}\frac{\hat{u}_{M_4}}{\hat{u}_{M_2}}\frac{\hat{u}_{M_6}}{\hat{u}_{M_2}}\cos\left(\varphi_{M_4} - \varphi_{M_6}\right) \qquad \text{Eq. (2.7)}$$

A similar mechanism also affects the suspended transport. However, relaxation effects can cause a net suspended load when there is no net transport. The concentration of sediment in suspension lags tidal velocity which can lead to a residual transport in flood-direction if the high-water slack is longer than the low-water slack and vice versa (Wang et al., 1999).

## 2.2 Study area

Because of the focus of this study, the upper part of the estuary will not be discussed.

### *2.2.1.1 Bathymetry*

The funnel-shaped geometry of the Western Scheldt is approximately 60 km long and covers an area of roughly 370 km$^2$. The width gradually decreases from 5 km at Vlissingen and Breskens, to about 1 km near the Dutch-Belgian border (van der Spek, 1997; Van der Werf et al., 2015). The Western Scheldt consists a multiple channel system, with a regular repetitive pattern of mutually evasive meandering ebb-channels and straight flood channels separated by intertidal shoals with secondary channels (Jeuken & Wang, 2010). Intertidal areas are present along the completely embanked shores.

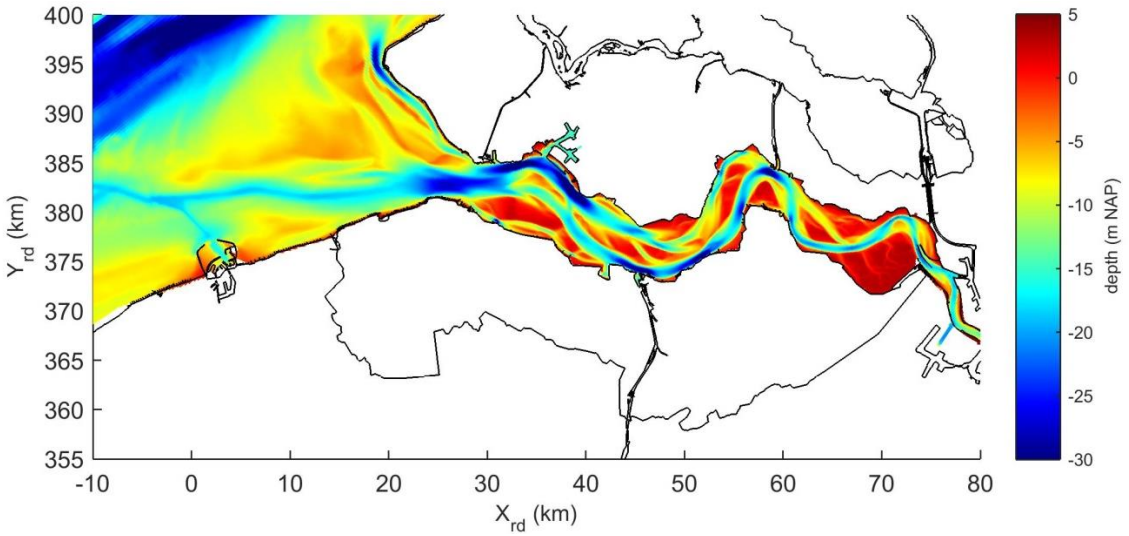


*Figure 2.3 Bathymetry for the year 2011*

The mouth faces the North Sea and is roughly the area between Westkapelle, Zeebrugge, Breskens and Vlissingen (Figure 2.4). The main tidal channel systems in the mouth are the Oostgat-Sardijngeul (along the coast of Walcheren) and Wielingen-Scheur (along the coast of Zeeuws-Vlaanderen). These last two channels form the main navigation route towards the Western Scheldt. North of the Wielingen, one can find the remainders of the old channel Spleet and a new ebb chute channel (hereafter referred to as Geul van de Sluissche Hompels) that has been formed during the last years. Towards the port of Zeebrugge an artificial entrance channel (Pas van het Zand) was constructed (see Section 2.2.1.4). The Oostgat channel runs close to the coast of Walcheren and is flanked by the Bankje van Zoutelande, separating it from the Deurloo Oost channel. In the north, the Oostgat meets with the Geul van de Rassen. In the south, the Oostgat is connected to the Sardijngeul. The area in the middle of the mouth consists of number flats. The large flat Vlakte van Raan is separated from the other flats by the Geul van de Walvischstaart (eastern side) and Deurloo West (north-eastern side). As wave energy can dissipate on the the Vlakte van de Raan, it forms a buffer between the sea climate and the milder climate within the Scheldt estuary.

East of the line Vlissingen-Breskens, there are the channels Honte and Schaar van de Spijkerplaat. The shoals Spijkerplaat and Hoogeplaten are located along these channels.

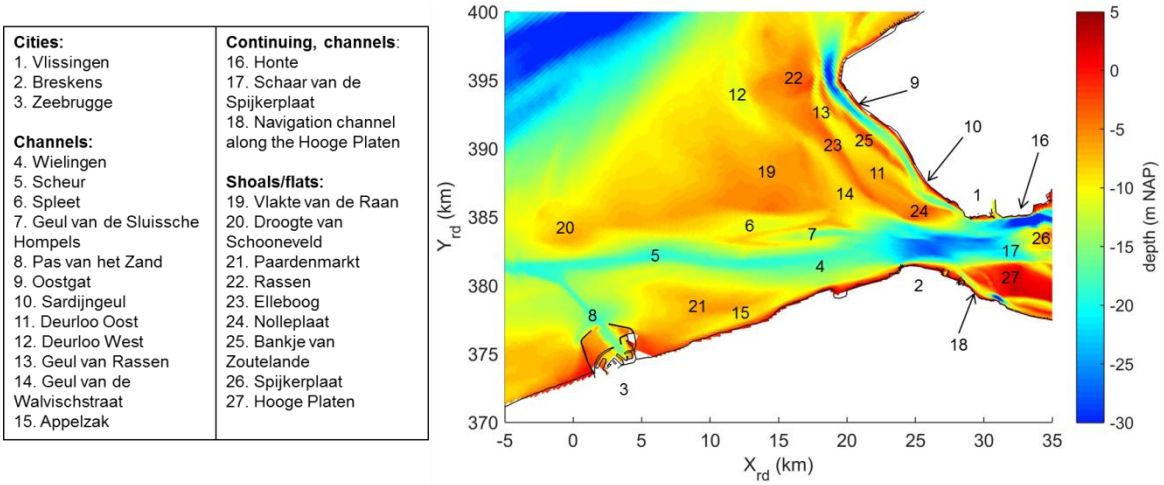


*Figure 2.4 Bathymetry of the mouth area and the most important cities, channels and shoals*

### 2.2.1.2 *Sediment characteristics*

The sediment in the channels and on the shoals of the Western Scheldt mainly consists of sand with less than 10% mud. Along the embankments and on the shoals, the percentage silt can sometimes be much higher. The median diameter $D_{50}$ in the channels is typically larger than 150 µm, on the shoals between 50 and 150 µm and along the estuarine margins smaller than 125 µm. (Consortium Deltares-IMDC-Svasek-Arcadis, 2013a; van Eck, 1999).

Also within the mouth area, the sediment composition is quite heterogeneous. The Vlakte van de Raan, shoals and channels in the south-western part of the mouth are characterised by fine sands (125-250 µm). Coarse sand is found in the Wielingen channel near the connection with the Western Scheldt which is explained by the strong currents over here. Near the port of Zeebrugge and Pas van het Zand, the median grain size is typically smaller than 125 µm. Moreover, this area contains silt fields and has high turbidity levels. The mouth is also characterised by hard, non-erodible layers of clay with a thickness of more than 10 cm that reduce/prevent erosion of the bed. For some areas, these layers are located at or near the bottom surface(Du Four & Van Lancker, 2011; Kuijper, 2015; Vroom et al., 2015b).

### 2.2.1.3 *Hydrodynamics*

The tide in the Western Scheldt is meso- to macro-tidal, semi-diurnal and has a tidal range that increases (because of convergence, shoaling and partial reflections) from 3.8 m at Vlissingen to 5.2 m near Antwerpen. As stated by Wang et al. (1999), the phase difference between the vertical and horizontal tide is about 2.5 to 3 hours, and makes the tidal wave neither completely progressive nor standing. The maximum flood flow occurs 1.5 hours before the end of flood and the ebb flow reaches its maximum 3-4 hours after the beginning of ebb. The maximum depth-averaged velocities in the channels are in the order of 1-1.5 m/s. Because the mean river outflow of the Scheldt (120 m³/s or $1x10^6$ m³ per semi-diurnal tide) is even less than 1% of the mean tidal prism (about $2x10^9$ $m^3$), it plays only a minor role in the hydrodynamics. Consortium Deltares-IMDC-Svasek-Arcadis (2013c) concluded that the return flow due to the Stokes drift (in the order of 0.05 m/s) is an order of magnitude larger than the residual flow due to river discharge (approximately 0.005 m/s). The Western Scheldt is a well to partially mixed system, the vertical density gradients are small and do not significantly influence the flow velocities (compared to the tidal current). Because the inner estuary is also fairly sheltered from the wind and waves climate of the North sea, the Western

Scheldt can be considered to be tide-dominated (Cancino & Neves, 1999; Wang, et al, 2002; Jeuken & Wang, 2010).

With the inference of the tidal waves entering the North Sea from the north (Atlantic Ocean) and southwest (Calais Strait), Coriolis effects and bottom friction, a complicated tidal pattern is created at the south of the North Sea (Dastgheib, 2012; Elias, et al.,2006). The tidal flow at the mouth consists of a northward propagating tide (amplitude decreases towards the north) and a tidal component flowing perpendicular to the coast (increasing amplitude) (Damen, 2014). The incoming tide mainly flows through the Wielingen into the estuary; the discharges and tidal prism through the Oostgat are significantly smaller. At the line Vlissingen-Breskens, the tidal current is based on the interaction of the tides that propagate through these channels and the in-/outflow of the Western Scheldt (Walstra, 2005).

For the channels in the southern part of the mouth, the tidal currents are mainly influenced by phase differences in the vertical tide between Vlissingen and Zeebrugge (near the outflow point of the Scheur). For the channels in front of the coast of Walcheren, also the tidal range difference between Vlissingen (3.8 m) and Westkapelle (4.3 m) is important. As result, slack water happens sooner in the Oostgat-Sardijngeul with respect to the channels in the south. In the north, maximum flow velocities occur at the beginning of the ebb and flood periods (then, the water level gradients are the largest). For the Scheur-Wielingen, the tidal currents are at their maximum at the end of the ebb and flood periods. Besides, the flow velocities at Westkapelle and Vlissingen are influenced by contraction. At the Vlakte van de Raan, the flow has a more circular pattern (Bliek et al., 1998; Plancke et al., 2014; Walstra, 2005)

With the amplification due to the estuary's funnel shape, tidal amplitudes in the mouth are smaller compared to the inner estuary (Dumon et al., 2006). The density-driven currents and river discharge are again of minor importance (Dam et al.,2007; Vroom et al., 2015a). The impact of wind and waves is more pronounced at the mouth compared to inner estuary (Van der Werf et al., 2015). The dominant wind direction is south to southwest and has average velocities of 5 to 7 m/s. The wind driven alongshore and landward sediment transports during average conditions are relatively small compared to the transports generated by tidal currents (Steijn & van der Spek, 2005; Walstra, 2005).

Waves are mainly coming from southwest and northwest and have significant wave heights of about 1 to 2 m at the North Sea (Dumon, et al. 2006). Because of the relatively larger water depths in the outer delta, the effect of average wave conditions is limited to the stirring up of sediment. These average waves break just in front of the coast. For larger storms however, waves can break on the outer delta and significantly increase the sediment transports (Steijn & van der Spek, 2005; Walstra, 2005).

#### *2.2.1.4 Human interventions*

The Western Scheldt has a long history of human interventions. Between the 11$^{th}$ and 20$^{th}$ century, interventions mainly focussed on the reclamation of land that had been silted up by natural processes. With this reclamation, large parts of the intertidal areas were permanently lost, erratic patterns of embankments emerged and the alignment of the estuary became largely fixed. Since the beginning of the 20$^{th}$ century, human interferences shifted towards sand extraction (about 2 million m³/year) and dredging-disposing to deepen and maintain the navigation route to the different ports in the estuary (Jeuken & Wang, 2010; Meersschaut et al., 2004; van den Berg et al., 1996; van der Spek, 1997). With increase in draught of the vessels, a number of deepening campaigns were carried out to keep the navigation route in the Western Scheldt accessible (1970s, 1977/1998 and 2010). Besides these large-scale projects, the maintenance dredging increased from less than 0.5 million m³/year before 1950 to about 10 million m³/year at present (Jeuken & Wang, 2010). The dredging activities take mainly place at the eastern end of estuary.

The ebb-tidal delta has been affected by the construction of the port of Zeebrugge in 1908, the extension of this port in 1986, the Deltaworks and the dredging operations. Currently, the annual dredging volume is about 20 million $m^3$ per year and is mainly dumped inside the mouth itself (Elias & van der Spek, 2015; Steijn & van der Spek, 2005). Van der Slikke (1998) concluded that the total dredged volume between 1960 and 1993 originated mainly from the Wielingen-Scheur (42.5%), Pas van het 't Zand (37%) and the Port of Zeebrugge (19.4%). Haecon (2000, 2006) and Nederbragt & Liek (2004) agree that the current dredging and disposal volumes are much smaller compared to the period 1970-1990. For the period 1985-2013, the sand extraction from the mouth was about 2 million $m^3$ sediment per year. This extraction took mainly place on the Belgian Continental Shelf (Vroom & Schrijvershof, 2015).

Recently, the Flemish government launched the Masterplan Flanders Bays (2014). This plan describes some ideas about large-scale interventions in the mouth of the Scheldt estuary and along the Flemish North Sea coastline to improve protection of the coast against sea-level rise and super-storms. The proposed interventions also focus on an integral long-term vision in which the sustainability and the attractiveness of the coastline should be improved, there is sufficient space for nature and economic development is stimulated.

Ten concrete projects have been developed as an inspiration for further efforts. Some of them aim at the longer term, others can be realised in the foreseeable future. An interesting intervention for this study is the construction of an island in front of Knokke-Heist (east of Zeebrugge) that protects the coast and can be used as tourist attraction, residential area and/or a nature area. This island is located on the Paardenmarkt, a relatively shallow area that is characterised by a bed level increase over past few years (see Section 2.2.1.5).

However, the projects that are proposed may affect the Wielingen-Scheur. The interventions may influence the flow and sediment transport patterns, but there can also be conflicts of interests (e.g. navigation vs. nature and the interests of tourists). A possible solution for this is the repositioning of the main navigation channel to the Geul van de Walvischvaart. By expanding and extending the Geul van de Walvischstraat, sea vessels can move in a straight line in and out of the estuary. The decreased distance towards the estuary enlarges the time slot for the tide dependent access.

#### *2.2.1.5 Changes in morphology*

The Western Scheldt evolved from the Honte, a tidal channel which has been expanding landward since the early Middle Ages. Over time, it gradually took over the function of the Eastern Scheldt which was originally the mouth of the river Scheldt. Whereas the Western Scheldt was first connected with the Eastern Scheldt with shallow, tidal-watershed-like areas and had several branches and tidal flats along the southern shore, these features disappeared (siltation and land reclamation) in the following centuries (van der Spek, 1997). Since approximately 1930, the configuration of the main ebb and flood channels remained unaltered at most locations. However a general steepening of the bathymetry is noticed since 1955. Human interferences are the main cause of this (Kuijper et al., 2004).

About a century ago, the morphological system of the mouth with three main channels (Wielingen-Scheur, Oostgat-Sardijngeul and Deurloo) changed into the current layout with two main channels. Around the $19^{th}/20^{th}$ century, the Deurloo was the main channel that regulated the discharge of water between the Western Scheldt and the sea. Over the years, the channel became divided in a western and eastern part. In between, the shoal Elleboog grew and merged with the Rassen and Nolleplaat. Whereas Deurloo West can still be found at the seaward boundary of the Vlakte van de Raan, Deurloo Oost currently forms an extension of the Sardijngeul. Possible causes seem to be the human interferences in the mouth and the inner estuary, the changing connection between the Western and Eastern

Scheldt and the growth of the Geul van de Walvischstaart (Steijn & van der Spek, 2005; Elias & van der Spek, 2015).

Since this large morphological change, the current positioning of the Wielingen-Scheur and the multiple channels did not change significantly. Although the Eastern Scheldt became partly closed since 1986 (Deltaworks) and human interfered in the Western Scheldt, the two channel system remained stable over the last 45 years. However, human interventions such as dredging-dumping operations had an impact on the morphology of the mouth. These effects were not only local, but also influenced the hydrological and morphological processes on larger scales (Elias & van der Spek, 2015). Bolle et al. (2006) showed that the deepening of the channels can influence the propagation of the tidal wave and the residual sediment transports that are generated by an tidal asymmetry.

By comparing the measured bathymetries of 2011 and 1964, Elias & van der Spek (2015) were able to provide sedimentation-erosion patterns for the last 47 years. As was also observed by Cleveringa (2008), the erosion and deposition rates are the highest along the and in the Oostgat and Wielingen. Their main observations were (Figure 2.5):

- Deepening of the Scheur and Wielingen [polygons 1 and 3]
- Disposal of dredged material in the areas north and south of these channels [2,10,13]
- Bed level increase in the mouth of the Western Scheldt [5-9]
- Deepening of the Oostgat channel, especially and the northern end [30-35]
- Deepening and extension of the Geul van de Walvischstaart [22]
- Growth of the shoal the Elleboog [25]

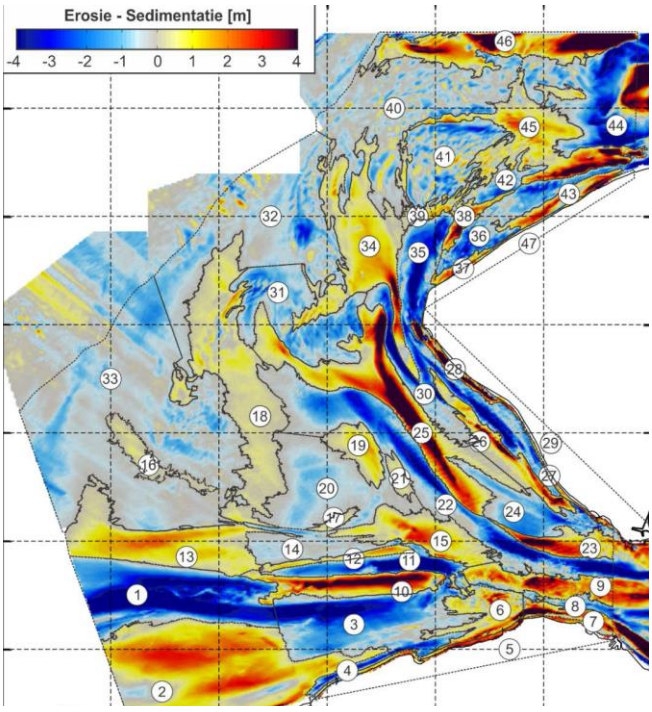


*Figure 2.5 Overview of the bed level changes between 1965 and 2011 (Elias & van der Spek, 2015)*

### 2.2.1.6 *Sediment balances*

Based on sediment balances, several studies agreed on the decreasing inflow of sediment through the inlet into the estuary over the last few decades (Nederbragt & Liek,2004; Nederbragt, 2006); Haecon 2006). Some even found a shift towards export. Consortium Deltares-IMDC-Svasek-Arcadis (2013c) confirmed the decreasing import at the inlet, but also concluded that the net sediment transport became more eastward directed in the central and eastern part of the inner estuary. These opposite trends are possibly caused by respectively a

decreasing flood asymmetry and decreasing residual flow compensating the Stokes Drift. Although based on a number of assumptions, Consortium Deltares-IMDC-Svasek-Arcadis (2013b) showed the importance of making a distinction between the sand and mud balances. They found that the trends at the western end of the inner estuary are different for different sediment fractions: the export of sand (0.52 million $m^3$/yr) and import of mud (0.74 million $m^3$/yr) resulted in an overall sediment import in the period 1994-2010.

In the past, multiple studies also used the measured bathymetries of the mouth to determine sediment balances (Nederbragt & Liek, 2004; Nederbragt, 2006; Haecon, 2006). However, Cleveringa (2008) showed that one cannot compute reliable sand balances for this area without taking into account the measurement inaccuracies. Based on this, Elias & van der Spek (2015) determined a sand balance by correcting for all the unrealistic changes in the bathymetry. For the Dutch part of the ebb-tidal delta, their results showed an increase of the total sediment volume untill 1978 (+1.4 million $m^3$/year) and an almost continious decline in the sediment volume afterwards (-1.4 million $m^3$/year). By also including the Belgian part, the erosion rate increases extremely (-4.9 million $m^3$/year between 1965-2010). This is due to the dumping of the dredged material from the port of Zeebrugge outside the study area.

A sediment balance would be an ideal tool to compute flows of sediment within the mouth. Due to the many degrees of freedom in the relations between the different meso cells and the fact one needs to define a boundary condition, it is impossible to provide a solid, complete and detailed overview of the fluxes within the mouth. Besides, there are they many uncertainties in the bathymetric measurements and data of dredging-dumping operations.

#### *2.2.1.7 Sediment transport patterns in the mouth*

To get an impression of the net bed load transports, one could look to the residual flow velocities and discharges. Based on this, Steijn & van der Spek (2005), Tonnon & van der Werf (2014) and Vroom et al. (2015a) came to the following conclusions (Figure 2.6, left). At the inlet (line Vlissingen-Breskens), the northern part of the inlet shows an ebb-dominant transport while the southern part is more flood-dominant. Moreover, the Wielingen, Scheur, Geul van de Walvischstaart, Geul van de Rassen and the northern part of the Oostgat show an ebb-dominance. The southern part of the Oostgat and Sardijngeul are flood-dominated. To estimate the suspended load transport, Steijn & van der Spek (2005) also computed the residual values with the velocities to the power of three. They came to the same conclusions.

Secondly, the pattern of the residual transports can be estimated by studying the maximum current velocities (Eq. 2.7). Following the KUSTSTROOK model used by Svašek (1998), the flow velocities in the Scheur, Wielingen and at the Vlakte van de Raan are at their maximum at the end of the flood period. Although less clear, the researchers concluded that maximum flow velocities in the Oostgat and Deurloo Oost happen during ebb.

As stated, the residual transport patterns are also influenced by the tidal asymmetry. Vroom et al. (2015a) computed the tidal asymmetry as result of the $M_2$ and $M_4$ constituents along the thalweg (line connecting the lowest points along the length of the main channel). Based on measurements and the newly validated Delft3D-Nevla model, they concluded that the tidal asymmetry within the Wielingen-Scheur shows flood-dominance. However, this dominance decreases when moving towards the west.

Summarized, an analysis of the hydrodynamics does not show unambiguous patterns for the residual sediment transport. However, Verduin (2009) and Tonnon & van der Werf (2014) also numerically calculated the sediment transport itself. In general, the results confirmed the findings about the net flows. However, their results showed a residual transport in the Wielingen in the flood direction. Both computed the sediment transports for a representative

period instead of the entire spring-neap cycle. It is unsure how these periods are exactly chosen and whether these choices significantly influence the results.

Based on a refined Delft3D-NeVla model, Damen (2014) did a detailed analysis of the transport patterns in front of the coast of Walcheren. His conclusions correspond with the sand waves measurements of Erkens (2003). At the northern part of the Oostgat, sediment is transport in northward direction. It is deposited at the Rassen or is deposited in front of the coast of Walcheren. For the central and southern part of the Oostgat, there seems to be a cross-channel imbalance of flows: flood-dominance at the seaward side of the channel (along the Bankje van Zoutelande) and a more ebb-dominated flow at the coastward side. The cross-channel differences can possibly be explained with the inertia of flood flowing around the bend at coast of Walcheren. With the high flow velocities during the incoming flood, flow cannot follow the rotation of the coast and is pushed against the seaward side of the channel. This mechanism eventually results in flood-dominance at the seaward banks of the Oostgat and ebb-dominance in the remaining area (Figure 2.6, lower right). Past the southern tip of the Bankje van Zoutelande (the Galgeput), sand is transported back in northern direction by the ebb-dominated flow in the Sardijngeul and Oost-Deurloo channels. This possibly causes a circulation cell.

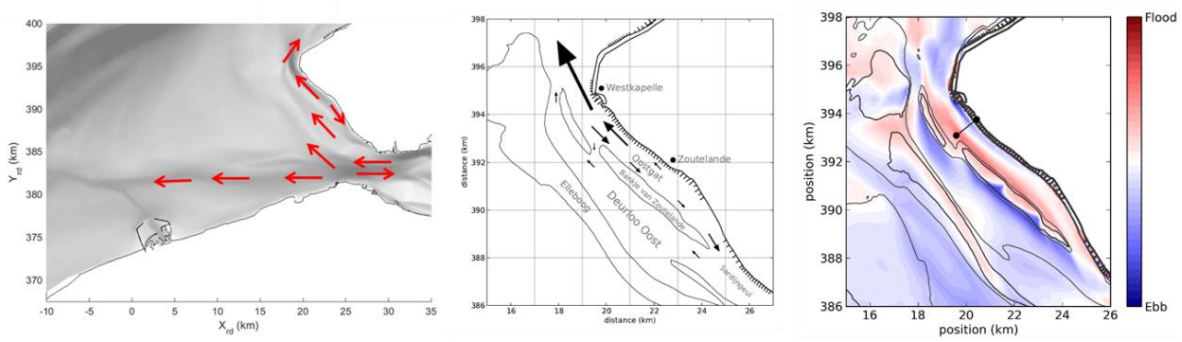


*Figure 2.6 Left: schematic overview of the residual flow patterns, found by Steijn & van der Spek (2005). Middle: schematic description of residual transport patterns for the tidal channel Oostgat. Right: tidal dominance based on a comparison of maximum ebb and flood depth-averaged velocities (Damen, 2014).*

## 2.3 Conclusion

As stated in Section 1.1, the recent attention of the Flemish government to explore large-scale interventions addresses the need for new knowledge and prediction tools for the mouth of the Scheldt estuary. The mouth consists of a number of shoals and channels. The main channel systems are the Oostgat-Sardijngeul and the Wielingen-Scheur. The tidal flow in the mouth consists of two components: a northward propagating tidal wave and a component perpendicular to the coast. Compared to the Western Scheldt, the effects of wind and waves are more pronounced in the mouth. Under average conditions however, the morphological developments outside the coastal area are expected to be mainly determined by the tide.

A number of studies discussed the residual flow and sediment transport patterns in the mouth area. Amongst others, results showed a cross-channel imbalance for the Oostgat and inlet, a circulation cell in front of the coast of Walcheren and ebb-dominance in the Geul van de Walvischstaart. Whereas the residual flow in the Wielingen-Scheur seem to be ebb-dominant, the calculations of Verduin (2009) and Tonnon & van der Werf (2014) showed a residual sediment transport in the flood direction.

# 3 Numerical modelling of sediment transport pathways

This chapter discusses the methods that can be used to numerically compute sediment transport pathways. As stated in Section 1.3, this study uses the Delft3D model. The model is further described in Section 3.1. Subsequently, this chapter discusses the graded sediment method (Section 3.2) and visualisation tool (Section 3.3). For future studies, appendix A.1 provides a manual of the visualisation tool. The chapter ends with a brief conclusion. A discussion of the conceptual differences and the pro's and con's will be given in Chapter 4.

## 3.1 Delft3D modelling software

The Delft3D software is developed by Deltares and the Delft University of Technology. The software solves the coupled, wave-averaged equations to allow the simulation of hydrodynamic flow, computation of the transport of water-borne constituents (e.g. salinity), short wave generation and propagation, sediment transport and morphological changes, and the modelling of ecological processes and water quality parameters (Lesser et al., 2004). This research uses the FLOW module. The module can compute non-steady flow and transport phenomena that result from hydrodynamic forcing on a rectilinear or a curvilinear, boundary fitted grid. The module can solve the shallow water equations in two or three dimensions. It uses a finite difference-scheme to solve the Navier Stokes equations for an incompressible free surface flow, under the shallow water and Boussinesq assumptions (Deltares, 2014).

To minimize the calculation time, the model is based on a depth-averaged regime (2DH). The approach does not include vertical circulations due to density-driven currents and phase shifts between near-bed and near-surface velocities. Secondary flow is not modelled in a 3D approach, but is parameterized. As discussed in Section 1.3, the approach has been successfully used in multiple morphological studies for the Scheldt estuary.

## 3.2 Traditional graded sediment approach

The sediment transport patterns can be determined by tracking multiple fractions in the Delf3D model (the graded sediment approach). It directly follows the dispersion of sediment fractions by studying the changes in concentrations in the bed and water column over time. For this study, the multiple sediment fractions that are followed have the same characteristics but have different labels within the Delft3D model. The differences in the dispersal rates are then solely caused by differences in the availabilities of the fractions in the bed (i.e. identical sediment characteristics). For this, one chooses a specific sediment volume at a specific location and label it as "tracer". The remaining sediment in the study area is then labelled as "native". By following how this tracer fraction is transported from a certain start location towards the surrounding area, transport pathways can be obtained.

Instead of tracking individual grains, the method follows the changes in tracer concentrations over time. The pathways are the straight "lines" that link the start location with the end locations of the tracer sediment at a certain time. The lines show that the tracer sediment in the surrounding can be traced back to the initial deposition location at the beginning of the simulation area. By looking to intermediate time steps, one can make hypotheses about the changes over time. However, the pathways do not contain data about the movement of individual grains in between the start and end of the simulation. For example: some grains may be transported towards the left while others are transported towards the right. This exchange of grains is not shown in the data of the graded sediment approach. There are two bed models that can be used for numerical calculations: the (well) mixed-bed approach and the layered bed approach (see next sections).

This study is uses the van Rijn et al. (2004) sediment transport formulations that compute the bed load and suspended load for each fraction individually. The effect of bed load transport on the bed composition depends on its spatial gradient ($q_{in} - q_{out}$) (Figure 3.1). The deposition (*D*) and erosion (*E*) rates of the suspended load are defined in a single grid cell. In case of the layered bed stratigraphy, there is also the flux *F* that represents the exchange between the upper two layers. The fluxes *E* and $q_{out}$ of a fraction depend on its availability in the bed. So, the erosion rate of a fraction lowers with a decreasing availability/concentration.

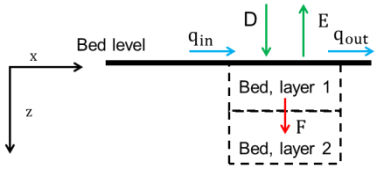


*Figure 3.1 Schematization of the different fluxes in the bed models. See text for an explanation of the fluxes. Flux F only exists in the layer bed approach*

### 3.2.1 Well mixed bed approach

This first approach assumes a bed that is well mixed over the entire depth, without burial or resurfacing of sediment in different layers. All sediment is available for erosion; there is no distinction between sediment depositions from a long time ago and the previous time step.

For this study, the bed level is fixed while the bed thickness ($z_b$) may change over time (Section 1.3). If the cumulative effect of the fluxes for the two fractions is positive (sedimentation, arrow 1 in Figure 3.2), there is an increase of the thickness in downward direction (arrow 2). The z-axis is flipped around; a positive change in the bed thickness is translated in the downward direction. With erosion (arrow 3), the bottom of the bed moves up and results in a thinner bed (arrow 4).

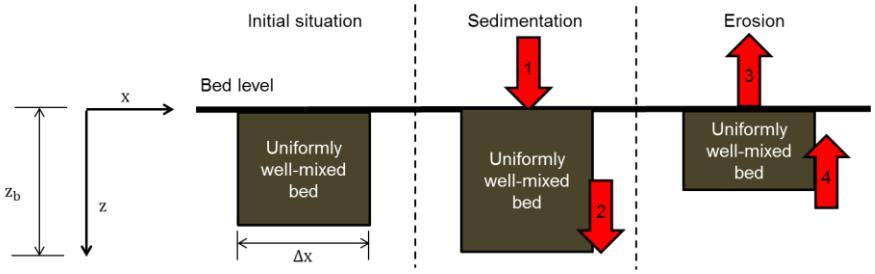


*Figure 3.2 Schematization of changes in the well mixed bed approach for sedimentation and erosion*

#### *3.2.1.1 Equations*

The bed thickness ($z_b$) change depends on the different fluxes of the two fractions:

$$\frac{\partial z_b}{\partial t} = \frac{1}{(1-\varepsilon)\rho\Delta x} * \sum_{i=1}^{2}\left(q_{in,i} - q_{out,i} + D_i - E_i\right) \qquad \text{Eq. (3.1)}$$

With t is time (s), $\varepsilon$ is the porosity, $\rho$ is the density of the sediment (kg/m$^3$) and $\Delta x$ is the width of the grid cell (m). For this study, the porosity and densities are the similar for all fractions. $q_{in}$, $q_{out}$, $D$ and $E$ are expressed in kg/s/m (2D schematization). The fluxes $q_{out,i}$ and $E_i$ are positively related to the mass fraction of fraction i in the bed. A higher mass fraction results in a higher contribution of the fraction to the eroded volume. The mass fraction ($p_i$) can be calculated by comparing the mass of fraction i with the total mass of sediment. Eq. (3.2) describes the mass fraction of tracer sediment ($p_t$), with $m_t$ and $m_n$ being the total masses (in kg/m) of respectively the tracer and native fraction within the bed of a certain grid cell. By rewriting Eq. (3.1), Eq. (3.3) describes the changes of the total mass over time.

$$p_t = \frac{m_t}{m_t + m_n} \qquad \text{Eq. (3.2)}$$

$$\frac{\partial m_i}{\partial t} = (1-\varepsilon)\rho\Delta x \frac{\partial p_i z_b}{\partial t} = (1-\varepsilon)\rho\Delta x \left( z_b \frac{\partial p_i}{\partial t} + p_i \frac{\partial z_b}{\partial t} \right) = q_{in,i} - q_{out,i} + D_i - E_i \qquad \text{Eq. (3.3)}$$

By rewriting the third and fourth part of Eq. (3.3), one can get:

$$\frac{\partial p_i}{\partial t} = \left( \frac{\left( q_{in,i} - q_{out,i} + D_i - E_i \right)}{(1-\varepsilon)\rho\Delta x} - p_i \frac{\partial z_b}{\partial t} \right) / z_b \qquad \text{Eq. (3.4)}$$

Changes in the availability of fraction i depend on (1) the fluxes of the fraction and (2) the changes in the total bed thickness. As shown with Eq. (3.1), the bed thickness changes in the thickness depend on the bed load and suspended load transports of *all* fractions.

#### *3.2.1.2 Bed layer thickness*

Because the contribution of each sediment class to the eroded volume only depends on the availability in the bed, the bed thickness ($z_b$) becomes an important parameter for the dispersal rate (Elias et al., 2011). Thick beds that only contain a small tracer mass (Eq. 3.2, relatively small numerator), result in very low tracer mass fractions and small fluxes $q_{out,i}$ and $E_i$. With thicker beds, the decay of tracer availability due to bed mixing is larger and results in lower dispersal rates.

### 3.2.2 Layered bed approach

Secondly, the morphological changes can also be modelled using the dynamic bed layer model. This model was introduced by Hirano (1971) and is still the most popular sediment continuity model able to deal with mixed sediment in a layered bed stratigraphy. In this study, the traditional one-layer theory is used. In the layered stratigraphy, the uppermost layer acts as a fully-mixed transport layer that exchanges sediment with the water column through erosion and deposition. The contribution of a fraction to the sediment fluxes depends on its availability in the transport layer. With this approach, the transported sediment out of the grid cell depends on the composition of the upper part of the bed. The transport layer has a constant thickness. As will be discussed later, this thickness influences the timescale of different processes at the bed.

The transport layer regulates the exchange with the substrate located underneath. The substrate underneath interacts indirectly with the water column due to the interference of the transport layer. To allow for varying bed composition with depth, this substrate can be defined with multiple layers. These bookkeeping layers account for the bed thickness changes, their thicknesses increase or decrease depending on the prevailing erosion or deposition (Van Der Wegen et al., 2011). In case of a fixed bed level, these changes result in movements of the underlayers in the z-direction (see below). The location of the transport layer is fixed.

When sediment is deposited (arrow 1, Figure 3.3), it is initially added to the transport layer. After mixing, sediment is transported towards the first bookkeeping layer below it (to ensure a constant transport layer thickness) where it mixes with the existing content (arrow 2). If deposition continues (arrow 3) and the predefined maximum layer thickness is reached, the deposited sediment is transported to a new underlayer (arrow 4). If sedimentation continues but the creation of a new layer exceeds the predefined maximum number of layers, the layer(s) at the bottom will stack and form the base layer. The base layer stores information that does not fit in the underlayers. The process of erosion gives a mirrored image. The eroded sediment from the transport layer (arrow 5), has to be compensated by a flux from the underlayer beneath it (arrow 6) to maintain the user-defined thickness (Dastgheib, 2012).

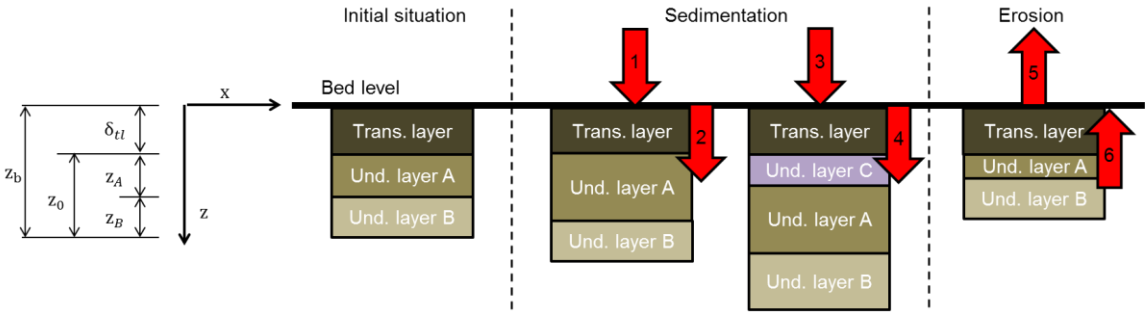


*Figure 3.3 Schematization of burial and resurfacing processes within the layered bed stratigraphy*

The sediment compositions within all layers (the transport layer and underlayers) are allowed to change over time. If the top underlayer is thick enough to facilitate for the entire eroded volume and if its maximum dimension is not reached yet, the exchange of sediment between transport layer and the substrate below is limited to the top underlayer.

### 3.2.2.1 *Equations*

The total bed thickness ($z_b$) is composed out of the transport layer ($\delta_{tl}$) and all the underlayers ($z_0$). As stated, $\delta_{tl}$ is fixed. The fluxes were presented in Figure 3.1.

$$z_b(t) = z_0(t) + \delta_{tl} \qquad \text{Eq. (3.5)}$$

$$\frac{\partial z_b}{\partial t} = \frac{\partial z_0}{\partial t} = \frac{1}{(1-\varepsilon)\rho\Delta x} * \sum_{i=1}^{2}\left(q_{in,i} - q_{out,i} + D_i - E_i\right) \qquad \text{Eq. (3.6)}$$

The change of the mass of sediment fraction i in the transport layer ($m_{i,tl}$) is stated in Eq. (3.7). The flux *F* represents the exchange with the substrate underneath.

$$\frac{\partial m_{i,tl}}{\partial t} = \delta_{tl}(1-\varepsilon)\rho\Delta x\frac{\partial p_{i,tl}}{\partial t} = q_{in,i} - q_{out,i} + D_i - E_i - F_i \qquad \text{Eq. (3.7)}$$

$$\frac{\partial p_{i,tl}}{\partial t} = \frac{\left(q_{in,i} - q_{out,i} + D_i - E_i - F_i\right)}{\delta_{tl}(1-\varepsilon)\rho\Delta x} \qquad \text{Eq. (3.8)}$$

If we assume that the first under layer (underlayer A) thick enough to compensate for the erosion volumes and does not reach the maximum thickness, one can rewrite the equations.

$$\frac{\partial\left(m_{i,tl} + m_{i,A}\right)}{\partial t} = q_{in,i} - q_{out,i} + D_i - E_i \qquad \text{Eq. (3.9)}$$

with $m_{i,A}$ the mass of fraction i in underlayer A and $z_A$ the thickness of this underlayer. Eq. (3.9) states that the cumulative effect of the bed load and suspended transport fluxes is reflected in the changes of the masses within the transport layer and first underlayer By rewriting this, 3.11 shows that the fluxes result in mass fraction changes within both layers and changes in the thickness of layer A.

$$\frac{\partial\left(m_{i,tl} + m_{i,A}\right)}{\partial t} = \delta_{tl}(1-\varepsilon)\rho\Delta x\frac{\partial p_{i,tl}}{\partial t} + \delta_{tl}(1-\varepsilon)\rho\Delta x\frac{\partial z_A p_{i,A}}{\partial t} \qquad \text{Eq. (3.10)}$$

$$\delta_{tl}\frac{\partial p_{i,tl}}{\partial t} + \frac{\partial z_A p_{i,A}}{\partial t} = \frac{\left(q_{in,i} - q_{out,i} + D_i - E_i\right)}{(1-\varepsilon)\rho\Delta x} \qquad \text{Eq. (3.11)}$$

The composition of the burial/resurfacing volume is determined after the erosion and deposition processes in the transport layer are completed and when the sediment in this layer is again fully mixed. In this way, the flux $F_i$ has to be calculated with a numerical scheme.

- Sedimentation, $\frac{\partial z_b}{\partial t} > 0$
  The deposited sediment of $t + \Delta t$ is first mixed within the existing composition of transport layer (determined at time $t$). To ensure a constant transport layer thickness, a sediment flux is created from towards the first underlayer. The composition of this flux is determined based on the new composition of the transport layer.
- Erosion, $\frac{\partial z_b}{\partial t} < 0$
  Due to erosion, the thickness of the transport layer becomes smaller than $\delta_{tl}$. To compensate for this, a sediment flux is created from the first underlayer towards the transport layer. The composition of this depends on the composition of the underlayer. As last step, the existing and new sediment in the transport layer are mixed.

If the first underlayer is not thick enough to fulfil the entire flux towards the transport layer or if its maximum thickness is reached, the transport layer exchanges sediment with multiple underlayers and the equations become more complicated (extra terms added).

#### *3.2.2.2 Transport layer thickness*

Having a transport layer is essential for the characterization of the sediment mixture available for transport (Ribberink, 1987). For numerical stability and the prevention of mass balance errors, bed level changes should not exceed or approximate this thickness (Van Der Wegen et al., 2011). Moreover, the thickness is an important parameter for the dispersal rate of the tracer fraction. With the decay of tracer availability due to bed mixing and lag effects due to burial and resurfacing of sediments, very thin and very thick transport layers can result in the "disappearance" of tracers (very low concentrations and low dispersal rate).

With the same tracer mass, a thin transport layer results in higher mass fractions compared to a thicker layer. As result, the dispersal of the tracers goes quicker. Also the effects of the burial and resurfacing processes are more pronounced with thinner transport layers. Tracer sediment that is deposited in a certain cell can be quickly buried, becomes inactive (until it moves back into the transport layer) and results in a decrease of the dispersal rate. A very thick transport layer can prevent that deposited material is quickly moved to the underlayers. However, this approximates the uniformly well-mixed bed (no vertical sorting profile). Moreover, a thicker transport layer results in larger decays in the tracer availability and lower dispersal rates. Also the impact of resurfacing processes is larger with thinner transport layers. The relative mass of the resurfaced sediment (compared to the total mass of the transport layer) increases with smaller thicknesses. In other words, the change in the mass fractions is larger.

With the multiple applications and multiple modifications of the bed layer model, there is no precise definition of the transport layer thickness. Previous studies took into account: the grain size distribution of the bed surface material, strength of the flow and bed forms (Wong et al., 2007). Ribberink (1987) for example stated that the thickness is half of the mean bed form height. Depending on the application and the bed level changes per time step, the thickness is typically in the order of 1-50 cm (Elias et al., 2011).

### 3.3 Sediment transport pathways visualisation tool

Based on the existing Matlab code as provided by E. Elias and M. van Ormondt and some improvements on the code, the remaining part of this section explains the concepts behind the visualisation tool. Currently, there is no other documentation available about the tool.

By solving the momentum, continuity and sediment transport equations, Delft3D computes sediment transport maps that represent the sediment transport ($s_{tot}$ in $m^3/m/s$) in u and v direction for each grid cell over time. By studying series of *time dependent* vector fields, someone can improve his/her understanding about a morphological system. As the maps may contain a lot of temporal and spatial variations, such an (visual) analysis can be difficult. It becomes even more difficult if somebody does not have enough knowledge about the study area and the theoretical background.

The sediment transport patterns are visualized by following the displacements of numerical *tracer particles* step by step through the vector fields. It uses Eulerian data to visualize the sediment transports in a Lagrangian way. As the particles do not interact with the bed, the dispersal of tracer particles is not influenced by decay in tracer availability due to bed mixing and lag effects due to burial and resurfacing. As stated in Section 1.3, the Delft3D simulations should be based on fixed bed levels and bed compositions. The analysis can be based on one or multiple particles that are released at once or continuously. With a continuous release, the effect of the release time (e.g. releasing during ebb vs. flood) can be studied. If the release time has no/little effect, the particles convergence to a single pathway. In the other situation, particles are distributed over a larger area.

### 3.3.1 Theory behind the visualisation tool

#### *3.3.1.1 Computing the sediment transport velocity*

In the visualisation method, particles move through a study domain with discrete time steps ($\Delta t_{pm}$, pm stands for particle movement) for which the vector field is updated with a specific interval ($\Delta t_{d3d-output}$). For simplicity, assume that the particle's location ($P_{t+1}$) at t+1 can be computed with the standard Euler's method:

$$\overrightarrow{P_{t+1}} = \vec{P_t} + \Delta t_{pm} * \vec{C_t} \qquad \text{Eq. (3.12)}$$

In words, the displacement at a specific time t depends on the magnitude and direction of the velocity at that time ($\vec{C_t}$) and the time step size. To distinguish this velocity from the flow velocity, $\vec{C_t}$ is referred to as the "transport velocity". The transport velocity (m/s) is a conversion of the total (bed and suspended load) sediment transport ($\vec{s_t}$ in $m^3/m/s$):

$$\vec{C_t} = \vec{s_t} * \alpha \qquad \text{Eq. (3.13)}$$

$U_t$ and $V_t$ refer to the transport velocities in respectively the x- and y-direction. The parameter $\alpha$ (1/m) is the so-called acceleration coefficient and accommodates the conversion from sediment transport to transport velocity. The word "acceleration" refers to the fact that it extrapolates the particle movement.

#### *3.3.1.2 Bilinear interpolation*

While the particle displacements and locations are determined in a "continuous" way (not bound by grid spacing), the transport velocity ($\vec{C_t}$) field is based on a grid. To obtain the transport velocity at an arbitrary point in space, an interpolation method is required. Based on the assumption that the grid is accurate enough for the usual Delft3D computations and the variation in the sediment transports between two neighbouring data points is relatively small, the present work is based on bilinear interpolation. The idea is to perform linear interpolation in one direction, and then again in the other direction. Eq. (3.14) shows the computation of the transport velocity at point 5 in Figure 3.4. The weighing factors are printed in red.

$$\vec{C_t} = \frac{a}{\Delta x} * \left( \frac{b}{\Delta y} * \vec{C_{t,1}} + \frac{\Delta y - b}{\Delta y} * \vec{C_{t,3}} \right) + \frac{\Delta x - a}{\Delta x} \left( \frac{b}{\Delta y} * \vec{C_{t,2}} + \frac{\Delta y - b}{\Delta y} * \vec{C_{t,4}} \right) \qquad \text{Eq. (3.14)}$$

### 3.3.1.3 *Numerical algorithm used for particle movement*

The computational time decreases (fewer time steps) and the numerical error increases with higher values $\Delta t_{pm}$. The numerical algorithm used for the determination of the particle's displacement can be used as a mediator between these two considerations. Section 3.3.1.1 already introduced one possible numerical algorithm: the Euler's method (Eq. 3.12). With this, the displacement of a particle depends solely on the transport velocity at the position $P_t$ (the start position). The method does not account for transport velocities the particle "feels" along the streamline. Instead of using the Euler's method that has an error estimate which is bounded by $O(\Delta t^2)^3$, one could also use a higher order Runge-Kutta (RK) algorithm (Joy, 2007). The commonly used 2nd order RK approach (RK2) states:

$$\overrightarrow{P_{t+1}} = \overrightarrow{P_t} + \frac{\overrightarrow{C_t} + \overrightarrow{C_{t,pr=1}}}{2}\Delta t_{pm} \qquad \text{Eq. (3.15)}$$

$\overrightarrow{C_{t,1}}$, the vector corresponding to the point $P'_{t,pr=1} = P_t + \Delta t_{pm}\overrightarrow{C_t}$

With this approach, the particle displacement depends on the transport velocity at the start location ($\overrightarrow{C_t}$) and the velocity ($\overrightarrow{C_{t,pr=1}}$) at one prediction point ($\overrightarrow{P_{t,pr=1}}$). Both velocities have to be derived with a bi-linear interpolation within the sediment transport map of time t. This method has an error estimate bounded by $O(\Delta t^3)$. The 4th order RK method (RK4) utilizes even more predictor and corrector steps (Figure 3.4, right). It combines the transport velocities of the start location ($\overrightarrow{P_t}$) and 3 prediction points ($\overrightarrow{P_{t,pr=1}}$, $\overrightarrow{P_{t,pr=2}}$ and $\overrightarrow{P_{t,pr=3}}$) to compute the particle's location at t+1 ($\overrightarrow{P_{t+1}}$). The error is now bounded by $O(\Delta t^4)$.

$$\overrightarrow{P_{t+1}} = \overrightarrow{P_t} + \frac{1}{6}\Delta t_{pm}\overrightarrow{C_t} + \frac{1}{3}\Delta t_{pm}\overrightarrow{C_{t,pr=1}} + \frac{1}{3}\Delta t_{pm}\overrightarrow{C_{t,pr=2}} + \frac{1}{6}\Delta t_{pm}\overrightarrow{C_{t,pr=3}} \qquad \text{Eq. (3.16)}$$

$\overrightarrow{C_t}$ , the vector corresponding to point $P_t$

$\overrightarrow{C_{t,pr=1}}$, the vector corresponding to the point $\overrightarrow{P_{t,pr=1}} = \overrightarrow{P_t} + \frac{1}{2}\Delta t_{pm}\overrightarrow{C_t}$

$\overrightarrow{C_{t,pr=2}}$, the vector corresponding to the point $\overrightarrow{P_{t,pr=2}} = \overrightarrow{P_t} + \frac{1}{2}\Delta t_{pm}\overrightarrow{C_{t,pr=1}}$

$\overrightarrow{C_{t,pr=3}}$, the vector corresponding to the point $\overrightarrow{P_{t,pr=3}} = \overrightarrow{P_t} + \Delta t_{pm}\overrightarrow{C_{t,pr=2}}$

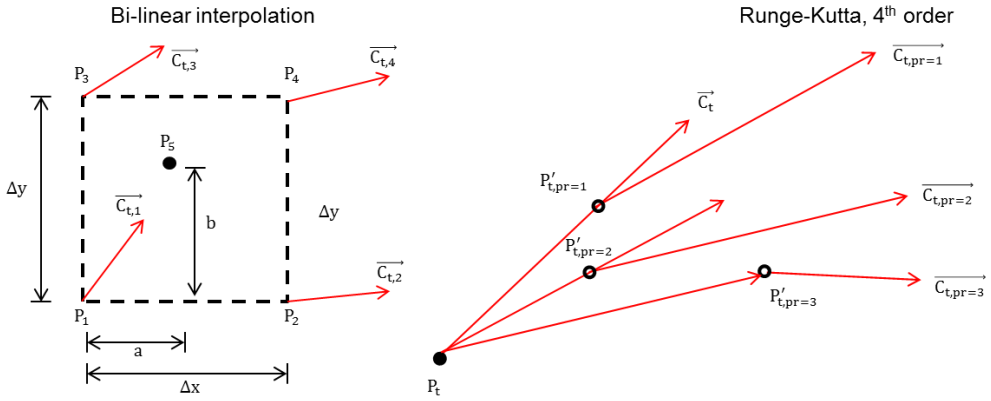


*Figure 3.4 Left: Example of bilinear interpolation. $P_5$ is the position for which the sediment transport vector has to be determined. For the other 4 locations, the vectors are already known. Right: schematization of 4th order Runge Kutta method. The transport vector at position $P_t$ is determined based on a number of prediction and correction steps. See text for a description of the symbols*

Figure 3.5 shows an example with a circular velocity field that is constant over time. Within this field, the x- and y-components of the transport velocities grow linearly with increasing distance from the origin (25, 25). For very small time steps, all three algorithms are able to give a reasonable approximation of the true transport pathway: a circular path. With a larger

time step (the example shown in Figure 3.5), one can see that Euler's method and 2nd order Runge-Kutta algorithm are not able to cope "centripetal force" that keeps particle at the original radius. The particle leaves the original orbital motion around the origin and moves to the outside. The extra intermediate steps in the RK4 method are able to correct for changes in the velocities the particle experiences when it moves along its streamline. There is still a numerical error however, the algorithm is not able to include all spatial information. Using an more sophisticated algorithm can improve the accuracy, but also requires more computational time. The original code was based on the RK2 method. To improve the accuracy and still keep acceptable computational times, this study replaces it with the RK4 method.

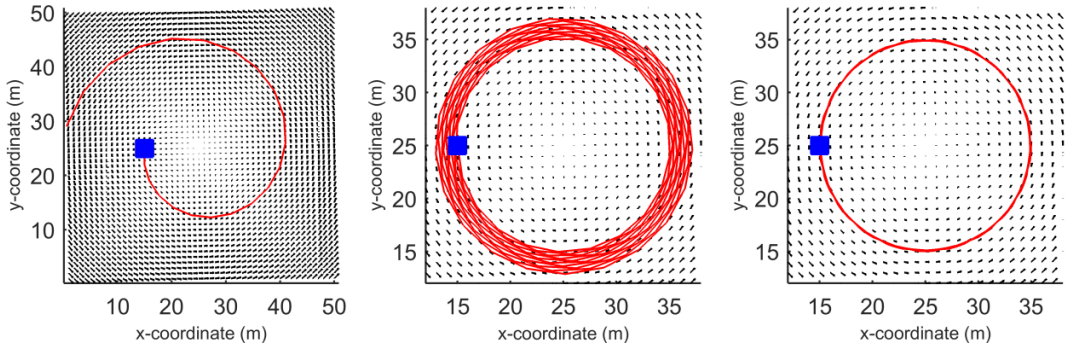


*Figure 3.5 Transport pathway of particle in circular velocity vector field (anti-clockwise). Left: Euler's method. Middle: 2nd order Runge-Kutta. Right: 4th order Runge-Kutta. Particle is released at location (15,25).*

### 3.3.1.4 *Time step for updating the sediment transport fields and interpolation between vector fields*

The numerical particles move through vector fields that are updated with a constant interval ($\Delta t_{d3d-output}$). Each field describes the time-averaged sediment transports between $t - 0.5 * \Delta t_{d3d-output}$ and $t + 0.5 * \Delta t_{d3d-output}$. Because of these time-varying vector fields, another interpolation method is used. The vector field that is used for the particle movement is based on an interpolation (over time) between the two vector fields that lie closest to time t. Eq. (3.17) shows how the velocity at a data point is computed based on the maps of $t_1$ and $t_2$.

$$\overrightarrow{C_t} = \frac{t - t_1}{t_2 - t_1}\overrightarrow{C_{t1}} + \frac{t - t_2}{t_2 - t_1}\overrightarrow{C_{t2}} \qquad \text{Eq. (3.17)}$$

### 3.3.1.5 *Random walk*

To get larger tracer dispersals and determine the sensitivity of the pathways for spatial variations in the sediment transport fields, one could select a large set of start locations and study their tracer dispersals. An easier and quicker way to do this, is adding a randomly generated velocity on top of the transport velocity determined with the sediment transport maps. This extra displacement should not be linked with the diffusive processes included in the momentum and advection-diffusion equations of the Delf3D calculations. The random walk component is just a way to get a larger spreading of particles and see whether a small deviation from the original pathway can result in large deviations in the end location.

In the equations below, "stv" and "rw" stand for the transport velocities related to the sediment transport vectors and random walk component. The extra random velocity has an angle that is randomly selected (θ), with a uniform probability function. The magnitude of the random velocity ($\|\overrightarrow{C_{t,rw}}\|$) depends on the transport velocity derived from the vector field ($\|\overrightarrow{C_{t,stv}}\|$) and a random number R that is generated from a folded normal distribution ($\mu = 0$ and $\sigma = \beta$). Thus, R is the scaling factor between the non-random and randomly generated velocity. The parameter β is the so-called random walk coefficient, indicates the standard deviation of the normal distribution and is a calibration coefficient. With a higher value for β, the probability that the particle gets a large random displacement increases.

$$\left\|\overrightarrow{C_{t,stv}}\right\| = \sqrt{\left(x_{t+1} - x_t / \Delta t_{pm}\right)^2 + \left(y_{t+1} - y / \Delta t_{pm}\right)^2} \qquad \text{Eq. (3.18)}$$

$$\left\|\overrightarrow{C_{t,rw}}\right\| = \left\|\overrightarrow{C_{t,stv}}\right\| R \qquad \text{Eq. (3.19)}$$

$$U_{t,rw} = \left\|\overrightarrow{C_{t,rw}}\right\| \cos\theta \qquad \text{Eq. (3.20)}$$

$$V_{t,rw} = \left\|\overrightarrow{C_{t,rw}}\right\| \sin\theta \qquad \text{Eq. (3.21)}$$

$$\overrightarrow{C_t} = \overrightarrow{C_{t,stv}} + \overrightarrow{C_{t,rw}} \qquad \text{Eq. (3.22)}$$

3.3.2 Selecting the time steps for particle movement calculations and updating the vector fields

Based on Section 3.3.1, the parameters $\Delta t_{pm}$ and $\Delta t_{d3d-output}$ can be further discussed. Both depend on the spatial and temporal scales of the sediment transport.

3.3.2.1 Spatial scale within sediment transport

Changing the time step for particle movement calculations affects the particle movement over $1x\Delta t_{pm}$ (Eq. 3.15). In other words, the value of $\Delta t_{pm}$ determines the number of steps a particle takes within a simulation period T. As an illustration, consider a single vector field that describes a uniform stationary flow (see example 1). In this case, the variable $\Delta t_{pm}$ does not directly influence the distance a particle travels within period T. With a higher value for $\Delta t_{pm}$, a particle just takes fewer steps to end up at the same location and ultimately leads to a reduction in the computational time. There are no side-effects for the pathways.

**Example 1, Figure 3.6**
Particle movement is monitored for two different values of $\Delta t_{pm}$ (cases A and B). As expected, the particles move in the direction of the vectors. The cases have the same pathway over the period t=70 seconds. However, the displacement per time step differs.

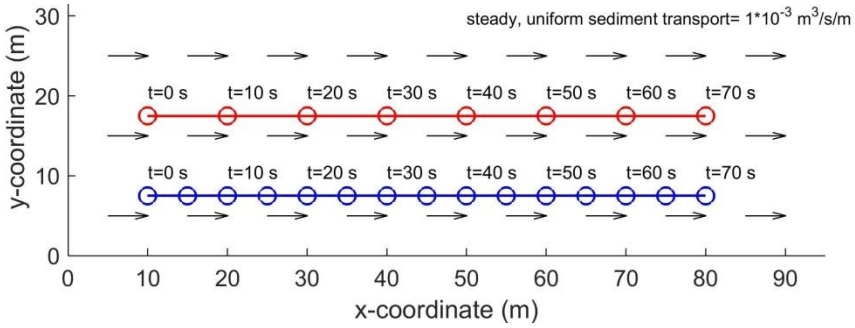


*Figure 3.6 Two cases as illustration for example 1.Case A (red): $\Delta t_{pm} = 10s$, $\alpha$ =1000m$^{-1}$ and T=35s. Case B (blue): $\Delta t_{pm} = 5s$, $\alpha$ =1000m$^{-1}$ and T=20s.*

As second case, assume a stationary flow pattern with spatial gradients in the sediment transport. For an algorithm that includes an unlimited amount of prediction and correction steps to determine the particle displacement over 1 time step, $\Delta t_{pm}$ can be increased to infinity and still lead to the pathways that follow the spatial variations in the vector field. However, this method requires a long computational time. Because the number of correction and prediction steps in the RK4 method is limited, the numerical error due to the spatial variations in the vector fields growths with higher values for $\Delta t_{pm}$. The RK4 method is unable to take into account all transport velocities a particle experiences when moving from A to B. The tool becomes more sensitive in case of higher velocities and larger spatial variations. In the circular velocity field of Figure 3.5 for example, higher values for $\Delta t_{pm}$ lead to the fact a particle leaves the circular motion. The box below discusses another example. The variable

$\Delta t_{pm}$ should be chosen such that the particle still follows the patterns presented in the vector field. Thus, the displacement per 1x$\Delta t_{pm}$ should be a lot smaller than the length scale seen in the spatial variation of the sediment transport.

**Example 2, Figure 3.7**
Figure 3.7 illustrates the transport pathways in a system with steady transport velocities and a meandering flow pattern. Based on the different values for $\Delta t_{pm}$, three cases are shown. The pathways of the first two cases still follow the curves of the vector field. For the last two cases (same $\Delta t_{pm}$, different release location), it is clear that $\Delta t_{pm}$ is too high and spatial variations of the vector field are not well incorporated in the pathways.

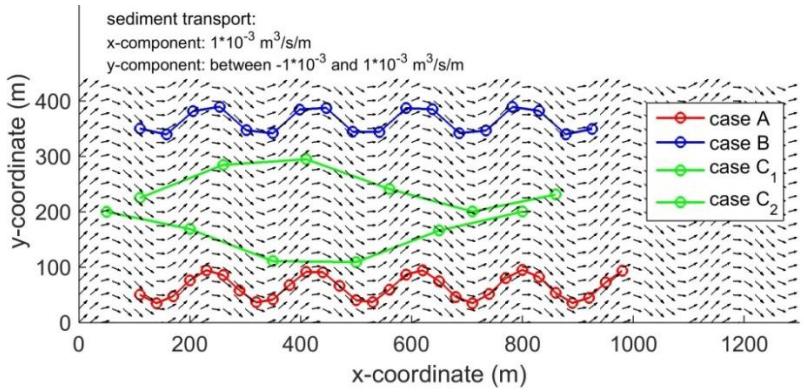


*Figure 3.7 Three cases as illustration for case 1. Case A: $\Delta t_{pm}$ =5s, $\alpha$ = 6000m$^{-1}$ and T=150s. Case B: $\Delta t_{pm}$ =8s, $\alpha$ =6000m$^{-1}$ and T=150s.Case $C_1$=$C_2$: $\Delta t_{pm}$ =25s, $\alpha$ =6000m$^{-1}$ and T=150s.*

For a system with time varying sediment transports, the numerical error varies over time and can be more difficult to analyse.

3.3.2.2 Temporal scale within sediment transport

The previous two examples assumed a system with stationary flow. However, the visualisation tool should also be applicable to study time-varying sediment transports. Let's assume a system with oscillating flow that is caused by tidal currents

The variable $\Delta t_{d3d-output}$ determines the temporal resolution of the vector fields. With increasing intervals, the transport conditions are averaged over longer periods and the linear interpolation method that is used for temporal variation (Section 3.3.1.4) deviates from the non-linear trend that really exists within this interval. The to and fro motion in the sediment transport conditions with its periods of acceleration, deceleration and slack water gradually turns into a constant transport. Example 3 discusses this effect in a system with uniform oscillating flow. Here, $\Delta t_{d3d-output}$ only influences the particle's orbital motion, it does not affect the end location. This statement is true as long as the simulation period is a multiple of the period of the composed tidal wave.

***Example 3. Movie 3.1***
To show the effect of $\Delta t_{d3d-output}$ on the orbital motion of a particle, we schematize the study domain as a straight channel with a uniform oscillating flow ($M_2$+$M_4$). The residual sediment transport is the same for the entire domain. In this example, particles are followed with four different values for $\Delta t_{d3d-output}$. $\Delta t_{d3d-output}$ is always a fraction (1/n, n being an integer) of the total tidal wave period. The parameter $\Delta t_{pm}$ is equal to 1 min for all cases. Movie 3.2 demonstrates that $\Delta t_{d3d-output}$ affects the to and fro motions, but does not influence the particle's location at the end of the simulation.

For a system *with* spatial and temporal variations, this orbital motion is of importance for the residual movement of a particle (will be explained in Section 3.3.3). Because of this, it is important that $\Delta t_{d3d-output}$ is chosen based on the temporal scale of the sediment transports. The interval should be sufficiently small to incorporate the relevant temporal trends. When we for example consider a tidal wave that consists of semi-diurnal, quarter-diurnal and sixth-diurnal constituents, $\Delta t_{pm}$ should at least be smaller than a third of the period of the semi-diurnal tide. However, this is just an upper limit. To correctly represent the slack water period and the accelerating and deceleration of the flow, the interval should be much smaller. However, this also increases the computational time and data volume.

The variable $\Delta t_{pm}$ defines the temporal variation for the particle movement (the output) and can refine the temporal resolution of the sediment transport maps. The ratio $\Delta t_{d3d-output}/\Delta t_{pm}$ should not be smaller than 1. One should not compute the particle movement based on a large time step when high resolution data is available.

*3.3.2.3 Procedures to select the parameter values*

As stated above, one should take into account multiple aspects when choosing the values for $\Delta t_{d3d-output}$ and $\Delta t_{pm}$: accuracy, computational time and amount of data. The sensitivity of the pathways for these variables increase with higher transport velocities and larger spatial variations.

The interval $\Delta t_{d3d-output}$ should be low enough to make sure that the vector fields are able to represent the important temporal variations in the sediment transport. For a system with tidal currents, one could say that there should be a number of maps (e.g. 10) representing the most important tidal constituents. Because these temporal variations can also differ spatially, the exact impact of $\Delta t_{d3d-output}$ on the transport pathways can only be found by trial and error. For a coastal zone with the semi-diurnal tide as the main driver, an interval of about 15-30 minutes seem reasonable.

To ensure that the temporal resolution of the input data is also used within the visualisation tool, $\Delta t_{pm}$ should be smaller or equal to $\Delta t_{d3d-output}$. Furthermore, $\Delta t_{pm}$ should be refined to make sure that the particle follows the spatial patterns presented in the vector fields. $\Delta t_{pm}$ can be selected with two procedures.

First, the time step $\Delta t_{pm}$ can be increased until the deviations in the pathways become too large. This stop criterion depends on the simulation period, spatial variations, the grid cell size and the user's preferences about the balance between numerical error and computational time. It can be based on a comparison of i) the computed pathway with the vector field(s) of interest, and/or ii) the pathways computed with different time step sizes.

Secondly, there is a more quantitative approach that compares the computed displacements with the grid resolution. This criterion can be expressed through the Speed-Number (SN):

$$\mathrm{SN} = \max\left(\frac{\left\|\overrightarrow{C_{t,tot}}\right\|\Delta t_{pm}}{R_{\Delta x,\Delta y}}\right), \mathrm{SN\ should\ be} < \mathrm{N} \qquad \text{Eq. (3.23)}$$

where $\left\|\overrightarrow{C_{t,tot}}\right\|$ is the magnitude of the particle transport velocity and $R_{\Delta x,\Delta y}$ is the grid resolution (square root of the grid cell surface area). The speed number (SN) is defined in a similar way as Courant-Friedrichts-Lewy number. The rule states that the particle displacements should be smaller than N times the grid cell resolution.

The equation can be solved by combining a user-defined maximum allowable relative displacement (N), the maximum transport velocities and grid resolution. The SN number should be based on the transport velocities and grid resolutions the particles really come across/"experience" during the simulation. In other words, it is unnecessary to use a very small time step size if the particles do not come close to the data points with high velocities and high grid resolutions that are located elsewhere in the study domain. If the particles only travel across an area with larger grid spacing and/or lower transport velocities, a very small time step may require too much computational time. However, this calculation of the SN number is based on data of the transport pathways and can only be performed at the end of the visualisation tool.

A save option could be to set N at 1. In this way, the movement of a numerical particle cannot be larger than the grid resolution. However, there is no strict rule for the value of N that should be applied for every case. Systems with small spatial gradients allow for larger values for N compared to systems with very large variations. Usually, the resolution of the computational grid is already coarsened and refined based on the spatial variation in the morphology, flow and sediment transport. If the grid resolution is perfectly adapted to the spatial variations in the sediment transport, the factor N does not have to be adjusted.

### 3.3.3 Selecting the acceleration coefficient

#### *3.3.3.1 Effect of transport velocities on particle movement*

The behaviour of a numerical particle with high and low velocities can differ. As the acceleration coefficient is the factor that converts the sediment transport ($m^3/m/s$) into transport velocities (m/s), it can influence the movements of particles.

To illustrate this, we consider an example where $\Delta t_{pm}$ and $\Delta t_{d3d-output}$ are small enough to significantly reduce the numerical error of the RK4 method and ensure that the temporal resolution is high enough. For this example, different cases are created by varying the magnitudes of the transport velocities (uniform over time and space). In situations with oscillating flow without spatial differences in the sediment transports, larger transport velocities just reduce the period a particle needs to travel from A to B. In case of larger transport velocities, the particle gets a larger oscillating motion and also the residual movement per tidal cycle is larger.

To make the different cases comparable, the simulation period has to be corrected for the differences in the magnitudes. For magnitudes that are X times as high compared to a certain reference case, the simulation period has to be X times as short. Now, the end location of the particle is the same for all cases. However, the particle still has different orbital motions for the various cases. Usually however, a morphological system *does* contain spatial variations in the sediment transports. In this situation, the magnitudes of the velocities *do* influence the particle's end location after the corrected simulation period.

With low values for transport velocities, a particle is displaced with small steps and the prediction points of the RK4 method (Eq. 3.15) lie close to start position ($P_t$). If a particle moves barely during one cycle, the distances between the particle and the 4 surrounding data points (the weighing factors in the bilinear interpolation) do not change significantly. In this way, the particle's residual movement over 1 cycle follows the residual transport that is present at the initial location.

The size of a particle's oscillating motion grows with higher transport velocities. In these cases, the distances between the particle and the 4 surrounding data points increase and decrease significantly with the to and fro motion over one cycle. When the velocities increase even further, the orbital motion becomes larger than spacing between the data points. If the

instantaneous and residual sediment transports are not uniform over space, the particle's residual movement starts to depend on the size of the orbital motion. With larger transport velocities, the particle travels over large distances and "meets"/"feels" multiple other data points. The sediment transport patterns at these points will have an effect on the particle's pathway and it is not only residual transport at the initial location that defines the residual movement. The longer a particle resides near a data point, the larger its influence on the residual movement. The effect of the orbital motion increases with larger spatial gradients. The effect of the orbital motion can best be further analysed with an extreme case: a morphological system that contains both ebb and flood-dominant zones.

**Example 4. Figure 3.8**
Figure 3.8 sketches a domain with an ebb and flood-dominant zone, the boundary lies exactly in the middle. The respectively ebb and flood-dominance increase when moving away from the boundary. The figure demonstrates the pathways of particles that are released during flood (towards the right) with high and low transport velocities. The particles are followed for 1 tidal cycle. The oscillating motions are described with the parameters $d_a$ and $d_b$. The size of this motion and the spatial variations over this length determine the particle's residual movement.

In case A, the transport velocities are small and the particle stays close to the initial location. The orbital motion ($d_a$) is small and shows that the particle stays in the ebb-dominant zone. Thus, the particle gets a residual movement towards the left. With larger transport velocities, the orbital motion growths and the particle may be may be able to move into the flood-dominant zone for a while. If the particle resides here only for a very short time and/or if the flood-dominance is only small compared to the ebb-dominance, the residual movement is still ebb-dominant. By increasing the magnitudes of the transport velocities, the size of the orbital motion and the penetration into the flood-dominant zone grow even further. At a certain point (illustrated with case B), the movement into the flood-dominant zone becomes so large that it can dominate the residual movement. Although the residual transport at the initial location is ebb directed, the particle gradually moves towards the right.

**Example 5. Movie 3.3**
In this example, the system consists of a straight channel. The sediment transport varies in the x-direction. The ebb- and flood zones are separated at x= 100 m. Again, there are a few cases with different magnitudes of the transport velocities. Due to the differences in the oscillating motions, the residual movements of the particles are not the same.

With larger transport velocities, the particle's residual movement is influenced by the sediment transport patterns of a larger area. In this way, its residual movement can deviate from residual transport seen at the initial location. With high transport velocities, the release time can be an important variable determining the particle's movement after one cycle. With a continuous supply of particles, one could see that they are starting to move apart (spread over larger area). Because of the large orbital motions, the particles experience different sediment transports regimes. With low transport velocities, the particles experience similar velocities and stay together (clustered).

To still keep acceptable computational times, the simulations of the visualisation tool usually do not allow very small time steps (simulation period of a couple of weeks, large set of particles, large study area). The time step $\Delta t_{pm}$ has to be increased and results in a growth of the numerical error. At this stage however, the numerical error starts to interact with the effect of the increased orbital motion and it is difficult to separate the two issues.

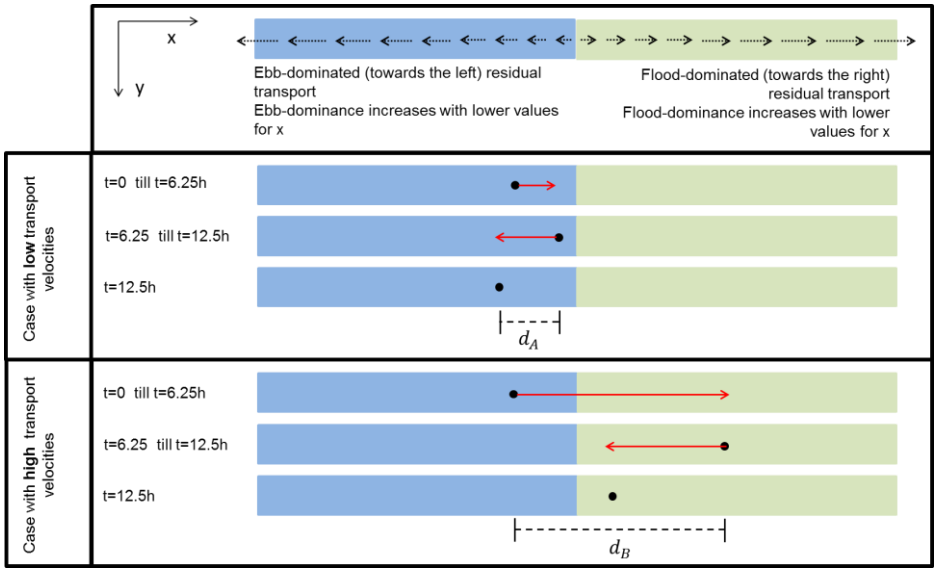


*Figure 3.8 Sketch of the pathways in case of low and high transport velocities. For each case, three different snapshots are presented.*

### 3.3.3.2 *Defining the acceleration coefficient*

For a better interpretation of the pathways and avoid vagueness about the physical meaning of the model results, the definition of the acceleration coefficient should be supported by physics as much as possible. The fact that sediment is transported by the moving water can be used for a first approximation. One could state that acceleration coefficient should not allow for *transport velocities* that are larger than the depth-averaged *flow velocities*. The non-uniform profile of the flow velocities and sediment transports over the water depth is not reflected in this rule. However, the numerical particles should not just move with flow velocities. The transport velocities in the visualisation tool should reflect the spatial and temporal variations in the sediment transport maps: higher velocities in case of higher sediment transports and vice versa. Because the relation between water flow and sediment transport is non-linear, the spatial and temporal variations are different for flow velocities.

This study is based on the sediment transport formulation of van Rijn et al. (2004) that distinguishes the bed load and suspended transport modes. Sediment in suspension travels with higher velocities than the particles that move as bed load transport. As discussed in Sections 3.3.2.3 and 3.3.3.1, higher transport velocities result in lager orbital motions (i.e. particle's residual movement depends on a larger area) and require a small time step size. For bed load transport, the residual movement of a particle does depend more on the local transport conditions and the numerical error of the RK4 method is less problematic. Because of simplicity reasons, the limited time available to conduct the study and the limited working/computational memory (more data sets result in a larger data volume), the simulations of the visualisation tool only consider the total sediment transports. However, the acceleration coefficient is based on a combination of the coefficients for both transport modes.

So, the visualisation tool should describe *realistic* transport velocities that *reflect all spatial and temporal variations* of the sediment transports. This can only be realized by applying a single acceleration coefficient for the entire domain and simulation period that does not allow transport velocities to be higher than the flow velocities. For this study, the single coefficient is derived based on the maximum sediment transports over the time and space. By finding this acceleration coefficient and applying it to all data points, the transport velocities in the entire domain and simulation period are scaled based on the fixed coefficient derived from a single area. The procedure of computation of the acceleration coefficient is described below.

Step 1: Computing the acceleration coefficient for suspended load

As stated in 2.1.2.1, suspended transport $\langle\overrightarrow{s_{sus}}\rangle$ can be computed based on product of the depth-averaged sediment concentration $\langle c\rangle$, specific density of sediment $\rho_s$ (2650 $m^3$/kg in case of sand), depth-averaged flow velocity $\langle\vec{u}\rangle$ and water depth $h$ (assume h>>a).

$$\langle\overrightarrow{s_{sus}}\rangle = \langle\vec{u}\rangle h \frac{\langle c\rangle}{\rho_s} = \langle\vec{u}\rangle \frac{1}{\alpha_{sus}} \qquad \text{Eq. (3.25)}$$

By rewriting this, one can obtain the formula of the acceleration coefficient for suspended transport. For step 1, the coefficient has to be derived for every grid cell in the study domain. In line with previous statements, the coefficient is based on the conditions that occur during maximum suspended sediment transport. To prevent that coefficient is based on an outlier, one should use a sample of the n (e.g. n=5) highest sediment transport peaks.

$$\alpha_{sus} = \frac{1}{\frac{1}{n}\sum_{i=1}^{n}\left(h_i \frac{\langle c_i\rangle}{\rho_{s,i}}\right)} = \frac{1}{\frac{1}{n}\sum_{i=1}^{n}\left(\frac{\left\|\langle\overrightarrow{s_{sus,i}}\rangle\right\|}{\left\|\langle\overrightarrow{u_i}\rangle\right\|}\right)} \qquad \text{Eq. (3.26)}$$

For this study, the derivation of the acceleration coefficient is based on the third term of Eq. (3.26). In this way, the transport velocities are explicitly linked to the flow velocities. Typically, the maximum suspended transport is around $10^{-4}$ $m^3$/s/m and the flow velocities are around $10^{-1}$~$10^{0}$ m/s. In this case, the acceleration coefficient is about $10^{3}$~$10^{4}$ 1/m. In this way, the velocities of the suspended transport ($\overrightarrow{C_{sus}}$) approximate the flow velocities.

Step 2: Computing the acceleration coefficient for bed load

As stated, bed load transport takes places near the bed. Here, the flow is significantly reduced by the friction with the bed. Moreover, the particles role, slide and saltate and move therefore slower compared to the flow velocities. All in all, the transport velocities of grains near the bed are significantly smaller than the depth-averaged velocities.

For the suspended load transport, the link between sediment transport and the concentration and flow velocities in the water column is quite straightforward. However, bed load transport is computed based on instantaneous hydrodynamics and sediment transport parameters. There is no integration over the depth. For this study, it is assumed that the depth-averaged bed load is a function of the specific density of sediment $\rho_s$, the height over which the sediment is transported (the reference height a, Section 2.1.2.1) and the depth-averaged concentration $\langle c_{bed}\rangle$ and flow velocity in $\langle\overrightarrow{u_{bed}}\rangle$ in this layer:

$$\langle\overrightarrow{s_{bed}}\rangle = \langle\overrightarrow{u_{bed}}\rangle a \frac{\langle c_{bed}\rangle}{\rho_s} = \langle\overrightarrow{u_{bed}}\rangle \frac{1}{\alpha_{sus}} \qquad \text{Eq. (3.27)}$$

Also in the second step, one has to compute the time independent acceleration coefficient for bed load transport for every grid cell in the domain determined based on the n peak values for bed load transport. By rewriting Eq. (3.27), one gets:

$$\alpha_{bed} = \frac{1}{\frac{1}{n}\sum_{i=1}^{n}\left(\frac{c_{bed,i}}{\rho_{s,i}}\right) a} = \frac{1}{\frac{1}{n}\sum_{i=1}^{n}\left(\frac{\left\|\langle\overrightarrow{s_{bed,i}}\rangle\right\|}{\left\|\langle\overrightarrow{u_{bed,i}}\rangle\right\|}\right)} \qquad \text{Eq. (3.28)}$$

The depth-averaged velocity in the layer between the bed and the reference height is an unknown parameter that is not computed in the transport formulation of Rijn et al. (2004). Because of this, the acceleration coefficient of bed load transport should be computed with

the second term of 3.28. In the definition by Rijn et al. (2004), the reference height has an upper limit of 1 cm.

The depth-averaged sediment concentration in the layer just above the bed ($c_{bed}$) is based on the following assumption: the reference concentration at height a ($c_a$) linearly increases towards the dry bed density ($\rho_{s,dry}$, 1600 kg/m$^3$ in case of sand) at z=0 m. This all adds up to the following formulation:

$$c_{bed} = (c_a + \rho_{s,dry})/2 \qquad \text{Eq. (3.28)}$$

If we assume that $c_a$ and the reference height are typically $10^0$~$10^1$ kg/m$^3$ and $10^{-2}$ m during maximum bed load transport, the acceleration coefficient of bed load transport is approximately $10^2$ 1/m. As the bed load transport can be in the order of $10^{-6}$~$10^{-5}$ m$^3$/s/m, the velocity of the grains at the bed is about $10^{-4}$~$10^{-3}$ m/s. This first approximation confirms that the particles in suspension are traveling with higher velocities.

Step 3: Computing a single acceleration coefficient for the entire grid
The sediment transports of the bed and suspended loads are added together:

$$\overrightarrow{s_{tot}} = \overrightarrow{s_{sus}} + \overrightarrow{s_{bed}} \qquad \text{Eq. (3.29)}$$

The acceleration coefficient that is used to compute the total transport velocity is based on the weighted averages of the acceleration coefficients for bed and suspended load. The weighing is based on peak values of bed and suspended load transports that are used in Eq. (3.26) and Eq. (3.28). Finally, the spatial variation is removed by selecting the maximum acceleration coefficient that is computed within the study domain. Instead of using a single grid cell, the coefficient can better be based on a slightly larger area with similar characteristics.

### 3.3.4 Selecting the random walk coefficient

As stated, one can add a random component on top of the transport velocity determined based on the sediment transport maps. The random walk coefficient $\beta$ ($\geq 0$) indicates the standard deviation of the random number R that is used to convert the magnitude of transport velocity derived from the vector field into magnitude of the random velocity (Eq. 3.18). For simplicity, let's refer to this first velocity as the "non-random transport velocity".

With $\beta$=0, the random velocity is always zero. There is no/less need to use a larger value when the non-random transport velocities themselves already generate a spreading of the particles in the horizontal directions. This happens for example when there is a continuous release of particles in an area with large transport velocities and large temporal and spatial variations. In this case, difference in the release times result in clear variations of the transport pathways. In addition, the random walk coefficient can equal 0 if the simulations are based on the release of particles at a cluster of release points (multiple start locations located close to each other) and already show enough horizontal spreading of the particles.

If the particles have almost identical pathways (stay clustered), one could increase the value of $\beta$. Increasing the random walk coefficient is not obligatory but can just be helpful to better visualize the spatial variations in the vector fields. It can show whether a small deviation from the original path results in large deviations in the pathway at later times.

However, the random walk coefficient cannot be increased till infinitely. With a larger value, the particles can be displaced over such large distances that they arrive at areas where you do not expect them based on the vector fields. Thus, the *absolute* random instantaneous displacements should not be too large compared to the spatial variation in the sediment

transport. As these random displacements also depend on the time step size and the non-random transport velocity, the upper limit of $\beta$ differs per case. Even more important, the coefficient should be limited to prevent that *relative* random displacement becomes too large. With larger values for $\beta$, the total velocities the particle receives do more and more depend on the randomly generated velocities. If these start to get dominant, the visualisation of the sediment transport vector fields more or less disappears and the particles move randomly through the system.

Based on all of this, a random walk coefficient of 0.5 seems to be a safe and good option. In this case, still about 95% of the random velocities are smaller than the transport velocities derived from vector fields. Whether or not this leads to displacements that are large enough (to observe), totally depend on the time step size and the acceleration coefficient (i.e. magnitudes of the transport velocities). However, these variables should be determined based on other principles.

## 3.4 Conclusion

By using the layered bed model, the graded sediment approach takes into account the decay of tracer availability due to bed mixing and lag effects due to burial and resurfacing. The transport layer thickness is an important factor; in practice its value is determined through calibration. When calibrated correctly, the method is able to provide physically accurate approximations of the tracer dispersal rates over time. This is also the goal of the method: to get a physically accurate overview of the dispersal of a specific tracer volume.

The visualisation tool helps to interpret the sediment transport vector fields by following numerical particles that move according to the sediment transport magnitudes and directions. Since bed mixing and burial-resurfacing are not included in the visualisation method, the numerical particles move faster than what is seen in reality. Although it is physically possible that a real tracer particle is not mixed, buried and resurfaced in the bed for a certain time, by far the major part of the tracer sediment is slowed down by the interaction with the bed. The transport pathways calculated with the visualisation tool should be interpreted as maximum movement rates and present the *preferred* transport pathways. It illustrates the pathway of a particle when it does not interact with the bed model. Defined differently, the model follows a set a particles. The sediment grain that is followed for a certain time and is mixed within the bed after a while, is replaced by another particle that is eroded out of the bed.

Chapter 4 discusses the application of the two transport pathway methodologies for a schematized case. Based on these findings and the theories that are discussed in this chapter, Section 4.4 describes the conceptual differences between the methods, the pro's and con's and discusses the practical applications.

# 4 Schematic test case

This chapter discusses the application of the two transport pathway methodologies for a simplified schematization. It demonstrates the theories and the effects of the different parameters. As the analyses of the methodologies depend on local sediment transport conditions, the findings cannot be directly applied to other cases but just form the background information for future studies

Chapter 4 starts with a description of the schematic case. Subsequently, Sections 4.2 and 4.3 discuss the tracer dispersal patterns for the respectively the graded sediment approach and visualisation tool. Section 4.4 combines the findings of Chapter 3 and 4 and explains which method is selected for the study about the Scheldt estuary.

## 4.1 Model set-up and hydrodynamics

The simplified Delft3D schematization describes a tidal basin with a domain of 5x5 km and grid cells of 50x50 m. The basin and open sea are areas of ~2x5 km and are connected via an inlet. The narrowest part of the inlet has a length of 400 m (Figure 4.1, left). Whereas the bed level is uniform inside the basin (-8 m), the sides of the headlands and bed profile at open sea are sloping. As reference case, the open boundary of the model (x=0 m, from y=0 m till y=5000 m) has an astronomic forcing condition with a combination of a $M_2$ (amplitude: 1.0 m) and $M_4$ (0.2 m) wave. For this boundary condition, the initial phase lag between the $M_2$ and $M_4$ wave is 0 degrees. The tide in the centre of inlet describes a standing wave, the vertical wave leads the horizontal wave with 2 hours (Figure 4.2). For the next analysis, two start locations have been selected. Start location 1 is exactly in the middle of the domain (2500,2500). The other location is just left of the inlet (2150,2500). The start location are also shown in Figure B.1 of appendix B. The other settings are presented in Table 4.1.

*Table 4.1 Delft3D model settings, simplified schematization*

| Setting | Value |
|---|---|
| Roughness | Manning: 0.024 $s/m^{1/3}$ in u and v direction |
| Horizontal eddy viscosity and diffusivity | 1 $m^2/s$ |
| Median sediment diameter ($D_{50}$) | 0.2 mm |
| Dry bed density | 1600 $kg/m^3$ |

As the right subplot of Figure 4.1 demonstrates, the depth-averaged velocities are the highest at the central horizontal axis (y=2500 m). Because the bathymetries south and north of this axis are each other mirrored images, the flow at the y=2500 m shows no vertical component. As the relation between flow velocity and sediment transport is non-linear, the spatial differences in residual transport are very large (Figure 4.3, left). Moreover, the residual transport around y=2500 m shows clear ebb- (east of the centre) and flood-dominant (west of the centre) zones. The residual transport in the middle of the inlet is slightly flood-domination. Because of the relatively small grain size, high flow velocities and shallow water depth, the sediment transport in and around the inlet is dominated by suspended load.

For the graded sediment approach, the dispersal of tracers will be followed over a period of 3 months and erosion and sedimentation are translated in respectively a decrease and increase of the bed thickness. In line with previous observations, the changes in the thickness are mainly concentrated in and around the inlet (Figure 4.3, right). Erosion has the largest impact in the centre of the inlet and the area around the narrowing/widening (where the flow converges). The largest depositions occur in the area where the maximum magnitude of the flow velocity drops significantly due to the divergence of the flow.

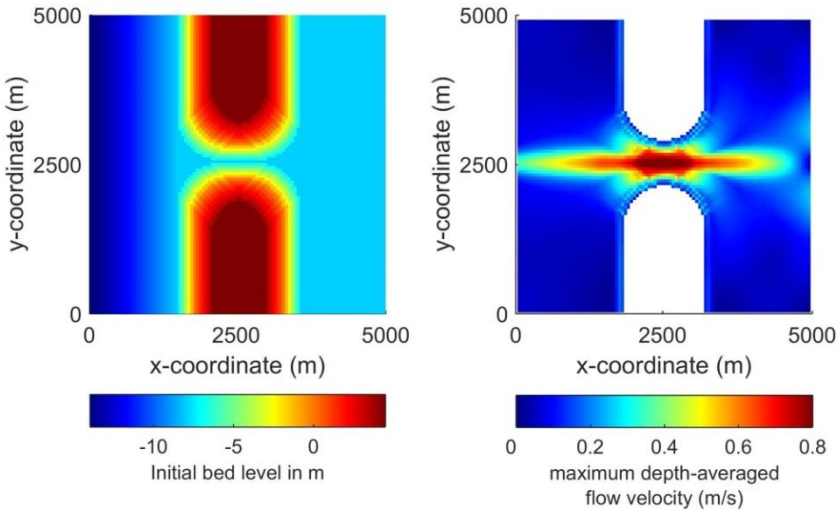


*Figure 4.1 Left: bathymetry of the tidal basin. Right: Maximum depth-averaged flow velocities*

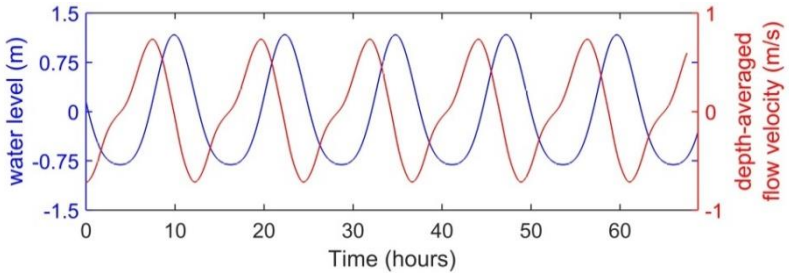


*Figure 4.2 Depth-averaged velocity in x-direction and water level in the centre of inlet. A positive velocity indicates a flow in the flood direction.*

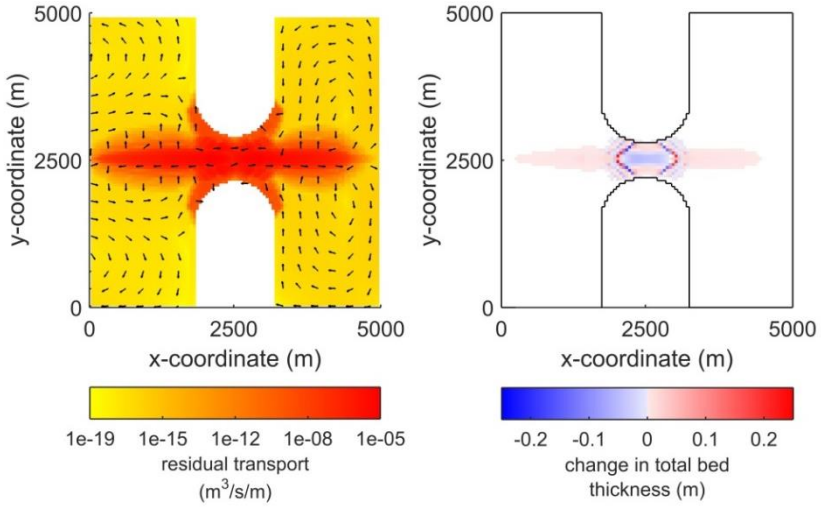


*Figure 4.3 Left: Residual sediment transport (averaged over 1 $M_2$ period). The colour scale is logarithmic. Right: Total change in the bed thickness after months. Red colors indicate sedimentation (bed thickness increase) and blue colors represent erosion (bed thickness decrease). Minimum threshold is 0.2 mm ($D_{50}$).*

## 4.2 Traditional graded sediment approach

Both the well-mixed bed and layered bed approach are discussed in separate sections (respectively 4.2.1 and 4.2.2). The model is based on two sediment fractions (“native” and “tracer”) that have the same sediment characteristics. The well mixed bed approach is used to study the effect of bed mixing in the upper most layer on the dispersal of the tracer fraction,

in absence of burial and resurfacing processes. Within the layered bed approach, also the burial and resurfacing of sediment influence the dispersal of the tracer fraction.

### 4.2.1 Well-mixed bed approach

#### *4.2.1.1 Model set-up and first analysis*

As start, the dispersal of tracer sediment is studied for start location 1 (middle of the domain). Here, the bed consist 5 cm of the tracer sediment. The remaining volume of bed is filled with the fraction native. For all the other grid cells, the bed consists entirely of the fraction native. In this way, the initial tracer deposit is the same for every case that will be discussed in this section (independent of the bed thickness).

Figure 4.4 depicts the dispersal of the tracer fraction after 3 months for two bed thicknesses. The comparison of the two cases will be discussed in the next section. To clearly visualize the tracer dispersal and to take into account the numerical accuracy of the Delft3D model (difficulties with small quantities in the advection-diffusion equations), only quantities higher than 3.2 x $10^5$ kg/m$^2$ (layer thickness of $10^{-4}$ x $D_{50}$) are displayed based on the colormap. The tracer sediment has mainly been spread towards the east and west. The concentrations are the highest around the start location and quickly decrease towards the edges of the tracer "cloud". The spreading of tracers is also visible in Figure 4.5, that provides the tracer concentration at the line y=2500 m for multiple times. While the tracer concentration at the start location lowers, the cloud is expands towards the east and west. For both cases, about 51-53% of the displaced tracer sediment is transported east of the start location. This is in line with the residual transports seen in Figure 4.3

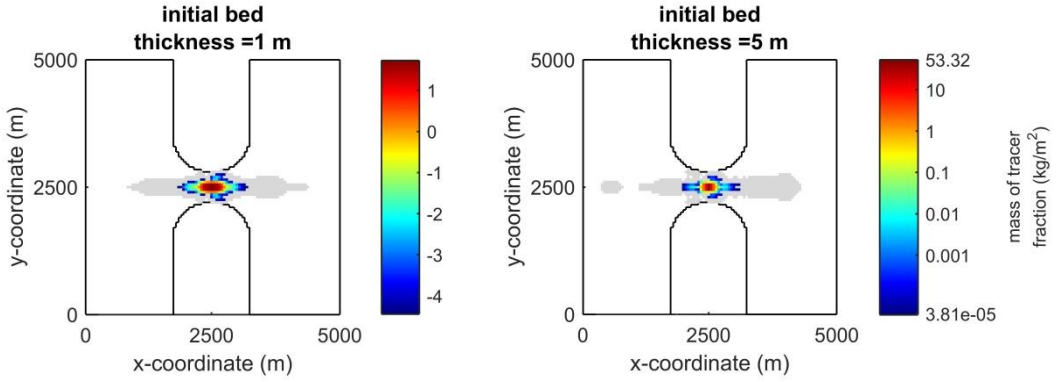


*Figure 4.4 Available mass of tracer fraction in the bed after 3 months. The colour scale is logarithmic. The grey area contains the cells with tracer concentrations lower than 3.2 x $10^5$ kg/m$^2$.Start location: (2500, 2500).*

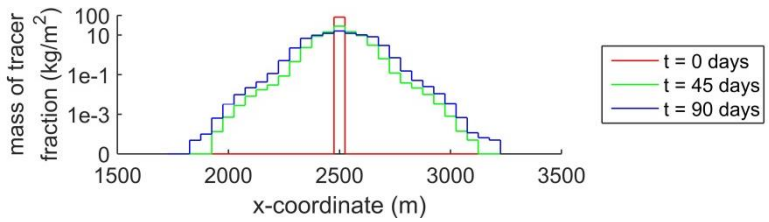


*Figure 4.5 Available mass of tracer sediment in the bed for the grid cells at line y=2500 m. Minimum available mass (threshold): 3.2 x $10^5$ kg/m$^2$. Start location: (2500,2500). Initial bed thickness: 1 m.*

#### *4.2.1.2 Effect of the total bed thickness*

As Figure 4.4 demonstrates, the area with tracer deposits higher than the threshold is larger in case of the thinner bed. Within this area, also the concentrations themselves seem to be higher with the smaller initial bed thickness. Figure 4.6 (left) confirms this and provides time series describing the total mass of tracer sediment that is transported out of the start location

(the so-called displaced sediment) for different bed thicknesses. As the graph shows, this displaced sediment mass is larger with thinner beds. Because the fractions have the same sediment characteristics, differences in erosion rates are solely influenced by the availabilities in the bed. With the same mass of tracer sediment, a thinner bed results in higher mass fractions (see Figure 4.6, right) and also higher erosion rates. Over time however, this mass fraction reduces quickly and eventually slows down the export of tracers.

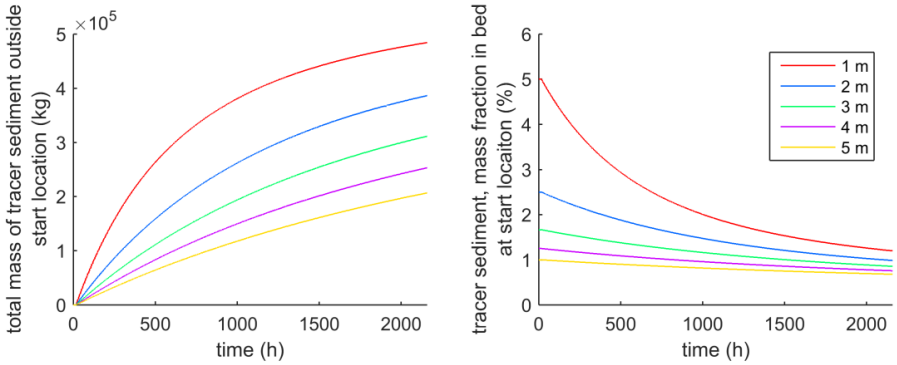


*Figure 4.6 Effect of initial bed thickness. Left: total mass of tracer sediment transported out of the start location 1. Right: mass fraction of tracer sediment in the bed at start location 1.*

The bed thickness also affects the dispersal rates outside the start location. Figure 4.7 shows the mass of tracer sediment within different areas. The areas describe the grid cells within a certain distance from the start location. For example: area 2 includes all the grid cells that lie 100 to 300 metres from the start location (see appendix B.2 for a map of the areas). For all areas, the mass of tracer sediment within the first 500 hours is the highest in case of a bed thickness of 1 m. Again, the spreading of tracers is quicker due to the higher mass fractions. For almost all cases and areas, the mass of the tracer fraction is increasing over time (inflow>outflow). There is one exception; the simulations with a bed thickness of 1 m show a decrease in the mass of the tracer fraction in area 1 after about 500 hours. This is caused by a decreasing tracer export out of the start location (source is depleted).

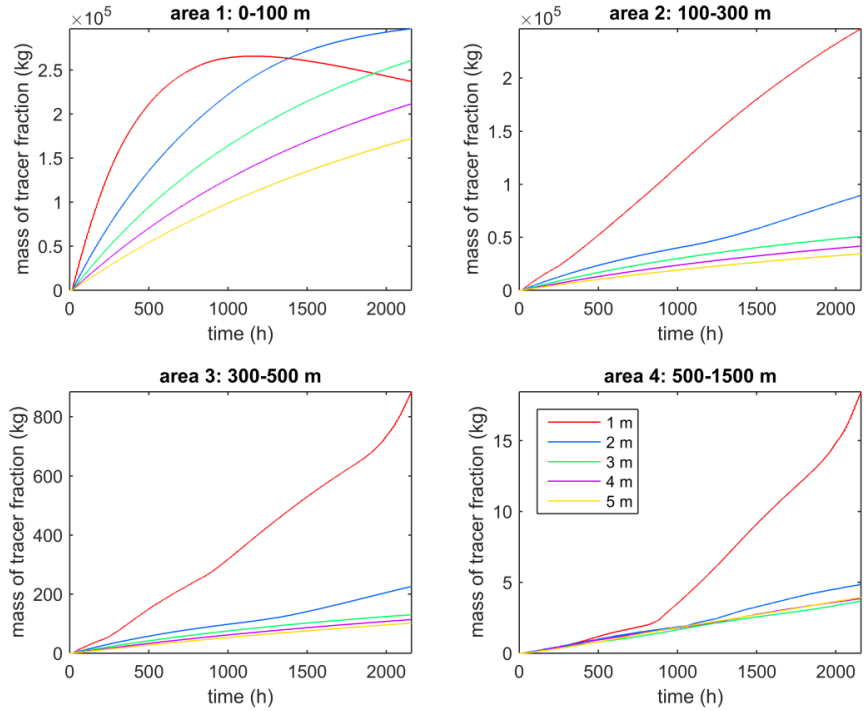


*Figure 4.7 Total mass of tracer fraction within a certain distance of start location 1, measured over time.*

### 4.2.2 Layered bed approach

For the layered bed approach, a small adjustment was made in the standard Delft3D code (appendix B). The adjustment does not affect the main conclusions of the analysis.

#### *4.2.2.1 Model set-up and first analysis*

For the next analysis, the transport layer at the start location is filled with 5 cm of tracer sediment and the remaining volume consists entirely of the fraction native. For the other grid cells, the transport layer consists for 100% out of native sediment. For all the grid cells, the underlayers are filled entirely with the fraction native. As start, the bed is initially composed of 8 underlayers with a thickness of 0.4 m (maximum set at 0.5 m).

Figure 4.8 gives an impression of the spatial pattern seen in the spreading of the tracer fraction after three months (transport layer thickness of 0.1 m) for both start locations. The left two maps show the presence of tracer sediment in the transport layer. The other two maps illustrate the total mass of the tracer fraction buried in one of the underlayers. Again, tracer sediment is mainly transported in the x-direction. In case of start location 1, 53% of the displaced tracer sediment is east of the start location. Because the second location lies in zone with ebb-dominant residual transport, this value is increased to 88%. The bed mixing and burial-resurfacing processes prevent that all sediment is transported towards the west.

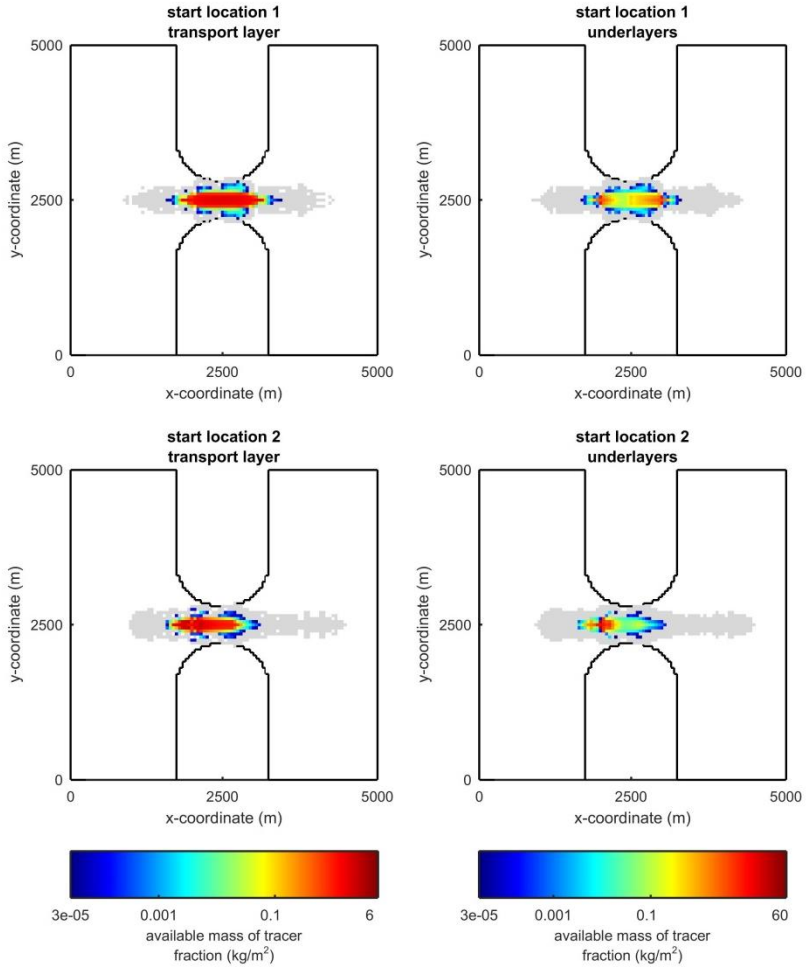


*Figure 4.8 Map of the available mass of tracer fraction in the bed after 3 months, for two different start locations (see Section 4.1). The transport layer is 0.1 m thick. Left graphs: availability of tracer sediment in transport layer. Right graphs: availability of tracer sediment, summed over all underlayers. The colour scale is logarithmic. The grey area contains the grid cells with tracer concentrations lower than 3.2 x $10^5$ kg/$m^2$.*

The maps show that there are spatial differences in the dispersal of the tracer fraction. The tracer concentration in the transport layer is still the highest near the start location. For the underlayers however (right maps in Figure 4.8), the highest concentrations are found in the grid cells with the largest sedimentation/bed thickness increase (Figure 4.3). For these cells, there is an almost constant burial of sediment due to the import of sediment.

#### 4.2.2.2 *Effect of the transport layer thickness*

Also for the layered bed approach, the analysis of the transport layer thickness is based on the results for start location 1. In line with the findings about the well mixed bed approach, the export of tracer sediment out of the start location is quicker with thinner transport layers (relatively higher mass fractions, Figure 4.9 left). Now however, the eroded tracer volume is compensated with a sediment flux from the upper underlayer that fully consists of the fraction native. The resurfacing of native sediment accelerates the decrease in the tracer mass fraction at the start location. The lower tracer availability slows down the export of tracers out of the start location. For thicker transport layers, the total mass of resurfaced sediment is relatively small compared to the total mass of sediment stored within the transport layer. Thus, the resurfacing has less impact on tracer mass fraction in the transport layer.

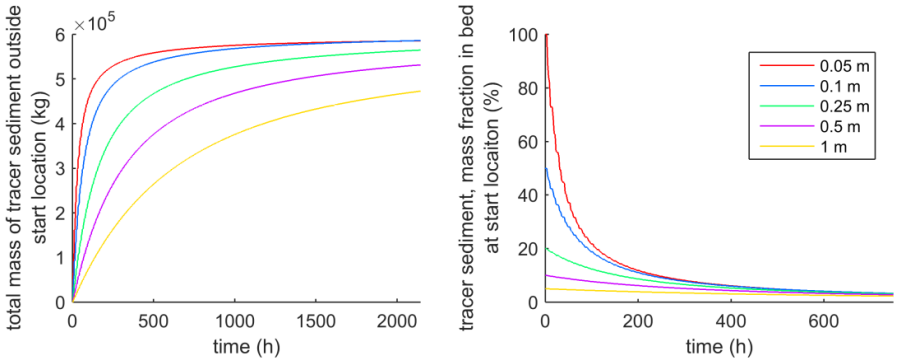


*Figure 4.9 Effect of the transport layer thickness on the dispersal of the tracer fraction. Start location 1. Left: total mass of tracer fraction that is located outside start location. Right: mass fraction of the tracer fraction at the start location 1.*

Also the tracer dispersal in the surrounding area is influenced by the processes in the bed. The effects of mixing and resurfacing were observed before. For the surrounding area, the dispersal of tracers is also influenced by the burial of the fraction in one of the underlayers. Figure 4.10 demonstrates that the percentage of the displaced tracer fraction buried in an underlayer increases over time. With more and more tracer sediment becoming inactive, the dispersal of tracers in horizontal direction decreases over time. Eventually, the dispersal rate may even become negligible. Figure 4.10 also shows that the percentage of displaced tracer sediment buried in one of the underlayers is higher with thinner transport layers. Thinner transport layers result in higher tracer availabilities and larger contributions of tracer sediment in the burial volumes (Section 3.2.2.1).

The right graph of Figure 4.10 demonstrates the effect of the transport layer thickness on the total coverage of the tracer “cloud”. Although the area calculated in a discrete way (grid cells) and is influenced by the cut-off point (same threshold as before), the graph clearly shows that the horizontal dispersal of tracer sediment is lager with thinner transport layers. The smaller effect of bed mixing seems to outweigh the larger impact of burial and resurfacing processes.

For this schematic case, there are no distinctive periods (apart from the variations within a $M_2$ cycle) during which the burial and resurfacing processes significantly change. The volume of sediment that is buried in an underlayer almost continuously increases. By for example adding a spring-neap cycle or time series describing the development of a storm, the burial

and resurfacing processes could show large temporal variations. For example: large tracer volumes that were first buried can be resurfaced during later periods.

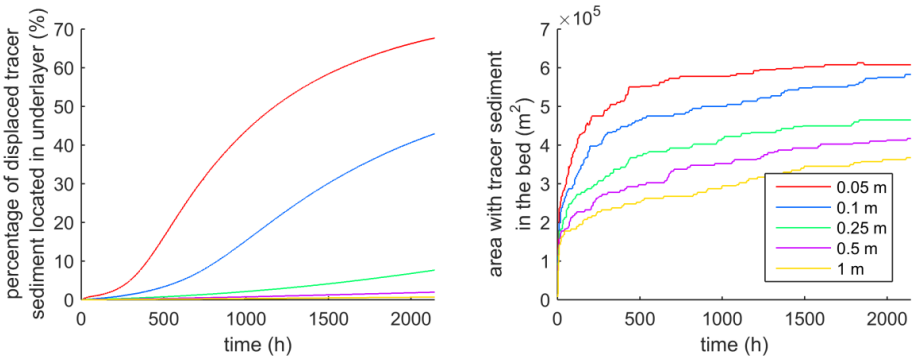


*Figure 4.10 Effect of the transport layer thickness on the dispersal of the tracer fraction. Start location: 1. Left: percentage of displaced tracer sediment (sediment that is not located at the start location) that is buried in one of the underlayers. Right: total area with tracer sediment stored within the bed (all layers). This area includes only cells with an available mass higher than 3.2 x $10^5$ kg/$m^2$.*

#### 4.2.2.3 *Other parameters in the layered bed approach*

The other user-defined variables in the layered bed stratigraphy of the Delft3D model are:

- The initial number of underlayers and their thicknesses
- The maximum number of underlayers
- The maximum thickness of the underlayers

The effects of these variables can be explained based on the equations of Section 3.2.1 and the results about the impact of the transport layer thickness. As was also demonstrated for the transport layer, the decay of the tracer availability due to bed mixing is larger for thicker underlayers. Moreover, the effects of resurfacing and burial on the mass fractions in the transport layer are more pronounced with thinner underlayers. The burial of 1 cm of tracer sediment in an underlayer with 4 cm of native sediment, results in a tracer mass fraction of 20%. If this underlayer contains 9 cm of the native fraction, this mass fraction is reduced to 10%. If the subsequent time step requires a flux of 1 cm towards the layer on top of it, the amount of tracer sediment that is moved upward is larger with the thinner under layer (0,2 cm against 0,1 cm). In other words, it takes less time to resurface the tracer sediment (smaller lag effect). Similarly, also the other variables can influence the burial and resurfacing processes and affect the transport rates of tracer sediment in vertical direction.

## 4.3 Visualisation methodology

This section discusses the dispersal patterns of numerical patterns calculated with visualisation tool. Following the method as discussed in Section 3.3.3, the acceleration coefficient in this study area should be 10000 $m^{-1}$ (appendix B.3). The variable $\Delta t_{\mathrm{d3d-output}}$ was already discussed extensively in Section 3.3 and will not be further analysed here. For this analysis, its value is set at 15 minutes. Section 4.3.1 gives a first impression of the spatial and temporal patterns seen in the dispersal of numerical particles. Besides, it briefly compares the results of the visualisation tool and the graded sediment approach. Sections 4.3.2 and 4.3.3 discuss the effect of $\Delta t_{\mathrm{pm}}$ and $\beta$.

### 4.3.1 Dispersal patterns of numerical particles

To neglect the numerical error of the RK4 method, the $\Delta t_{\mathrm{pm}}$ is equal to 1 s. The random walk component is turned off. Below, one can find the tracer dispersals for both start locations. These locations form a continuous release, one particle is released every 5 minutes for a period of 1 week.

The upper subplots of Figure 4.11 show the concentration of tracer particles after 1 week for start location 1. Because the particles are released in the centre of the domain and the oscillating motion of the particles are large enough to feel both the ebb and flood-dominant zones, particles are transported towards both the west and east. Due to the small flood-dominance at the start location, 60% of the particles end up at the eastern part of the domain. Although the tool is based on different concepts, this flood-dominance was also observed with the graded sediment approach. As the release point is located at the central horizontal axis, there is no transport of particles in the y-direction.

The bottom subplots of Figure 4.11 demonstrate the dispersal of numerical particles after 1 week for start location 2. Although the start location and immediate vicinity have a net ebb-directed sediment transport, 55% of the numerical particles end up at the eastern part of the domain (x > 2500 m). Although the start location is different, the dispersal patterns looks quite similar compared to the previous case.

Because the transport velocities are quite high, the oscillating motion of a particle is large and covers both the ebb and flood-dominant zone. For some particles that are released at location 2, the penetration into the flood-dominated zone is so large that it is relatively “easy” for the particle to overcome the ebb-dominance at the initial position. These particles get a residual movement towards the east. The flood-dominance the particles “experience” during the oscillating motion outweighs the ebb-dominance (based on the residence time of the particle in the different zones and strength of the residual transports). Concluding, the residual movement of these particles depend on the sediment transport patterns of a large area.

When moving start location 2 towards the left, the percentage of particles ending up at the eastern part of the domain increases. For fewer particles, the reach of the oscillating motion into the area right of the inlet is large enough to overcome the ebb-dominance. At a certain turning point, this value is higher than 50%. If the start location is shifted even further, 100% of the particles stay within the ebb-dominant zone.

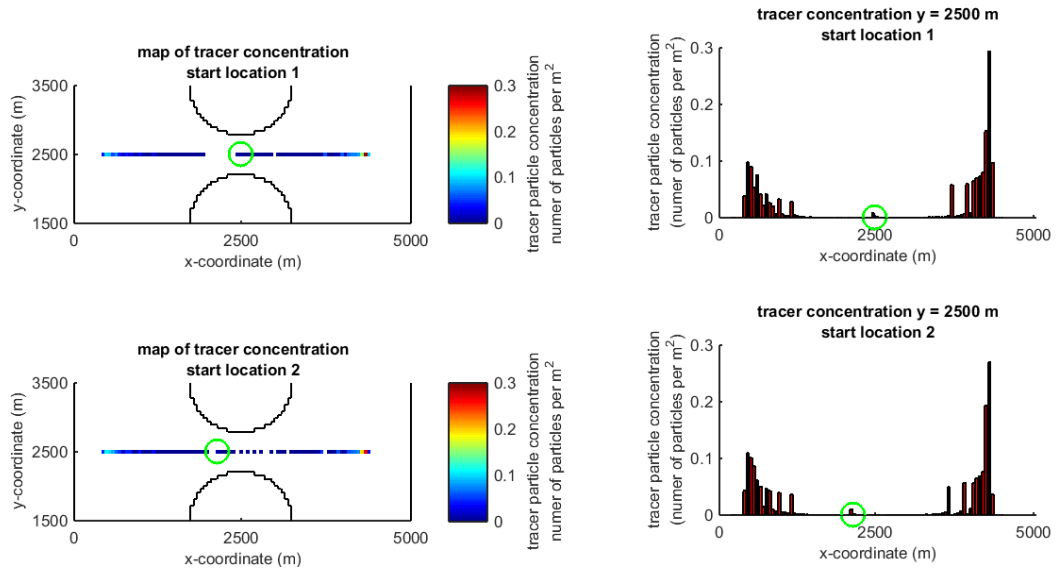


*Figure 4.11 Left: particle concentrations after 1 week with start locations 1 and 2 (indicated with green circles). Grid size: 50 x 50 m. Right: bar chart (bin size: 50 m) of particle concentrations in x-direction*

The two transport pathway methodologies show different dispersal patterns for the second start location. The graded sediment approach demonstrates that the main part of the tracer sediment is transported towards the west; the visualisation tool shows an opposite pattern. Whereas the sediment in the graded sediment approach is slowed down by bed mixing and

burial-resurfacing processes, the numerical particles in the visualisation tool do not interact with the bed and have large oscillating movements. As the numerical particles are displaced over large distances during a tidal cycle, they can easily experience sediment transport conditions that are not observed in the immediate vicinity of the start location. As the tracer dispersal rate in the graded sediment approach is lower, the orbital motions are smaller and are less affected by the flood-dominant zone. As shown in 4.2, the tracer dispersal is affected by the dimensions used in the bed model. For situations with more dominant sediment transport conditions (i.e. start locations further away from the inlet), the results of the two methodologies would have been are more alike.

### 4.3.2 Effect of the time step for particle movement calculations

To make sure that the numerical error can be neglected, the previous analysis was based on a time step equal to 1 s. In reality however, the value for $\Delta t_{pm}$ should also be chosen based on the consideration of minimizing the computational time. This section will further explain the effect of the parameter $\Delta t_{pm}$ on the transport pathways and discuss how its value should be chosen based on the different considerations. The analysis that is presented in this section is based on a continuous release of particles at start location 1. The particles are released with an interval of 5 minutes for a period of 12.5 hours (150 particles in total). Again, the particles are followed for 1 week.

As stated in Section 3.3.2, the parameter $\Delta t_{pm}$ has to be equal or smaller than the interval $\Delta t_{d3d-output}$ (i.e. 15 minutes). However, $\Delta t_{pm}$ has to be refined even further to make sure that the spatial variations in the transport velocities are include in the pathways. At the central horizontal axis, these variations only occur in the x-direction. At y = 2500 m, the magnitudes of the transport velocities decrease when moving to the right or left of the inlet. Thus, particles that move away from the domain's centre should be quickly decelerated. The y-component of the transport velocities is zero for the entire horizontal axis.

The SN number can be used for a first approximation of the time step. At first, one could state that N=1, the particle movements per time step should be smaller than one times the grid resolution. Based on the simulation that is shown in Section 4.3.1, we know the transport velocities the numerical particles experience. The maximum transport velocities can be found in the inlet and are in the order of 0.9 m/s. The grid cells are 50 x 50 m within the entire study domain. Following Eq. (3.23), the maximum time step is 65 seconds. Due to the absence of curvatures in the vector fields at y = 2500 m, a visual comparison of the transport pathways and the vector fields is difficult. Thus the time step should be further refined by sensitivity analysis of the transport pathways. Assume that a time step of 1 second can be used as reference case and does not contain any numerical error.

The effect of $\Delta t_{pm}$ strongly depends on the release time of a particle. Figure 4.12 demonstrates the most extreme scenario. It compares the x-coordinates of three particles that are released at the same time (during ebb), but move with different time steps. The results show that the particles with $\Delta t_{pm}$= 1 s and $\Delta t_{pm}$ = 2.5 min stay relatively close to each other. Although they are released during ebb, the particles have residual movements towards the flood-dominant zone. The green line shows the x-coordinate of a particle that moves with steps of 5 minutes. Because the movement in the ebb-direction during the first hours is overestimated, the particle gets a pathway (residual movement towards the east) that is totally different from the reference case. In other words, the slightly larger penetration of the oscillating into the ebb-dominant zone has large consequences. After 1 week, the first two particles end up in the flood-dominant zone within a distance of 1 meter from each other . At this time, the third particle is located 4 kilometres towards the west.
Instead of looking to only a single particle, let's now study to the entire set of particles that are released at location 1. Different cases are created by varying the time step between 2.5 s and

2.5 min. Figure 4.13 demonstrates the effect of the parameter $\Delta t_{pm}$ by comparing the locations of the 150 particles of a certain scenario with the 150 particles of the reference case ($\Delta t_{pm}$= 1 s). Thus, the results are based on a comparison of the particles that are released at the same time but move with different time steps.

The subplots of Figure 4.13 show that both the mean and maximum distances between the particle locations increase with larger time steps. With larger steps, the translation of the spatial variations in the transport fields into the transport pathways is worse and the prediction of the tracer dispersal becomes less accurate. The distances between the particles' end locations after 1 week are small (0.1-1 m) when we compare it with the geometry of the inlet, the grid size dimension and the spatial variation in the sediment transport. In between the start and end of the simulation however, the distances between the particles can sometimes be very high (>300 m).

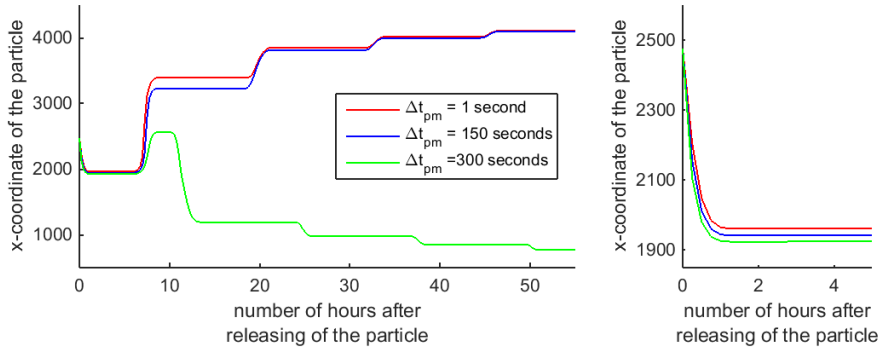


*Figure 4.12 X-coordinate of the three particles that are released at start location 1 during ebb, but move with different time steps ($\Delta t_{pm}$). The right subplot is just a detailed visualisation of the first few hours.*

Looking to the trends over time, the graphs show that the distances increase in the first hours and decrease during the remaining part of the simulation. In the beginning, the particles are located in and near the inlet and move with large velocities. The shortcoming of the RK4 method results in large deviations from the reference pathways. As the particles stay on the horizontal axis, they are decelerated when moving towards the boundaries of the domain. Therefore, the distances compared to the reference case decrease and the particles are converged to approximately the same area.

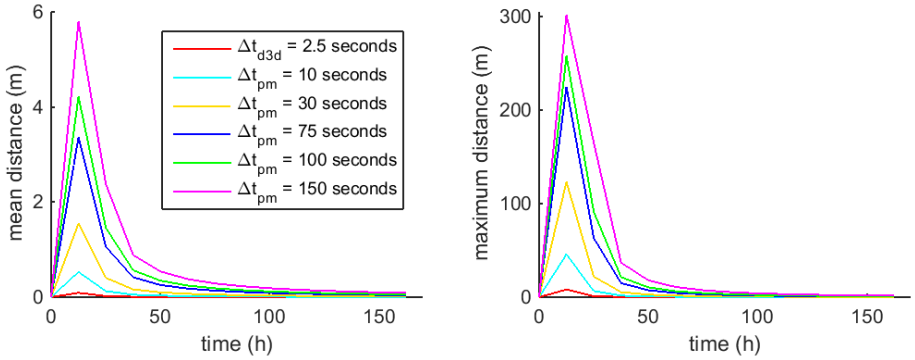


*Figure 4.13 The mean (left) and maximum (right) distances between the particles of the specific cases (variations in $\Delta t_{pm}$) compared to the reference case ($\Delta t_{pm}$=1 s). The particles are released at start location 1. The intra-tidal variations are filtered out by only plotting the distances after each tidal cycle (12.5 hours).*

The effect of parameter $\Delta t_{pm}$ should not only be analysed based on the end locations, but also the deviations in the transport pathways in between the start and end of the simulation are important. Table 4.2 tries extends this analysis and introduces some statistics. It shows

the percentage and number of particles that deviated more than 50 metres from the reference pathway somewhere during the simulation. With a time step of 2.5 minutes, this is for example the case for 25.33% of the particles. For a smaller time step, this percentage of course decreases. Summarized, the table confirms that the accuracy of the model decreases with higher values for $\Delta t_{pm}$.

*Table 4.2 Number and percentage of particles with pathways that deviated more than 50 metres from the reference scenario at some point during the simulation. Start location 1.*

| Time step $\Delta t_{pm}$ (seconds) | Particles with deviation from reference pathways of more than 50 metres | |
|---|---|---|
| | Number of particles | Percentage of particles |
| 2.5 and 10 | 0 | 0 % |
| 30 | 2 | 1.33 % |
| 75 | 3 | 2 % |
| 100 | 12 | 8 % |
| 150 | 38 | 25.33 % |

As the size of the time step is strongly related to the calculation time of the visualisation tool, a time step of for example 75 seconds seems to be fine in this schematic test case. In this way, the error in the pathways is still limited while still keeping acceptable calculation times.

### 4.3.3 Effect of random walk component

When the random walk component is turned off ($\beta$=0), the release time is the only variable that determines the variations in the pathway. In this schematic case, the cloud of numerical tracers that are released at start location 1 is a straight line (as shown in Figure 4.11). To better visualize the spatial variation in the sediment transports, one could increase the parameter $\beta$. In this way, the particles get a random movement on top of the displacement they receive from the sediment transport maps. Figure 4.14 demonstrates the effect of the random walk coefficient on the dispersal of tracers with start location 1. Again, there is a continuous release of particles of 1 particle per 5 minutes during the entire simulation.

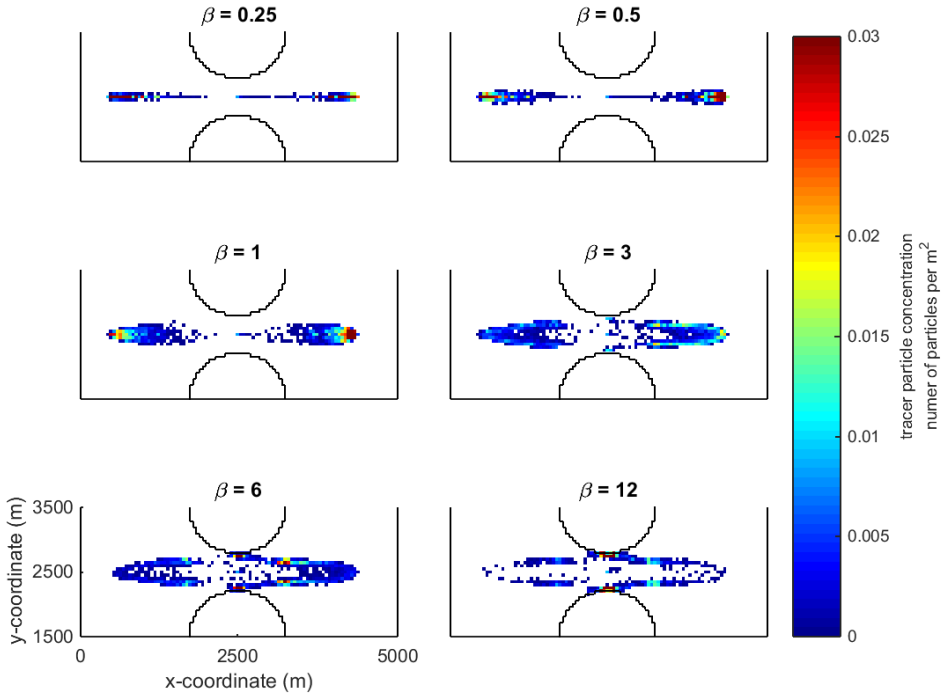


*Figure 4.14 Particle concentrations after 1 week with different values for the random walk component. Start location 1.*

When $\beta$ is increased till about 1, the straight cloud of tracer particles turns into an oval shape. The results show that the random walk component results in a small spreading of the tracers in the y-direction. The particles are still located around the central horizontal axis, the area with the highest transport velocities. In other words, the transport pathways of these particles are not very sensitive for small changes in the particle movements. A small deviation from the original path does not result in large differences in the particle's end location.

With higher values for $\beta$, the random displacements start to dominate the movements of the particles. The patterns become more scattered and the particles move away from the central horizontal axis. The cloud of tracers still has an oval shape because the particle displacements (both non-random and random) quickly reduce outside the central horizontal axis. The highest concentrations can be found at the edges of the inlet. This cannot be explained by the patterns of the vector fields.

Summarized, the maps of tracer concentrations clearly show that random walk coefficient has a certain upper limit. As explained in 3.3.4, a safe option could be to set the random walk coefficient at 0.5. In this way, the transport velocities from the vector fields are still dominant.

## 4.4 Conclusion

Based on the analysis of the concepts behind the graded sediment approach and visualisation tool (Chapter 3) and the application on schematic test case (Chapter 4), it is possible to give a summary of the conceptual differences between the two methods. It is important to state one method is not better than the other; both methods have their strengths and weaknesses.

### 4.4.1 Graded sediment approach

The graded sediment approach follows how a certain deposit volume of tracer sediment is dispersed over time. Instead of tracking individual grains, the method follows the changes of tracer concentrations in bed and water column over time. Compared to the well mixed bed approach, the layered bed stratigraphy is physically more accurate as it is able to reproduce the vertical sorting profile within the bed. With the layer bed approach, the dispersal of tracer sediment in the horizontal direction is affected by the decay of tracer availability due to bed mixing and lag effects due to burial and resurfacing processes. The transport layer thickness is an important factor in this; in practice its value is determined through calibration.

Depending on the dimensions of the bed model, the size of the initial tracer deposit and the size of the numerical accuracy and stability of Delft3D, the dispersal of tracer sediment reduces over time and eventually even stops/become negligible. This process is physically correct and is also observed in physical tracer experiment. Tracers are left behind in the bed while the tracer "cloud" is expanding in the horizontal direction. The tracers (that are left behind) can be transported at later times, but their transport rates have been slowed down by the interaction with the bed.

After calibration, the graded sediment approach is able to provide physically accurate approximations of the tracer dispersal rates over time. This can be seen as one of the strengths of the method. Although it is not applied in this context, one could also vary the sediment characteristics of the different fractions. In this way, the graded sediment approach can be used to describe the sorting processes in case of heterogeneous sediment. Because the tracer dispersal is slowed down by the interaction with the bed and can even become negligible after a certain period, the graded sediment approach requires a long computational time to obtain large-scale transport pathways (e.g. few kilometres) with a single tracer deposit. This is a disadvantage of the method, if one wants to quickly obtain information about the sediment transport conditions within a large area.

### 4.4.2 Visualisation tool

The tool visualizes the sediment transport maps that are generated as output by the Delft3D model. The tool follows the movement of individual numerical particles through the sediment transport maps that are updated with a certain interval to represent the time-varying sediment transport conditions. The particles move according to the direction and magnitude of the sediment transports. In this way, the tool visualizes the Eulerian-computed sediment transports in a Lagrangian way

As shown with the simplified schematization and the examples of Section 3.3, the tool has four important parameters that have to be chosen based on multiple considerations. The acceleration coefficient has to be fixed over time and space and can be derived based on physics and some assumptions. The coefficient determines the magnitudes of the transport velocities and the size of the particle's orbital motion. In its turn, this orbital motion can affect the residual movement of a particle. The parameter $\Delta t_{d3d-output}$ should be chosen such that the relevant temporal variations in the sediment transports are represented in the vector fields. The time step for the particle movement calculations ($\Delta t_{pm}$) has to be smaller than this interval and should be further refined to minimize the numerical error of the RK4 method. Based on the user's preferences, the parameter $\beta$ can get a non-zero value to activate the random walk component and stimulate the dispersal of tracers.

As the numerical particles are not mixed or buried within the bed, they are always moving when there is a certain sediment transport. The predicted tracer transport rates must be interpreted as maximum movement rates. It shows the behaviour of grains in case they would not be mixed, buried and resurfaced in the bed. This makes the visualisation tool conceptually different compared to graded sediment approach. Whereas the sediment transport fields are correct; the visualisation of this data is based on a number of assumptions that make the time scale of the tracer dispersal less realistic.

However, Chapter 3 also demonstrated that the dispersal patterns of the two methodologies can significantly differ. This is especially the case for situations with large spatial variations in the sediment transport conditions. With the visualisation tool, the oscillating motion of a numerical particle during one cycle can be relatively large and the particle can experience transport conditions that are not observed in the vicinity of the initial location. With the graded sediment approach, the residual movement of sediment during one single does depend more on the local conditions.

However, the lack of interaction between the numerical particles and the bed is also one of the main strengths of the visualisation tool. The visualisation tool is able to provide large-scale transport pathways (e.g. number of kilometres) with minimum computational time. In this way, the tool can be used to quickly obtain insights about large-scale sediment transport patterns. Another clear advantage of the visualisation tool is the fact that it can use the output of one Delft3D simulation to study the pathways of multiple sources (post-processing). The graded approach requires a Delft3D simulation of the hydrodynamic and bed composition changes for each individual dump/start location.

The tracer dispersal patterns and the underlying transport pathways can be a useful for communication with non-experts. Because of the different techniques that are used and the multiple parameters that have to be chosen, running/applying the model can only be done by experts in numerical modelling and morphodynamics. This was also the case for the graded sediment approach. Now however, the definitions of the different parameters are less transparent and the values cannot be obtained based on a calibration with measured data.

# 5 Delft3D-NeVla model schematization and results

In order to answer the research questions described in Chapter 1, the sediment transport patterns within the mouth of the Scheldt estuary are studied for 3 cases. At first, there is the reference case that is used to describe the sediment transports in the current situation. Cases 2 and 3 describe the Scheldt estuary after applying two large-scale human interventions: (2) the construction of an island in front of Knokke-Heist and (3) the construction of a new navigation channel by extending and deepening the Geul van de Walvischstaart and Deurloo West channels. As explained in Section 2.2.1.4, these interventions are two examples that are taken from the Masterplan Flanders Bay (2014). The Masterplan presents these interventions as first ideas that can serve as inspiration for future efforts. These explorative cases are included to test the applicability of the visualisation tool; they are meant as real-life show cases/proofs of concept.

The analyses are based on the existing Delft3D-NeVla model (Section 5.1). Section 5.2 explains the model set-up and discusses how the second and third case are created. The two human interventions are implemented by changing the model bathymetry in the areas of interest. The boundary conditions are not changed. To answer the second research question, Section 5.3 analyses the Delft3D output in a regular/standard way. It discusses the hydrodynamic conditions and sediment transports for the three cases. The insights will also be used to understand the results of the visualisation tool (Chapter 6).

## 5.1 Delft3D-NeVla model

As introduced in Section 3.1, this study is based on the process-based Delft3D model and uses the FLOW module to model hydrodynamic conditions and sediment transports. The study about the Scheldt estuary is based on the existing Delft3D-NeVla model that is develop by Consortium Deltares-IMDC-Svasek-Arcadis (2013a), based on the NeVla-Simona model of Maximova et al. (2009ab). The boundary conditions are derived from the year 2006 and the bathymetry is mainly based on data from 2011. Vroom et al. (2015a) recently developed a newer version, with a update of the bathymetry and the different obstacles/(hard) structures within the estuary and new boundary conditions that are derived for the years 2013 and 2014.

For this study, the model is applied in a depth-averaged approach (2DH). The approach does not include vertical circulations due to density-driven currents and phase shifts between near-bed and near-surface velocities. Secondary flow is not modelled in a 3D approach, but is parameterized. By excluding these 3D effects, the calculation time can be reduced. As discussed by Vroom et al. (2015), the 3D effects are expected to be limited for calculations of sand transport in the mouth of the Scheldt estuary. The 2DH Delft3D-NeVla model has been successfully validated for the Western Scheldt (hydrological and morphological) by Consortium Deltares-IMDC-Svasek-Arcadis (2013a) and Maximova et al. (2009ab). Based their updated model, Vroom et al. (2015a) also showed promising results in the hydrodynamical validation for the mouth. An extensive morphological validation for the mouth has not been performed yet. Recently, the Delft3D-NeVla model have been applied successfully in morphological studies by such as Damen (2014), Tonnen & van der Werf (2014), van der Werf et al. (2015), Groenenboom (2015) and van Schaik (2015).

## 5.2 Model setup

### 5.2.1 Computational grid

The Delft3D-NeVla grid covers the entire Scheldt estuary: the ebb-tidal delta, Western Scheldt and all Flemish rivers until the upper limit of tidal influence. The grid resolution varies between ~400 m on the Continental Shelf, to in between 50 and 100 m in the Western

Scheldt to ~10 m upstream (Consortium Deltares-IMDC-Svasek-Arcadis, 2013c)(Figure 5.1). To reduce the computational time of the Delft3D model, the grid upstream of Schelle is not used in this model study (Figure 5.1). The relocation of the upstream boundary towards Schelle has no significant effect on the model results (Appendix C.1).

### 5.2.2 Boundary conditions and simulation period

The conditions for the three seaward boundaries are generated from the ZuNo (Southern North Sea) SIMONA model (Consortium Deltares-IMDC-Svasek-Arcadis, 2013ac). To exclude the meteorological effects, the time series are converted into astronomic constituents (van Rooijen, 2015). For the north-western sea boundary (Figure 5.1), the boundary conditions are based on Riemann invariants. For the other two seaward boundaries, the conditions are based on flow velocities. The new boundary at Schelle is based on times series with discharges derived from simulations with the entire grid (appendix C.1). For the sand concentrations at the boundaries, a Neumann condition (zero concentration gradient) is used. All Delft3D simulations cover one full spring neap tide (09-03-2006 00:45 until 23-03-2006 10:45). Every time, the simulations are preceded by (hydrodynamic) spin-up period of 3 days during which the hydrodynamic conditions can adjust to the boundary conditions.


*Figure 5.1 Computational grid Delft3D-NeVla model. The light blue area indicates the grid upstream of Schelle.*

### 5.2.3 Other model settings

The Delft3D-NeVla model includes a “generic” Manning roughness with a stepwise variation in the longitudinal variation (values between 0.022 and 0.028 $s/m^{1/3}$ in the area of interest) (Maximova et al., 2009ab). As also used by multiple other studies (e.g. Damen 2014 and Consortium Deltares-IMDC-Svasek-Arcadis 2013a, 2013c), the sediment is composed of a uniform grain size with a $D_{50}$ of 0.2 mm (sand). Sediment transport of this non-cohesive sediment is based on the van transport formulation as described by van Rijn et al.(2004). Based on the findings of Section 2.2.1.3, the effect of salinity is not included in the model. For practical reasons (e.g. simplicity) also the effects of wind and waves are neglected. As discussed in Section 2.2.1.3, the tidal currents are expected to be the main driver of the morphological developments in the mouth area.

### 5.2.4 Model bathymetry

#### *5.2.4.1 Case 1: Bathymetry 2011*

The bathymetry in the Delft3D-NeVla model is based on data from 2011 for the Western Scheldt and Lower Sea Scheldt (including the 3rd deepening) and somewhat older data for the more down- and upstream areas (Figure 5.2). As discussed above, the study of Vroom et al. (2015a) used more recent data. For this study, the model accounts for the non-erodible layers, updated for the year 2011.

As stated by Schoellhamer et al. (2008), adequate spin-up time is required to initialise models. Otherwise, the solution may contain bathymetric changes (i.e. sediment transports) that are not due to environmental forcing, but rather improper specification of initial conditions, boundary conditions and other model parameters. This study uses a (morphological) spin-up period of 3 spring-neap cycles during which the bathymetry can adjust (appendix C.2). The resulting bathymetry is applied in the actual simulation that is used in to study sediment transports. Within this last simulation, the bed level and bed thickness are fixed. All simulation (3+1) are preceded by another (hydrodynamic) spin-up interval to adjust the hydrodynamic conditions (Section 5.2.2).

#### 5.2.4.2 *Cases 2 & 3: Human interventions*

The bathymetries of cases 2 and 3 are shown in Figure 5.2. The bathymetric changes in the mouth area compared to case 1 are shown in appendix C.3. The report of Masterplan Flanders Bay (2014) and their website[1] present some first ideas about the construction of a single large island or multiple small islands in front of the Flemish coast. For simplicity, this study only considers this fist alternative. Based on some available sketches, the bathymetry of 2011 is adjusted by construction of a single large island in front of the coast of Knokke-Heist. The island has a length of about 7 km and a width of about 500 m. Compared to case 1, 123 million $m^3$ extra sediment is added. The new navigation channel has a width of about 1 km. Its depth is approximately the same as the depth of the current Wielingen channel (~18 m NAP). Compared to case 1, 250 million $m^3$ sediment is removed. For both cases, the designs of the interventions are subjected to a spin-up interval of 3 spring-neap cycles to remove the largest irregularities and smooth the bathymetries.

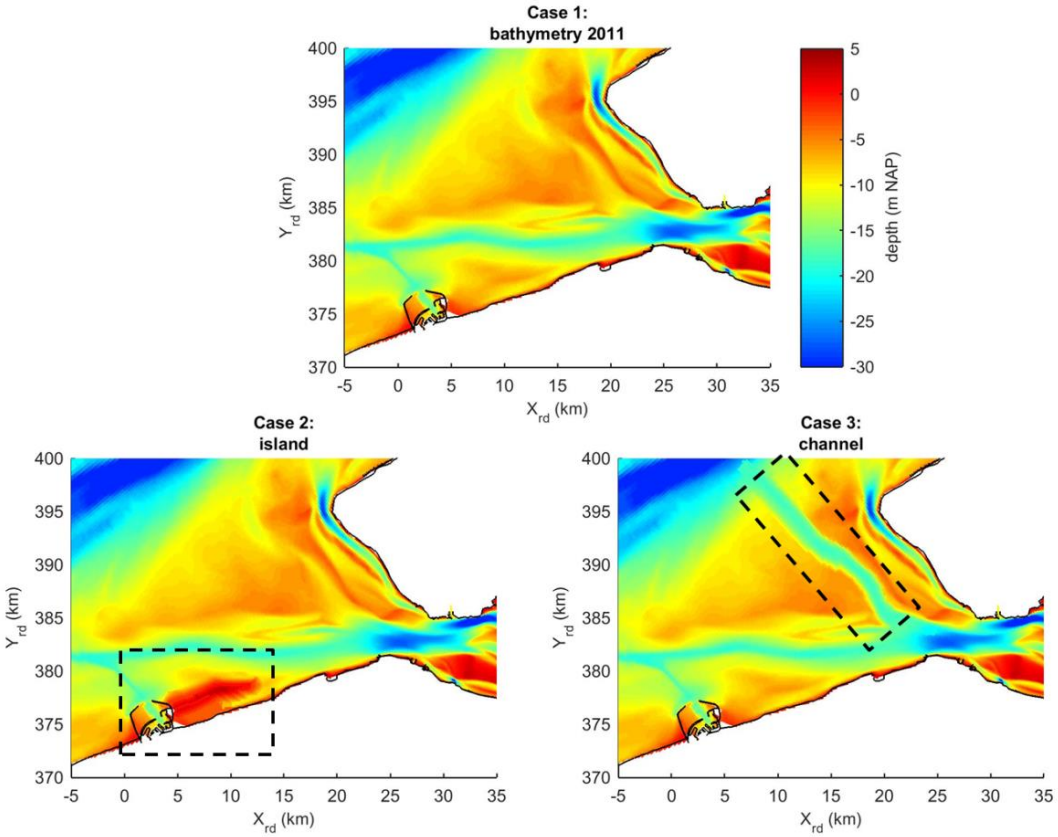


*Figure 5.2 The three bathymetries that will be studied with the visualisation tool. Appendix C.4 shows a comparison of the bathymetries of case 1 with respectively cases 2 and 3*

[1] *http://www.vlaamsebaaien.com/04-strand-knokke-heist-zwin*

## 5.3 Model results

This section presents the analysis of the hydrodynamics and sediment transports in the mouth based on the "standard" Delft3D model output. The hydrodynamics are analysed to better explain the sediment transports. The findings of this section help to answer the second research question and can be used when studying the sediment transport pathways (Chapter 6). In the text below, the three cases are discussed separately. For the impact of the human interventions (cases 2 and 3), this section only describes the most important findings. To limit the length of the report, the other figures are included in appendix C.4.

When interpreting the results, it is important to consider that the Delft3D simulations are based on a depth-averaged approach and do not take into account density=driven currents and the impact of wave and wind. It is also important to recognize that the computations are solely based on a single sediment type: fine sand with $D_{50}$ equal to 0,2 mm. Especially in the area around Zeebrugge, the sediment in the bed is characterized by high percentages of silt and clay (Kuijper, 2015; Van Lancker et al., 2012; Vroom & Schrijvershof, 2015). Together with organic material and water, silt and clay form mud. Mud behaves more cohesive compared to a sand layer. Therefore, a larger bed shear stress is needed to get these particles in suspension than one would infer from their grain size. Due to the small fall velocity, the mud can remain long in suspension. Because of this settling lag, the period of slack water can be an important determinant for the residual transport of fine sediment.

### 5.3.1 Case 1: Bathymetry 2011

#### *5.3.1.1 Hydrodynamics*

An analysis of the tidal amplitude is described in appendix C.4. To get an impression of the hydrodynamics, the tidal wave propagation within the mouth area is visualized in Movie 5.1.

Maximum flow velocities

Figure 5.3 shows the maximum flow velocities (averaging over the different $M_2$ periods of the spring neap tide). As expected, the flow velocities are at their maximum in the inlet and the different channels. Within the Oostgat, the maximum flow velocities are detected at the southern and northern ends. The maximum flow velocities decrease when moving towards the middle of the channel. In the Wielingen, the maximum flow velocities decrease when moving towards the west.

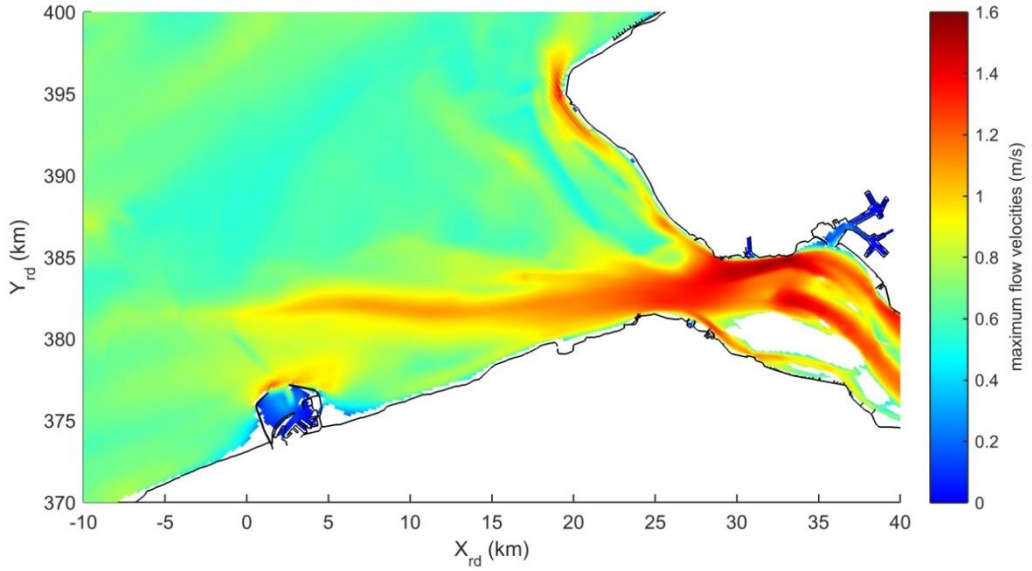


*Figure 5.3 Maximum flow velocities for case 1. The velocities are computed by taking the average of the maximum flow velocities that are detected within the different $M_2$ periods of the spring neap cycle*

Tidal ellipses

The flow velocities within the spring neap cycle can be summarized in tidal ellipses. Whereas these ellipses are normally drawn for a single astronomic constituent, Figure 5.4 draws the ellipses of the entire spectrum (the total flow velocities, the so-called “stroomrozen”). The ellipses are made as follows. For an observation points, one plots all the vectors that represent the flow velocities during one spring-neap cycle. Each arrow originates at the observation point and has a length and direction according to respectively the magnitude and direction of the flow velocity at that specific time. In this way, there is scatter of arrows that are directed in different directions. The ellipses are created by drawing the edge around this set of arrows. Each ellipse is normalized with its largest magnitude to make the sizes of the ellipses comparable. The goal of this figure is to show the dispersion/spreading in the direction of the flow velocities. Most of the ellipses in the channels are flat. Here, water flows mainly in the longitudinal direction. For the Vlakte van de Raan and the shoals in front of Walcheren (e.g. Elleboog and Rassen), the ellipses have a more circular shape. Here, the flow velocity has similar magnitudes in all directions. This circular pattern was also found with measurements of the flow velocities at the Vlakte van de Raan (Plancke et al., 2014).

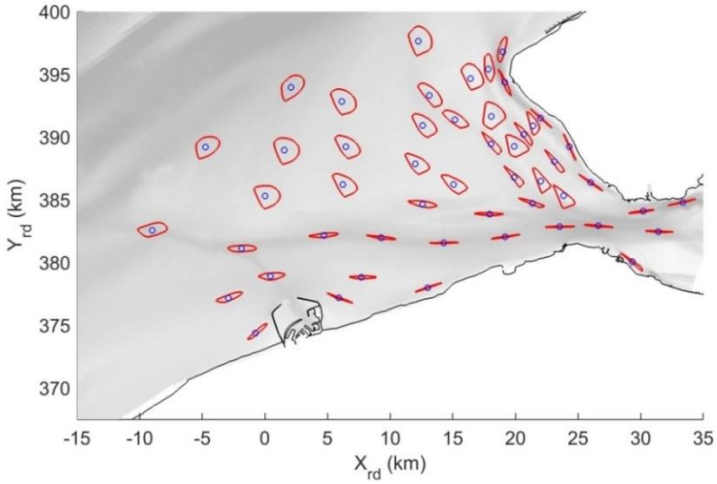


*Figure 5.4 Tidal ellipses describing the flow velocities for case 1 (see text above for the method that is used). The ellipses are normalized and therefore have the same size. The blue dots represent the measurement points.*

Discharges

The gross and net discharges (million $m^3$/tide) through the different cross-sections that are shown in Figure 5.5, correspond with the findings of Tonnon & van der Werf (2014). The gross discharges show that the Wielingen and Scheur are responsible for the main part of the tidal discharges in the mouth. On average, there is a discharge of 3 to 4 million $m^3$/tide from the Western Scheldt towards the mouth. This corresponds with the average discharge of the Schelde (~100 m3/s). As also concluded with the literature review of Chapter 2, there is a cross-channel imbalance at the inlet (Vlissingen-Breskens). The net discharge through the cross-section at the northern part is ebb-dominant (towards the west), while the southern part shows a flood-dominant (towards the east) net discharge. The southern part of the Oostgat and Sardijngeul contain net discharges in the flood direction. Furthermore, the result show net discharges in the ebb direction for the eastern part of the Wielingen, Geul van de Walvischstaart, Geul van de Rassen and northern part of the Oostgat. The net discharges through the cross-sections at the connection of the Wielingen and Scheur (x<10 km) are directed towards the east. However, the cross-sections are large and also cover parts of the Paardenmarkt and Vlakte van de Raan. The large flood directed net discharge through the cross-section at the eastern end of the Scheur results in a large northward directed transport of water over the Vlakte van de Raan. At last, Figure 5.5 demonstrates that the net discharges over the Elleboog and Bankje van Zoutelande are directed towards the northeast.

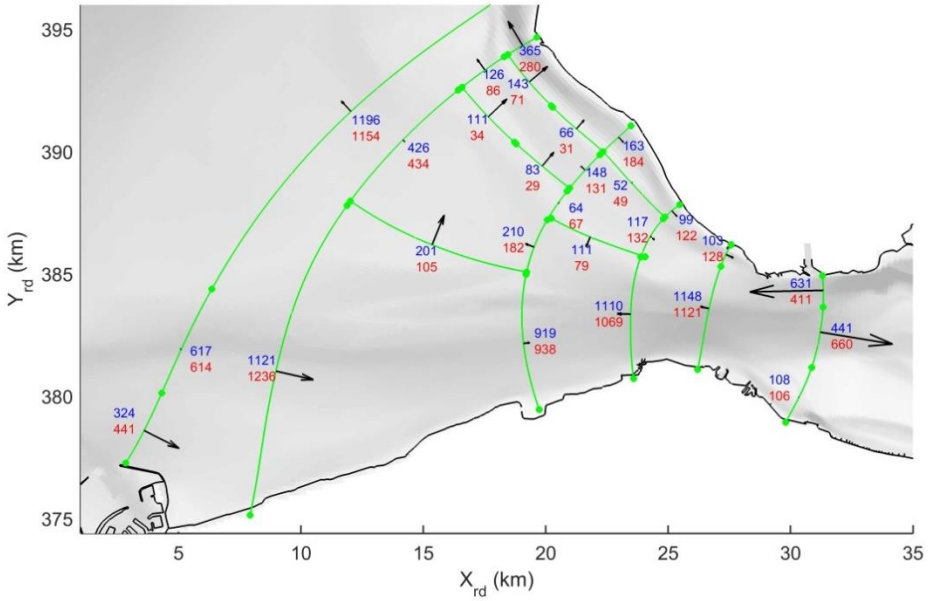


*Figure 5.5 Gross discharges through cross-sections (million $m^3$/tide) for case 1 (averaged over spring neap cycle). The blue numbers indicate the flood discharges (west/south). The red numbers present the average discharge during ebb (east/north). The arrows represent the size and direction of the net discharges.*

Residual flow velocities

The directions of the residual flow velocities (Figure 5.6) correspond with the patterns of the net discharges. The modelled net flow velocities range between 0 and 0.2 m/s. The net velocities show an ebb-dominance (towards the west/north) in the entire Wielingen, Scheur, Nolleplaat, Geul van de Walvischstaart, Geul van de Sluissche Hompels and the northern part of the Oostgat. The southern part of the Oostgat and the Sardijngeul contain net flow velocities in the flood direction (towards the south). The net flows reproduce the cross-channel imbalance at the inlet. Moreover, the results show a circular pattern in the clockwise direction over the Deurloo-Oost, Elleboog and Geul van de Walvischstaart. Lastly, there is also a circulation cell northeast of Zeebrugge. The net flows correspond with the findings of Steijn & van der Spek (2005), Tonnon & van der Werf (2014) and Vroom et al. (2015a).

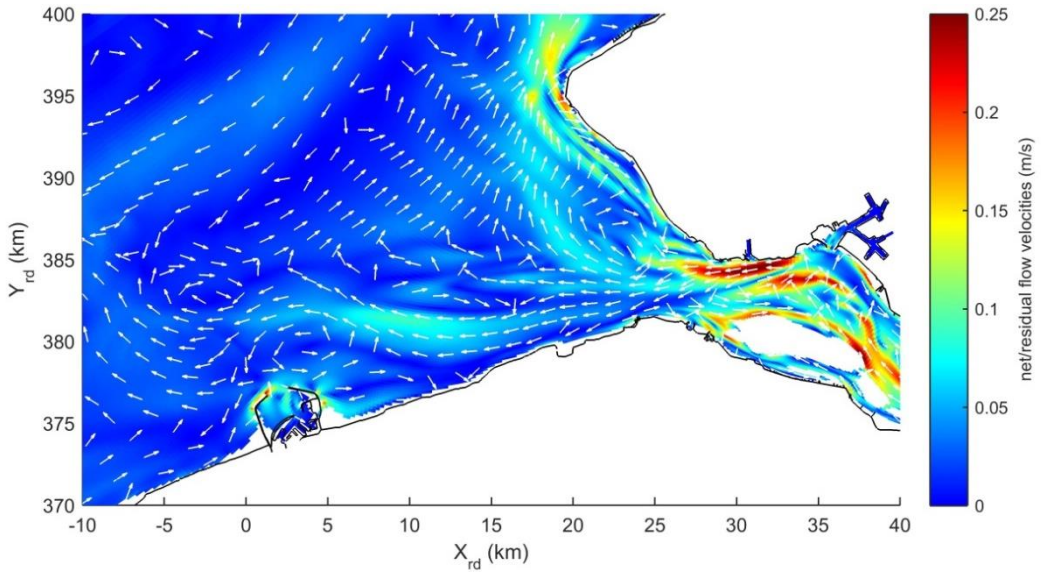


*Figure 5.6 Net flow velocities for case 1. Arrows are normalized with the magnitudes (equal length) and only indicate the direction.*

Tidal asymmetry

Finally, an analysis of the tidal asymmetry based on the $M_2$ and $M_4$ constituents in the vertical and horizontal tide can help to better understand the hydrodynamics. The harmonic analysis of the time series is carried out with the Matlab program T-tide (Pawlowicz et al., 2002).

First of all, let's analyse the vertical tide. In Figure 5.7, one can find the phases of the $M_2$ component within 3 channel "systems": Wielingen-Scheur, Deurloo West-Geul van de Walvischstaart and Oostgat-Sardijngeul. Only consider the red lines, the blue and green lines represent the results of cases 2 and 3 (Sections 5.3.2 and 5.3.3). The observation points that are used for these plots are shown in appendix C.4. The figure shows that the phases of $M_2$ component increase when moving from the seaside towards the Western Scheldt. This indicates that the tidal wave propagates from the seaside towards the inlet as would be expected. The trend of the $M_2$ amplitude along the channel axes is shown in appendix C.4.

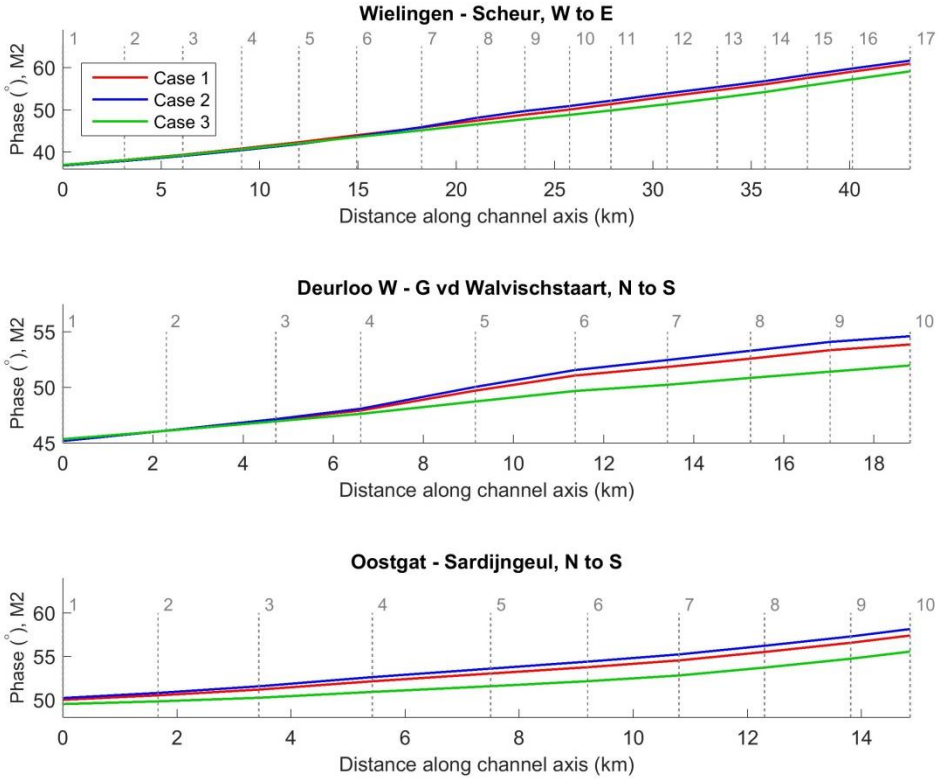


*Figure 5.7 Phase of the $M_2$ component within the vertical tide, shown along different channel axes. The grey lines and numbers refer to the different observation points along the channel axes (see appendix C.4)*

Figure 5.8 demonstrates the phase difference between the $M_2$ and $M_4$ constituents for the vertical tide along the channels (again, only consider the red lines). For the transport of sand, the peak velocities are an important indicator of the ebb or flood dominance. A phase difference for the vertical tide between 0 and +180 degrees indicates that the ebb period is longer than the flood period. As result, peak flow velocities are highest in case flood and the tide can be considered flood dominant. For phase differences larger than +180 degrees, the vertical tide shows ebb dominance. Looking to Figure 5.8, we can see that the vertical tide is flood-dominant for all channels. However, the phase differences are only small and indicate that the wave is quite symmetric. The flood-dominance in the system Deurloo West-Geul van de Walvischstaart is increasing when moving towards the inlet. For the other channel systems, this trend smaller. The amplitude ratios are shown in appendix C.4.

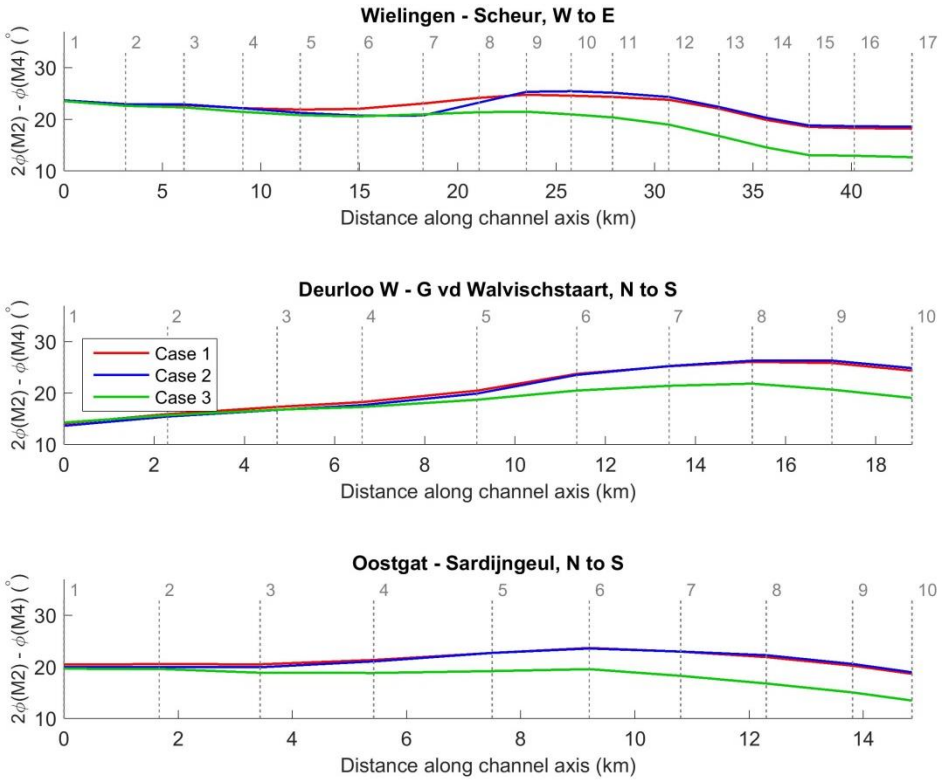


*Figure 5.8 Phase difference of the $M_2$ and $M_4$ components within the vertical tide, shown along different channel axes. The tidal wave is symmetric in case of phase difference of 0 or 180 degrees. The grey lines and numbers refer to the different observation points along the channel axes (see appendix C.4)*

Secondly, one can compute the tidal asymmetry based on the flow velocities. Whereas the water level describes scalar time series, the flow velocities consist of x- and y-components and are vector time series. It is possible to determine the phases of the $M_2$ and $M_4$ constituents of the vector time series (Pawlowicz et al., 2002). However, it is no longer possible to characterise the asymmetry by an amplitude ratio and relative phase difference. Each constituent is characterised by ellipses with certain major and minor axis, the inclination (direction of major axis) and the corresponding phase. So, there are four independent parameters instead of two (Wang et al., 1999)

As shown in Figure 5.4, water in the Wielingen-Scheur and Oostgat-Sardijngeul flows mainly in the longitudinal direction. Here, we can do a harmonic analysis of the flow velocities in the direction of the channel axis. In this way, the small cross channel velocities are neglected. The flow velocities in the longitudinal direction are obtained by converting the velocities of the x- and y-direction towards velocities on the major and minor axis. The phase differences between the $M_2$ and $M_4$ components fof the flow velocities on the major axis are shown in Figure 5.14. The horizontal tide is flood dominant with phase differences between -90 and +90 degrees. For phase differences between +90 and +270 degrees, it is flood dominant. Appendix C.4 includes a figure that describes the amplitude ratios.

In line previous findings, also the harmonic analysis of the flow velocity shows flood dominance within the Wielingen and Scheur. The phase angle decreases when moving towards the east. At the inlet (x=45 km), the phase difference is close to -90 degrees and indicates that the horizontal tide in the main direction is almost symmetric. This trend of the phase differences within the Wielingen and Scheur was also observed in the study of Verduin (2009). The results demonstrate that the horizontal tide is ebb-dominant within the Oostgat-Sardijngeul. From north to south, the ebb-dominance increases at the beginning and later on decreases. The differences between the tidal asymmetries that are found with the vertical and

horizontal tide can be explained by the non-linear relation between the two. With hypsometrical effects, both storage width and cross-sectional area depend on the water level.

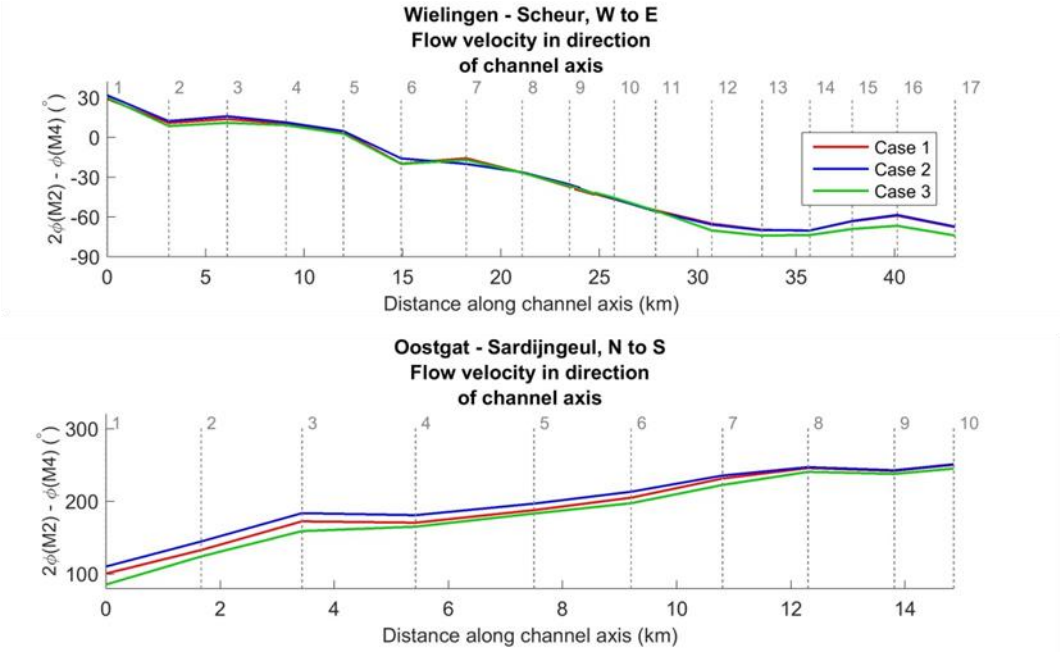


*Figure 5.9 Phase difference of the $M_2$ and $M_4$ components within the flow velocity in the direction of the channel axis. The tidal wave is symmetric in case of phase difference of -90 or 90 degrees. The grey lines and numbers refer to the different observation points along the channel axes (see appendix C.4)*

For other areas within the domain, the flow is more circular and the difference between the minor and major axis is smaller. To still visualize the horizontal tidal asymmetry, another approach is used. By using T-tide, the original vector time series is decomposed in different constituents; each constituent describes the flow velocities in x- and y-direction (i.e. tidal ellipses with certain axes, inclinations and phases). Subsequently, the tidal velocities vectors in the mouth of the Scheldt estuary are reconstructed by only taking into account the data from the $M_2$ and $M_4$ constituents. The tidal asymmetry can be studied by determining the direction and magnitude of the maximum reconstructed flow velocities. Figure 5.10 again shows that the Wielingen is flood dominant, while the Oostgat is ebb dominant. Besides, also the other channels in front Walcheren and the Vlakte van de Raan have peak values of the reconstructed flow velocities that are directed towards the northeast/north (ebb). To see more details, appendix C.4 contains a figure that zooms in at the area in front of Walcheren.

Lastly, there is another alternative to study the reconstructed flow velocities. The flow velocities can be converted into instantaneous sediment transports, by making use of the simplified transport formula of Section 2.1.2 (Eq. 2.5 with f=1 and n=3). The tidal asymmetry can be determined by computing the residual value of the (reconstructed) sediment transports that occur during one tidal cycle. In this way, the simplified residual sediment transport takes into account the magnitude of the peak velocities and the duration of ebb and flood periods. The results are presented in appendix C.4 and are similar compared to the Figure 5.10.

#### 5.3.1.2 *Sediment transport*

The directions (arrows) and magnitudes (colormap) of the residual sediment transports over one spring neap cycle are presented in Figure 5.11. Figure 5.12 uses same data, but visualizes the direction of the residual transport with a colormap. As this figure may be difficult to interpret, let's consider an example. The Wielingen is colored yellow and green. This indicates that the direction of the residual transport has an angle of 270-300 degrees compared to the north (clockwise). Thus, the residual transport is directed towards the west.

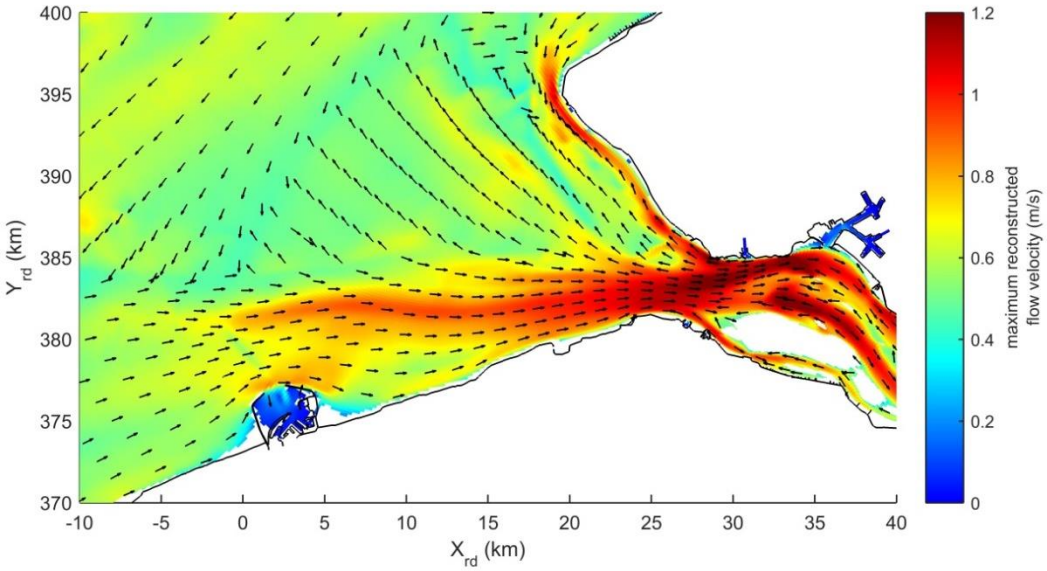


*Figure 5.10 Maximum flow velocity of the reconstructed flow velocity (based on $M_2$ and $M_4$). The colormap indicates the magnitude of the maximum velocity. Arrows are normalized (equal length) and indicate the direction. The directions give an indication of the tidal asymmetry in the horizontal tide.*

The results show that the residual transports are highest in the inlet. Here, also the flow velocities are at their maximum (Figure 5.3). The patterns of ebb- and flood-dominance in the residual transports are quite similar compared to the patterns of the residual flow velocities. The total residual sediment transports at the Wielingen, Scheur, Geul van de Walvischstaart, Deurloo Oost, Deurloo West, Geul van de Sluissche Hompels and the northern part of the inlet are clearly ebb-dominated. The southern part of the inlet contains residual sediment transports in the flood direction. The results in the Oostgat correspond with the conclusions of Damen (2014). There is a divergence of the residual transport over both the cross-section and longitudinal direction in the Oostgat. The residual transport in the northern part of the Oostgat is ebb-dominant, while the southern part shows flood dominance. The cross-channel imbalance shows that the coastward side of the channel is ebb-dominant, while the seaward side is flood dominant. At the port of Zeebrugge, there is an alongshore residual transport in north-eastern direction. Due to the low flow velocities, the instantaneous and residual transports are relatively low at the Vlakte van de Raan compared to channels. Based on these maps, it is difficult to determine a clear dominant direction for the residual transport for the Vlakte van de Raan. As expected, the directions of the residual transports on the shoals can clearly deviate from the transports in the adjacent channels. Figure 5.12 clearly shows that this is the case for the Bankje van Zoutelande, Nolleplaat, Elleboog and Rassen and the shallow area between the Spleet and Wielingen-Scheur.

However, the computed residual sediment transports are somewhat different compared to the results of Verduin (2009) and Tonnon & van der Werf (2014). The major difference lies within the Wielingen (especially the eastern part), the other studies found a flood-dominant residual transport. Especially for the study of Tonnon & van der Werf (2014), this is surprising. They also applied the Delft3D-NeVla model and the transport formula of van Rijn et al. (2004).

Both studies computed the sediment transports only for a representative period. It is unknown whether these periods are chosen based on the representation of the hydrodynamics, sediment transports and/or bed level changes in the mouth. An analysis of the model results shows that the residual transports in the Wielingen and other channels can alternate between ebb and flood-dominance for some tidal cycles within the spring neap cycle (appendix C.4 and Movie 5.2). In other words, the selection of a tidal cycle can certainly have an effect on the residual transport patterns that are found. Compared to the study of Tonnon & van der

Werf (2014), there are two other clear differences. Their simulations included the effect of wind and were based on time series boundary conditions. However, it is expected that the effects of these differences are limited (e.g. due to the large water depths in the channel). As the current Delft3D-NeVla model is based on the model as developed by Consortium Deltares-IMDC-Svasek-Arcadis (2013a), there is enough confidence to use these model results for the remaining part of this study.

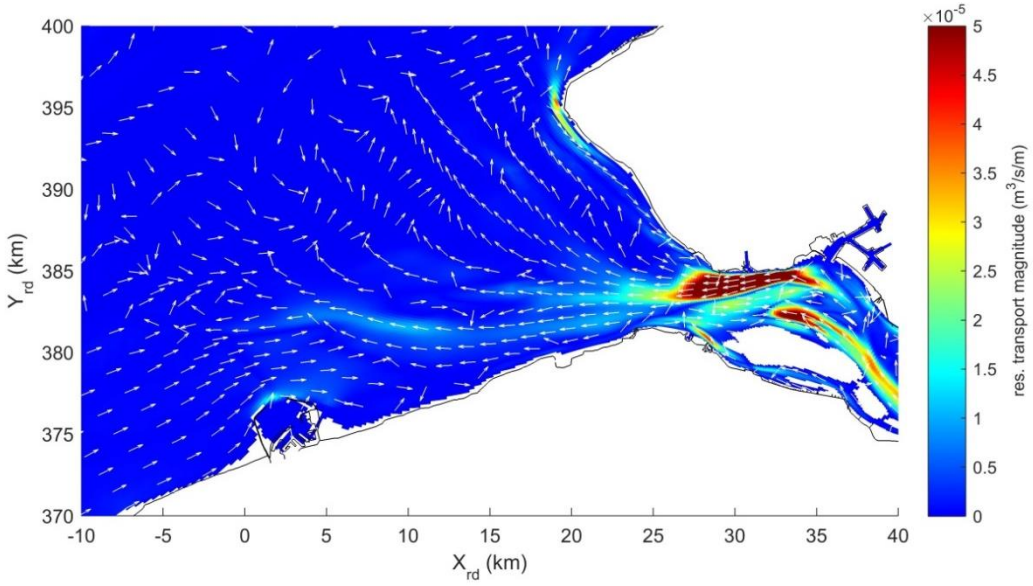


*Figure 5.11 Modelled residual sediment transport (computed for one spring-neap cycle) for case 1 (reference case). The arrows are normalized (with the magnitudes) and only indicate the direction.*

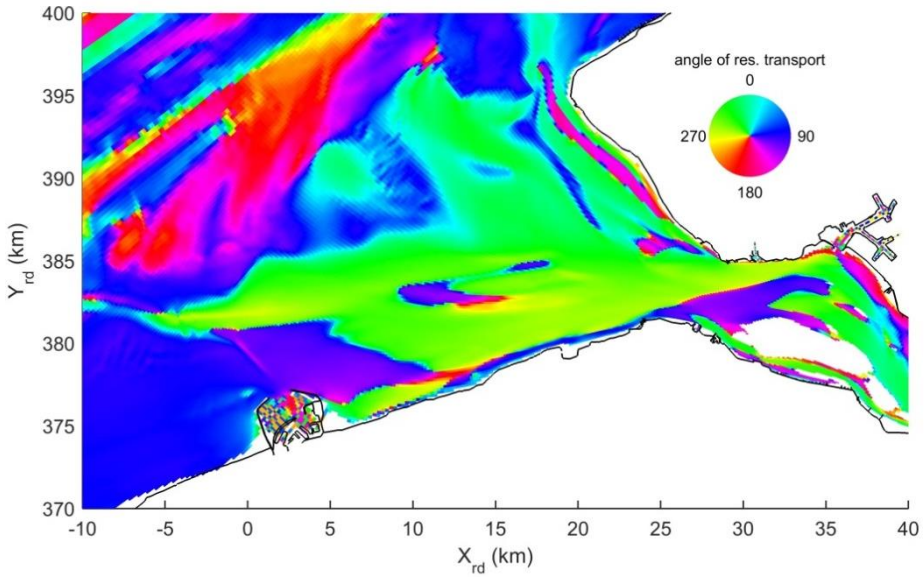


*Figure 5.12 Direction of the residual sediment transport (computed for one spring-neap cycle) for case 1. The map describes the same dataset as Figure 5.11, but just uses colorscale to visualize the directions of the vectors.*

Similar to flow velocities (Figure 5.4), also the variation in the direction of the total sediment transport at a certain can be expressed in ellipses. The results are shown in appendix C.4. Figure 5.13 compares the suspended and bed load transports. The left subplot compares the magnitudes of the residual sediment transports. The right subplot is based on a comparison of the peak suspended and bed load sediment transports. For both subplots, a higher ratio indicates that suspended transport is dominant. The grey areas indicate a ratio between 0 and 1 (bed load is dominant). In area east of the line Westkapelle-Zeebrugge, the sediment

transports are clearly dominated by the suspended transport mode (Figure 5.13). In case of the Wielingen for example, the magnitudes of the residual suspended transports are more than 10-15 times as high compared to the bed load residual transports. For the more seaward area, the suspended transport often still dominates but the differences are smaller. This is probably caused by the larger water depths and lower flow velocities.

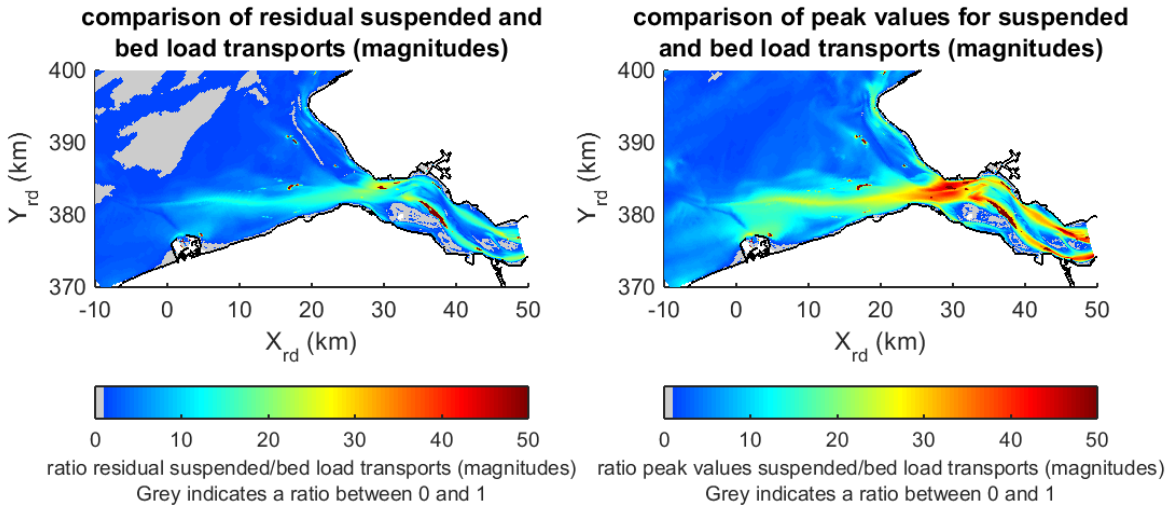


*Figure 5.13 Comparison of suspended and bed load sediment transports for case 1. The left subplot compares the magnitudes of the residual transports. The right subplot compares the maximum sediment transports. The grey colour represents the areas for which the ratio is smaller than 1 (bed load transport is dominant)*

### 5.3.1.3 *Erosion-Sedimentation patterns*

For a better interpretation of the result, it is useful to get an impression of the modelled erosion-sedimentation patterns. For this brief analysis, the erosion and sedimentation are translated in the change of the bed thickness and the bed level is still fixed. In this way, there is no feedback loop between the hydrodynamics and the morphological changes. For the other simulations that are discussed in this chapter, the bed thickness and bed level are still fixed (as required for the visualisation tool).

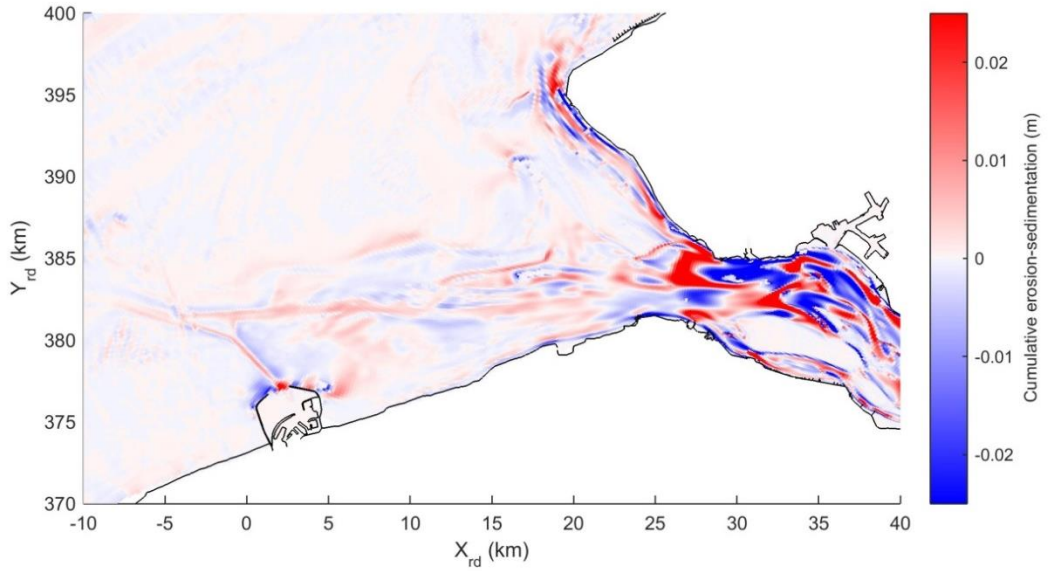


*Figure 5.14 Cumulative bed thickness change after one spring neap cycle, for case 1. Red colors indicate sedimentation and blue colors represent erosion.*

Following Figure 5.14, the largest modelled erosion and sedimentation rates can be found near the inlet (Vlissingen-Breskens). There are alternating areas of erosion and sedimentation. If we compare Figure 5.14 and Figure 5.11, these areas seem to correspond with respectively the increase and decrease of the residual sediment transport magnitudes. The Wielingen, Scheur, Pas van het Zand, Oostgat and Sardijngeul all show an increase in the bed thickness. For these first three channels, this is in line with the current dredging operations (to ensure the navigability). The sedimentation at the northern-end of the Oostgat channel does not correspond with the bed level decrease as found by Elias & van der Spek (2015) (Section 2.2.1.5). First of all, this could be caused by the assumptions that are being made in the model (2DH, no wind and waves, fine sand as single grain size). However, these observed bathymetric changes happened over the period 1964 and 2011 and were influenced by many other conditions (e.g. Delta Works, dredging and dumping operations etc.). As found by Elias & van der Spek (2015), the bed at the Vlakte van de Raan is more stable.

## 5.3.2 Case 2: Island in front of Knokke-Heist

### *5.3.2.1 Hydrodynamics*

Figure 5.15 shows the changes in the gross discharges compared to case 1. The gross discharges themselves are shown in appendix C.4. The construction of the island results in lower gross discharges through many of the cross-sections in front of the southern coast. The island forms an obstruction and reduces the cross-sectional area for the flow near Knokke-Heist. The discharges through the Geul van de Walvischstaart, Deurloo Oost, Deurloo West and Oostgat are increasing. The gross discharges in the inlet do not change significantly.

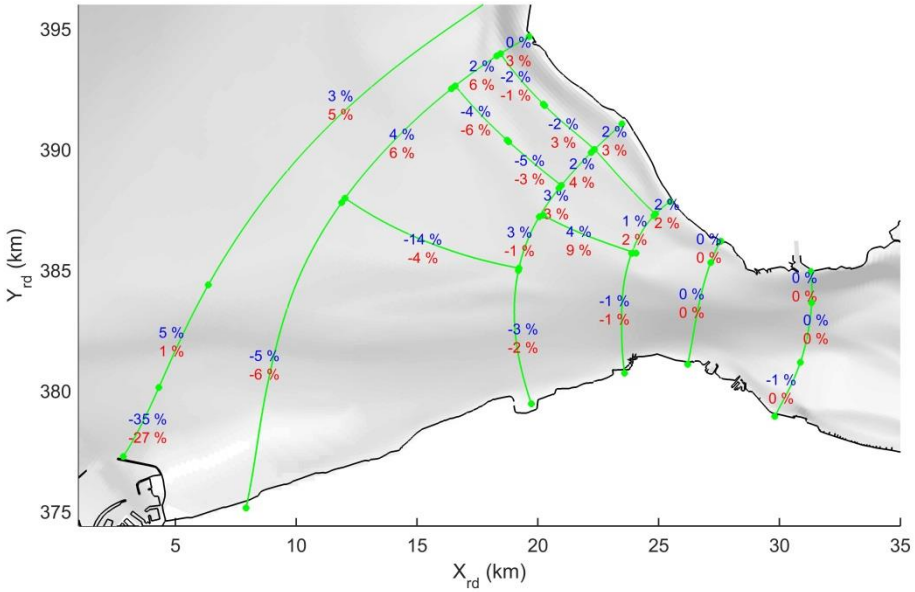


*Figure 5.15 Relative changes in gross discharges for case 2 compared to case 1. The blue numbers indicate the changes in the flood discharges (west/south). The red numbers represent the ebb discharges (east/north).*

In Figure 5.16, one can find two snapshots of the flow velocities near the island during ebb and flood. Whereas the flow was converging and diverging in front of the port of Zeebrugge for case 1, this contraction of the now happens over a longer distance. The construction of the island results in an increase of the flow velocities locally. In other words, the reduction in the cross-sectional area is not fully compensated by a decrease in the discharges.

Figure 5.17 demonstrates the change in the maximum flow velocities compared to case 1. The maximum flow velocities for case 2 themselves can be found in appendix C.4. In line with previous observations, there is a clear increase of the maximum flow velocities north and

northeast of the island. Further upstream and downstream, the reduced discharges (here, there is no change in the cross-sectional area) result in lower maximum flow velocities. Although the changes are more irregular/scattered, the intervention results also in an increase of the net flow velocities in the vicinity of the island and a decrease of the net flow velocities in the middle and eastern part of the Wielingen (appendix C.4).

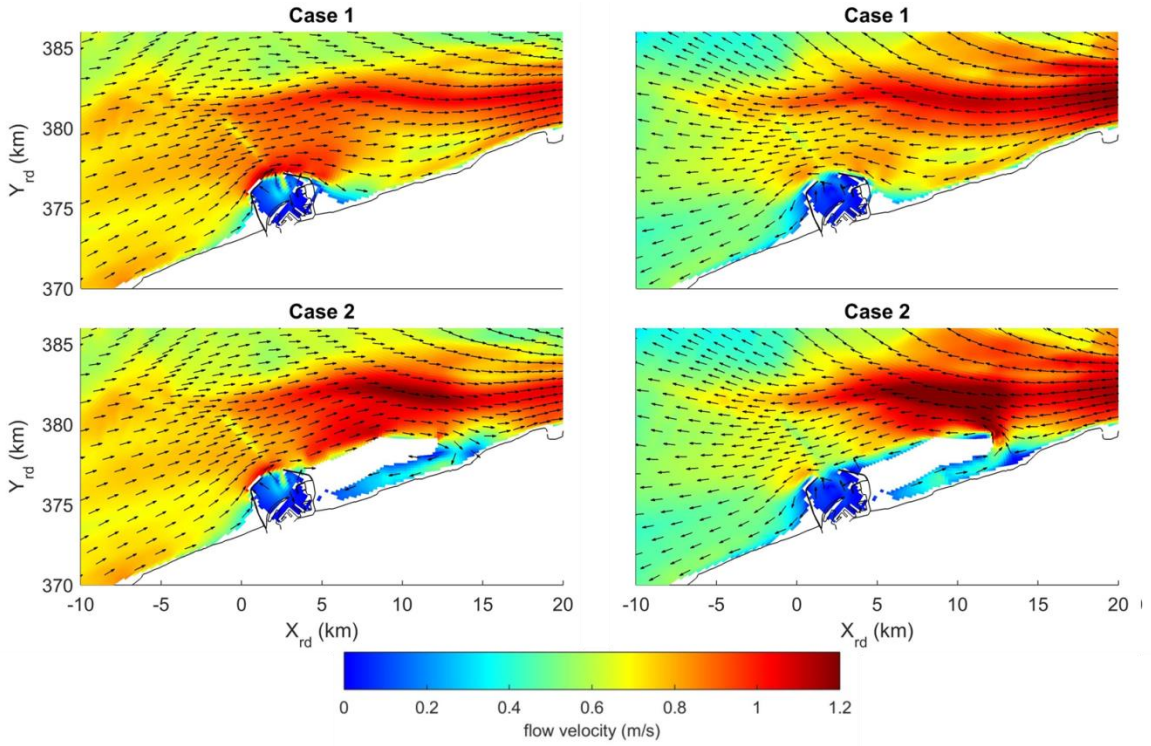


*Figure 5.16 Left: flow velocities 1.5 hours before high water at Vlissingen (maximum flow velocities in flood direction, 21-3-2006 4:30). Right: flow velocities 2 hours before low water at Vlissingen (maximum flow velocities in ebb direction, 20-3-2006 21:00).*

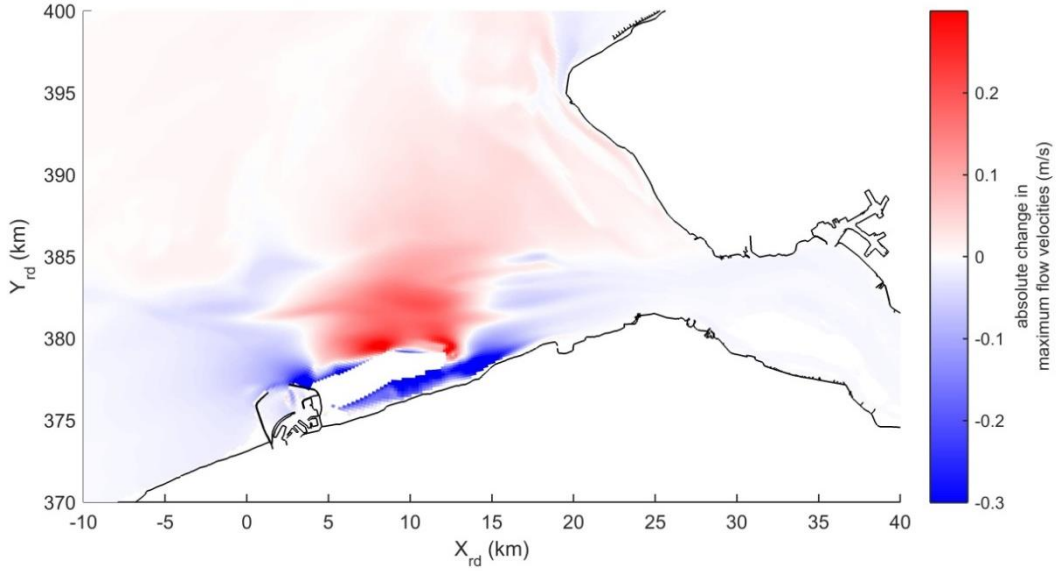


*Figure 5.17 (Absolute) change in the maximum flow velocities, case 2 compared to case 1. Red colors indicate higher maximum velocities; blue indicates lower maximum velocities.*

Next, one can study the effect of the human interventions on the tidal asymmetry. Figure 5.7 demonstrates that the phases of the $M_2$ constituent in the vertical tide increase slightly for

Wielingen-Scheur, Deurloo West-Geul van de Walvischstaart, as well as the Oostgat-Sardijngeul. Although the change is only small, it seems that the tidal propagation through all three channel-systems is somewhat slower with the construction of the island. Moreover, also the amplitude of $M_2$ wave in the different channels is lowered (appendix C.4). Based on Figure 5.8 and Figure 5.9, one can conclude that the changes in the tidal asymmetry based on the vertical tide and horizontal tide are only small.

#### 5.3.2.2 *Sediment transport*

Figure 5.18 shows the residual transports for case 2. Maps of the absolute and relative changes can be found in appendix C.4. Because of the increased flow velocities, the residual transports directly north of the island increase. Within the section of the Scheur in front of the island, the effect is directed towards the west (ebb). The orientation of the residual sediment transports in front of the island also slightly changes. The area east of the port was sheltered from the alongshore flow of sediment in case 1, but disappears with the construction of the island. Moreover the area where the ebb-dominant residual transport from the Scheur and the alongshore residual transport meet; moves slightly towards the east.

The lower maximum flow velocities in the middle and eastern sections of the Wielingen and northwest of Zeebrugge result in lower residual sediment transports. In other words, the change in the residual transport in the Wielingen is flood directed (i.e. smaller ebb dominance). For the area north-northwest of Zeebrugge, the effect is ebb directed (i.e. smaller flood dominance). For the Vlakte van de Raan, the Geul van de Walvischstaart and the channels in front of the coast of Walcheren, the effect of the island on the residual transports is directed towards the north/northeast. However, the absolute change is small.

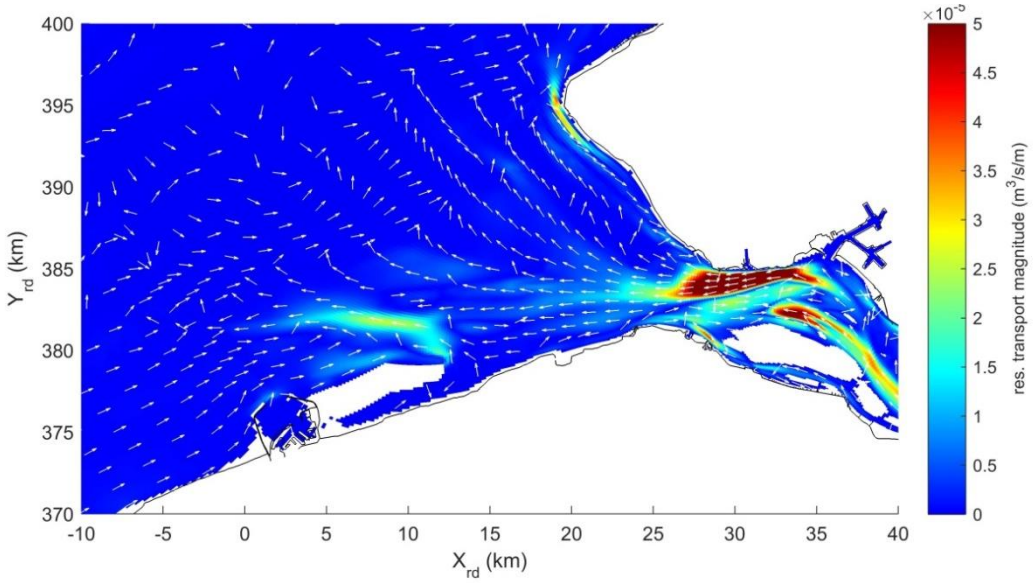


*Figure 5.18 Modelled residual sediment transport (computed for one spring-neap cycle) for case 2. The arrows are normalized (with the magnitudes) and only indicate the direction.*

#### 5.3.2.3 *Erosion-sedimentation patterns*

Figure 5.19 shows the bed thickness changes for case 2. Due to the construction of the island, the sedimentation and erosion patterns in front of the southern coast change. At the western (near the port of Zeebrugge) and eastern ends of the island, the results show erosion. In between these areas, the bed thickness increases (sedimentation). The part of the Scheur in front of the island shows a larger sedimentation. This means that construction of the island could increase the need to frequently dredge the navigation channel. The changes in the erosion-sedimentation patterns compared to case 1 can be found in appendix C.4.

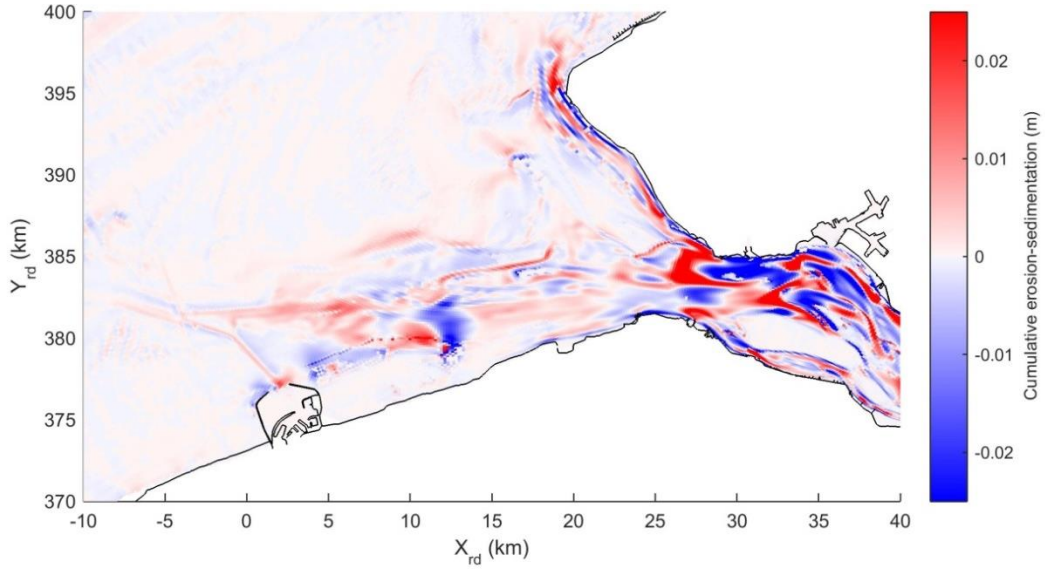


*Figure 5.19 Cumulative bed thickness change after one spring neap cycle, for case 2.*

### 5.3.3 Case 3: Extension of the Geul van de Walvischstaart

#### *5.3.3.1 Hydrodynamics*

The impact of the new navigation channel on the gross discharges per tide is presented in Figure 5.20. After the construction of the intervention, the gross and net discharges in the Geul van de Walvischstaart and Deurloo West increase and become more ebb-dominant. The discharges through the Wielingen, Oostgat, Deurloo Oost and Geul van de Rassen decrease. Thus, the new navigation channel withdraws discharges from the other large channels supports in discharging the water that is required for filling and emptying the Western Scheldt. Another major change is the increase of the gross discharge of water over the Vlakte van de Raan towards the northeast. Again, it suggests that water is "sucked" towards the new navigation channel. The net flow velocities show similar changes (appendix C.4). The net flows through the Geul van de Walvischstaarts and Deurloo West increase, while the net flow velocities in Wielingen, Scheur and Oostgat reduce.

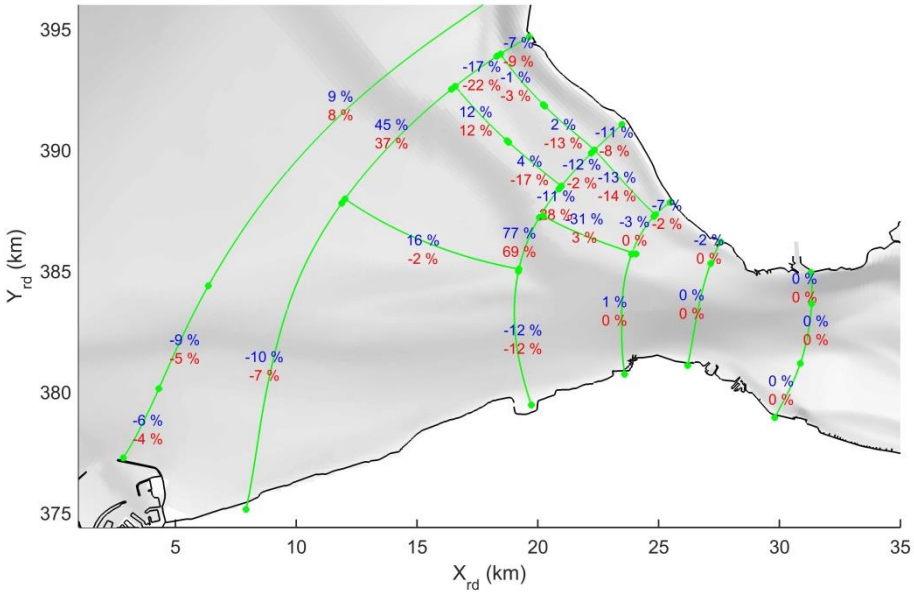


*Figure 5.20 Relative changes in gross discharges for case 3 compared to case 1. The blue numbers indicate the changes in the flood discharges (west/south). The red numbers represent the ebb discharges (east/north).*

As Figure 5.21 shows, also the maximum flow velocities within the new channel increase significantly. This means that the change in the discharge is larger compared to the change in cross-sectional area. The maximum velocities also increase at the start and end of the channel. Due to the reduced bed shear stresses and higher flow velocities, the flow just outside the new channel is sucked into it ("kopeffecten"). In line with the lowered discharges, the new channel lowers the maximum velocities within the Wielingen, Scheur and Oostgat.

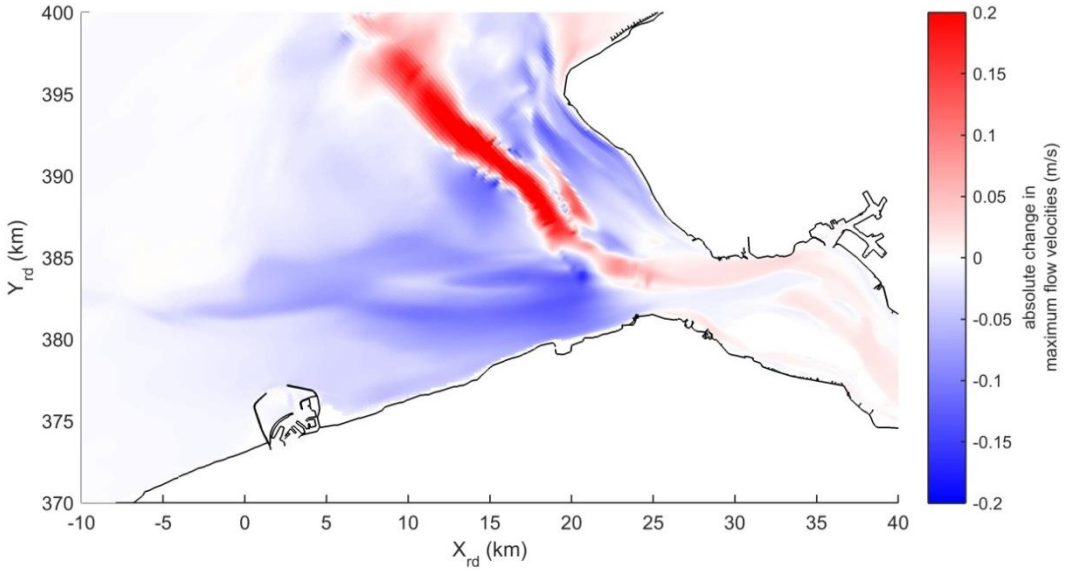


*Figure 5.21 (Absolute) change in the maximum flow velocities, case 3 compared to case 1. Red colors indicate higher maximum velocities; blue indicates lower maximum velocities.*

Figure 5.7 demonstrates that the $M_2$ phase within the vertical tide for the Deurloo West and Geul van de Walvischstaart decreases with the deepening and extension of the channels. Due to the larger depth, the deceleration of the wave propagation by the friction at the bed is smaller. The reduced friction results in a small increase of the amplitudes of the $M_2$ wave (appendix C.4). If we look to the asymmetry in the vertical tide based on the $M_2$ and $M_4$ constituents (Figure 5.8), we can see that the phase differences decrease and results in a decrease of the flood dominance. In line with the theory of Friedrichs & Aubrey (1988), the decrease in the flood dominance can be explained by the increase of ratio between the tidal amplitude and the water depth. However, all these effects can also be observed for the Wielingen-Scheur and the Oostgat-Sardijngeul. In other words, the deepening and extension of the channel affects the tidal asymmetry of the $M_2$ and $M_4$ constituents over a large area.

#### 5.3.3.2 *Sediment transport*

Figure 5.22 shows the residual sediment transports for case 3. A comparison of the residual transports for cases 1 and 3 is shown in appendix C.4. The residual transports within the Geul van de Walvischstaart and Deurloo West are higher compared to case 1 as result of the increase in the discharges, net flow velocities, maximum flow velocities and decrease of the flood dominance that is observed with the vertical tide. As the new navigation channel partly takes over the discharge function, the residual transports within the Oostgat, Wielingen. Scheur and Geul van de Sluissche Hompels decrease. The ebb-dominance of the residual transport within the navigation channel of the Western Scheldt increases.

#### 5.3.3.3 *Erosion-sedimentation patterns*

As shown in Figure 5.23, the model predicts sedimentation inside the new navigation channel, especially at the northern end. This sedimentation is caused by the decrease in the flow velocities and sediment transports when moving towards the north. This suggests that dredging operations are required to keep the channel navigable. The sides of the channels

are eroding as water is sucked into the channel, flows over these sides and is accelerating. However, the pattern is still a bit irregular at some places. Although a spin-up interval is used, the bathymetry has not been able to fully adapt itself. As discussed, flow within the Wielingen is sucked into the new channel. Figure 5.22 shows that the residual transports decrease when moving from the Wielingen towards the new channel. This gradient explains the sedimentation at the southern end of the new channel.

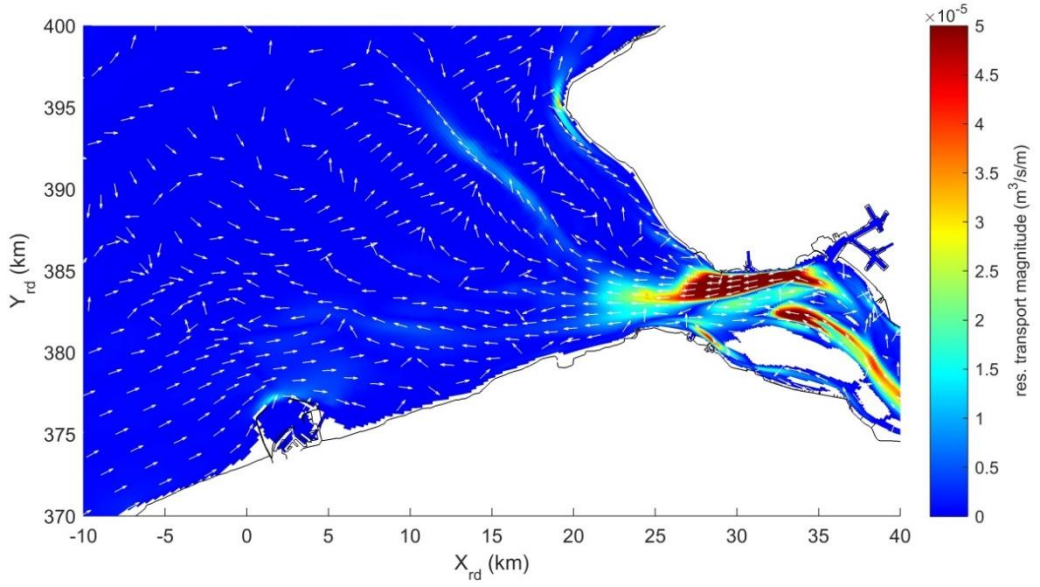


*Figure 5.22 Modelled residual sediment transport (computed for one spring-neap cycle) for case 3. The arrows are normalized (with the magnitudes) and only indicate the direction.*

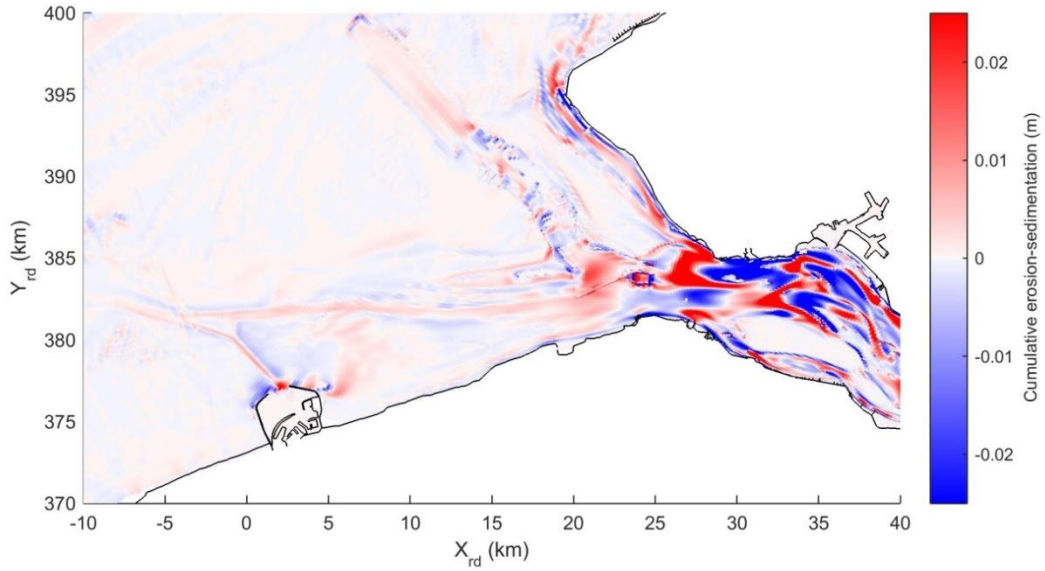


*Figure 5.23 Cumulative bed thickness change after one spring neap cycle, for case 3.*

## 5.4 Conclusion

### 5.4.1 Case 1

For case 1, the modelled total residual sediment transports at the Wielingen, Scheur, Geul van de Walvischstaart, Deurloo Oost, Deurloo West and Geul van de Sluissche Hompels are ebb-dominated. The results show a cross-channel imbalance within the inlet (Vlissingen-Breskens): the residual transport at the northern part is ebb-dominant, while the southern part is flood-dominant. A similar cross-channel imbalance was found within the middle part of the

Oostgat, between the coastward (ebb-dominant) and seaward (flood-channel) side. There is also a divergence of the residual transports in the Oostgat over the longitudinal direction. The residual transport in the northern part of the Oostgat is ebb-dominant, while the southern part shows flood dominance. At the port of Zeebrugge, there is an alongshore residual transport in northern direction. The residual transports at the Vlakte van de Raan are relatively low and it is difficult to find a dominant direction of the residual transports.

Looking back at the analysis of the hydrodynamics, one can conclude that the residual sediment transports are highest at the locations with high velocities (i.e. channels). The obtained residual sediment transports show similar patterns as the net flow velocities. However, the tidal asymmetry of the vertical and horizontal tide expressed by the $M_2$ and $M_4$ often shows different patterns. In case of the Wielingen for example, the residual sediment transports ebb-dominant while the asymmetry based on the $M_2$ and $M_4$ components indicates that the hydrodynamics are flood dominant. The tidal asymmetry based on the semi-diurnal and quarter-diurnal tidal waves cannot (directly) explain the computed residual sediment transports, it seems that also the net flow velocities and the tidal asymmetry from the other astronomic components are important determinants.

### 5.4.2 Case 2

The impact of the island is studied with case 2. Because the construction of the island reduces the space that is available for the flow of water, the gross discharges per tide within the Wielingen and Scheur decrease. For the shallow area and within the section of the Scheur in front of the island, the contraction of the flow leads to higher flow velocities. Further upstream and downstream of the island, the reduced discharges result in lower maximum flow velocities. The effect of the island on the tidal asymmetry is limited.

Because of the increased flow velocities, the residual transports in the shallow area north of the island increase. Within the section of the Scheur in front of the island, the effect is directed towards the west (ebb). The lower flow velocities in the middle and eastern sections of the Wielingen and north-northwest of Zeebrugge result in lower residual sediment transports. The change in the residual transport in the Wielingen is flood directed (i.e. smaller ebb dominance). For the area north-northwest of Zeebrugge, the effect is ebb directed (i.e. smaller flood dominance). For the Vlakte van de Raan, the Geul van de Walvischstaart and the channels in front of the coast of Walcheren, the effect of the island on the residual transports is directed towards the north/northeast. However, the absolute change in the residual sediment transport is small.

### 5.4.3 Case 3

The deepening and extension of the Deurloo West and Geul van de Walvischstaart have a significant effect on the hydrodynamics. The new navigation channel supports the other channels in discharging water that is required for filling and emptying of the Western Scheldt. Because also the maximum flow velocities in the area of the new channel increase significantly, one can state that the change in the discharge is larger than the change in the cross-sectional area. As more water is “sucked” into the Deurloo West and Geul van de Walvischstaart, the discharges through the other channels decrease. The reduced discharges result in lower flow velocities. As result of the larger water depth, the tidal wave propagates faster through the mouth and into the Western Scheldt. Moreover, the flood dominance that is found with the vertical tide increases with the construction of the new channel.

As result of the increased discharges, flow velocities, net flow velocities and the reduced flood dominance that is found within the vertical tide, the residual transport within the Geul van de Walvischstaart and Deurloo West increases. As the new navigation channel lowers the flow velocities in the Oostgat, Wielingen, Scheur and Geul van de Sluissche Hompels; the residual transports in these channels decrease.

# 6 Sediment transport pathways in the mouth of the Scheldt estuary

This chapter describes the results of the visualisation tool applied to the mouth of the Scheldt estuary. Section 6.1 discusses the transport pathways for the reference case (case 1). Section 6.2 discusses the impact of human interventions (cases 2 and 3). Section 6.3 describes the conclusions of this chapter. It summarizes the findings and discusses the added value of the visualisation tool for the mouth.

When interpreting the results, it is important to consider that the computed transport pathways do not represent the actual sediment grain movement. The tool visualizes the move of tracers when they do not interact with the bed. Moreover, one should take into account that the Delft3D-NeVla model is based on a 2DH approach and does not take into account density-driven currents, wind or waves. Furthermore, the model takes into a single grain size ($D_{50}$=0,2 mm) that is not the characteristic/the main sediment type for all areas within the mouth. This is especially the case in the area around Zeebrugge, samples that were taken from the bed showed high amounts of silt and clay in this area (Vroom & Schrijvershof, 2015). Because the transport of silt and clay (e.g. longer in suspension) is different compared to the grain size that is considered here, one should be cautious when linking the model results with the observed morphological changes.

## 6.1 Transport pathways in case 1

### 6.1.1 Introduction

#### *6.1.1.1 Release locations*

Based on previous chapters, a number of release locations are selected to discuss the sediment transport patterns in the mouth. Each location exists of a cluster of release points that are situated close to each other. By not looking to a single pathway but allowing small differences in the start locations of particles, it is possible to get a better impression of the spatial variation in the sediment transport (e.g. do pathways converge or diverge). The various release locations are discussed in sub-sections.

Thus, the pathways show the flows of sediment through the system. This fact is used for the selection of the release locations. If the pathways show that numerical particles flow from area A to area C but also come along area B, it is unnecessary the separately compute the pathways when releasing the particles in area B. The first case already proved that there is a flow of particles from area B to area C.

First of all, particles are released in the inlet to further study the cross-channel imbalance (section 5.3.1.2). By following the numerical particles for a longer time, the pathways also visualize the distribution of sediment over the various channels within the mouth. In addition, particles are released within the Wielingen to study the sediment transports in the main navigation channel and see whether there are flows of sediment onto the shallow areas Vlakte van de Raan and/or Paardenmarkt. Thirdly, particles are released in the Oostgat and Deurloo Oost to better understand the sediment transport patterns in front of Walcheren. As fourth scenario, particles are released near Zeebrugge to study the alongshore sediment transport, the effect of the port and its entrance channel (Pas van het Zand) and the interaction with the nearby channel system Wielingen-Scheur. To better explain the added value of visualisation tool for engineers, the fifth scenario shows the pathways of particles when they are released at the various sediment disposal locations. As mentioned in Section 1.1.2, knowledge about these pathways can help to optimize the dredging and disposal

activities. Lastly, particles are released at different locations on the Vlakte van de Raan to improve the insights about the sediment transport patterns in this large shallow area.

#### 6.1.1.2 *Sediment transport pathways*

For each release location, a map is shown that visualizes the transport pathways of all particles at the end of the simulation period. Because there are hundreds of pathways that are plotted in one map (green lines, for example see Figure 6.2), they can no longer be distinguished from each other. Thus, the green areas represent the areas the particles came across during their movements. The start locations are indicated with red dots. The blue dots are the locations of the particles at the end of the simulation period. For some release locations, the dispersal of the numerical particles is also visualized with a movie. These movies show the development in the tracer concentrations over time and space. The names of the movies are mentioned in the tables at the start of each sub-section.

One should be aware that the numerical particles are constantly moving (i.e. not mixed or buried within the bed) and the locations of the particles change with variations in the simulation period. In other words, the end locations that are presented in the figures and movies are not the final locations at which the numerical particles stay for ever. However, the particles barely move if they arrive in areas with low transport velocities (e.g. Vlakte van de Raan and northern and of the Deurloo West).

As stated, the gradients in the residual sediment transport (Figure 5.11) can explain erosion and sedimentation patterns (Figure 5.14). The visualisation tool can support these analyses and by suggesting where sediment is going to or is coming from. Again, assume that all particles move from area A, to area B and finally to area C. If area C is a sedimentation area, the transport pathways suggest that this sediment can originate from area A and eventually also area B. However, this does not rule out other areas that may contribute to the sedimentation in area C. Lastly, it is also important to state that a sedimentation area is not characterized by slowly moving numerical particles. If the particles are displaced over small distances, this just means that the transport velocities are low. The erosion and sedimentation patterns themselves are represented by the acceleration and deceleration of the particles along the transport pathways. However, one should take into the entire set of particles to study all the transport conditions that occur at a certain area. As this is a difficult task, the fact whether an area shows erosion or sedimentation can best be studied based on the gradients in the residual sediment transport. The pathways help to better understand from in which directions the sediment is going to or is coming from.

#### 6.1.1.3 *Simulation period and time steps for updating vector fields and particle movement*

The transport pathways are simulated based on the sediment transport maps that are updated each 15 min ($\Delta t_{d3d-output}$). The available data describes the sediment transports for one spring-neap cycle (Section 5.2.2). For longer simulation periods (T), the single spring-neap cycle is repeated n times (n being an integer). The particles should be moved at least a couple kilometres, to be able to say something about the large-scale sediment transport patterns. Because of the spatial differences in the magnitudes of the sediment transport, the simulation period that is required to obtain long pathways differs for the various release locations. For the Vlakte van de Raan for example (low sediment transports), a period of 8 years is used to obtain large-scale pathways.

In line with the guidelines that are presented Section 3.3.2, the time step for each simulation was first determined with the SN number (Eq. 3.23). For this study, we assume that the maximum allowable particle displacement is 1 time the grid resolution (N=1). If we for example consider the area around the inlet (highest transport velocities and relatively small grid cells), the maximum time step equals 37 s. For other areas, the transport velocities are

higher and/or the grid cells are larger. The SN number indeed show that the time step can be increased and it is unnecessary to use the small time step size that is derived for the inlet.

As explained in Section 3.3.2, $\Delta t_{pm}$ should also be selected based on the actual impact of $\Delta t_{pm}$ on the pathways and the considerations of maximizing the accuracy and minimizing the computational time. Appendix. D.2 describes a sensitivity analysis of the pathways with variations in $\Delta t_{pm}$. The analysis shows that the pathways in the inlet should indeed be computed with a time step of around 30 s. For areas with lower transport velocities and smaller gradients, the time step can much higher (e.g. 100 s in the Scheur).

#### 6.1.1.4 *Acceleration coefficient*

The acceleration coefficient for the mouth of the Scheldt estuary is computed based on the method described in Section 3.3.3, using the total sediment transports of the spring neap cycle. Following this method, the acceleration coefficient in the mouth should be 1600 $m^{-1}$ (constant in time and space). Figure 6.1 shows the maximum transport velocities within the mouth. In line with the guidelines that are discussed in Section 3.3.3, the maximum flow velocities (Figure 5.3) and transport velocities are approximately the same, namely ~1.6 m/s. Moreover, both variables show that the velocities are highest in the channels. The maximum flow velocities decrease when moving away from the inlet. Because of the non-linear relation with sediment transport, the reduction in the transport velocities is a much larger.

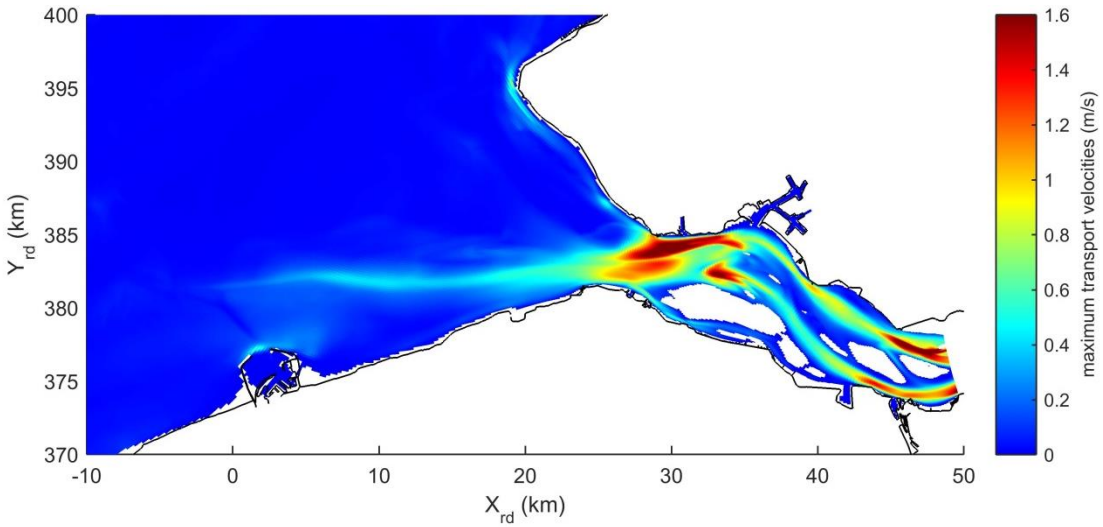


*Figure 6.1 Map showing the transport velocities detected within the spring-neap cycle. The transport velocities are computed based on total sediment transports and an acceleration coefficient of 1600 $m^{-1}$*

#### 6.1.1.5 *Random walk coefficient*

As stated, the particles are released based on a clustered group of start points. The deviations at the start of the pathways (different starting positions) make it possible to visualize the spatial variation in sediment transport pathways. In other words, the simulations can show whether the small deviations at the beginning result in large differences of the pathways at later times. As will be shown Section 6.1.1.5, also the non-random transport velocities (the velocities generated by the sediment transport maps) themselves result in a spreading of the particles in the horizontal directions. Especially in inlet, the transport velocities are high and the particle displacements per $\Delta t_{pm}$ are large. Here, the particles with the same start location but different release times clearly get different pathways. The deviations at the beginning of the pathways (e.g. releasing during ebb or flood) can have large consequences for the particle locations at later times. Concluding, the study about the mouth can use a random walk coefficient (β) that equals 0.

### 6.1.2 Spatial patterns in sediment transport pathways

#### *6.1.2.1 Inlet*

| | | |
|---|---|---|
| T = 173 days | $\Delta t_{pm}$= 30 s | β = 0 |
| Release of particles = first 14.4 days | Interval of release = 1 particle per 45 min | Movie 6.1 |

As the particfles are released in an area with high transport velocities and relatively small grid cells, the simulations have to be based on a relatively small time step (30 s).

First of all, we consider the release points in the southern part of the inlet (Figure 6.2). The particles have a to and fro motion due to the alternating ebb and flood sediment transports. At the end of the simulation period, the particles are mainly displaced towards the west (83%). In other words, the flood directed residual transports at the release points (Figure 5.11) do not result in high numbers of particles ending up within the Western Scheldt. Most of the particles come in contact with the ebb-dominance of the Honte and are transported into the mouth. About 8% of the particles end up at the Hooge Plaaten. Due to the low transport velocities there, the particles are not able to escape from the shoal within the simulation period. Only for a few particles, it is possible to move further into the Western Scheldt.

The results of the visualisation tool demonstrate that the numerical particles from these release points are mainly distributed to the different channels of the mouth. The pathways follow the orientation of the channels. There are clear (separations of) flows of sediment into the Wielingen-Scheur, Geul van de Sluissche Hompels, Geul van de Walvischstaart and Deurloo West. At the eastern boundary of the Geul van de Walvischstaart, the Elleboog forms a clear barrier along which sediment is transported. There is no exchange with the Deurloo Oost. However, there are particles that are transported from the Geul van de Walvischstaart into the Deurloo West. In other words, the visualisation tool shows that there is an exchange of sediment between the two channels. Moreover, the pathways indicate that the particles from the inlet are not transported into the Appelzak or onto the Paardenmarkt. The particles that travel through the Wielingen and Scheur are eventually transported onto Vlakte van de Raan (near the Droogte van Schooneveld).

For the particles that are released in the northern part of the inlet (Figure 6.3), the pathways are quite similar to the ones of the particles released in the southern part (Figure 6.2). However, none of the particles are located at the Hooge Platen at the end of the simulation. In total, 99% of the particles is transported into the mouth. The particles that are released very close to the coast of Walcheren are transported into the circulation cell around the Bankje van de Zoutelande (see Section 6.1.2.2).

If we look into the erosion and sedimentation patterns for case 1 (Figure 5.14), we can see a large sedimentation area just southwest of Vlissingen (eastern tip of the Nolleplaat and eastern end of the Wielingen). The results of the visualisation tool indicate that the numerical particles that move through this area, were first located in the Honte. In this way, the results indicate that the sediment from the large erosion area in the Honte (just south of Vlissingen) is transported towards the sedimentation area just west of it. Also in the Schaar van de Spijkerplaat, the erosion and sedimentation areas can be linked. The numerical particles that are released in the southern part of the inlet, initially have a residual movement towards the east. In this way, one can link the erosion area north of Breskens (southern part of the inlet) with the sedimentation area west of it (in the Schaar van de Spijkerplaat).

Lastly, the results have shown that many of the particles are transported from the inlet into the Wielingen and Scheur. As explained with an example in section 6.1.1.1, the results also

suggest that for start locations in the middle of these pathways, many of the numerical particles will be transported through the navigation channel in westward direction. Concluding, the visualisation tool demonstrates that the sedimentation in the Wielingen and Scheur (that need to be dredged) can be linked with flows of sediment out of areas further upstream. However, there are probably also other areas that contribute to this sedimentation in the navigation channel. These have to be studied with other release locations.

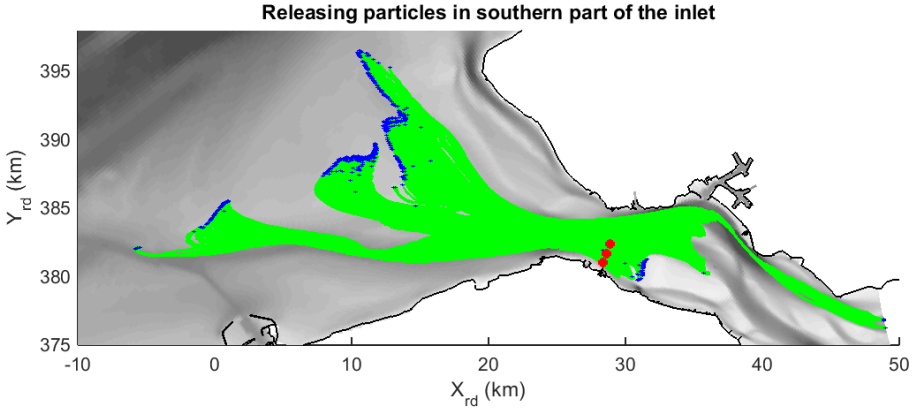


*Figure 6.2 Pathways (period of 173 days) of particles that are released in the southern part of the inlet. Case 1. Red dots indicate the start locations. The blue dots are the particle's locations at the end of the simulation. The pathways are displayed as green lines. Due to the high density, the pathways are stacked together and form a green area. The grey colormap shows the bathymetry. Darker grey means a larger water depth.*

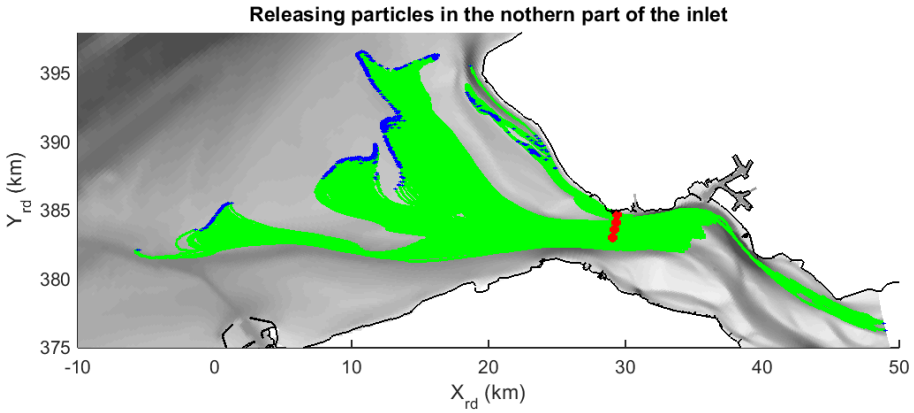


*Figure 6.3 Pathways (period of 173 days) of particles that are released in the northern part of the inlet. Case 1.*

### *6.1.2.2 Wielingen*

| | | |
|---|---|---|
| T = 173 days | $\Delta t_{pm}$= 50 s | β = 0 |
| Release of particles = first 14.4 days | Interval of release = 1 particle per 45 min | |

Figure 6.4 shows the pathways of the particles that are released in the Wielingen and south of it (eastern end of the Appelzak). As the particles stay away from the inlet (area with the highest transport velocities), it is possible to increase the time step to 50 seconds. As also mentioned in Section 6.1.2.1, the numerical particles are transported from the middle of the Wielingen into the Scheur and onto the Vlakte van de Raan. However, the results visualize that also particles that are released close the coast are transported into the Wielingen. Thus, also this area contributes to the sedimentation of the navigation channel. In addition, the pathways indicate that the sedimentation at the Paardenmarkt (the shallow area directly in front of the coast) is not caused by flows of sediment from the Wielingen.

The current-driven transports in the Scheur seem to be concentrated at the northern part of the channel. Especially near the meeting point with the Pas van het Zand, the pathways show a large shift of towards the north. Thus, the particles do not move into the Pas van het Zand or the large deep area in which the Scheur and Pas van het Zand come together. Looking in to the shape of the most southern located pathways, we can see that they follow the shape of the boundary between the ebb dominant zone (the Scheur) and the zone with flood dominant transport along the shore (Figure 5.12).

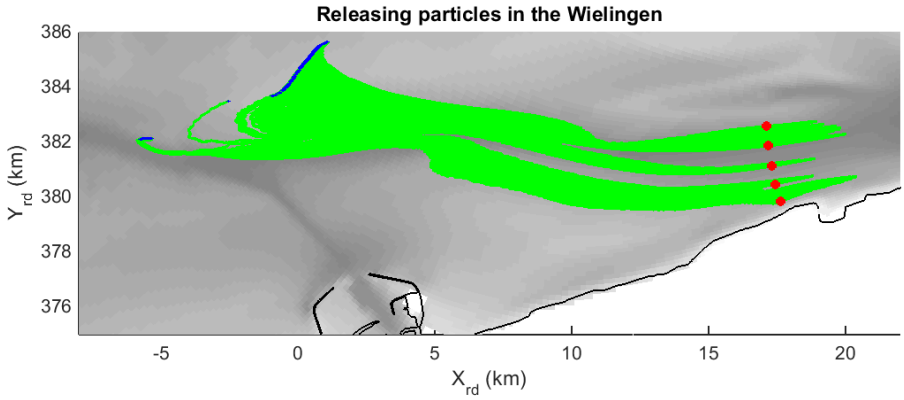


*Figure 6.4 Pathways (period of 173 days) of particles that are released in the Wielingen. Case 1.*

### 6.1.2.3 *Oostgat & Deurloo Oost*

| | | |
|---|---|---|
| T = 288 days | $\Delta t_{pm}$= 100 s | β = 0 |
| Release of particles = first 14.4 days | Interval of release = 1 particle per 45 min | Movie 6.2 |

The two left subplots in Figure 6.5 show the pathways of the particles when they are released in the middle of the Oostgat, at the coastward and seaward side of the channel. Because of the low magnitudes of the transport velocities, the value for $\Delta t_{pm}$ can be increased to 100 s and the simulation period is increased to 288 days. Due to the cross-channel imbalance and the divergence of the residual sediment transport directions (Section 5.3.1.2), the pathways for these two release locations are very different.

First, we consider the release at the coastward side of the channel (left subplot). When the particles are released really close to the coast, the oscillating motions result in residual movements in the flood direction. Further towards the middle of the channel's cross-section, the particles initially move towards the south. However, the particles arrive in the flood-dominant zone after a while and the pathways are bended in the flood direction. All particles end up in front of the northern coast of Walcheren. Due to the lower transport velocities over here, the particle moves a lot slower.

For the release locations at the seaward side of the channel (middle subplot), the pathways are different. Particles initially have a residual movement in the flood direction. For some particles this movement continues till the connection point between the Oostgat and the Sardijngeul (southern end of the Bankje van Zoutelande). Here the particles move into the Deurloo Oost, along the seaward side and on top of the Bankje van Zoutelande in northern direction. The sediment transports over the Bankje van Zoutelande and through the Geul van de Rassen are such that the particles are able to move back into the Oostgat and end up at approximately the same location as where they started. During the simulation period, some particles follow this circulation pattern multiple times. Most particles eventually arrive in the flood-dominant zone of the Oostgat and move towards the north. If particles are released more in the western part of the Deurloo Oost, they do not follow this circulation pattern (right

subplot). The particles are transported out of the Geul van de Rassen in northern direction. They follow the orientation of the Oostgat or are transported more towards the west.

The pathways suggest that the flows of sediment from the eastern part of the Deurloo Oost and Bankje van Zoutelande (circulation cell) contribute to sedimentation at the seaward side of the Oostgat (Figure 5.14). The sedimentation area at the northern end of the Oostgat seems to be caused by flows of sediment from the south. However, it is important to mention that the existing computational grid is quite coarse (grid cells of about 60x160m, the width of the Oostgat is covered by 7-8 grid cells) for this detailed study about the channels in front of the coast of Walcheren. This will be further discussed in the Chapters 7 and 8.

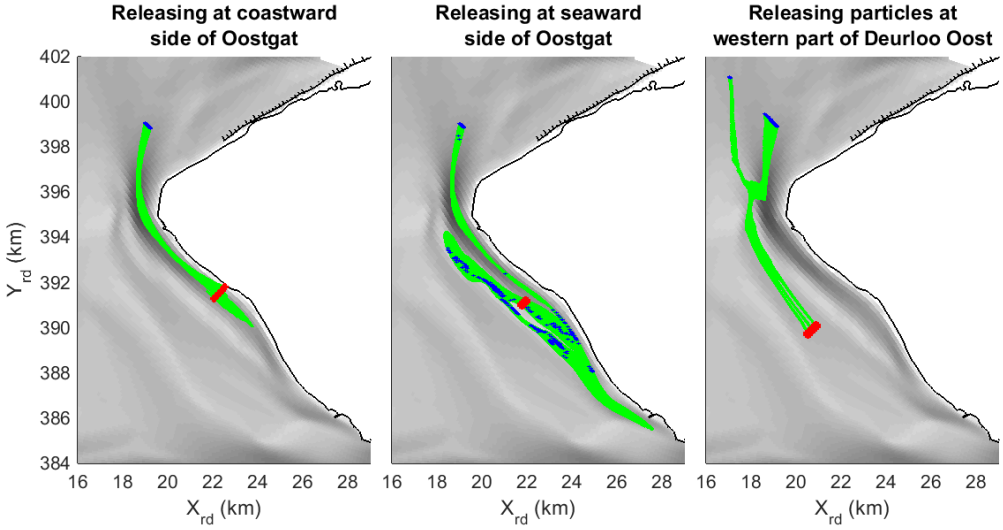


*Figure 6.5 Pathways (period of 288 days) of particles that are released in the Oostgat and Deurloo Oost. Case 1.*

### 6.1.2.4 *Area around Zeebrugge*

| | | |
|---|---|---|
| T = 288 days | $\Delta t_{pm}$= 100 s | β = 0 |
| Release of particles = first 14.4 days | Interval of release = 1 particle per 45 min | Movie 6.3 |

The release of particles in the area around Zeebrugge is based on $\Delta t_{pm}$ of 100 s. As shown in Figure 5.11, the residual transports to the west and north of Zeebrugge are flood-dominant. Directly east of the harbour, the flow is more sheltered and the residual transports are a lot smaller. The transport pathways are shown in Figure 6.6. When particles are released west of the port and neary nearby the coast (left subplot), they are able to bypass the Pas van het Zand. Eventually, they arrive and stay (they barely move) on the Paardenmarkt. The particles that are released further north (right subplot) are also transported in flood direction. However, at a certain point the particles come in contact with the ebb-dominance of the Scheur and the pathways bend. The particles are transported into the channel and end up at the Vlakte van de Raan, near the Droogte van Schooneveld. If we look to the middle two start locations, we can see that the pathways are almost overlapping at the Pas van het Zand. However, the small differences in the pathways results in large differences of the particles' locations at the end of the simulation.

The pathways indicate that sedimentation areas in front of the coast can be linked with sources west of it. The sedimentation within the Pas van het Zand seems to be caused by flows of sediment from the updrift side. The eroded sediment at the eastern margin of the Pas van het Zand can be linked with the sedimentation area on the Paardenmarkt. Previous analyses showed that deposited material in the Scheur can be traced back to sources further

towards the east. This scenario demonstrates that also the Paardenmarkt contributes to the sedimentation that is observed in the Scheur.

However, one should take into account that the Delft3D-NeVla model is solely based on fine sand with $D_{50}$ equal to 0,2 mm. As previous studies already mentioned, the sediment in the area around Zeebrugge is characterized by high percentages of silt and clay (Kuijper, 2015; Van Lancker et al., 2012; Vroom & Schrijvershof, 2015). It is expected that these different sediment types have different transport pathways.

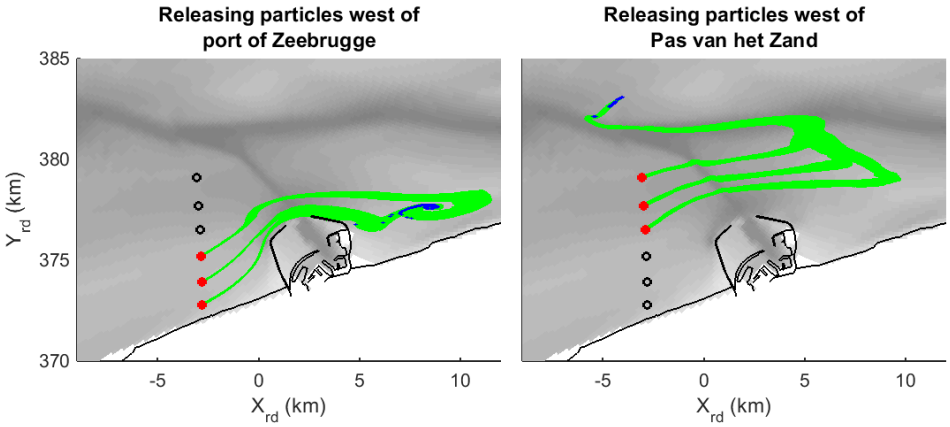


*Figure 6.6 Pathways (period of 288 days) of particles that are released west of the port of Zeebrugge and Pas van het Zand. Case 1. The red dots are the start locations of the particles. The black dots are the start locations that are not used in that particular scenario.*

### 6.1.2.5 *Sediment disposal locations*

| | | |
|---|---|---|
| T = 288 days | $\Delta t_{pm}$= 100 s | $\beta$ = 0 |
| Release of particles = first 14.4 days | Interval of release = 1 particle per 45 min | Movie 6.4 |

The visualisation tool can also help to better understand the impact of the dumping sediment at the various disposal locations. Figure 6.7 displays the transport pathways of numerical particles that are released in four disposal areas that are currently used and have been used most frequently in the past (Vroom & Schrijvershof, 2015). Also for these simulations the simulation period is set at 288 days and the time step is 100 s.

The particles that are released in front of the Belgian coast, are transported into the Scheur. As was also shown in previous sections; the transport of particles in the Scheur towards the west stops at a certain moment (around x= -5 km). At this location west of the meeting point between the Scheur and Pas van het Zand, particles are transported onto the Vlakte van de Raan. Most of the particles that are released in the two northern disposal locations stay close to the start locations on the Vlakte van de Raan.

If we look again into the results of the visualisation tool, we can see that the particles from the two dump areas in front of the coast have longer pathways than the particles that are released in the two other areas. The visualisation tool suggests that these first two dump areas are less stable and sediment is easily transported into the Scheur. Here, the accumulation of sediment can lead to bed level increases that have to be removed by dredging operations (to ensure the navigability). In this way, sediment circulates due to the transport by natural and human processes. Based on the current results, the visualisation tool suggests that the dredged sediment can best be brought to the dump locations in the north. In the short-term, this may cost more money (further away from the dredging location). On the long-term, it can reduce the need for dredging operations.

Again, it is important to recognize that this study only takes into account fine sand. There is no data about the ratio sand and mud within the dredged material from the mouth. However, studies have shown that bed heterogeneous is composed out of clay, silt and sand (Van Lancker et al., 2012). Based on personal communication with the responsible authorities, Vroom & Schrijvershof (2015) stated that the dredged material from the port mainly consist of mud. The dredged material from the navigation channels does consist of sand.

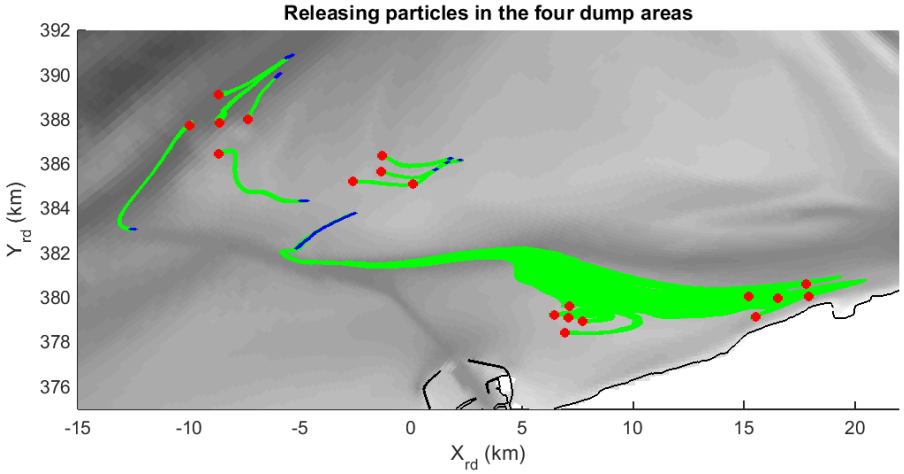


*Figure 6.7 Pathways (period of 288 days) of particles that are released at the four dump area. Case 1.*

### 6.1.2.6 *Vlakte van de Raan*

| | | |
|---|---|---|
| T = 2881 days (~8 years) | $\Delta t_{pm}$= 900 s | $\beta$ = 0 |
| Release of particles = first 14.4 days | Interval of release = 1 particle per 1 h | Movie 6.5 |

Previous results have shown that the Wielingen, Scheur, Geul van de Walvischstaart and Geul van de Sluissche Hompels transport numerical particles onto the Vlakte van de Raan. To demonstrate what happens at Vlakte van de Raan itself, 7 release locations are selected. The time step is increased to 15 minutes. To obtain large-scale transport pathways, the simulation period is increased to almost 8 years, which is much larger than the other cases.

As Figure 6.8 shows, all transport pathways converge towards a single path. All particles are transported to the northern end of Deurloo West. Looking back at the maps (retrospectively) of the residual sediment transport (Figure 5.11 and Figure 5.12), it is indeed shown that the residual transports on the Vlakte van de Raan have directions towards the north and northwest. However, the maps can be difficult to interpret and do not explicitly show that the transport pathways converge. The tool demonstrates its value in (orderly and clear) showing transport patterns that are difficult to obtain by a visual inspection of the sediment transport maps. As the sediment transports in this area are very low, it took a long time to compute the pathway on the Vlakte van de Raan. With bed mixing, burial and resurfacing of sediment, it would be almost impossible to obtain these results with the graded sediment approach.

The numerical particles seem to be stuck at a single point at the northern end of the Deurloo West. This point is located in an area where different flows of sediment come together (Figure 5.12). The area is the meeting point of the residual transport from the Deurloo West that is directed towards the north and the southward directed residual transported that is found at the delta front. As illustration, appendix D.4 includes a figure that shows this area within the map of the residual transport. It is expected that with longer simulation periods, the particles have a small residual movement towards the east and eventually ends up on the Rassen. Here, the residual transport is directed towards the northern end of the Oostgat (eastward).

Summarized, a lot of the previous sections demonstrated that particles out of the Wielingen, Scheur, Paardenmarkt, Geul van de Walvischstaart and Geul van de Sluissche Hompels are transported onto the Vlakte van de Raan. Based on the analysis that is discussed here, it seems that all these particles will eventually all be transported to the northern/north-eastern corner of the mouth. However, the sediment transports in this shallow area are very low and probably sensitive for many of the model settings. Due to the low water depths, it is for example expected that waves affect the residual transport patterns. Moreover, also small changes in the boundary conditions may affect the results.

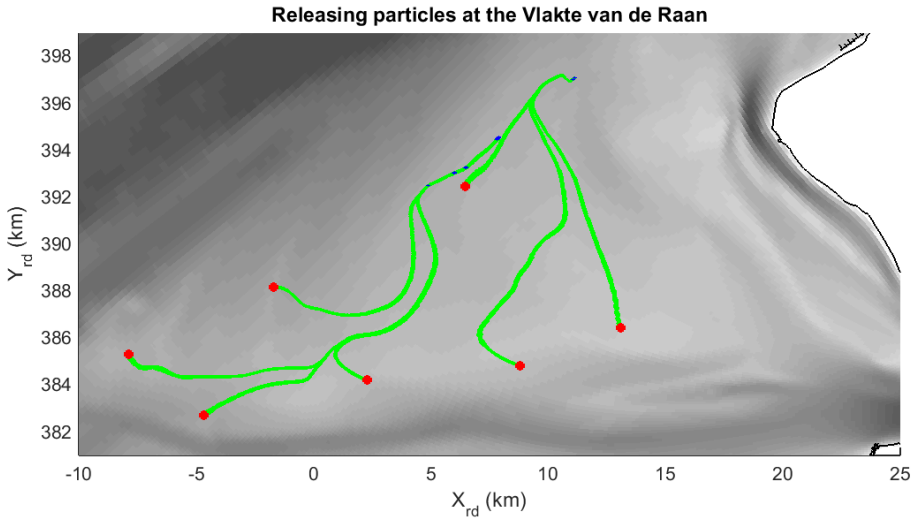


*Figure 6.8 Pathways (period of 8 years) of particles that are released at the Vlakte van de Raan. Case 1.*

The acceleration coefficient of 1600 $m^{-1}$ was chosen such that the maximum transport velocities in the inlet equal the maximum flow velocities at this location. The acceleration coefficient is derived for a small area in the inlet, but is applied to the entire mouth. The Vlakte van de Raan is one of the area for which this leads to very low transport velocities. For the simulation that was discussed above, the maximum particle movement over a single time step (900 s) was 42 metres. Translated to a transport velocity, this is 0.047 m/s. This does not approximate the maximum flow velocities (0.4 to 0.8 m/s) that are observed in this area (Figure 5.3). As discussed in Section 3.3.3, low transport velocities mean that particles have small orbital motions and move according to the residual transport patterns. The Vlakte van de Raan (still dominated by suspended transport) is a useful case to test whether a locally derived acceleration coefficient (so for the Vlakte van de Raan itself) results in different pathways. This analysis is shown in appendix D.4. The locally derived acceleration coefficient is 16000 $m^{-1}$, 10 times as small as the original acceleration coefficient. If we adjust the simulation period for this change (from 2881 days to 288.1 days), we obtain transport pathways that are quite similar. The pathways still converge and end up at the northern part of the Deurloo West. However, the larger transport velocities result in larger orbital velocities and transport pathways that are less clustered/stacked together. Based on these results, there is enough confidence to state that all acceleration coefficients between 1600 and 16000 $m^{-1}$ lead to similar transport pathways for the Vlakte van de Raan. With acceleration coefficients that are much higher, the transport velocities become unrealistically high and probably result in tracer dispersals that are more scattered. More tests are required to determine whether locally derived coefficients also lead to similar results for other areas.

### 6.1.3 Temporal variation in sediment transport pathways

In addition to the spatial analysis, the transport pathways can also be used to analyse the temporal variability in the sediment transports. Although based on a different method to model the tracer dispersals, Elias et al. (2011) for example successfully applied transport pathways

of artificial tracers to explain the temporal variations in the exchange of sediment at the mouth of the Columbia River during a spring-neap cycle and with storm conditions.

The study about the temporal variations in the mouth of the Scheldt estuary is described in appendix D.3. It confirms what is currently known and what could be expected about sediment transports in the mouth. The numerical particles have oscillating motions due to ebb and flood currents that are generated by the tidal wave. The higher flow velocities that occur during spring tide compared to neap tide result in higher sediment transports, higher transport velocities and larger oscillating motions. The study did not show other large changes in the sediment transport patterns within the spring-neap cycle. By extending the Delft3D-NeVla model with wave and wind conditions, the visualisation tool could be useful to study the impact of these metrological conditions over time (e.g. simulation the development of a storm) and the impact on the sediment transports that are generated by the tidal currents.

## 6.2 Impact of human interventions

This section discusses the effects of the two human interventions (cases 2 and 3). Based on the findings of the previous section, this section solely studies the spatial changes in the transport pathways. As the maximum flow velocities and sediment transports still occur within the inlet and only change a little bit, also the simulations for cases 2 and 3 are based on an acceleration coefficient of 1600 $m^{-1}$. Also the other model settings are kept the same.

### 6.2.1 Case 2: Island in front of Knokke-Heist

To show the effect of the island, the sediment transport pathways are analysed for two release locations: the area around Zeebrugge and the inlet. To better structure the discussions, Figure 6.9 gives a schematization of five important areas in the vicinity of the island that show large erosion (blue) and sedimentation (red) rates.

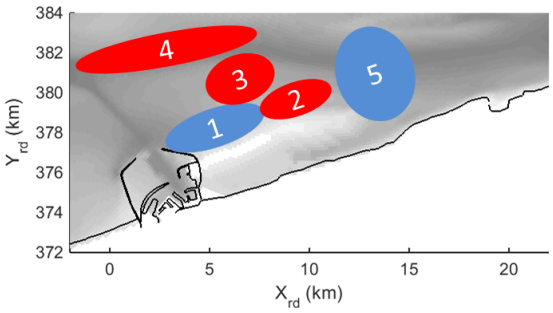


*Figure 6.9 Schematization of the erosion and sedimentation areas in front of the island (case 2)*

#### 6.2.1.1 *Area around Zeebrugge*

| | | |
|---|---|---|
| T = 288 days | $\Delta t_{pm}$= 100 s | $\beta$ = 0 |
| Release of particles = first 14.4 days | Interval of release = 1 particle per 45 min | Movie 6.6 |

First of all, consider the release points near the coast (Figure 6.10, left subplot). With the construction of the island, the particles cannot move into the sheltered area that used to exist east of the harbour. The particles are now transported along the northern side of the island. When they arrive at the eastern end of the island, they are transported into the Scheur or stay in a small circulation cell. It is yet unknown whether particles can escape from the circulation cell after a while and whether this cell would also have been existed with a locally refined grid (now a cell is about 180x130 m, the slope in front of the island is only 7-8 cells wide).

The particles with start locations further into the sea used to be transported into the Scheur and finally onto the Vlakte van de Raan. Now, the particles are still transported into the

Scheur but stay in a local circulation cell. This circulation cell is the meeting point of the alongshore transport that is directed towards the northwest and the ebb-dominant transport in the Scheur. It seems that this circulation cell also existed in existed case 1 (Figure 5.12). The fact that the particles are now stuck in this area seems not to be caused by large-scale changes in the sediment transports, but rather by small adjustments in the pathways that bring the particle to a slightly different location in the Scheur.

The results of the visualisation tool provide insights about the erosion and sedimentation patterns (Figure 5.19). The larger number of particles that is now transported into the Scheur can explain the increased sedimentation in area 4. Particles that used to be transported to the sheltered area east of the port are now transported into the new navigation channel. In addition, one can see that the tracers that are transported through the erosion area at the western end of the island (area 1) do also move through the sedimentation area directly right of it (area 2). In other words, the two areas can be linked with each other. The location of the circulation cell at the eastern end of the island corresponds with the area 2. Lastly, Figure 6.10 shows that a lot of particles that are transported into the Scheur have a similar route. The high density of pathways on the shallow area directly south of the Scheur (area 3) corresponds with the sedimentation pattern that is found here.

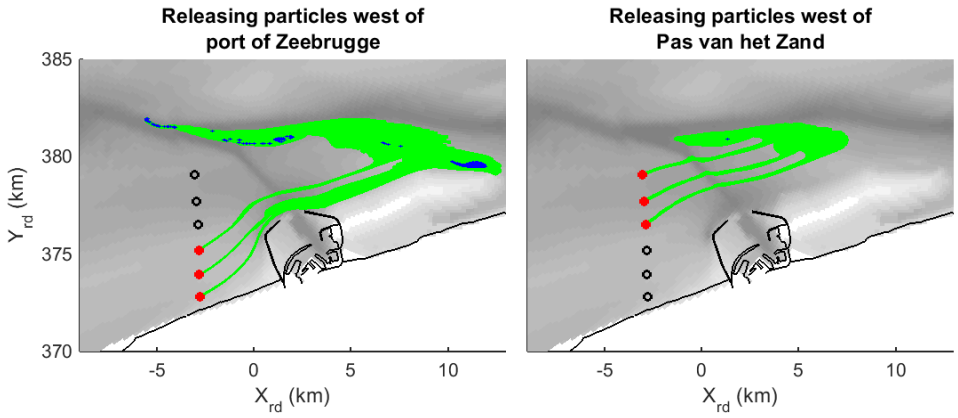


*Figure 6.10 Pathways (over period of 288 days) of particles that are released west of the port of Zeebrugge and Pas van het Zand. Case 2. The red dots are the start locations of the particles. The black dots are the start locations that are not used in that particular scenario.*

Again, it is important to recognize that the pathways are computed for fine sand while measurements have shown that the sediment in the area near Zeebrugge consist for a large part out of silt and clay. These sediment types are transported under different conditions and probably have different pathways. Moreover, also the exclusion of waves may limit the applicability of the findings. Depending on the conditions, waves could break in the shallow area or on the beaches of the island and change the sediment transport patterns.

#### 6.2.1.2 *Inlet*

| | | |
|---|---|---|
| T = 173 days | $\Delta t_{pm}$= 30 s | β = 0 |
| Release of particles = first 14.4 days | Interval of release = 1 particle per 45 min | Movie 6.7 |

Figure 6.11 shows the pathways of the particles when they are released in the inlet, for case 2. The pathways confirm that the ebb dominance of the residual transports for the Vlakte van de Raan, Geul van de Walvischstaart and the channels in front Walcheren increases (Figure 5.22 and appendix C.4). The particles that are initially transported into the Geul van de Sluissche Hompels, are brought into the Geul van de Walvischstaart and Deurloo West at later times. This bending of the pathways was already observed in case 1, but to a lesser

extent. As discussed in 5.3.2, the residual transports in the Oostgat and the surrounding area become more flood-dominant/less ebb-dominant. This could explain the transport of numerical particles out of the Oostgat. However, this area is characterized by larger gradients in the sediment transports and a coarse computational grid. It is unsure how the pathways would have reacted with a more refined grid.

Moreover, the pathways demonstrate that some particles are transported from the Deurloo West into the Geul van de Rassen (over the Elleboog and the Rassen). This connection can also be observed in the map of the residual sediment transport for case 1 (Figure 5.11). Because the sediment transports were orientated slightly different, the numerical particles did not move into this small channel. However, using a slightly different start location or a low random walk coefficient would maybe show similar results for case 1.

As shown in Figure 6.9, the increased flow velocities and sediment transports result in a large erosion area located northeast of the islan/in the western end of the Wielingen (area 5). The pathways that are shown in Figure 6.11 indicate that this eroded sediment is transported towards the west and contributes to the sedimentation in area 4 (the navigation channel).

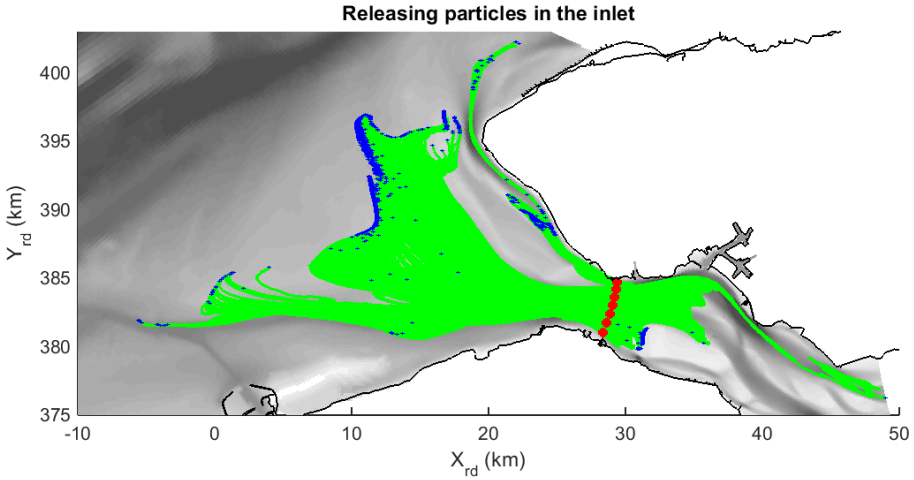


*Figure 6.11 Pathways (period of 288 days) of particles that are released in the inlet. Case 3.*

### 6.2.1.3 *Implication*

Although the intervention is just designed based on some first ideas that are presented in the Masterplan Flanders Bays (2014), one could brainstorm about how the insights can be used to improve the design of the island. To prevent large morphological developments directly in front of the island, the pathways indicate that one should adjust the alongshore flow of sediment that is directed towards the northeast. By extending the jetties or even the entire port of Zeebrugge into the sea, the area in front of the island can become more sheltered (lower flow velocities and lower sediment transports). However, this possibly has also other negative side effects (e.g. large sedimentation west of the port, increased flow velocities perpendicular to the Pas van het Zand). A cheaper and easier solution could be to move the entire island closer towards the coast, where the flow velocities and sediment transport are lower.

Moreover, the pathways indicated that erosion area in the Wielingen (area 5) contributes to the sedimentation within the navigation channel Scheur (area 4). In other words, reducing the erosion rates in the Wielingen can lower the need for dredging operations in the Scheur. By for example shorting the island at the eastern end, the island is less of an obstruction and the contraction of the flow around the eastern of the island can be moved towards the west (away

from the Wielingen). One could also make a smoother bathymetry that lowers the gradients in the residual sediment transports and changes the erosion and sedimentation patterns.

### 6.2.2 Case 3: Extension of the Geul van de Walvischstaart

To show the effect of the navigation channel, the sediment transport pathways are analysed for two release locations: the inlet and the Vlakte van de Raan. The release points and other model settings are exactly the same as the ones that are used in Section 6.1.

#### *6.2.2.1 Inlet*

| | | |
|---|---|---|
| T = 173 days | $\Delta t_{pm}$= 30 s | $\beta$ = 0 |
| Release of particles = first 14.4 days | Interval of release = 1 particle per 45 min | Movie 6.8 |

Because the effects for the northern and southern part of the inlet are quite similar, they are not studied separately in this section. Table 6.1 gives an overview of the percentages of the particles that are transported from the inlet into the different channels of the mouth. The percentages do not exactly describe the changes in the distribution of sediment transports through the various channels, but can give an indication of these changes. Because the Geul van de Walvischstaart and Deurloo West withdraws discharges from the other main channels, the higher flow velocities in these channels and the reorientation of the flow; a lot of the particles are transported into the new navigation channel. As shown in the table, the increase of the number of particles in the Geul van de Walvischstaart and Deurloo West mainly happens at the cost of the Wielingen, Scheur and Geul van de Sluissche Hompels. Apart from the fact that fewer particles are transported into these channels, the pathways here are also shorter. All these patterns correspond with the increase of the residual sediment transport magnitudes in the new navigation channel and the reductions that are found in the other channels (see Section 5.3 and appendix C.4).

If we consider the results for case 1, we can see that the pathways in the Geul van de Walvischstaart and Deurloo West were first spread over the entire widths of the channels. For the third case, the pathways are more concentrated in the centre of navigation channel.

*Table 6.1 Percentages of the total number of particles that are transported into the different channels*

| | **Wielingen-Scheur** | **Geul van de Sluissche Hompels** | **Geul van de Walvischstaart – Deurloo West** | **Oostgat – Deurloo Oost** | **Other** |
|---|---|---|---|---|---|
| Case 1 | 11.2% | 23.8% | 41.1% | 16.5% | 7.4% |
| Case 3 | 6.7% | 8.5% | 62.5% | 14.3% | 7.9% |

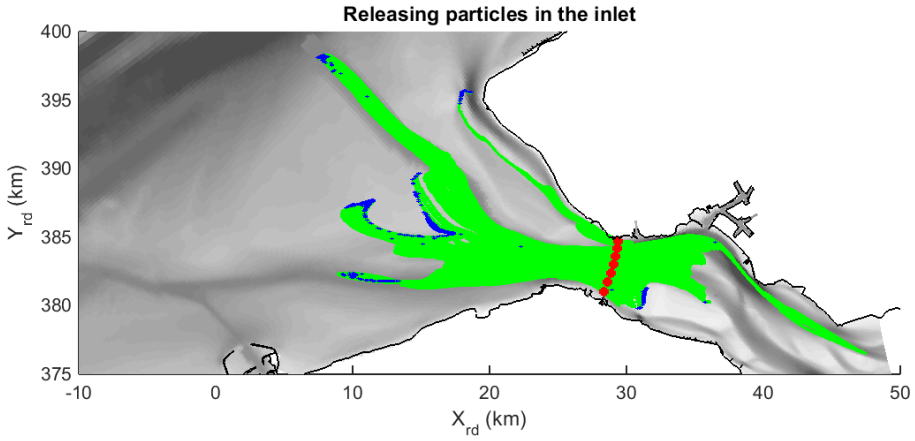


*Figure 6.12 Pathways (period of 288 days) of particles that are released in the inlet. Case 3.*

Again, the transport pathways can help to interpret the erosion and sedimentation patterns (Figure 5.23). First of all, the pathways indicate that the sedimentation within the navigation channel (especially in the northern part) can be traced back to sources further south (e.g. erosion at the edges of the channel). However, there are possibly also other sources that have not been shown with these pathways.

As shown in Figure 5.23, the Delft3D model predicts a large sedimentation area at the southern end of the Geul van de Walvischstaart (Figure 5.23, around x=22 km and y=382 km). In other words, this area has to be dredged regularly to ensure the navigability. If we trace back the particles that are transported through this area, we can see that they originate from the eastern part of the Wielingen and inlet.

#### 6.2.2.2 *Vlakte van de Raan*

| | | |
|---|---|---|
| T = 2881 days (~8 years) | $\Delta t_{pm}$= 900 s | $\beta$ = 0 |
| Release of particles = first 14.4 days | Interval of release = 1 particle per 1 h | Movie 6.9 |

Figure 6.13 shows the pathways for the numerical particles that are released on the Vlakte van de Raan. If we compare Figure 6.8 and Figure 6.13, we can see that the pathways at the western part of the Vlakte van de Raan (x<2.5 km) are almost unaffected. For the remaining part of the Vlakte van de Raan, the results show large changes. Instead of numerical particles that are gradually moving towards the north, the pathways indicate that the flows of particles in the middle and western part of the Vlakte van de Raan are now directed perpendicular to the new navigation channel. They more or less indicate that the particles try to find the shortest route to flow into the Geul van de Walvischstaart and Deurloo West. Once the particles are in these channels; they are transported towards the north (longitudinal direction of the navigation channel) and end up (after 2881 days) at almost the same location as seen in case 1. This happens for 6 of the start locations. For one of the start location (located in an area with lower transport velocities), the simulation period is not long enough for the particles to reach the navigation channel.

Yet, there is no clear explanation for this large change in the residual transports. Because of high discharges and the large flow velocities in the new navigation channel, one may expect that the water flow on the Vlakte on Raan is sucked into the channel. However, it is not expected that withdrawal of discharges can explain these large-scale changes. Probably, the asymmetry in the horizontal tide on the Vlakte van de Raan has also changed significantly.

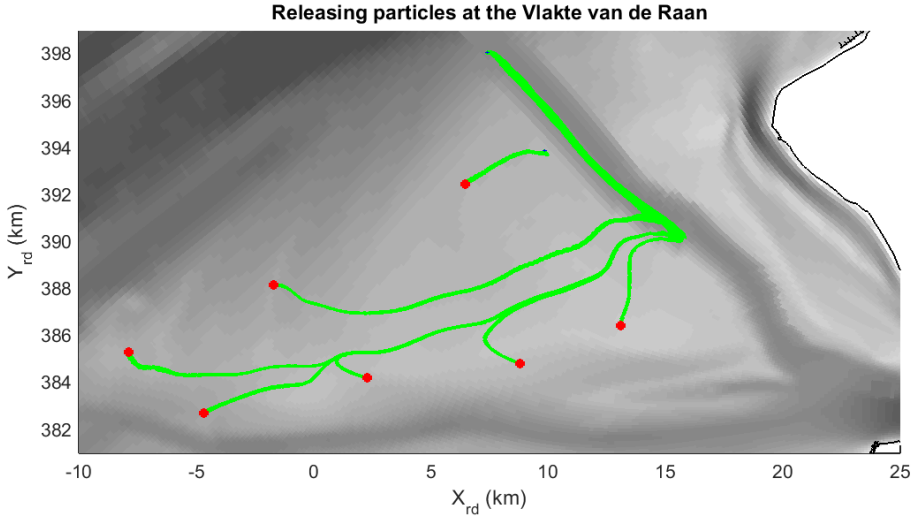


*Figure 6.13 Pathways (period of 8 years) of particles that are released at the Vlakte van de Raan. Case 3.*

It is difficult to see this reorientation of the residual transports in the vector plots for cases 1 and 3 (Figure 5.11 and Figure 5.22). However, this study also provided maps that used colormaps to visualize the direction of the residual transports (Figure 5.12 and Figure C.30 in appendix C.4). If we look back to the figures, the reorientation is indeed visible. However, these maps can be difficult to interpret and do not show that the pathways of different release locations converge. The change of the residual transports is also shown in two other maps of appendix C.4, namely Figure C.31 and Figure C.32. The figures show in which directions the residual transports have changed. Again, these results may be difficult to interpret. Concluding, the visualisation tool can be a useful method to interpret the spatial variations and changes in the sediment transports on the Vlakte van de Raan.

Thus, the new navigation channel also strongly affects the pathways at the Vlakte van de Raan. The particles move towards the new navigation channel, before they are transported towards the north. In addition to the findings of Section 6.2.2.1, these results suggest that deposited sediment in the navigation channel can also originate from Vlakte van de Raan.

#### *6.2.2.3 Implication*

Also for the third case, the insights about the pathways could be user to further improve the design of the human intervention. One could for example use the dredged material from the navigation channel to construct small barriers that can redirect the pathways on the Vlakte van de Raan to more favourable areas in the navigation channel. By constructing a high barrier west of the new channel that blocks these paths, the channel can become even more sheltered. However, also the erosion of this barrier itself (e.g. also due to breaking waves) can lead sedimentation within the new navigation channel. To reduce the sedimentation rates in the new navigation channel and area in between the Wielingen and Geul van de Walvischstaart, the cheapest and easiest option may be to replace the current design with a smaller channel (higher bed level and narrower) that withdraws less discharge and has lower flow velocities. In this way, fewer numerical particles from the inlet move into the new navigation channel. In other words, the channel “attracts” less sediment.

## 6.3 Conclusion

### 6.3.1 Transport pathways in the mouth of the Scheldt estuary

#### *6.3.1.1 Case 1*

Figure 6.14 summarizes the different pathways that are being found within the mouth. With the selected release locations, it is possible to explain a large part of the sediment transport patterns and the resulting erosion and sedimentation areas

The erosion and sedimentation patterns in front of the coast of Walcheren can be related with existence of the circulation cell of sediment and the divergence of the residual transports over both the cross-section and longitudinal direction in the Oostgat. Within the inlet, the transport pathways confirmed that the cross-channel imbalance that was also seen in the maps of the net discharges, net flow velocities and net sediment transports. The ebb dominance and the northern part and flood dominance in the southern part can be used to link the erosion and sedimentation areas that are observed in the inlet. The visualisation tool indicates that the modelled erosion and sedimentation in front of Zeebrugge is caused by the alongshore transport of sediment. In addition, the pathways show that the sedimentation within the Scheur and Wielingen is caused by transports of sediment from the east (the inlet) and the Paardenmarkt. The computed transport pathways also revealed that the flows of sediment on the Vlakte van de Raan converge and export sediment at the north/northeaster corner of the large shallow area. At last, the transport pathways have also been used to analyse the behaviour of the different disposal areas that are currently used. The pathways demonstrate that the two disposal locations on the Vlakte van de Raan perform better compared to the two

locations in front of the coast of Belgium. For these last two locations, the pathways indicate that the disposed sediment can quickly move to the area where it again needs to be dredged away: the navigation channel Scheur. When using these two southern locations, the dredging and disposal operations would result in recirculation of sediment for which the natural flow of sediment compensates for the human-induced bed level changes.

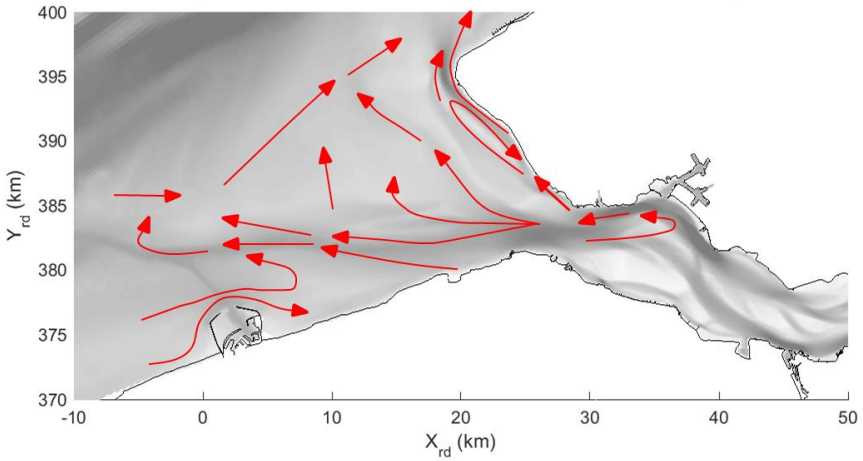


*Figure 6.14 Sketch showing the directions of the most important sediment transport pathways found with the visualisation tool. The arrows are not scaled but just give an idea of the directions of the pathways.*

The observed transport pathways can be used to better understand the sediment balances that are computed by for example Nederbragt & Liek (2004), Haecon (2006), Consortium Deltares-IMDC-Svasek-Arcadis (2013c) and Elias & van der Spek (2015). Some studies computed that the eastern part of the Western Scheldt exports sediment towards the mouth. This corresponds with the findings of this chapter. Almost all numerical particles that are released in the inlet are transported into the mouth. Besides, most of the sediment balance studies concluded that there is a reduction in the total sediment volume for the mouth area. As this study did not find large flows of sediment towards the Western Scheldt or towards the area west of the mouth, the results of the visualisation tool suggest that this loss of sediment is caused by an export of sediment at the north/north-eastern corner of the study domain.

The current study also used the modelled pathways to analyse the temporal variations in the sediment transports for case 1. It confirmed what can be expected based on the analysis of the standard Delft3D model output. The numerical particles have oscillating motions due to the alternating ebb and flood currents. Moreover, results confirmed that the displacements of the numerical particles (i.e. sediment transport magnitudes) are higher during spring tide compared to neap tide. The study did not find large temporal variations in the directions of the residual sediment transports for the different $M_2$ periods within the spring-neap cycle.

#### 6.3.1.2 *Cases 2 and 3*

First of all, let's consider the construction of the island in front of Knokke-Heist. The standard Delft3D model output already showed that erosion and sedimentation patterns in the vicinity of the island change due to the increased flow velocities north and northeast of the island and the changes in the alongshore transport of sediment (Section 5.3.2). This study showed how the pathways can be used to link these sedimentation and erosion patterns directly in front of the island. Furthermore, the pathways indicate that flows of sediment from the shallow area directly north of the island and the large erosion area in the Wielingen contribute to the computed increase in the sedimentation in the navigation channel Scheur.

The new navigation channel affects the sediment transport patterns over a large area. A lot of the pathways are now more orientated towards the Geul van de Walvischstaart and Deurloo

West. In addition, the results confirm that the sediment transports in the Geul van de Walvischstaart and Deurloo West increase at the cost of the other channels (Section 5.3.3.2). A lot of the particles that used to be move into the Wielingen, Scheur and Geul van de Sluissche Hompels, are now transported through the new navigation channel.

Moreover, the pathways indicate that sediment on the Vlakte van de Raan is moved into the new navigation channel. The numerical particles are first transported perpendicular (towards the west, shortest route) to the new channel, before being moved in northern direction. The results indicate that the computed sedimentation in the northern part of the new channel can be traced back to flows of sediment from the south and the Vlakte van de Raan. The large sedimentation at the southern inlet of the Geul van de Walvischstaart can be linked with flows of sediment out of the Wielingen.

For both these interventions, suggestions were given how the findings about the transport pathways can be used to improve the interventions in such a way that the morphological developments are steered into the desired state. However, one should keep in mind that the interventions are just some first ideas that were presented in Masterplan Flanders Bays (2014) and are examples to show the application of the tool in a real-life situation.

### 6.3.2 Added value of the visualisation tool

By applying the visualisation tool on the mouth of the Western Scheldt, its usage and added value are demonstrated. If we consider case 1, we can state that many of the sediment transport patterns that were found with the visualisation tool (Chapter 5) are a confirmation of the findings of the literature review (Chapter 2) and the analysis of the standard Delft3D model output (Chapter 3). However, the tool provides a useful alternative to demonstrate these findings and visualize the same (sediment transport) data with a different technique. This technique presents the sediment transport patterns in an orderly way and makes them easy understandable. In addition to this, case 1 has shown that the transport pathways can be useful to link the various erosion and sedimentation areas.

For case 1, the added value of the tool was especially demonstrated with the release of particles at the Vlakte van de Raan and the different disposal locations. The convergence of sediment flows at the Vlakte van de Raan is revealed by the visualisation tool and was not clearly visible in the map of the residual transport. The visualisation tool also demonstrated that the tool can be used by engineers in a preliminary study to evaluate disposal locations. As the tool is a post-processing method, one can quickly and easily study various disposal locations and eventually also analyse how these locations respond on different hydrodynamic conditions (e.g. by including waves and wind).

With the second and third case, this study demonstrated that the tool can be helpful to evaluate how a certain morphological system responds on the construction of a large-scale intervention. The computed pathways again confirm many of the findings of Chapter 5 and are useful to explain and link the various erosion and sedimentation areas. The most remarkable and revealing results were obtained in case 3 about the sediment transport patterns on the Vlakte van de Raan. The results of Chapter 5 did not provide clear evidence that the construction of the new channel affects the sediment transports on the Vlakte van de Raan in such a strong way.

# 7 Discussion

This chapter discusses the choices and assumptions that were made and their implications. The study about the concepts of the two transport pathway methodologies is part of the first research question and is mentioned in the conclusion (Chapter 8).

## 7.1 Visualisation tool

In the current set-up of the visualisation tool, the transport velocity at a certain point is determined with bilinear interpolation. The method could be replaced by a higher-order interpolation scheme to better take into account non-linear gradients in the sediment transport maps. However, this adjustment requires more calculation time. The bilinear interpolation is accurate enough if the grid resolution of the Delft3D simulations is defined based on the spatial variations in the bathymetry, hydrodynamics and morphological processes; which should be the cases in a proper model set-up.

Also the RK4 algorithm could be replaced by a more sophisticated numerical scheme to improve the accuracy of the transport pathways. However, the extra computational time that is required for these calculations is not in line with the goal of the tool: provide quick insights into a morphological system. Therefore, the current set up seems to be fine. By choosing the time step following the 2 procedures as presented in Section 3.3.2.3, the user can determine the balance between computational time and numerical error.

The acceleration coefficient is used to convert the sediment transports ($m^3/s/m$) into transport velocities (m/s). As explained in Section 3.3.3, the acceleration coefficient is an important variable as it affects the tracer dispersals that are found with the visualisation tool. The coefficient determines the size of the particle's to and fro motions that follow the tidal currents. In its turn, these oscillating motions can determine the residual movements of particles. The pathways are especially sensitive in areas with high sediment transports and larger gradients.

Moreover, the acceleration coefficient determines to what extent the temporal variations in the sediment transport are translated in variations of the pathways. With for example a larger acceleration coefficients, the differences in sediment transports (e.g. spring and neap tide) over time result in larger differences in the particle displacements. In this way, also the analysis about the temporal variations of the sediment transports in the mouth of the Scheldt estuary is influenced by the chosen value for the acceleration coefficient.

Concluding, it is important that the definition of the acceleration coefficient is well-founded. As will be discussed in the next chapter, the role and the definition of the acceleration coefficient requires more research.

## 7.2 Delft3D-NeVla model

Apart from the visualisation tool, the study about the mouth of the Scheldt estuary is also influenced by the assumptions that are made with the Delft3D-Nevla model. All of these issues should be seen in the context of the user's goals. Whereas the Delft3D simulations should include all relevant processes and parameters, minimizing the computational effort is an important aspect when using it in combination with the visualisation tool.

To reduce the computational time, this study is based on the 2DH-approach. The expectation is that the 3D effects (Chapter 1) on the sand transport in the mouth are limited (Vroom et al., 2015a). However, these 3D effects are more important for the transport of silt and clay. Silt has for example lower fall velocities, the transport is not limited by the transport capacity and the effects of diffusion are more pronounced. As the bed of the mouth is heterogeneous and

has a turbidity maximum east of Zeebrugge, a sand-mud model with a 3D approach may be required for future studies. The interaction between sand and mud can be of importance to predict the morphological development in this area

Moreover, the Delft3D-NeVla model did not include the effect of waves and wind. For average conditions, the effect on the sediment transports within the deeper areas is expected to be limited. For the coastal zone and possibly also for the sloping bed in front of the new island, breaking waves can locally increase the sediment transport rates. With large storms, the effect on the sediment transports is much higher (Steijn & van der Spek, 2005; Walstra, 2005). However, the morphological developments within the mouth do largely dependent on the tidal driven sediment transport. The findings of this study can already be useful for future studies that apply more sophisticated and extended versions of the Delft3D-Nevla model.

Next, the spin-up period may still be too short for the model to adapt to the imposed boundary conditions and smoothen/level off the steep gradients in the bathymetry near the new human interventions. Moreover, the boundary conditions themselves are not adjusted for the changes in the bathymetry and its effect on the tidal system. As the visualisation tool is mainly used as technique to get first insights and is meant to be used during preliminary studies, this is probably less of a problem. Furthermore, the designed interventions are relatively small and are just meant as a proof of concept of the visualisation tool.

The grid resolution seems to be fine enough to model large-scale flow and erosion-sedimentation patterns. However, the resolution is too coarse for a detailed study into the transport pathways in a specific area. For the study about the circulation cell around the Bankje van Zoutelande, one could for example use the more refined computational grid of (2014). Also for the analysis of the area around the newly constructed island in front of Knokke-Heist, a more refined grid may be needed.

As already discussed in Section 5.3.1, the residual sediment transports within the Wielingen deviate from the findings of Verduin (2009) and Tonnon & van der Werf (2014). An exact cause of this is yet unknown. It is possibly caused by the fact that the other studies are looking to a specific period that is not representative for the residual sediment transports within the mouth over the spring neap cycle. However, the Delft3D-NeVla model has not been validated yet for the morphological processes and developments in the mouth of the Scheldt estuary. A validation could facilitate in the discussion and increase the confidence about the modelled sediment transports and morphological developments.

# 8 Conclusions and recommendations

## 8.1 Conclusions

The objective of this study is to assess the added value of transport pathways generated by the visualisation tool to better understand the natural and human-induced morphodynamics of the mouth of the Scheldt estuary. The three research questions (RQ) are answered below.

*RQ1: How should the visualisation tool be used and its output be interpreted compared to the more traditional graded sediment approach? Chapters 3 and 4.*

Tracking sediment from a particular location can be implemented in principle with the graded sediment approach. This approach defines the transport pathways by following concentrations of different sediment fractions over time. Because the method describes changes in the tracer concentrations with an Eulerian approach, the pathways do not provide data about the movements of individual grains. The dispersal of tracers is influenced by the decay in mass fractions due to bed mixing and lag effects due to the burial and resurfacing of sediment to/from deeper underlayers. The interactions with the bed result in tracer dispersal rates that quickly decrease after the tracers have been released and can eventually even become negligible. When calibrated correctly, the method is able to provide physically accurate approximations of the tracer dispersal rates over time. Although it depends on the model settings, the approach generally requires a long computational time to get an impression of the transport pathways in a large area with a single tracer deposit.

The visualisation tool is conceptually different. It visualizes transport pathways based on the sediment transport maps. For this study, the sediment transport conditions are computed with the Delft3D model. The tool follows the movement of individual numerical grains through the sediment transport maps that are updated with a certain interval to represent the time-varying sediment transport conditions. The numerical particles move according to the directions and magnitudes of the sediment transports. In this way, the tool visualizes the Eulerian-computed sediment transports in a Lagrangian way. The visualisation tool shows the behaviour of grains in case they would not have been mixed, buried and resurfaced in the bed. As the numerical particles are not slowed down by interactions with the bed, the predicted tracer dispersals must be interpreted as maximum movement rates. Because of this assumption, the visualisation tool is able to provide compute large-scale transport pathways with a minimum computational time. If one wants to get quick insights about the sediment transport patterns in a certain system for which the accuracy of the timescale of tracer dispersals is not of major importance, the visualisation tool should be preferred above the graded sediment approach.

The user has to define 4 parameter values before the tool can be used. The roles of these parameters were presented in the theoretical analysis of the tool and in the simplified schematization. First of all, one has to choose an appropriate interval for updating the vector fields. The second parameter is the time step over which particle displacements are computed. For these parameters, one should take into account the numerical accuracy of the tool, the computational time and amount of input data. The sensitivity of the pathways for these parameters increase with higher sediment transport rates, larger temporal variations and larger spatial variations. Thirdly, the random walk coefficient can be used to add a randomly generated velocity on top of the transport velocity determined with the sediment transport maps. In this way, the tracer dispersal becomes larger and one can analyse the sensitivity of pathways for spatial variations in the sediment transport fields. However, it is not mandatory to use a random walk coefficient higher than 0. Last but not least, the user has to determine the acceleration coefficient. It is not a calibration coefficient. It should be linked with physics (e.g. flow velocities, concentrations etc.) and be based on a number of assumptions.

*RQ2: What are the sediment transport patterns controlling the morphological developments in the mouth of the Scheldt estuary currently and in the case of large-scale morphological human interventions? Chapter 5.*

As start, we consider the current situation (case 1, Figure 5.11). The total residual sediment transports are ebb dominant in a number of channels: the Honte, Wielingen, Scheur, Geul van de Walvischstaart, Deurloo Oost, Deurloo West and Geul van de Sluissche Hompels are ebb-dominated. At the inlet (Vlissngen-Breskens), one can find a cross-channel imbalance of the residual transports: the residual transport at the northern part is ebb-dominant, while the southern part is flood-dominant. There is also a divergence of the residual transports over both the cross-section and longitudinal direction in the Oostgat. Combined with the residual transports in the Sardijngeul, Deurloo Oost en Geul van de Rassen; these result in a circulation cell around the Bankje van Zoutelande. At the port of Zeebrugge, there is an alongshore residual transport in north-eastern direction.

The human interventions that are considered in this study are: an island in front of Knokke Heist (case 2) and the construction of a new navigation channel by deepening and extending the Geul van de Walvischstaart and Deurloo West (case 3). For case 2, the model showed an increase of the flood dominant residual transport in the shallow area directly in front of the island. For the Wielingen and Scheur in front of the island, the intervention leads to an increase of the ebb dominant residual transport (again due to contraction of the flow). Both are caused by increase flow velocities as result in the reduction of the cross-sectional area. The lower flow velocities in the middle and eastern sections of the Wielingen and northwest of Zeebrugge result in lower residual sediment transports.

Next, we can analyse case 3. The new navigation channel supports the other channels in discharging water that is required for filling and emptying of the Western Scheldt. As result of the increased discharges, maximum flow velocities, net velocities and the reduced flood dominance that is found within the vertical tide, the residual transport within the Geul van de Walvischstaart and Deurloo West increases. As the new navigation channel partly lowers the flow velocities in the Oostgat, Wielingen, Scheur and Geul van de Sluissche Hompels; the residual transports in these channels decrease.

*RQ3: What are the characteristic sediment transport pathways in the mouth of the Scheldt estuary following the visualisation tool, currently and in the case of large-scale morphological human interventions? Chapter 6.*

Again, we start with case 1. By releasing the numerical particles at various locations within the mouth, the tool is able to reproduce the sediment transport patterns that were discussed at the previous research question. The particles that are release near the coast of Walcheren, are exported through the Oostgat and Geul van de Rassen in northern direction. For the other particles, the visualisation tool demonstrated that the numerical particles are located at the edges on the Vlakte van de Raan at the end of the simulation. The results revealed that on the Vlakte van de Raan itself, the transport pathways converge and are directed towards the northern end of the Deurloo West. As this pattern cannot be easily extracted from the standard maps of the residual transport, the added value of the tool in visualizing sediment transport is confirmed. Studies such as Cleveringa (2008) and Elias & van der Spek (2015) concluded that the mouth is exporting sand. As none of the particles were transported out of the mouth at the western end of the Scheur and also the transport in the inlet is mainly ebb-directed, the results suggest that this export mainly occurs at the north/north-eastern corner of the study domain (Oostgat and Deurloo West).

By analysing the transport pathways and tracing back particles, it is possible to see from which directions and areas the sediment in the sedimentation areas is coming from. In this

way, the tool van be useful when analysing the link between disposal and dredging locations. The pathways for example demonstrated that the disposal locations directly in front of the Belgian coast can contribute to the sedimentation in the navigation channel. To save money, these results suggest that one can better use the more stable disposal areas in further north.

The impact of the new island in front of Knokke-Heist on the flood directed alongshore residual sediment transport is also shown in the transport pathways. Particles that used to be transported to the sheltered area east of the port are now transported into the new navigation channel. In addition, the pathways have been useful to link the various erosion and sedimentation areas directly in front of the island. Moreover, the results indicate that the increased sedimentation in the Scheur can be related to flows of sediment out of the Paardenmarkt and the large erosion area at the western end of the Wielingen.

With the extension and deepening of the channels, the transport pathways demonstrate that more particles are transported into the Geul van de Walvischstaart and Deurloo West. This corresponds with the increased flow velocities and discharges that are found here. Also for the surrounding area, the transport pathways are more orientated towards the new navigation channel. The large number of particles that flow from the Wielingen towards the Geul van de Walvischstaart can explain the existence of the increased erosion area that is found in between the channels. The fact that particles are attracted towards the deepened channels is also observed when the particles are release at the Vlakte van de Raan. The particles try to find the shortest route towards the new navigation channel, before being transported in northern direction. The pathways indicate that the deposited material in the northern part of the channel could be traced back to locations in the south and the Vlakte van de Raan.

The current study also used the modelled pathways to analyse the temporal variations in the sediment transports. It confirmed what can be expected based on the analysis of the standard Delft3D model output. The numerical particles have oscillating motions due to the alternating ebb and flood currents and these are higher during spring tide compared to neap tide (higher sediment transport). The study did not find other large temporal variations in the directions of the residual sediment transports for the different $M_2$ periods within the spring-neap cycle.

Concluding, the visualisation tool has proven its added value in visualizing the sediment transport pathways within the mouth and explaining the erosion and sedimentation patterns. Comparing the findings for RQ2 (Chapter 5) and RQ3 (Chapter 6), it seems that the results about the sediment transports on the Vlakte van de Raan were most surprising and do contribute most to the insights that can already be obtained by studying the standard Delft3D model output. By including more factors in the Delft3D-NeVla model (e.g. waves and wind) or by looking to a different study area, the visualisation tool could also lead to a better understading of temporal variations in the sediment transports. Apart from gaining new insights, the study also demonstrated that the visualisation tool can be useful for engineers in a preliminary phase when evaluating different disposal locations or the construction of large-scale morphological interventions.

## 8.2 Recommendations

### 8.2.1 Visualisation tool

This study already made a start in defining the acceleration coefficient and studying its impact on the tracer dispersals. However, this analysis can be complicated as the tool visualizes the movement of numerical particles for which the physical processes are simplified (no interaction with the bed) and cannot be easily calibrated and validated. Because of this difficulty and the fact that the tool has not been documented before nor thoroughly tested, it is recommended to do more research about the current definition of the acceleration coefficient (i.e. equations and assumptions) and alternatives. In this study, the coefficient is derived from

a single representative area and then applied to the entire study domain and simulation period. A possible alternative is to use a locally derived acceleration coefficient (only looking into the area of interest), that is still constant over time and space. As demonstrated for the Vlakte van de Raan (Section 6.1.2.6), a locally derived coefficient may be desirable to bring the maximum transport velocities and flow velocities in the area of interest closer together. Furthermore, it recommended to study if the coefficient could be varied over time and space within a single simulation and what this means for the concepts behind the tool.

The current set-up of the visualisation tool computes the displacements of particles based on total sediment transports. With some adjustments, the tool could also be used to analyse the dispersal of tracers that are transported with suspended or bed load transport. This can be done separately, one simulation for each transport mode. However, it is recommended to study whether it is possible and desirable to combine the tracer dispersals of the two transport modes in a single model. This adjustment requires a definition of the distribution of numerical particles to the transport modes.

The definitions of the parameters in the visualisation tool are complicated and are based on a balance between minimizing the computational time and improving the accuracy. Moreover, the sensitivities of the transport pathways depend on the magnitudes and gradients in the transport velocities. Thus, choosing the parameters values can be a labour-intensive and difficult job. As the algorithm consists of a few hundred code lines in Matlab, the task of understanding and applying the visualisation tool is assigned to experts in morphodynamics and numerical modelling. To make the tool better accessible and understandable, future studies can spend time in standardizing the parameter definitions, setting up a more user-friendly interface and improving the user manual (appendix A.1). After doing this, it is recommended to test the tool in real-life projects with engineers and clients. This study stated some of the practical advantages (e.g. quick, easy to interpret, useful for communication with non-experts) of the visualisation tool. The application of the tool in these projects can help to verify these statements and see if there certain difficulties that have to be solved.

### 8.2.2 Application of visualisation tool for the mouth of the Scheldt estuary

The two human interventions that are discussed in this study are just two examples that are based on some sketches provided by the Masterplan Flanders Bays (2014). Based on the results of this study, it can be recommended to use the visualisation tool also for future (preliminary) research about the ideas that are introduced in the Masterplan. This can be directly the first real-life project in which the tool can be tested. The tool can also be used to study the historical changes in the bathymetries (e.g. construction of the port of Zeebrugge, the disappearance of the Deurloo channel).

As stated in the discussion (Chapter 7), future studies should extend the Delft3D-NeVla model by using a 3D approach and including the effect of wind, waves, heterogeneous sediments and sand-mud interactions. In this way, the results can better predict the observed morphological developments.

The level of detail presented with the visualisation tool depends on the grid resolution used in the Delft3D simulations. Chapter 5 mainly discussed large-scale sediment transport patterns in the mouth area. For detailed studies about the movement of numerical particles in a small area, it is recommended to use a more refined grid. As presented by Damen (2014), the fine grid can cover an smaller area and be nested in the original Delft3D-NeVla model.

# 9 References

Bliek, B., de Gelder, A., Gautier, C., & Les, B. (1998). *De rol van het getij in de morfologische ontwikkeling van de Westerscheldemond (project K2000*KOP)*. Rotterdam, Netherlands: Svašek.

Bolle, A. (2006). *Sediment Exchange between the Dutch Coast and the Tidal Basin Western Scheldt (Master Thesis)*. Southampton, United Kingdom: University of Southampton, Faculty of Engineering, Science and Mathematics.

Cancino, L., & Neves, R. (1999). Hydrodynamic and sediment suspension modelling in estuarine systems. Part II: Application to the Western Sheldt and Gironde estuaries. *Journal of Marine Systems*, *22*, 117–131.

Cleveringa, J. (2008). *Morphodynamics of the Delta coast (report: A1881R1r2)*. Delft, Netherlands: WL|Delft Hydraulics.

Consortium Deltares-IMDC-Svasek-Arcadis. (2013a). *Actualisatierapport Delft3D Scheldeestuarium (report: LTV V&T A-27)*.

Consortium Deltares-IMDC-Svasek-Arcadis. (2013b). *De rol van slib in de Westerschelde (report: LTV V&T G-3)*.

Consortium Deltares-IMDC-Svasek-Arcadis. (2013c). *Influence morphology on tide and sand transport (report: LTV V&T G-4)*.

Dam, G., Bliek, A., & Labeur, R. (2007). Long term process-based morphological model of the Western Scheldt Estuary. In *Proceedings of the 5th River, Coastal and Estuarine Morphodynamics conference* (Vol. 56, pp. 1077–1084). Enschede, Netherlands: IAHR.

Damen, J. (2014). *Coastal erosion processes in tidal channel Oostgat (Master Thesis)*. Enschede, Netherlands: University of Twente, Faculty of Engineering Technology.

Dastgheib, A. (2012). *Long-term process-based morphological modeling of large tidal basins (Dissertation)*. Delft, Netherlands: Delft University of Technology & UNESCO-IHE Institute for Water Education.

Deltares. (2014). *Delft3D - FLOW User Manual (version 3.15.34158)*. Delft, Netherlands.

Du Four, I., & Van Lancker, V. (2011). *Physical impact of dredged material disposal sites and their recovery after cessation of dumping: a case study in the Belgian coastal zone (Project EV/18)*. Ghent, Belgium: Ghent University, Renard Centre of Marine Geology.

Dumon, G., Balcaen, N., Huygens, M., & Hyde, P. (2006). *Hydrodynamica ter hoogte van de Vlakte van de Raan*. *VLIZ Special Publication 35*. Oostende, Belgium: Vlaams Instituut voor de Zee.

Elias, E., Gelfenbaum, G., Van Ormondt, M., & Moritz, H. (2011). Predicting sediment transport patterns at the mouth of the Columbia River. In *Proceedings of the Coastal Sediments 2011* (pp. 588–601). Miami, United States.

Elias, E. P. L., Cleveringa, J., Buijsman, M. C., Roelvink, J. a., & Stive, M. J. F. (2006). Field and model data analysis of sand transport patterns in Texel Tidal inlet (the Netherlands). *Coastal Engineering*, *53*(5-6), 505–529.

Elias, E. P. L., & van der Spek, A. (2015). *Uitwerking sedimentbudget van de Westerscheldemonding (project: 1210301-012)*. Delft, Netherlands: Deltares.

Erkens, G. (2003). *Analyse Multibeam data Oostgat (report RIKZ/OS/2003.168x)*. Ministerie van Verkeer en Waterstaat, Rijksinstituut voor Kust en Zee.

Friedrichs, C. T., & Aubrey, D. G. (1988). Nonlinear tidal distortion in shallow well-mixed estuaries. *Estuarine, Coastal and Shelf Science*, *27*(6784), 521–545. http://doi.org/10.1016/0272-7714(90)90054-U

Groenenboom, J. (2015). *Modelling sand-mud-bed interaction in the Scheldt estuary (Master Thesis)*. Delft, Netherlands: Delft University of Technology.

Haecon. (2000). *K2005 WSmond. Zandbalans WS-mond Belgisch gedeelte (report: NST2155)*. Belgium, Drongen.

Haecon. (2006). *Actualisatie van de zandbalans van de Zee- en Westerschelde. (report: 1249760008/lvp)*. Bergen op Zoom, Netherlands.

Hirano, M. (1971). River bed degradation with armoring. *Translation, Japan Society of Civil Engineers*, *3*, 194–195.

Hordijk, D. (2002). *Geulwandsuppletie Oostgat westerschelde (report: C-5702 712)*. Ministerie van Verkeer en Waterstaat, Rijksinstituut voor Kust en Zee.

Jeuken, M. C. J. L., & Wang, Z. B. (2010). Impact of dredging and dumping on the stability of ebb–flood channel systems. *Coastal Engineering*, *57*(6), 553–566.

Joy, K. I. (2007). *Numerical Methods for Particle Tracing in Vector Fields (lecture notes)*. Berkeley, United States: University of California, Department of Computer Sciences, Visualization and Graphics Research Laboratory.

Kuijper, C., Steijn, R., Roelvink, D., van der Kaaij, T., & Olijslagers, P. (2004). *Morphological modelling of the Western Scheldt, Validation of DELFT3D (report Z3648 / A1198)*. Delft, Netherlands: WL| Delft Hydraulics & Alkyon.

Kuijper, K. (2015). De rol van slib in de morfodynamica van de vaarpassen en stortvakken in de Schelde-monding (concept, project: 1210301-012). Delft, Netherlands: Deltares.

Lesser, G. R., Roelvink, J. A., van Kester, J. A. T. ., & Stelling, G. S. (2004). Development and validation of a three-dimensional morphological model. *Coastal Engineering*, *51*, 883–915.

*Masterplan Vlaamse Baaien*. (2014). Antwerp, Belgium: Departement Mobiliteit en Openbare werken, Afdeling Maritieme Toegang.

Maximova, T., Ides, S., de Mulder, T., & Mostaert, F. (2009). *Verbetering hydrodynamisch NeVla model ten behoeve van scenarioanalyse (report: LTV V&T deelproject 1, WL 756_05)*. Antwerp, Belgium: Flanders Hydraulics Research.

Maximova, T., Ides, S., van Lede, J., de Mulder, T., & Mostaert, F. (2009). *Verbetering 2D randvoorwaardenmodel. Deelrapport 3: Kalibratie bovenlopen. (report: WL 753_09)*. Antwerp, Belgium: Flanders Hydraulics Research.

Meersschaut, Y., Parker, W. R., Peters, J. J., & Plancke, Y. (2004). A dredging and disposal strategy for managing the Western Scheldt's morphology and ecology. In *WODCON Conference* (pp. B1–3, 1–11). Hamburg, Germany.

Moerman, E. (2011). *Long-term morphological modelling of the Mouth of the Columbia River (Master Thesis)*. Delft, Netherlands: Deltares.

Nederbragt, G. (2006). *Zandvoorraden van het kustsysteem, onderbouwing van een conceptueel model met behulp van trends van de winst- en verliesposten over de periode 1973-1997 (Rapport RIKZ/2005.033)*. Ministerie van Verkeer en Waterstaat, Rijksinstituut voor Kust en Zee.

Nederbragt, G., & Liek, G. (2004). *Beschrijving zandbalans Westerschelde en monding (report: RIKZ/2004.020),*. Ministerie van Verkeer en Waterstaat, Rijksinstituut voor Kust en Zee.

Pawlowicz, R., Beardsley, B., & Lentz, S. (2002). Classical tidal harmonic analysis including error estimates in MATLAB using T_TIDE. *Computers & Geosciences*, *28*(8), 929–937. http://doi.org/10.1016/S0098-3004(02)00013-4

Plancke, Y., Vereecken, H., Claeys, S., Verwaest, T., & Mostaert, F. (2014). *Hydro - en sedimentdynamica in het mondingsgebied van het Schelde - estuarium (concept report, project WL2014R14_083_1*. Antwerp, Belgium: Flanders Hydraulics Research.

Ribberink, J. S. (1987). *Mathematical modelling of one-dimensional morphological changes in*

*rivers with non-uniform sediment (Dissertation)(report: TR diss 1570)*. Delft, Netherlands: Delft University of Technology.

Schoellhamer, D. H., Ganju, N. K., Mineart, P. R., & Lionberger, M. A. (2008). Chapter 31 Sensitivity and spin-up times of cohesive sediment transport models used to simulate bathymetric change. *Proceedings in Marine Science*, *9*(Kirby 1990), 463–475.

Steijn, R. C., & van der Spek, A. J. F. (2005). *Mogelijkheden voor geulwandversterking of verlegging Oostgat/Sardijngeul (report A1431)*. Alkyon.

Svašek. (1998). *De rol van het getij in de morfologische ontwikkeling van de Westerscheldemond, een modelmatige onderbouwing (report: 98154/1034)*.

Tonnon, P. K., & van der Werf, J. (2014). *Geulopdringing Zuidwest Walcheren (report: 1208921-000)*. Delft, Netherlands: Deltares.

van de Kreeke, J., & Robaczewska, K. (1993). Tide-induced residual transport of coarse sediment: application to the Ems Estuary. *Netherlands Journal of Sea Research*, *31*(3), 209–220.

van den Berg, J. H., Jeuken, M. C. J. L., & van der Spek, A. J. F. (1996). Hydraulic processes affecting the morphology and evelotion of the Westerschelde estuary. In C. Roman (Ed.), *Estuarine shores: Evolution, Environment and Human Alterations* (pp. 157–183). Chichester, England: John Wiley & Sons.

van der Slikke, M. (1998). *Grootschalige en interne zandbalans Westerscheldemonding (1969-1993)(report: R98-05)*. Utrecht, Netherlands: University of Utrecht.

van der Spek, A. J. F. (1997). Tidal asymmetry and long-term evolution of Holocene tidal basins in the Netherlands: Simulation of palaeo-tides in the Schelde estuary. *Marine Geology*, *141*(1-4), 71–90.

Van Der Wegen, M., Dastgheib, A., Jaffe, B., & Roelvink, D. (2011). Bed composition generation for morphodynamic modeling: Case study of San Pablo Bay in California, USA. *Ocean Dynamics*, *61*, 173–186.

Van der Werf, J., Van Oyen, T., De Maerschalck, B., Nnafie, A., Van Rooijen, A., Taal, M., … Van der Wegen, M. (2015). Modeling the morphodynamics of the mouth of the Scheldt estuary. In *E-proceedings of the 36th IAHR World Congress* (p. 7). The Hague, Netherlands: 36th IAHR World Congress.

van Eck, G. T. M. (1999). *De ScheldeAtlas, een beeld van een estuarium*. Schelde informatiecentrum.

Van Lancker, V., Baeye, M., Du Four, I., Janssens, R., Degraer, S., Fettweis, M., … Goffin, A. (2012). *Quantification of erosion/sedimentation to trace naturally-from anthropogenically-induced sediment dynamics "QUEST4D" (SD/NS/06B)*. Science for a sustainable development.

van Rijn, L. C. (1993). Principles of sediment transport in rivers, estuaries and coastal seas. Amsterdam, Netherlands: Aqua publications.

Van Rijn, L. C. (2001). *Approximation formulae for sand transport by currents and waves and implementation in DELFT-MOR (report Z3054.40)*. Delft, Netherlands: Deltares.

van Rijn, L. C., Walstra, D. J. R., & Van Ormondt, M. (2004). *Description of TRANSPOR2004 and Implementation in Delft3D-ONLINE (report Z3748.10)*. Delft, Netherlands: WL|Delft Hydraulics.

van Rooijen, A. (2015). *Memo: wave climate Schelde project*. Delft, Netherlands: Deltares.

van Schaick, S. (2015). *Morphological development after the July 2014 flow slide on the tidal flat of Walsoorden in the Western Scheldt (Master Thesis)*. Delft, Netherlands: Delft University of Technology.

van Veen, J., van der Spek, A. J. F., Stive, M. J. F., & Zitman, T. (2005). Ebb and Flood Channel Systems in the Netherlands Tidal Waters 1. *Journal of Coastal Research*, *216*, 1107–1120.

Verduin, F. (2009). *Sediment Transport in the Westerschelde Delta (Master Thesis)*. Delft, Netherlands: Delft University of Technology.

Vroom, J., de Vet, P. L. M., & van der Werf, J. J. (2015a). *Validatie waterbeweging Delft3D-NeVla model Westerscheldemonding (project: 1210301)*. Delft, Netherlands: Deltares.

Vroom, J., & Schrijvershof, R. (2015). *Overzicht van menselijke ingrepen in de Westerschelde en haar mondingsgebied in de periode 1985-2014 (memo, project 1210301)*. Delft, Netherlands: Deltares.

Vroom, J., Tonnon, P. K., Schrijvershof, R., van Rooijen, A., van Maren, B., & van der Werf, J. J. (2015b). *3D zand-slib morfologisch model Schelde-monding (concept, project: 1210301-002)*. Delft, Netherlands: Deltares.

Walstra, D. J. R. (2005). *Haalbaarheidsstudie Geulwandsuppletie Oostgat (project Z4056)*. Delft, Netherlands: WL|Delft Hydraulics.

Wang, Z. B., Jeuken, M. C. J. L., & De Vriend, H. J. (1999). *Tidal asymmetry and residual sediment transport in estuaries (report: Z2749)*. Delft, Netherlands: WL|Delft Hydraulics.

Wang, Z. B., Jeuken, M. C. J. L., Gerritsen, H., De Vriend, H. J., & Kornman, B. A. (2002). Morphology and asymmetry of the vertical tide in the Westerschelde estuary. *Continental Shelf Research*, *22*(17), 2599–2609.

Wong, M., Parker, G., de Vries, P., Brown, T., & Burges, S. (2007). Experiments on dispersion of tracer stones under lower-regime plane-bed equilibrium bed load transport. *Water Resources Research*, *43*(3).

Wright, J., Colling, A., & Park, D. (1999). *Waves, tides, and shallow-water processes*. Milton Keynes, England: Butterworth-Heinemann, in association with the Open University.

# A Appendix of Chapter 3 - Numerical modelling of sediment transport pathways

## A.1 Manual visualisation tool

The standard morphodynamic calculations compute the bed level changes and the underlying sediment transports magnitudes and directions. This Eulerian approach does not directly link sediment sinks and sources. A Lagrangian approach does resolve sediment transport pathways, providing information about the direction of the sediment flows and linking sinks and sources. The pathways are not a replacement of the traditional sediment transport modelling; they do not show the erosion-sedimentation rates, but just provide extra qualitative information about the sediment transport patterns.

Traditionally, the numerical modelling of tracer dispersals is based on the graded sediment approach. However, this study looks into the concepts behind the newly developed visualisation tool. Understanding and applying the visualisation tool can be a complicated task as it is captured in a few hundred Matlab code lines. Moreover, the tool requires a number of user-defined variables and describes the dispersal of numerical tracer particles with a physically inaccurate time scale. Because of all these aspects and the fact that the tool has not been well documented yet, this appendix provides a brief manual of the visualisation tool.

### A.1.1 Description

The tool visualizes the times series of sediment transport maps that are generated as output by the Delft3D model. The tool follows the movement of individual numerical particles through these sediment transport maps that are updated with a certain interval. The particles move according to the direction and magnitude of the sediment transports. In this way, the tool visualizes the Eulerian-computed sediment transports in a Lagrangian way. The tool is able to show valuable information about the sediment transport conditions that are difficult to interpret by the human brain. In case of the mouth of the Scheldt estuary for example, the tool was able to provide insights about the Vlakte van de Raan that were difficult to obtain when solely looking to the maps of the residual sediment transports. In general, the pathways can help to understand the erosion and sedimentation patterns and be used to evaluate designs of large-scale interventions.

Because the numerical particles do not interact with the bed, the predicted tracer transport rates must be interpreted as maximum movement rates. It shows the behaviour of grains in case they would not be mixed, buried and resurfaced in the bed. Although it is physically possible that a real tracer particle is not mixed, buried and resurfaced in the bed for a certain time, by far the major part of the tracer sediment is slowed down by the interaction with the bed. The transport pathways calculated with the visualisation tool should therefore be interpreted as maximum movement rates.

Although the assumption about bed interaction leads to tracer dispersals with an unrealistic timescale, it is also the basis of the main advantage of the tool (compared to the graded sediment approach). The visualisation tool is able to provide insights about large-scale sediment transport patterns with minimum computational time. Another advantage of the visualisation tool is the fact that it can use the output of a single Delft3D simulation to study the pathways of multiple sources (post-processing).

### A.1.2 Input

The input of the visualisation tool is formed by the sediment transport maps/vector fields that are generated by the Delft3D model. The model solves horizontal momentum, continuity,

sediment and turbulence equations based on effects such as wind, waves, tides, density-driven currents and river discharges. The current version of the visualisation tool is based on the 2DH Delft3D model.

The spatial resolution of the sediment transport maps is similar to the resolution of the computational grid in the Delft3D simulations. As stated in the manual of the Delft3D model (Deltares, 2014), it is important the grid resolution is coarsened and refined based on the local spatial variations in the bathymetry and the hydro- and morphodynamic processes. If one does this correctly, the resolution is also sufficient enough for the visualisation tool.

The time step that is used by the Delft3D model to compute the hydro- and morphodynamic processes (~seconds) cannot be applied for the temporal resolution for the sediment transport maps. With a large simulation area and/or simulation period, this would mean that the visualisation tool has to process gigabytes of data. To reduce the data volume, the sediment transport data in the tool should be updated with a larger interval ($\Delta t_{d3d-output}$, see below). However, the temporal resolution has to be high enough to represent the relevant temporal variations in the sediment transport. The same interval should be used for interval of storing map results in Delft3D model (to prevent an abundance or shortage of data).

### A.1.3 Parameters for particle movement

When applying the visualisation tool, the user has to define four parameters that influence the movement of particles. The values have to be chosen based on the allowed computational time, required accuracy and the user's preference about non-random particle displacements. It is important to state that the effects of the parameter values depend on magnitudes and the temporal and spatial variations of the sediment transport. There is no single set of parameter values that should be applied in all studies. Even within a study domain, one may choose to vary the parameter values.

<u>The time step/interval for updating the vector fields:</u>

The variable ($\Delta t_{d3d-output}$) was already introduced before. The interval has to be chosen based on the time scale of the sediment transports and the need to minimize the total data volume. The effect of interval on the movement of numerical particles can only be found by trial and error and depends on the local conditions. In study domains where the $M_2$, $M_4$ and $M_6$ constituents of the tidal wave are the main driver of sediment transport, an interval of 15 minutes seems to be legitimate.

<u>The time step for particle movement calculations</u>

The particles move through the sediment transport maps with the time step $\Delta t_{pm}$. The size of this step has to be at least smaller than $\Delta t_{d3d-output}$ to make sure that the temporal resolution of the input data is include in the movement of particles. Often, the size of the time step has to be refined even further to ensure that pathways of the particles reflect the spatial variations in the sediment transport (numerical error of the RK4 method) as much as possible. The correct value totally depends on the local conditions. The time step can be determined based on the SN number (maximum displacement should be smaller or equal to N times the grid resolution) and a comparison of the pathways and the vector fields. A more time consuming analysis is a comparison of the transport pathways computed with different values for $\Delta t_{pm}$. By increasing the time step gradually (starting very low), one can find the time step that still lead to acceptable predictions of the transport pathways. As the time step determines the number of jumps a particle makes within the simulation period, it strongly influences the computational time (especially with a large number of particles) and a good analysis of $\Delta t_{pm}$ can save time during later stages of the research. For the mouth of the Scheldt estuary, time step between 30 and 100 seconds were used.

The acceleration coefficient

The acceleration coefficient $\alpha$ (1/m) is used to convert the sediment transports ($m^3/s/m$) into *transport* velocities (m/s). Subsequently, these transport velocities can be used for the movement of numerical particles. Currently the visualisation tool is based on total sediment transports. The acceleration coefficient for the total transport is computed as the weighted averaged of acceleration coefficients for suspended and bed load. The acceleration coefficient for suspended load is defined such that the peak transport velocities are of the same order as flow velocities ($10^3$~$10^4$ 1/m). The coefficient for bed load transport is computed based on the reference height and an assumption about the concentration of sediment between the bed and the reference height (~$10^2$ 1/m). The acceleration coefficient is set constant over the entire study domain and study period. This single coefficient is derived from the representative area with the maximum transport velocities. In this way, the transport velocities are never (an order magnitude) higher than the flow velocities.

Random walk coefficient

On top of the transport velocities the particles receive from the sediment transport maps, it is possible to add an extra random velocity. In this way, the results can show whether a deviation of the original pathway results has consequences for the movement of the particle in the remaining part of the simulation. Does the particle move away from the original path (divergence) or is it converged to the similar end location (convergence). The random walk is meant to tweak/play with the model and analyse the spatial variations in the vector fields.

The effect of the random walk coefficient on the (absolute) random displacement in terms of metres, depends on magnitude of the non-random velocities and the $\Delta t_{pm}$. For the selection of the coefficient, that *relative* random displacement is more important. With larger values for $\beta$, the total velocities the particle receives do more and more depend on the randomly generated velocities. If these start to get dominant, the visualisation of the sediment transport vector fields more or less disappears and the particles move randomly through the system. A safe option would be to setting $\beta$ at 0.5. In this way, about 95% of the random velocities are smaller than the transport velocities derived from vector fields.

### A.1.4 Other model settings

There are a number of other model settings that can be defined by the user, but do not have a direct impact on the movements of numerical particles. The user can select:

- Start and stop times of particle tracking
- Continuous (for a certain period) or instant release of particles
  - In case of continuous release: interval of releasing particles and number of particles that are released every time
  - In case of instantaneous release: number of particles that are released

Also for the output of the visualisation tool, the user can make a number of choices:

- Yes/No: save the pathways of the individual particles
- Yes/No: save maps of the tracer concentration over time
  - In case of yes, the user can define the grid resolution of these maps
- The time step/temporal resolution of the output data
- Yes/No: provide statistics about the particle movement. The visualisation tool is able to compare the displacements with the local grid resolution and provide statistics about this (in line with the SN number)
- Yes/No: provide statistics about the random displacements. The tool is able to provide statistics (largest instantaneous random displacement, largest cumulative random displacement etc.) about the random movement.

For all these points, it is important to consider that they have an impact on the computational time.

# B Appendix of Chapter 4 - Schematic test case

## B.1 Release locations

The two release locations that are used in the analysis of schematic test case are shown in Figure B.1.

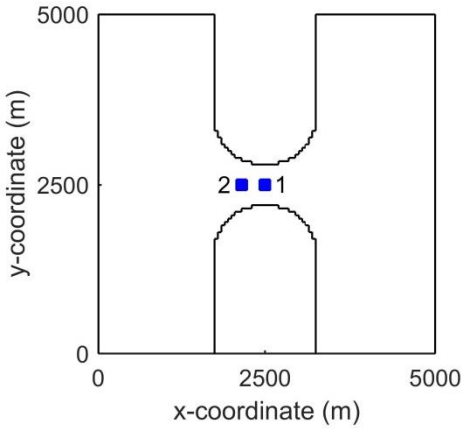


*Figure B.1 The two release locations that are used in the analysis of the schematic test case*

## B.2 Graded sediment approach

### B.2.1 Well mixed bed approach, partitioning the study area

The analysis in Section 4.2.1.2 shows how the dispersal of tracer sediment in the area around the start location is influenced by the bed thickness. For Figure 4.7, the study domain is divided in a number of areas (based on the distance between the grid cell and the start location). Figure B.2 shows these areas in a map.

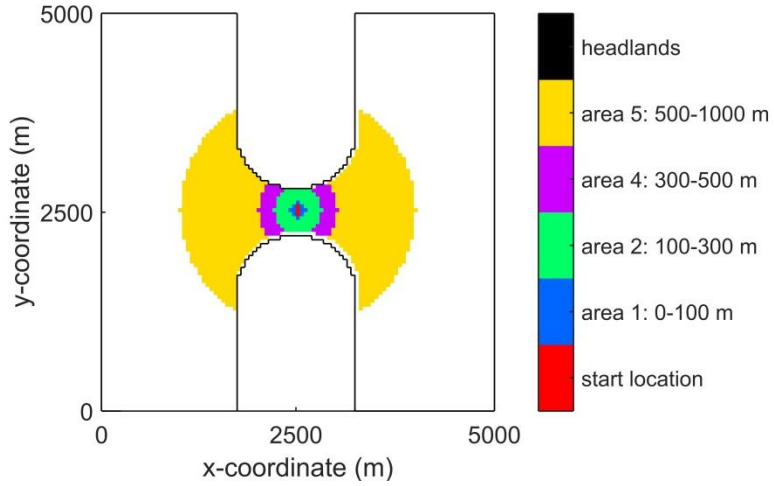


*Figure B.2 Areas contain grid cells within a certain distance of the start location (used in Figure 4.7).*

### B.2.2 Adjustment of the Delft3D code for the layered bed approach

For the sensitivity analysis of graded sediment approach, the standard Delft3D code is slightly adjusted. This was done with the help of Delft3D experts Aukje van Spruyt, Adri Mourits and Bert Jagers. The adjustment is merely meant as a way to align the well mixed bed and layered bed approaches and makes it possible to easily compare the two. The adjustment involves a redefinition of the fixfac factor in case of the layered bed approach. The adjustment

changes the dispersal pattern of a small volume of the tracer fraction. It removes the scattered pattern/extreme quick dispersal that was seen for a very small volume of the tracer fraction (close to the numerical accuracy of the numerical model). Because the dispersal of the major part of the tracer fraction is not influenced significantly, the adjustment does not influence the main conclusions of the sensitivity analysis.

A comparison of the well mixed and layered bed methods with similar dimensions showed small deviations in the dispersal of tracer sediment. With the layered bed approach, a small volume of tracer sediment is quickly displaced (~ within a few minutes) towards the boundaries of the domain (Figure B.3). Apart from this extreme quick dispersal, figure B.1 also shows a lot of empty cells and addresses the problem of numerical accuracy. These issues were not observed with the well mixed bed approach (Section 4.2.1.)

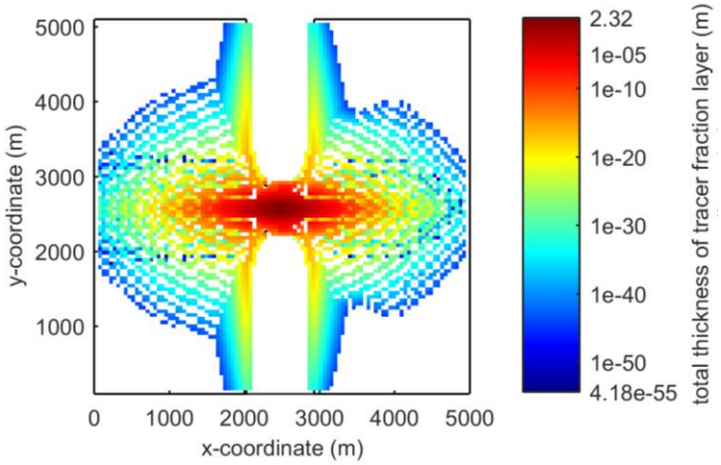


*Figure B.3 Map of the layer thickness consisting of the tracer fraction after 3 months. Start location: (2500,2500). Initially, the transport layer is 5 m.*

The cause of this issue is a small difference in the definition of the fixfac factor. The factor reduces the erosive fluxes of a specific fraction in case the available mass in the upper layer of the bed passes a certain threshold. Whereas the availability of a specific fraction already controls the erosion rate (with lower mass fractions, less sediment is picked up), the fixfac factor forms a second technique that slows down this process.

Originally, the fixfac factor was meant to simulate the effect of the non-erodible (fixed) layer when there is almost no erodible sediment left. If excessive erosion occurs, the finite quantity of erodible sediment at the bed may become exhausted and be unavailable to supply sediment to suspended and bedload transport modes. In case the bed is covered by bedforms, the troughs of the bedforms will start to expose the non-erodible layer before sediment runs out completely. This results in a gradual reduction of the transport capacity (by the fixfac factor) over a certain sediment thickness. The factor thus makes sure that mass of sediment cannot be reduced to 0 kg instantly, this process is slowed down.

With the mixed bed approach, the fixfac factor of fraction A is determined by looking to total mass of that fraction in the bed. In case this value is below a certain threshold, the erosive fluxes are gradually reduced. In the original code of the layered bed method, the erosive fluxes of fraction A are reduced when the total mass of sediment in the bed (all the fractions and summed over all bed layers) is below the user pre-defined threshold. To get similar results from both methods, the definition of the fixfac factor for the layered bed approach is changed. Instead of looking to the total mass of all fractions in all layers, the new code states that the fixfac factor of fraction A should be determined based on the mass of fraction A in the transport layer. In line with the concept of the layered bed stratigraphy, the underlayers do not directly determine the erosion rates at the top of the bed.

It is unsure whether or not redefinition of the fixfac factor is better in line with the physical processes. The numerical technique and its applicability for different scenarios are not fully understood yet. But as stated, the redefinition of the fixfac factor is not really important for the main conclusions of the sensitivity analysis. It just gives smoother (less scatter) developments in the dispersal of the tracer fraction and makes sure that the well mixed bed and layered bed approaches use the same concepts.

## B.3 Visualisation tool

By using the method discussed in Section 3.3.3 (with n=5, reference height of 1 cm), the acceleration coefficient for total sediment transport can be computed based on the depth-averaged velocities, suspended sediment transport rates, reference concentration and the ratio between suspended en bed load transport. As these variables are varying over space, the acceleration coefficient in the simplified schematization initially also contains spatial variation (Figure B.4). For the visualisation tool however, a single coefficient has to be used. For the schematic case, the coefficient is set at 10000 $m^{-1}$. In this way, the maximum transport velocities and flow velocities have the same magnitude in the inlet (Figure B.5).

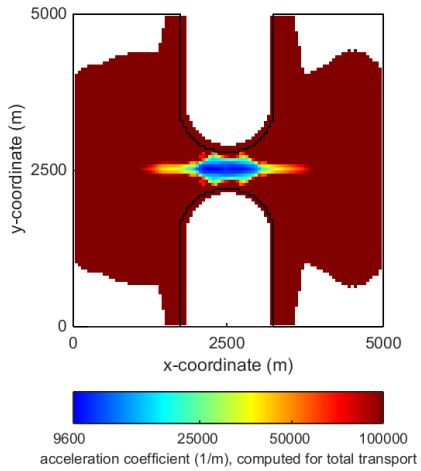


*Figure B.4 Spatial variation in the computed acceleration coefficient. For the visualisation tool, a single coefficient has to be selected for the entire domain and simulation period*

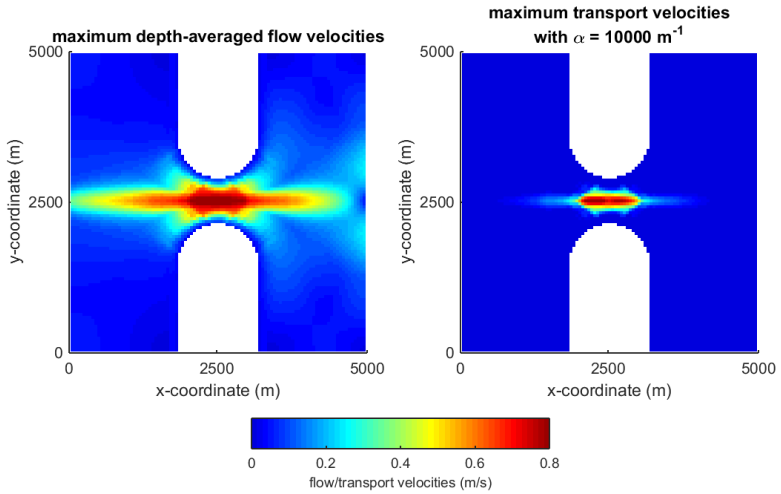


*Figure B.5 Maps, showing the maximum flow and transport velocities. The transport velocities are computed based on total sediment transports and an acceleration coefficient of 10000 m-1*

# C Appendix of Chapter 5 - Delft3D-NeVla model schematization and results

## C.1 Adjusting the upstream boundary

To save computational time, the number of cells in the computational grid is reduced. The upstream part of the Scheldt estuary (upstream of Schelle), is removed. To impose a new boundary condition at Schelle, a Delft3D simulation was performed with the original computational grid. The water levels and depth-averaged flow velocities at observation points 'Antw Loodsgebouw' (near the new upstream boundary) and 'Breskens' (near the study area) for the simulations with the original and adjusted grid are illustrated in Figure C.1 and Figure C.2. The figures also show the differences between the two simulations. As can been seen, the relocation of the boundary does not have a large effect on the two parameters. The deviations are insignificant compared to the parameter values themselves.

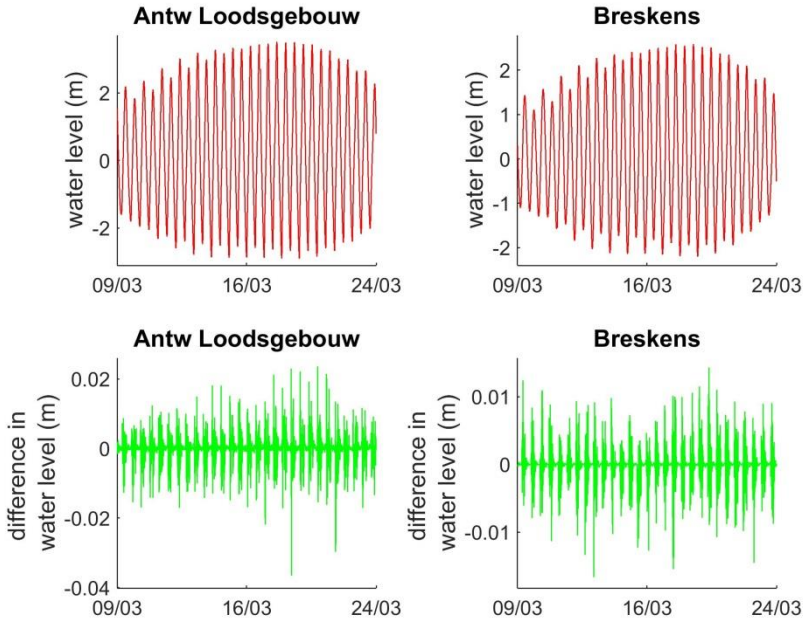


*Figure C.1 Modelled water levels (upper plot) and water level differences (lower plot) with simulations based on the original computational grid (blue line, upper plot) and adjusted grid (red line, upper plot). Because the differences between the two simulations are so small, they are not observable in the upper plot*

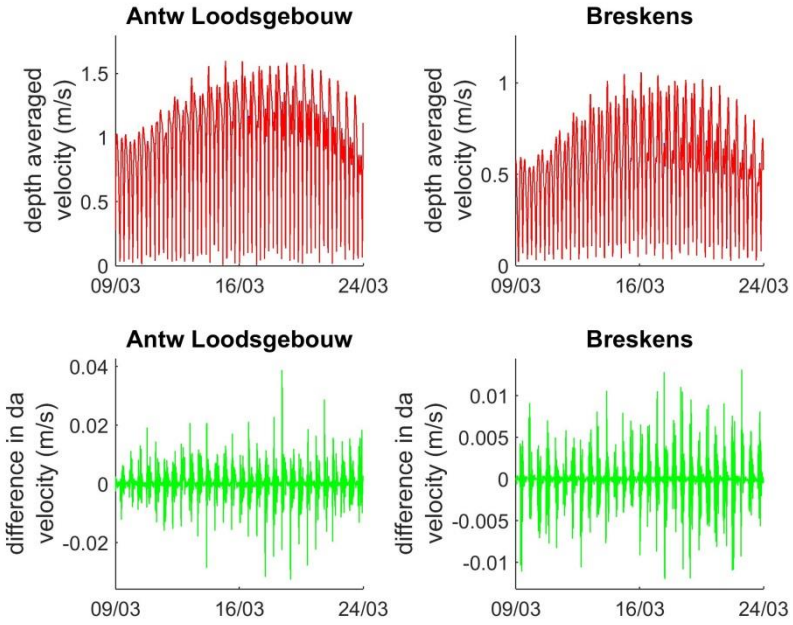


*Figure C.2 Modelled depth average velocities (upper plot) and difference between the depth average velocities (lower plot) with simulations based on the original computational grid (blue line, upper plot) and adjusted grid (red line, upper plot). Because the differences between the two simulations are so small, they are not observable in the upper plot*

## C.2 Spin-up

The Delft3D-NeVla model with the 2011 bathymetry requires a spin-up time to adjust itself to match the boundary and initial conditions. As the hydrodynamic processes develop faster from initial values into more realistic values compared to the morphology, this last aspect determines the required warm-up period. Because the study is not focussing on bed composition changes (e.g. redistribution of mud), the required spin-up period can be relatively short. Moreover, the visualisation method is meant as a tool to get a feeling/first insights about the sediment transport patterns in a certain system.

All in all, the spin-up period is used to remove irregularities in the bathymetry that are caused by errors in the measurements and interpolation. In this way, the sediment transport patterns depend less on the initial conditions and are better predictable. For this study, the spin-up period is realized by using loops of simulations. For each simulation, the morphological developments are determined based on 1 spring neap cycle without the effects of wind or waves. By setting the morphological factor at 25, the morphological developments are scaled up to yearly values. The initial conditions of a specific loop depend on the output of the previous run. The boundary conditions are similar for each run.

The cumulative erosion and sedimentation patterns of the different simulation loops are presented in Figure C.3. The largest redistribution of sediment occurs in the first loop. For the second and third simulation, the erosion-sedimentation patterns are already more smooth and quite similar. Although the model results still depend (till some extent) on the initial conditions, the developments are better predictable and of sufficient quality for the purpose of this study. Based on this and the fact that the bathymetry should also not deviate too much from the bathymetry that was measured in 2011, the spin-up period is set at three spring neap cycles.

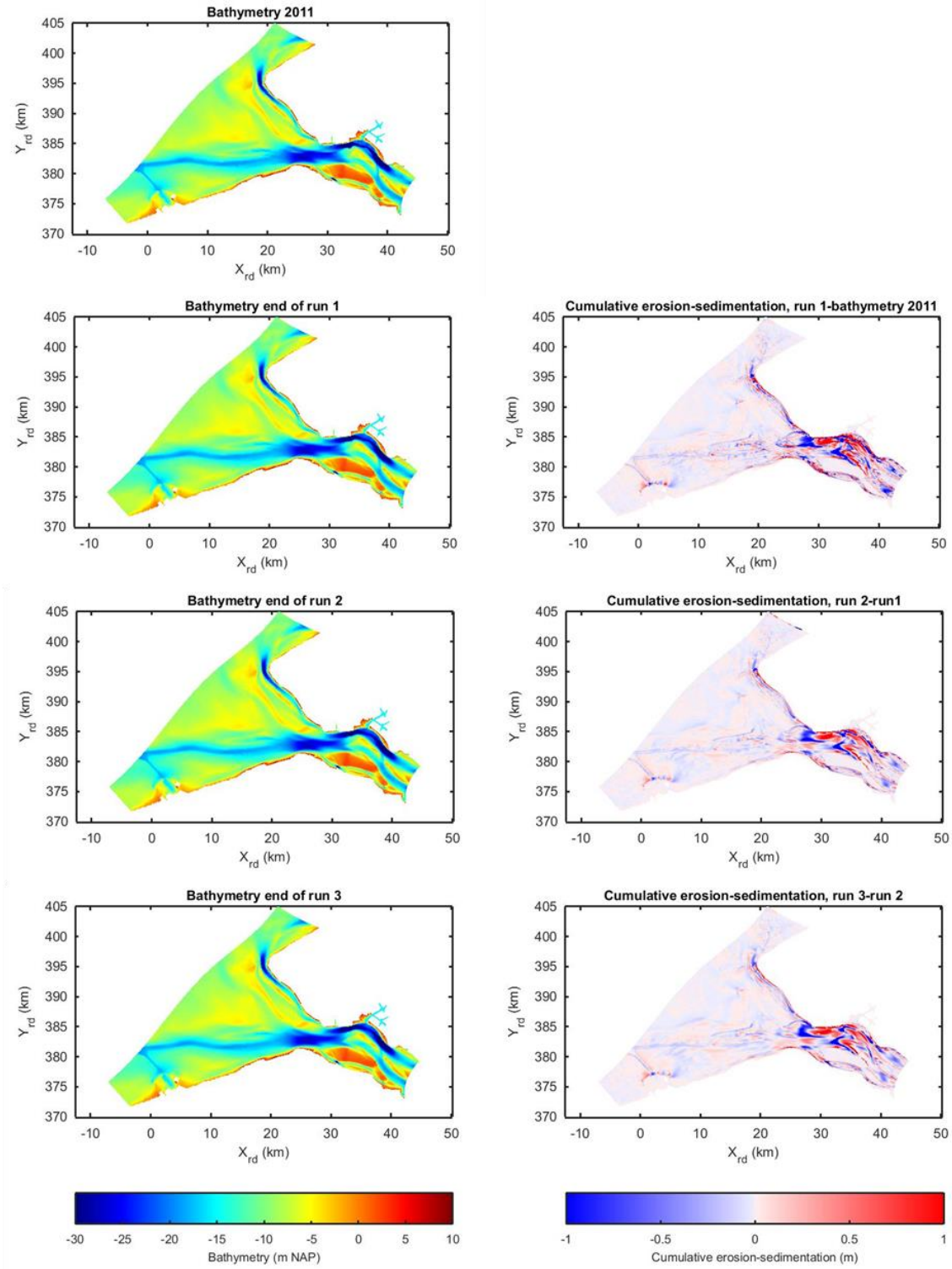


*Figure C.3 Left: bathymetries at different points in the simulation loops. Right: modelled erosion (blue) and sedimentation (red) patterns. With a morphological factor of 25, the bed level changes are scaled up to yearly values*

## C.3 Human interventions

The changes in the bathymetry due to the construction of the two human interventions are shown on Figure C.4.

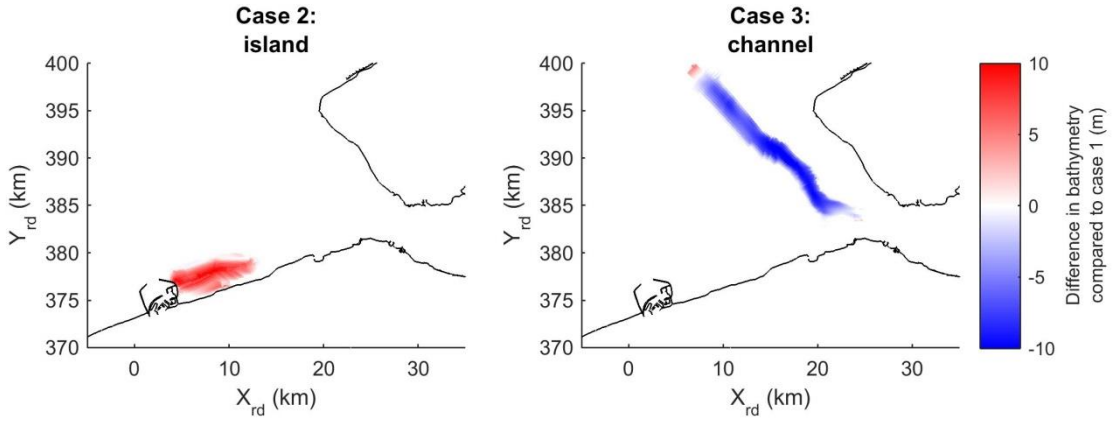


*Figure C.4 Changes in the bathymetry due to the construction of the two human interventions*

## C.4 Model results Delft3D-NeVla model

This section of the appendix includes all the figures that are related to the analysis of the hydrodynamics and sediment transports. This analysis itself is included in Section 5.3.

### C.4.1 Case 1: Bathymetry 2011

#### *C.4.1.1 Hydrodynamics*

Mean tidal range

Figure C.5 shows the mean tidal range (averaged over spring neap cycle) for a few locations in the mouth of the Scheldt estuary. For the moment, only consider the tidal ranges of case 1 (black numbers). The results show a decrease of the tidal range in the alongshore direction (towards the north). Furthermore, the tidal range increases in upstream direction.

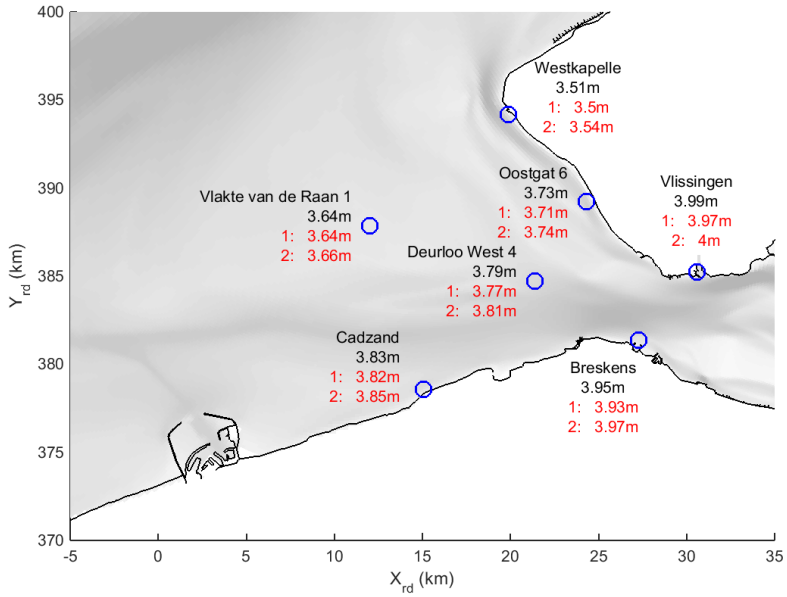


*Figure C.5 Mean tidal range. The black numbers indicate the tidal ranges in case 1 (bathymetry 2011). The red number represent the tidal ranges for cases 2 (island) and 3 (channel).*

Tidal asymmetry

Section 5.3 discusses the tidal asymmetry along three different channel systems: Wielingen-Scheur, Deurloo West-Geul van de Walvischstaart and Oostgat-Sardijngeul. For this analysis, a number of observation points on the channel axes are used. The observation points are shown in Figure C.6.

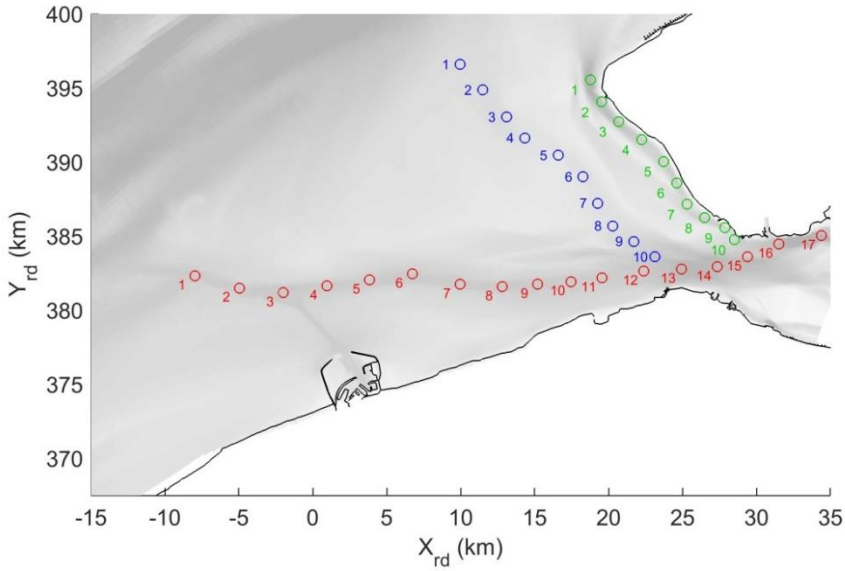


*Figure C.6 Observation points along the different channel axes that are used to study the tidal asymmetry.*

The amplitude of the $M_2$ component within the vertical tide is shown in Figure C.7. Whereas the construction of the island slightly lowers the amplitude, the amplitude increases with the constriction of the new navigation channel.

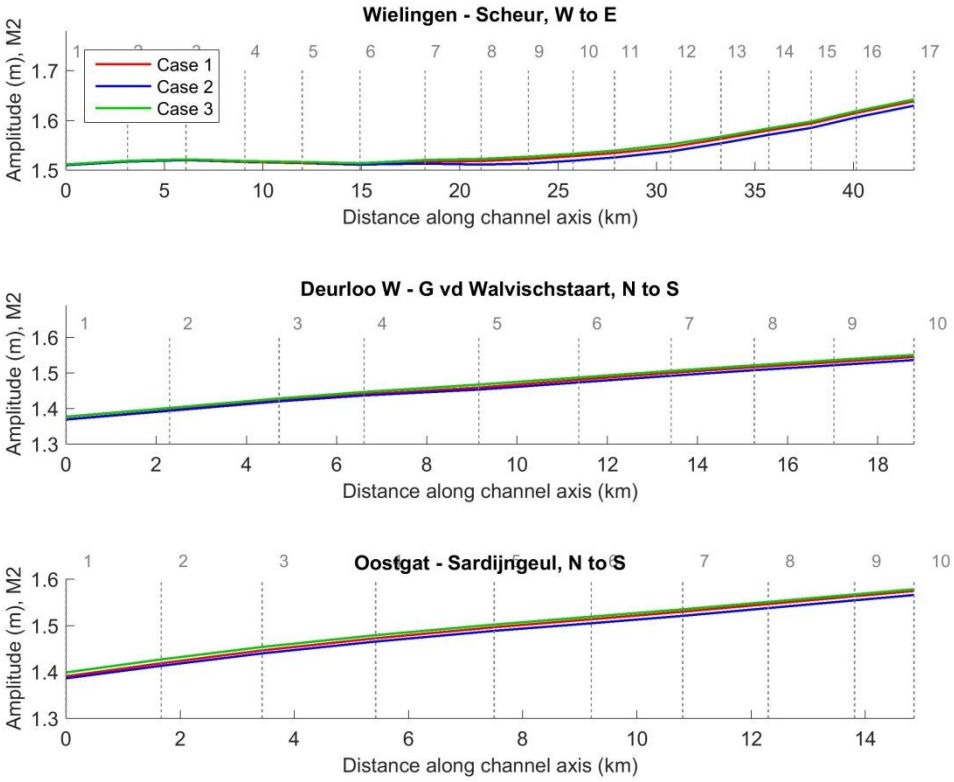


*Figure C.7 Amplitude of the $M_2$ component within the vertical tide, shown along different channel axes. The grey lines and numbers refer to the different observation points along the channel axes (see appendix C.4)*

Section 5.3.1.1 already discussed the phase differences of the $M_2$ and $M_4$ components in the vertical tide for case 1. Figure C.6 shows the amplitude ratios of these components. Figure C.9 shows the amplitude ratios of the two components within the time series of the horizontal tide. For this, only the flow velocities in the direction of the channel axes are considered (see Section 5.3.1.1).

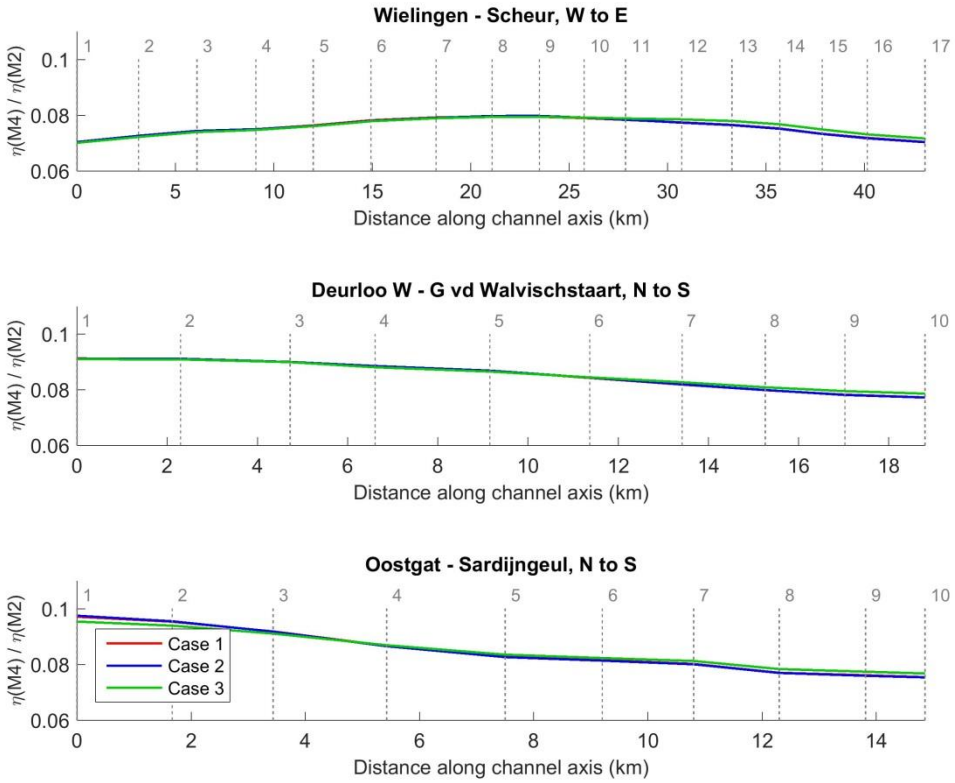


*Figure C.8 Amplitude ratio of $M_2$ and $M_4$ components within the vertical tide, shown along different channel axes. The grey lines and numbers refer to the different observation points along the channel axes (Figure C.6).*

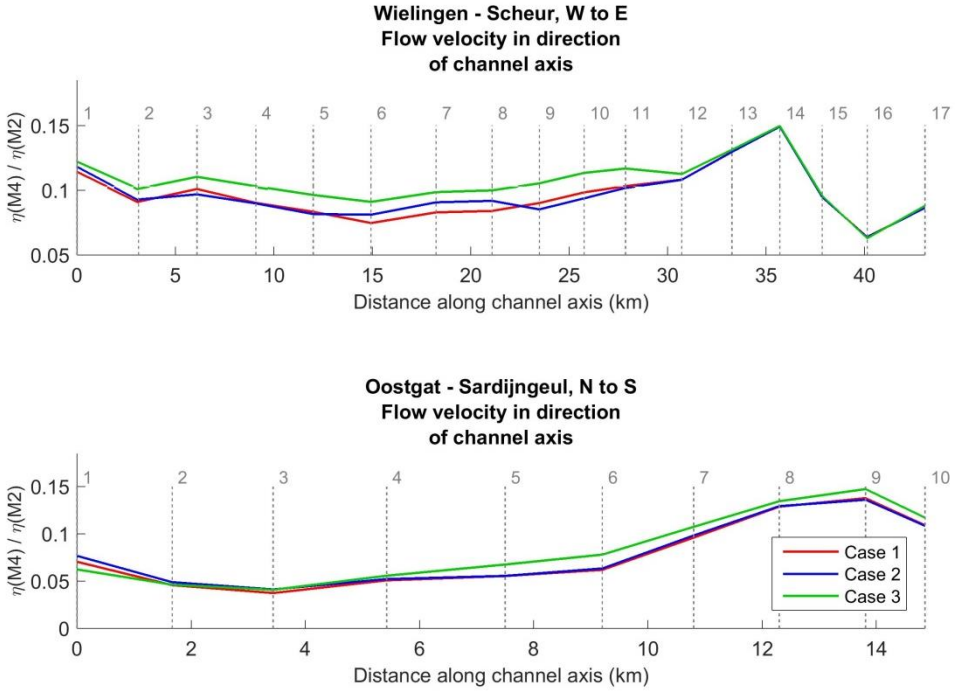


*Figure C.9 Amplitude ratio of $M_2$ and $M_4$ components within the flow velocity in the direction of the channel axis. , The grey lines and numbers refer to the different observation points along the channel axes (Figure C.6).*

As discussed in Section 5.3.1.1, one can perform a harmonic analysis on the original vector time series of the depth-averaged velocities. However, it is not possible to express the tidal asymmetry in these vector time series based the phase differences. As a solution, Section 5.3.1.1 proposed two alternatives. For both, the tidal velocities have to be reconstructed based on the $M_2$ and $M_4$ components.

First of all, the tidal asymmetry can be studied by visualizing the direction of the maximum reconstructed flow velocity. For the entire mouth, the results were already shown in Figure 5.10. Figure C.10 visualizes the same data, but zooms in at the area in front of Walcheren. Most of the areas show ebb dominance. For the northern part of the Oostgat, one can see differences between the coastward (ebb directed) and seaward side (flood directed) of the channel.

There is a second alternative. The flow velocities can be converted into instantaneous sediment transports, by making use of the simplified transport formula of Section 2.1.2 (Eq. 2.5 with f=1 and n=3). The tidal asymmetry can be determined by computing the residual value of the (reconstructed) sediment transports that occur during one tidal cycle. In this way, the simplified residual sediment transport gives an indication about the asymmetry in the depth-averaged velocities and takes into account the magnitude of the peak velocities and the duration of ebb and flood periods. The results are shown in Figure C.11 and are in line with the other findings of Section 5.3.1.1.

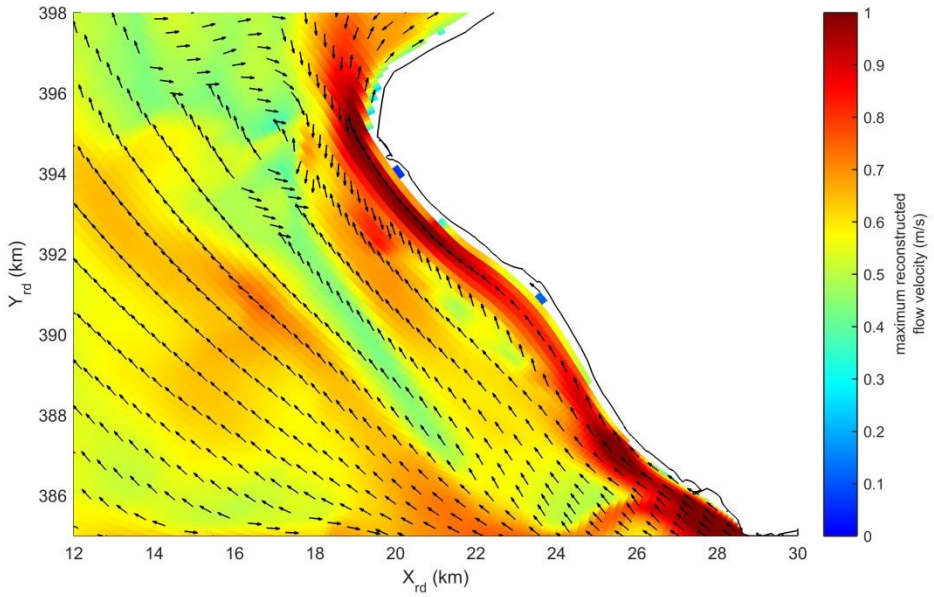


*Figure C.10 Maximum reconstructed flow velocity (based on $M_2$ and $M_4$). The map uses the same data as Figure 5.10, but zooms in at the area in front of Walcheren. The colormap indicates the magnitude of the maximum velocity. Arrows are normalized (equal length) and indicate the direction.*

### *C.4.1.2 Sediment transport*

Figure C.12 shows the mean total sediment transport through a cross-section in the Wielingen (see Figure C.14, it is the cross-section that starts at x=20 km and y=379 km) for the different $M_2$ periods within the spring neap cycle. As shown, the mean sediment transport through the cross-section alternates between ebb and flood-dominance for some period of the spring neap cycle. Movie 5.2 shows that this happens for multiple areas in the study domain.

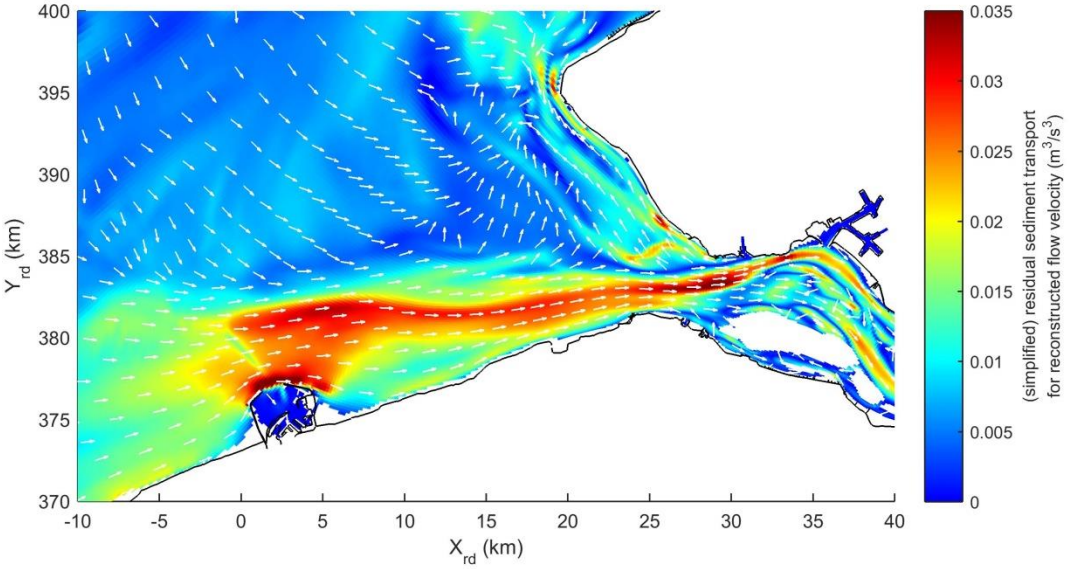


*Figure C.11 Residual transports that are computed based on the reconstructed flow velocities and the simplified transport formula Eq. 2.5 with f=1 and n=3. The colormap indicates the magnitude of the maximum velocity. Arrows are normalized (equal length) and indicate the direction.*

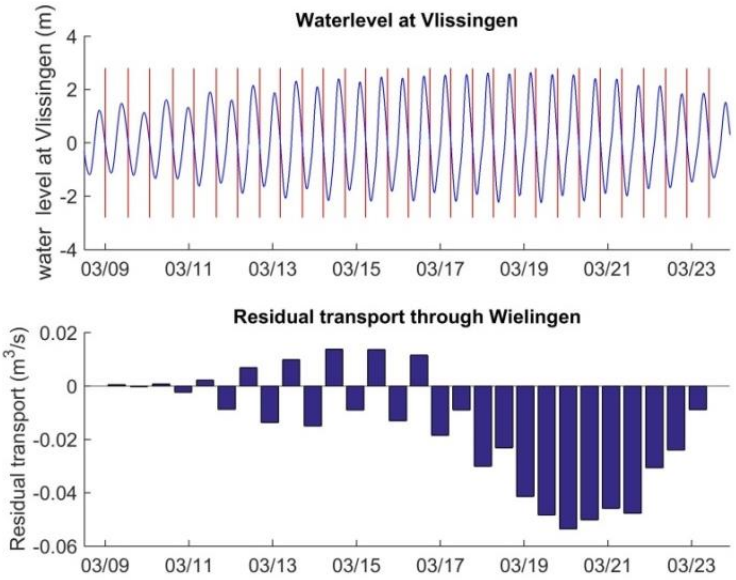


*Figure C.12 Upper: water level at Vlissingen during spring neap cycle. Lower: residual transport through Wielingen cross-section for the different $M_2$ periods*

Similar to flow velocities (Figure 5.4), also the variation in the direction of the total sediment transport at a certain can be expressed in ellipses. The results are shown in Figure C.13. The method that is used to construct these ellipses can be found in Section 5.3.1.2. Because of the non-linear relation between flow velocities and sediment transport, most of the ellipses are flatter compared to Figure 5.4

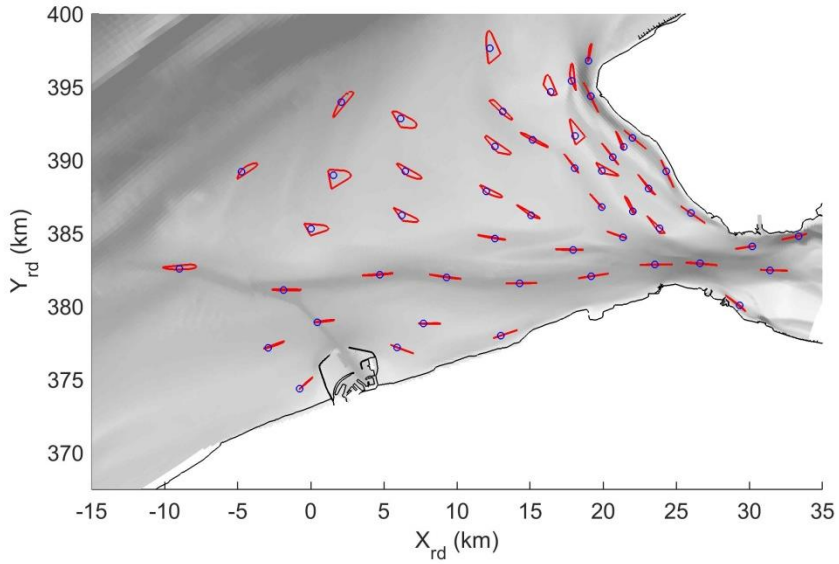


*Figure C.13 Tidal ellipses describing the total sediment transports (see Section 5.3.1.2 for the methodology that is used). The ellipses are normalized and therefore have a similar size. The blue dots present the measurement points.*

## C.4.2 Case 2: Island in front of Knokke-Heist

### *C.4.2.1 Hydrodynamics*

Mean tidal range

The tidal ranges within the mouth were already shown in Figure C.5. The effect of the new island in front Knokke-Heist on the tidal ranges is negligible. The vertical tide is the result of a large-scale tidal system that emerges due to the interaction of the tidal wave from the North Sea and the filling and emptying of the Western Scheldt. A relatively small morphological intervention does not affect this significantly.

Gross and net discharges

Section 5.3.2.1 already showed the relative changes in the gross discharges by comparing case 2 with case 1 (the reference case). Figure C.14 shows the absolute gross discharges for case 2.

Maximum flow velocities

Section 5.3.2.1 already discussed the absolute changes in the maximum flow velocities after the construction of the island in front of Knokke-Heist. Figure C.15 shows what the actual modelled maximum flow velocities for case 2. Figure C.16 shows the relative change in the maximum flow velocities (comparing cases 2 and 1).

Net flow velocities

The net flow velocities in case of case 2 are shown in Figure C.17. Figure C.18 and Figure C.19 show respectively the absolute and relative changes compared to case 1. The island mainly affects the net flow velocities in the surrounding area. Compared to the maximum flow velocities, the net flow velocities are small and sensitive for changes in the bathymetry. In line with previous observations, the net flow velocities at the seaward side of the island increase. The intervention also increases the flow velocities in the section of the Scheur in front of the island. For the Wielingen (northeast of Cadzand, between x=15 km and x=25), Geul van de Sluissche Hompels and the Spleet, a more complicated pattern emerges. While the magnitude of the net flow decreases in the south, it increases in the north. This is caused by

an interaction between the reduced discharge in this area and a decrease in the cross-sectional area near the island.

Tidal asymmetry

The amplitude ratios of the $M_2$ and $M_4$ components in the vertical and horizontal tides were already shown in Figure C.8 and Figure C.9.

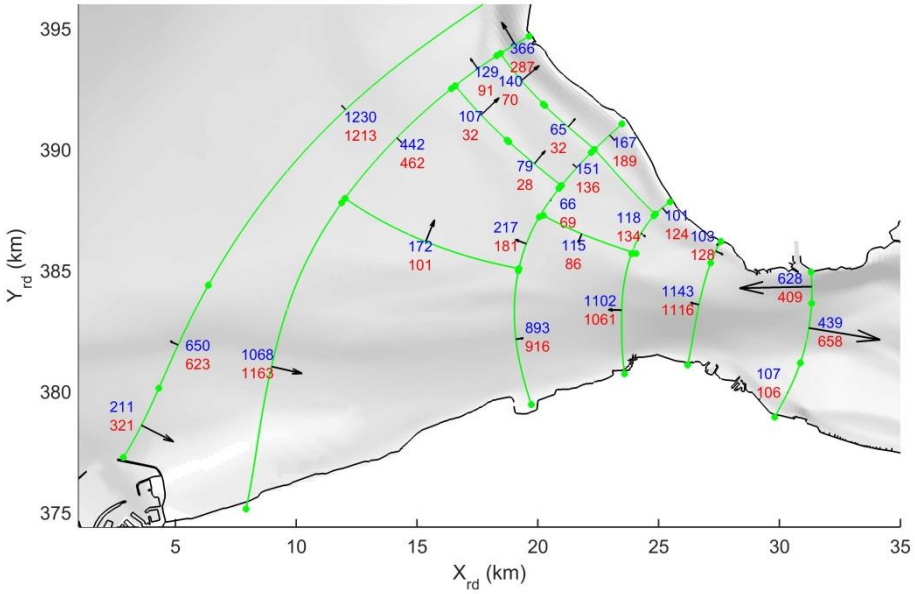


*Figure C.14 Gross discharges through cross-sections (million $m^3$/tide) for case 2 (averaged over spring neap cycle). The blue numbers indicate the flood discharges (west/south). The red numbers present the average discharge during ebb (east/north). The arrows represent the size and direction of the net discharge.*

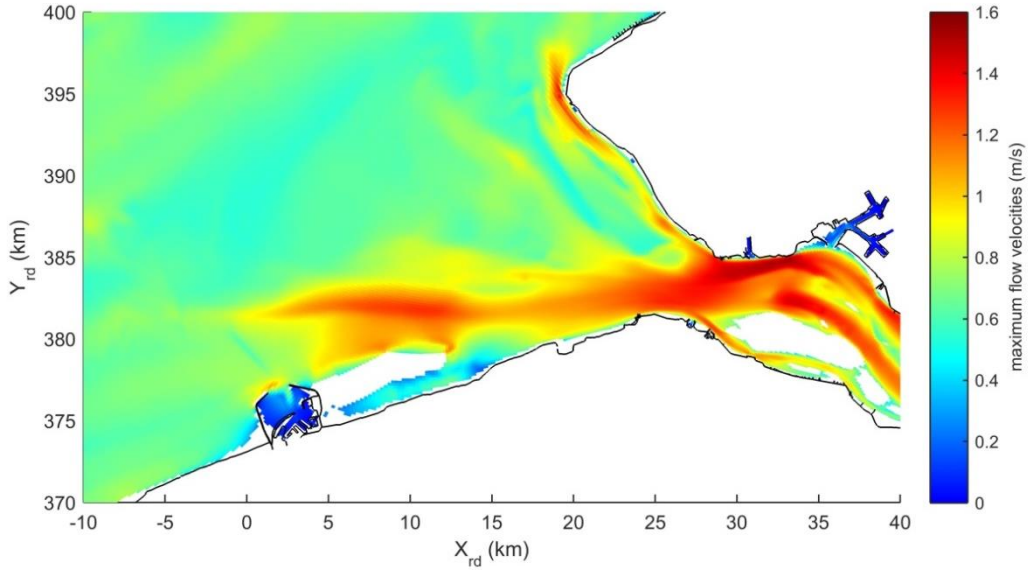


*Figure C.15 Maximum flow velocities for case 2. The velocities are computed by taking the average of the maximum flow velocities that are detected within the different $M_2$ periods of the spring neap cycle*

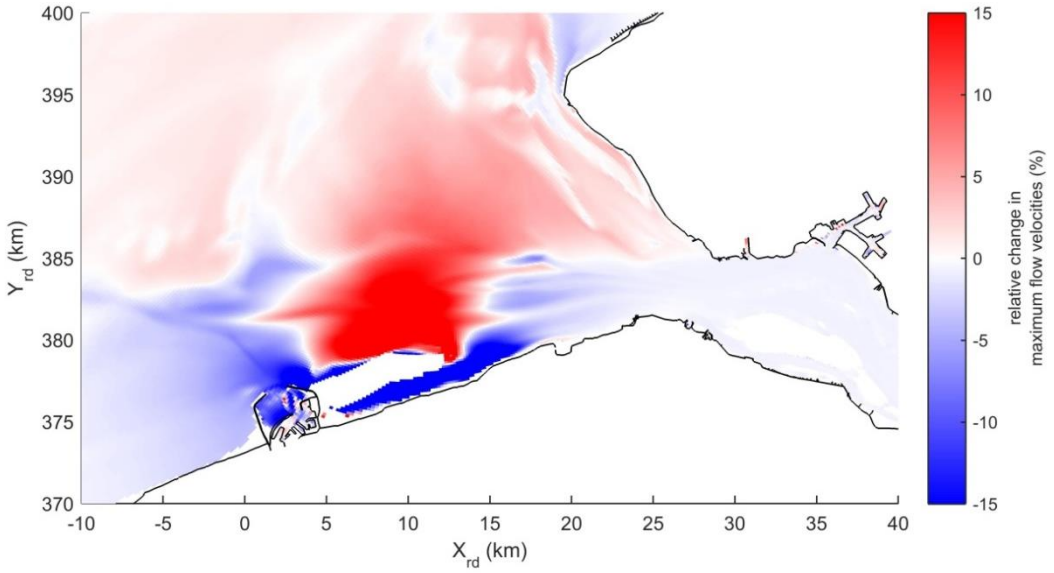


*Figure C.16 Relative change in the maximum flow velocities, case 2 compared to case 1. Red colors indicate higher maximum velocities; blue indicates lower maximum velocities.*

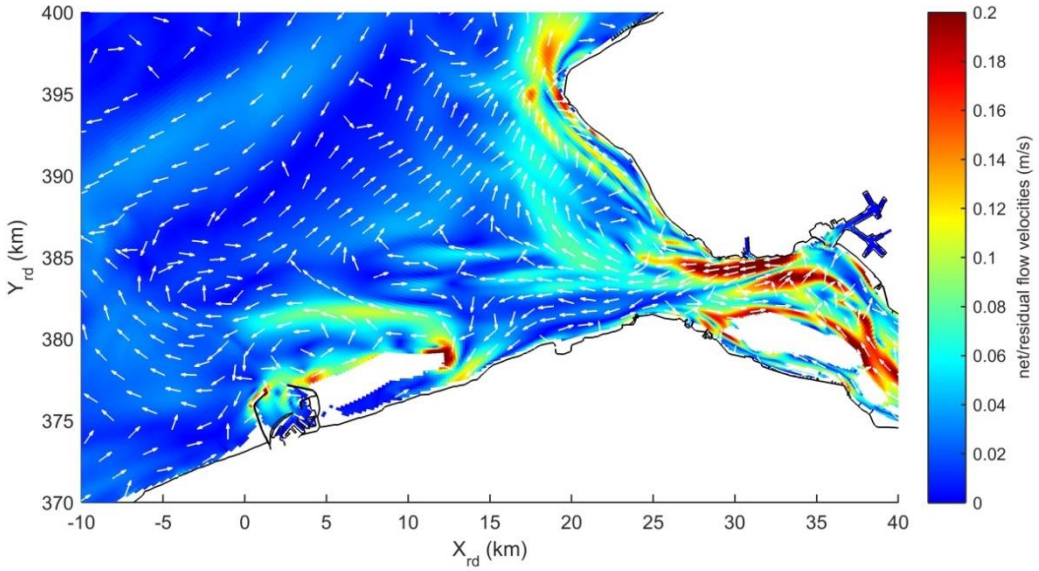


*Figure C.17 Net flow velocities for case 2. Arrows are normalized with the magnitudes (equal length) and only indicate the direction.*

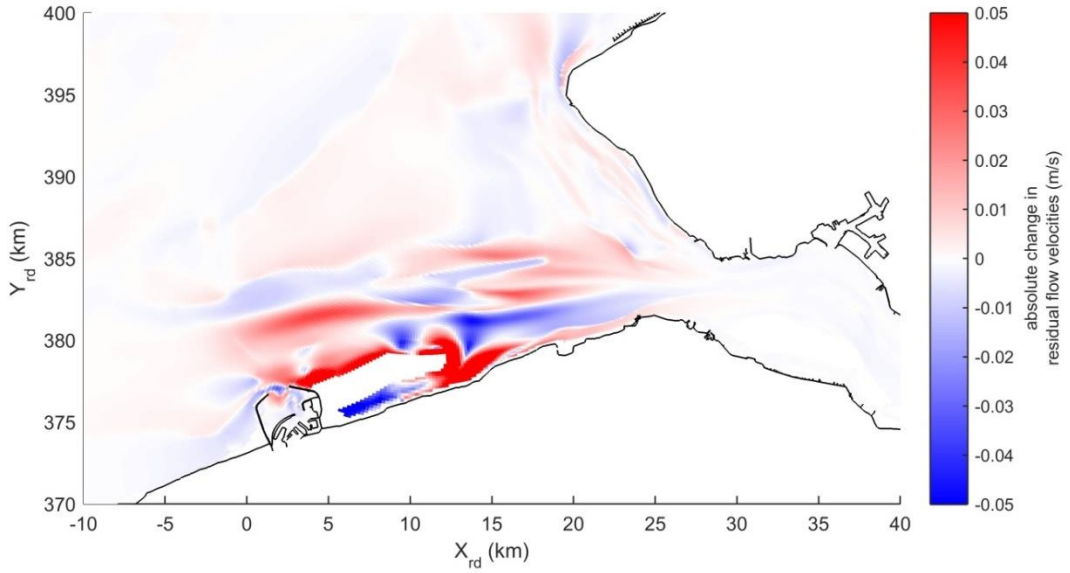


*Figure C.18 Absolute change in the net flow velocities, case 2 compared to case 1. Red colors indicate higher net flow velocities; blue indicates lower net flow velocities.*

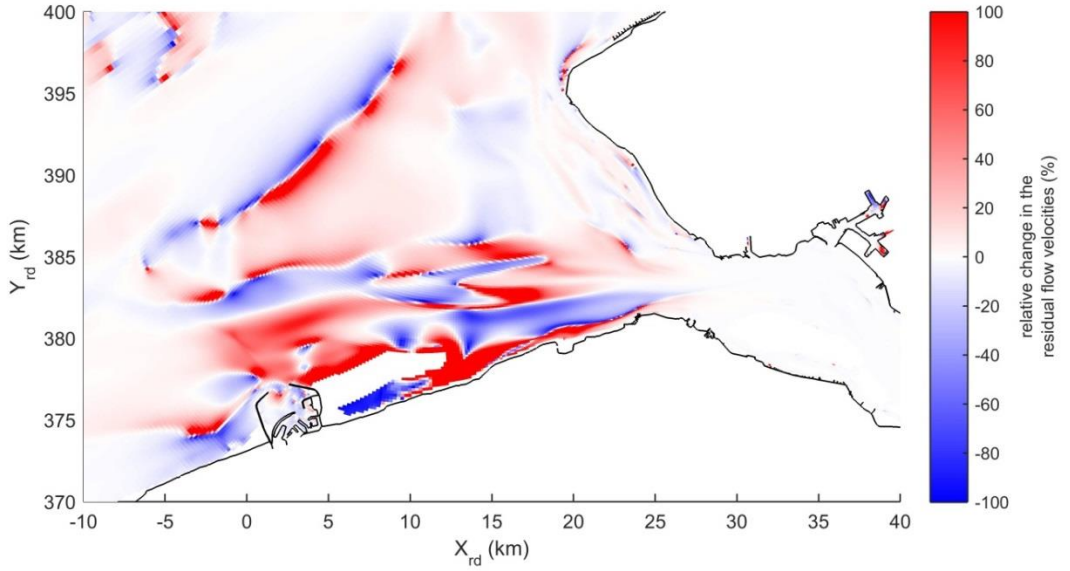


*Figure C.19 Relative change in the net flow velocities, case 2 compared to case 1. Red colors indicate higher net flow velocities; blue indicates lower net flow velocities.*

### *C.4.2.2 Residual sediment transport*

The residual transports for case 2 were already shown in Figure 5.18 (main report). As was also done for case 1, the spatial variations in the direction of the residual sediment transport can also be visualized with a colormap (Figure C.20). Figure C.21 and Figure C.22 show respectively the absolute and relative changes in the residual sediment transport. The colorscale are used to indicate the change in the magnitude. The arrows (normalized) describe the direction in which the residual transport has changed.

The results demonstrate that the island affects the magnitudes over a large area (even within the Western Scheldt). The increase in the residual sediment transports north-northeast of the island correspond with the increased maximum flow velocities. The lower maximum flow velocities in the middle section of the Wielingen and west of Zeebrugge result in lower residual sediment transports.

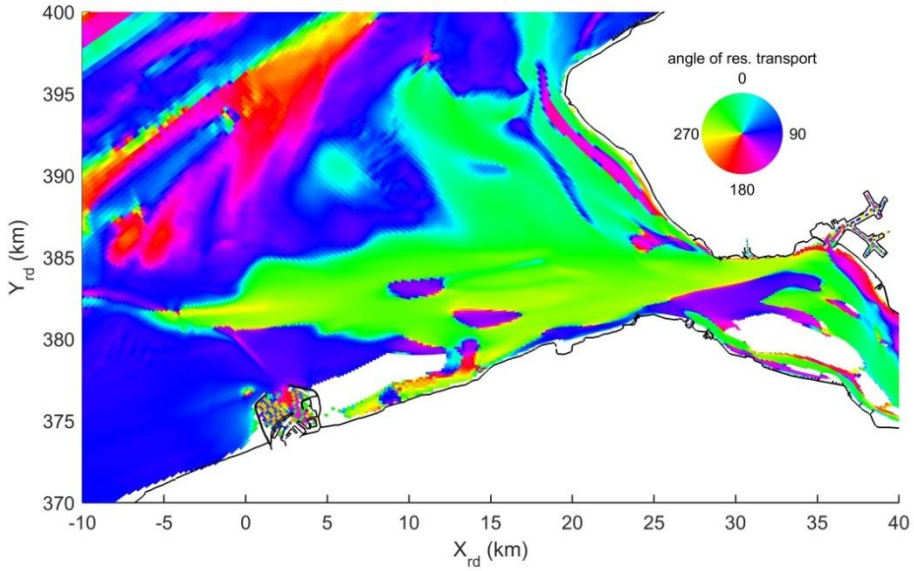


*Figure C.20 Direction of the residual sediment transport (computed for one spring-neap cycle) for case 2. The map describes the same dataset as Figure 5.11, but just uses colorscale to visualize the directions of the vectors.*

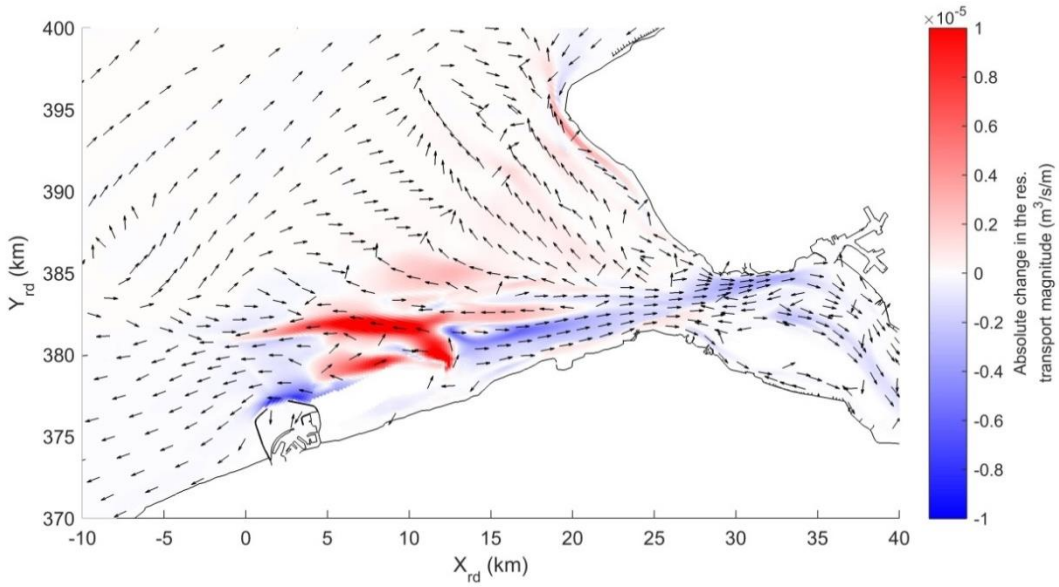


*Figure C.21 Absolute change in the residual transport (over one spring neap cycle), case 2 compared to case 1.The colormap indicates the change in the magnitude. Arrows are normalized (have an equal length) and only indicate the direction in which the residual transport changed*

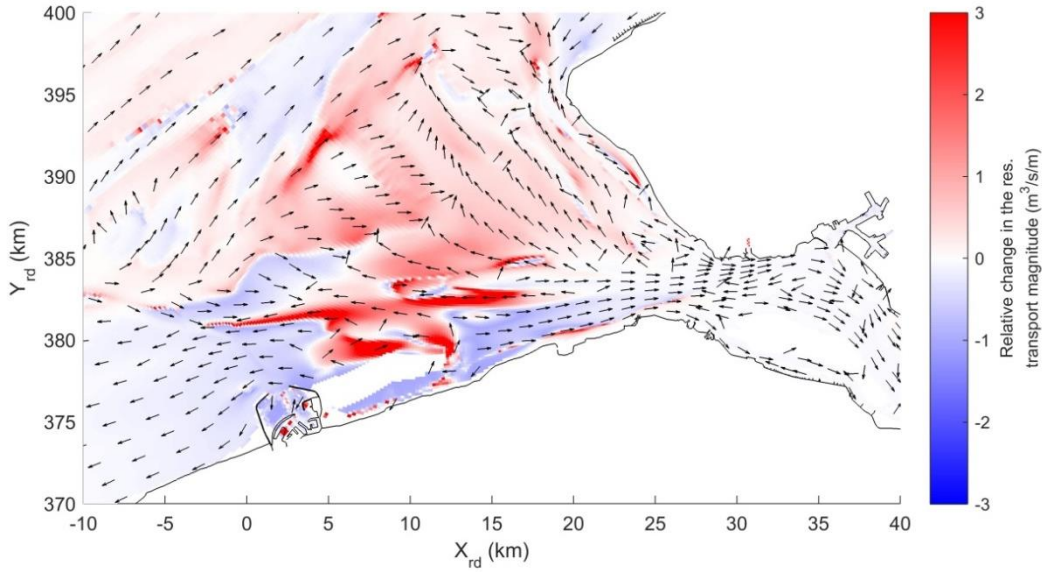


*Figure C.22 Relative change in the residual transport (over one spring neap cycle), case 2 compared to case 1.The colormap indicates the change in the magnitude. Arrows are normalized (have an equal length) and only indicate the direction in which the residual transport changed*

### *C.4.2.3 Erosion-sedimentation patterns*

Figure C.23 compares the erosion-sedimentation patterns of cases 1 and 2. Changes in the patterns can be mainly observed near the new island. In front of the island, one can find three distinctive areas with large differences in the bed thickness changes. The sedimentation in the Wielingen increase while the Pas van het Zand shows a decrease.

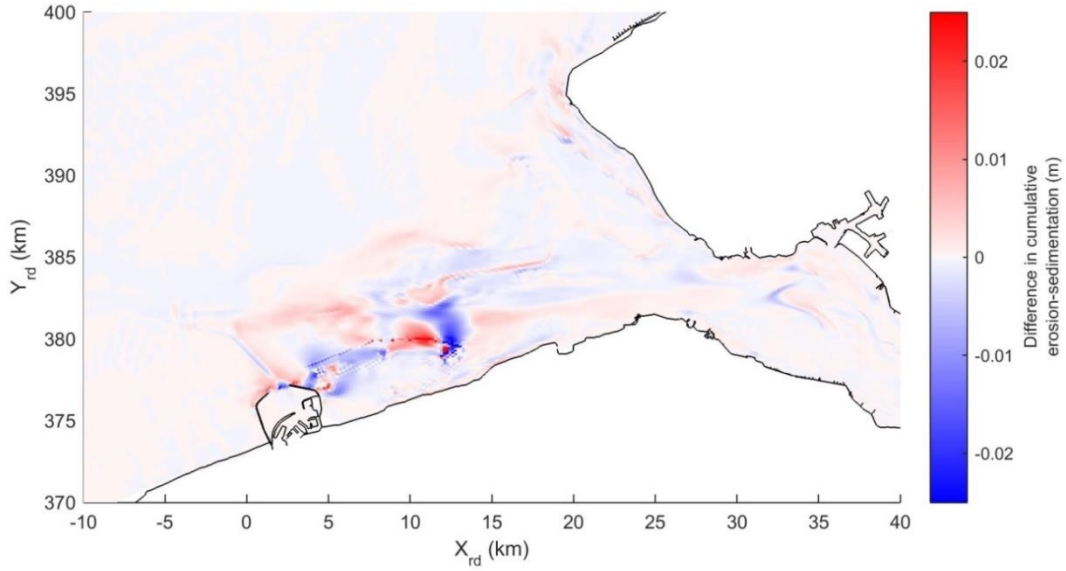


*Figure C.23 Difference between the erosion/sedimentation of cases 1 and 2. Red colors indicate relatively more (less) sedimentation (erosion) in case 2. Blue colors indicate less (more) erosion (sedimentation).*

## C.4.3 Case 3: Extension of the Geul van de Walvischstaart

### *C.4.3.1 Hydrodynamics*

Mean tidal range

Also for the third case, the changes in the tidal range are very small (Figure C.5).

Gross and net discharges

Figure C.24 shows the absolute gross discharges for case 2.

Maximum flow velocities

Figure C.25 shows what the actual modelled maximum flow velocities for case 3. Figure C.26 shows the relative change in the maximum flow velocities by comparing cases 3 and 1.

Net flow velocities

The net flow velocities for case 3 are shown in Figure C.27. In terms of the relative changes compared to case 1 (Figure C.29), the new navigation channel affects a larger area. In absolute sense however (Figure C.28), the net flow mainly changes in the Geul van de Walvischstaarts and the direct surrounding area. The results shows that the flow is now more oriented in the direction of the new channel. In this way, the circulation cell through/over the Rassen, Deurloo Oost, Elleboog, Nolleplaat and the new channel gets a more oval shape. This was also observed by Tonnon & van der Werf (2014). The new channel reduces the net flows in the Wielingen and Oostgat.

Tidal asymmetry

The amplitude ratios of the $M_2$ and $M_4$ components in the vertical and horizontal tides were already shown in Figure C.8 and Figure C.9.

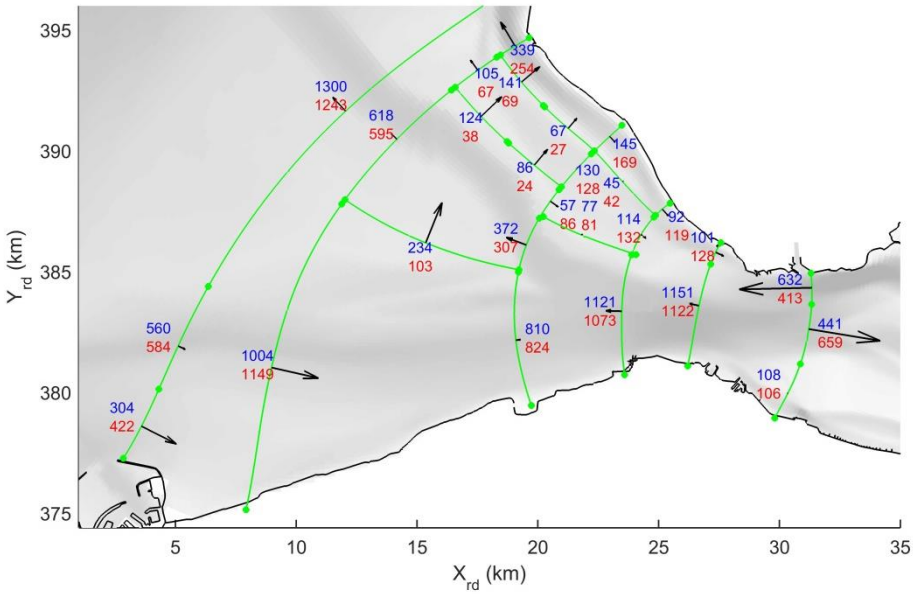


*Figure C.24 Gross discharges through cross-sections (million $m^3$/tide) for case 3 (averaged over spring neap cycle). The blue numbers indicate the flood discharges (west/south). The red numbers present the average discharge during ebb (east/north). The arrows represent the size and direction of the net discharge.*

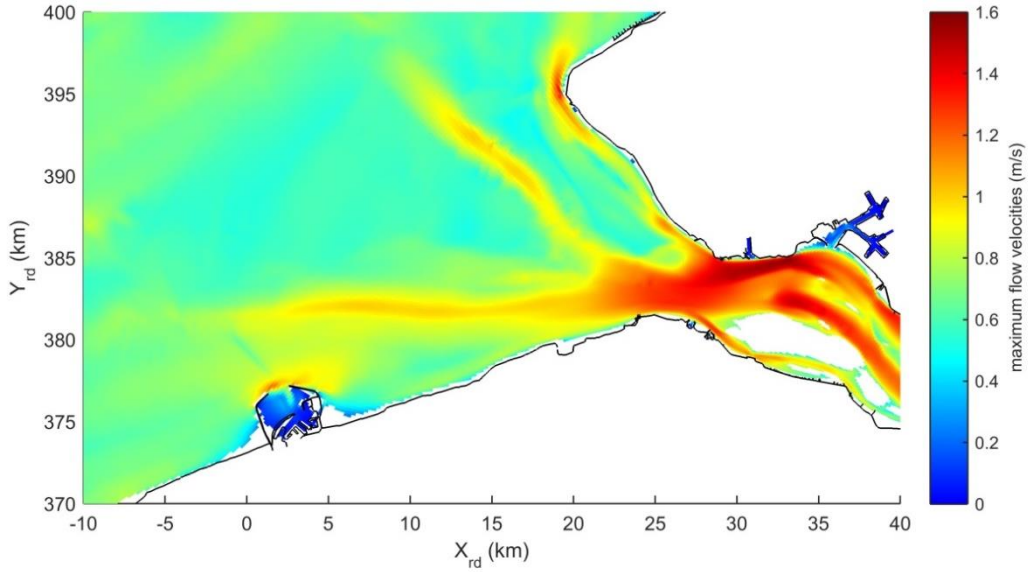


*Figure C.25 Maximum flow velocities for case 3. The velocities are computed by taking the average of the maximum flow velocities that are detected within the different $M_2$ periods of the spring neap cycle*

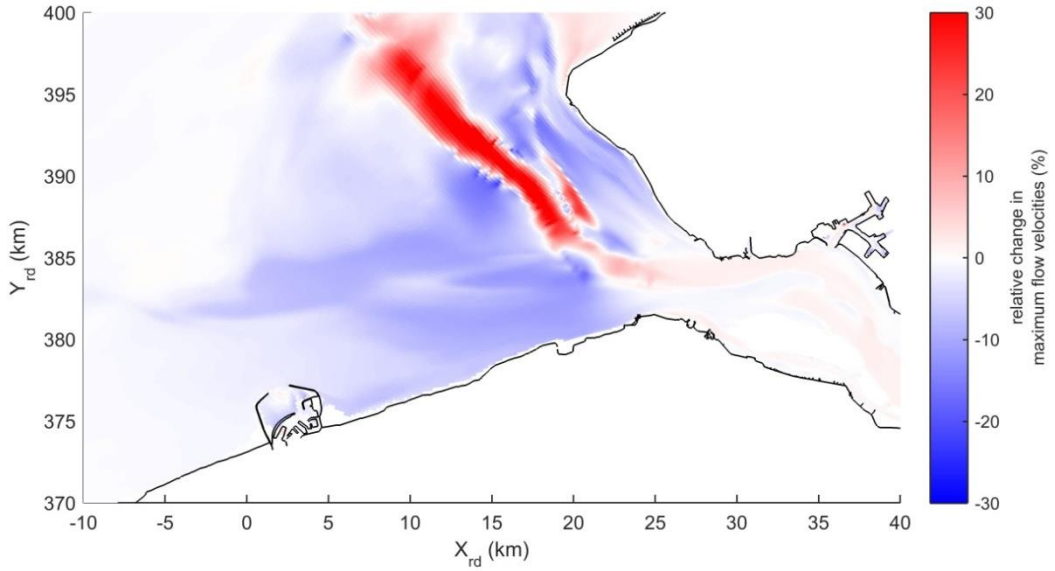


*Figure C.26 Relative change in the maximum flow velocities, case 3 compared to case 1. Red colors indicate higher maximum velocities; blue indicates lower maximum velocities.*

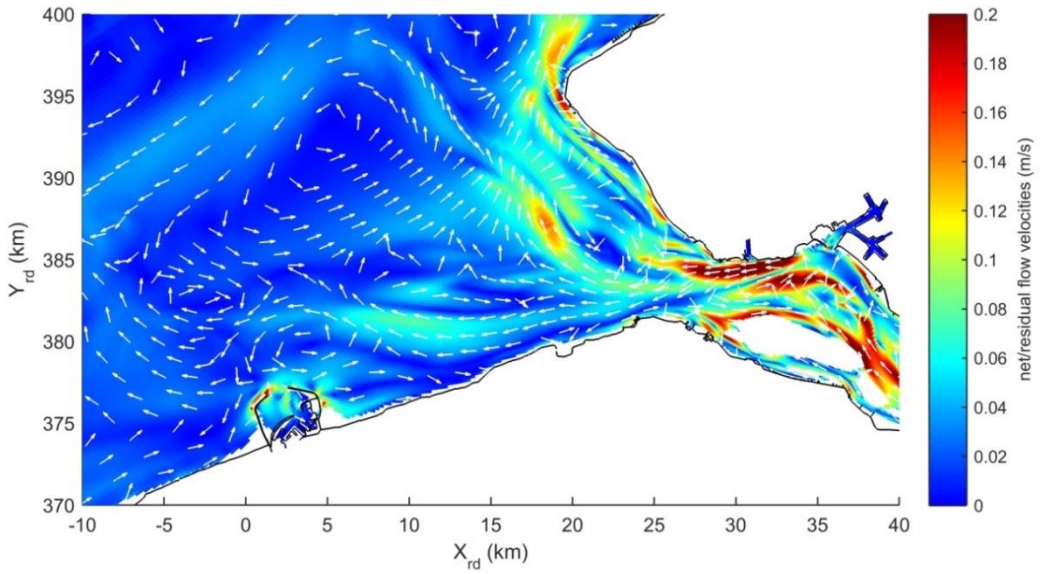


*Figure C.27 Net flow velocities for case 3. Arrows are normalized with the magnitudes (equal length) and only indicate the direction.*

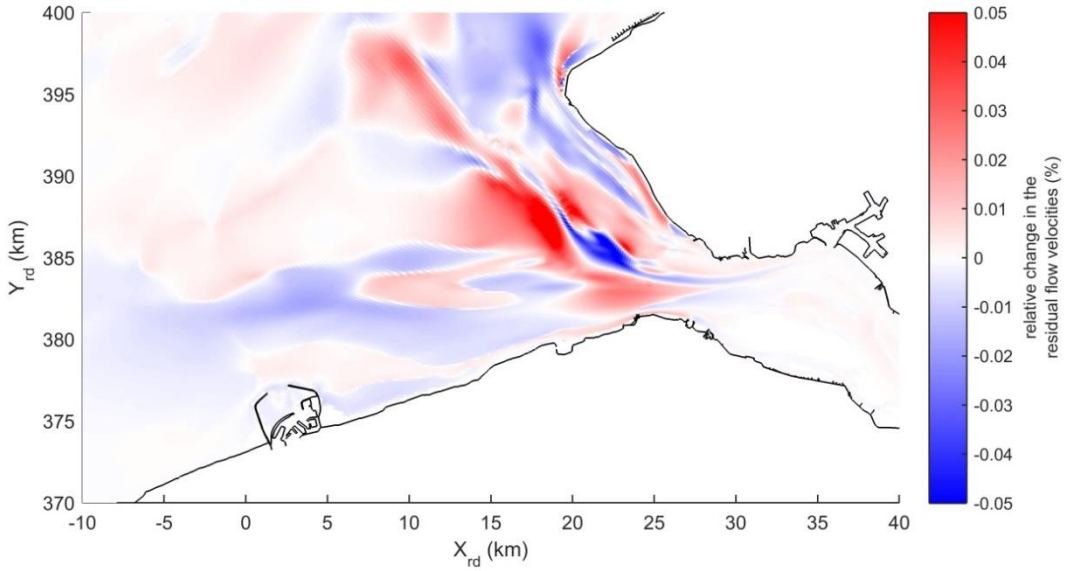


*Figure C.28 Absolute change in the net flow velocities, case 3 compared to case 1. Red colors indicate higher net flow velocities; blue indicates lower net flow velocities.*

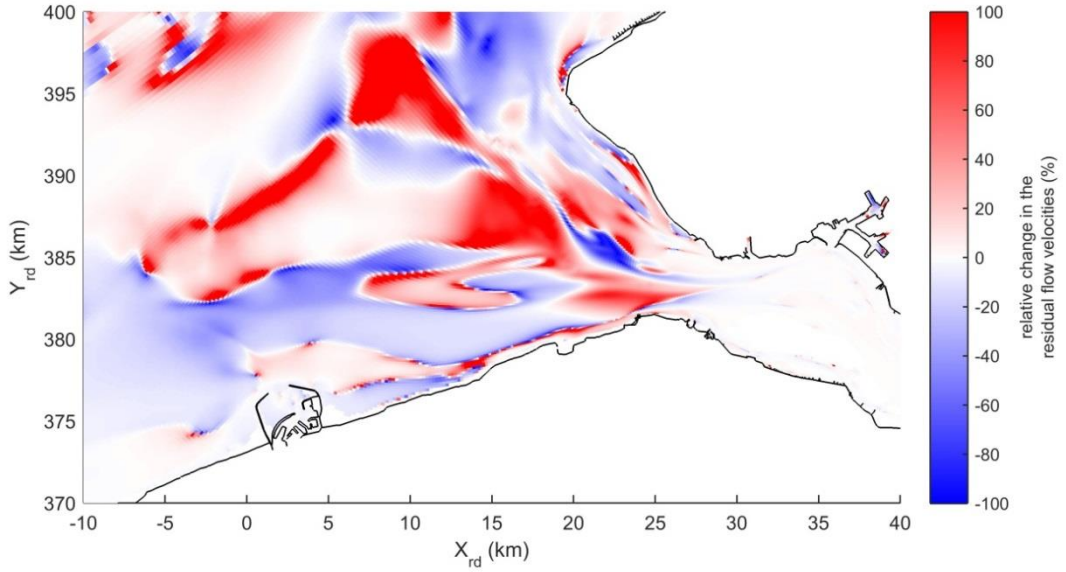


*Figure C.29 Relative change in the net flow velocities, case 3 compared to case 1. Red colors indicate higher net flow velocities; blue indicates lower net flow velocities.*

### *C.4.3.2 Residual sediment transport*

The directions of the residual sediment transports in case of case 3 are visualized with a colormap (Figure C.30). The new navigation channel connects the Geul van de Walvischstaart and Deurloo West. The channels still have ebb-dominant residual transport after the navigation channel is constructed. If we compare it Figure 5.12, we can see that the ebb-dominance has extended towards the north. The extension of the Geul van de Walvischstaart also changes the direction of the residual transport just north of the Wielingen (x = 15 km, south of Geul van de Sluissche Hompels). Here the residual transport is now directed towards the west/southwest. At the northern end of the Geul van de Rassen, the area with ebb-directed residual transport growths.

The effect of the intervention is also studied by subtracting the residual transports of case 1 from the residual transports of case 3. The absolute differences in residual transport are shown in Figure C.31. Figure C.32 shows the relative change in the residual transport. The different maps show that the change in the residual transport for the new navigation channel is ebb directed. In other words, the ebb-dominance is strengthened. For the Wielingen, Geul van de Sluissche Hompels, Deurloo Oost and the northern part of the Oostgat, the effect of the new navigation channel on the residual transport is flood directed. For the ebb-channels in the Western Scheldt, the ebb-dominance increases. All of this corresponds with the analysis of the hydrodynamics. The new channel is discharging water for the filling and emptying of the Western Scheldt. Because of the high velocities (low bed shear stress), flow is sucked into this new channel.

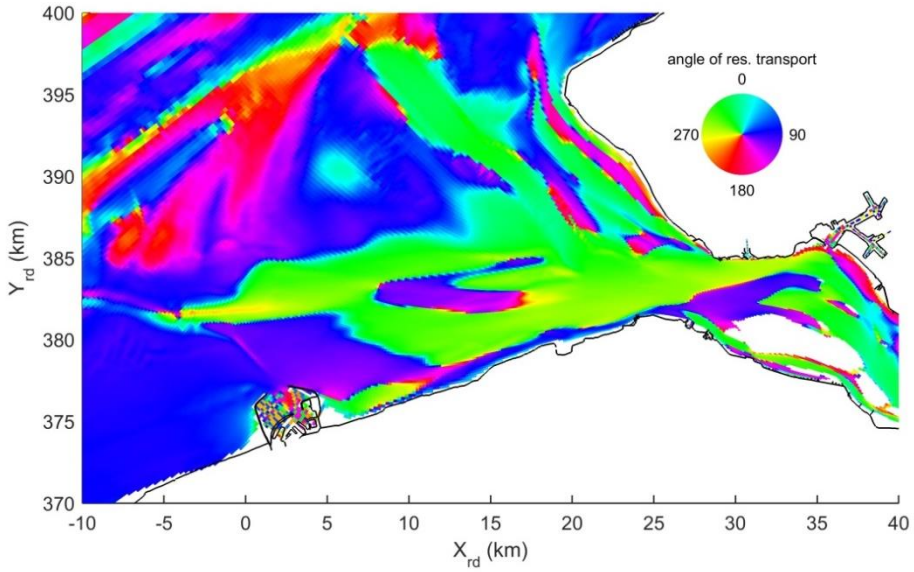


*Figure C.30 Direction of the residual sediment transport (computed for one spring-neap cycle) for case 3. The map describes the same dataset as Figure 5.18, but just uses colorscale to visualize the directions of the vectors.*

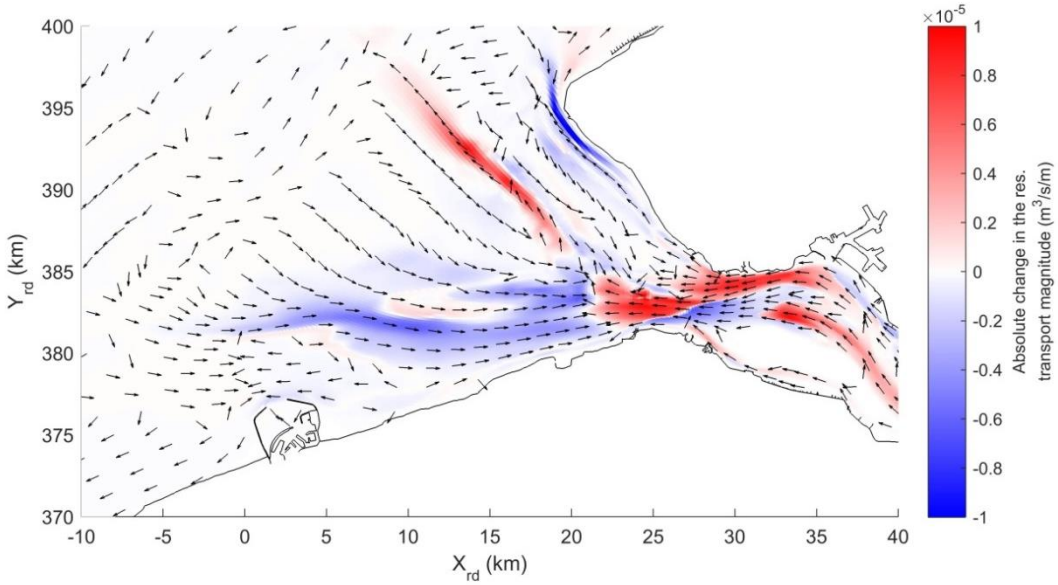


*Figure C.31 Absolute change in the residual transport (over one spring neap cycle), case 3 compared to case 1.The colormap indicates the change in the magnitude. Arrows are normalized (have an equal length) and only indicate the direction in which the residual transport changed*

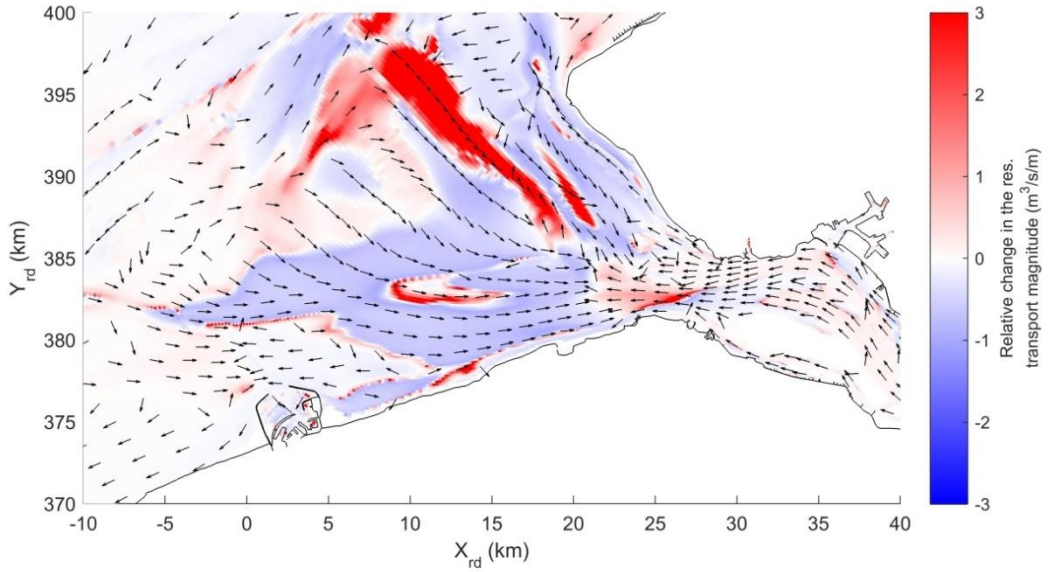


*Figure C.32 Relative change in the residual transport (over one spring neap cycle), case 3 compared to case 1.The colormap indicates the change in the magnitude. Arrows are normalized (have an equal length) and only indicate the direction in which the residual transport changed*

### *C.4.3.3 Erosion-sedimentation patterns*

Figure C.33 compares the erosion-sedimentation patterns of cases 1 and 3. The main difference is located at the meeting point of the Geul van de Walvischstaart and the Wielingen. With the new navigation channel, there is a large area with high erosion rates.

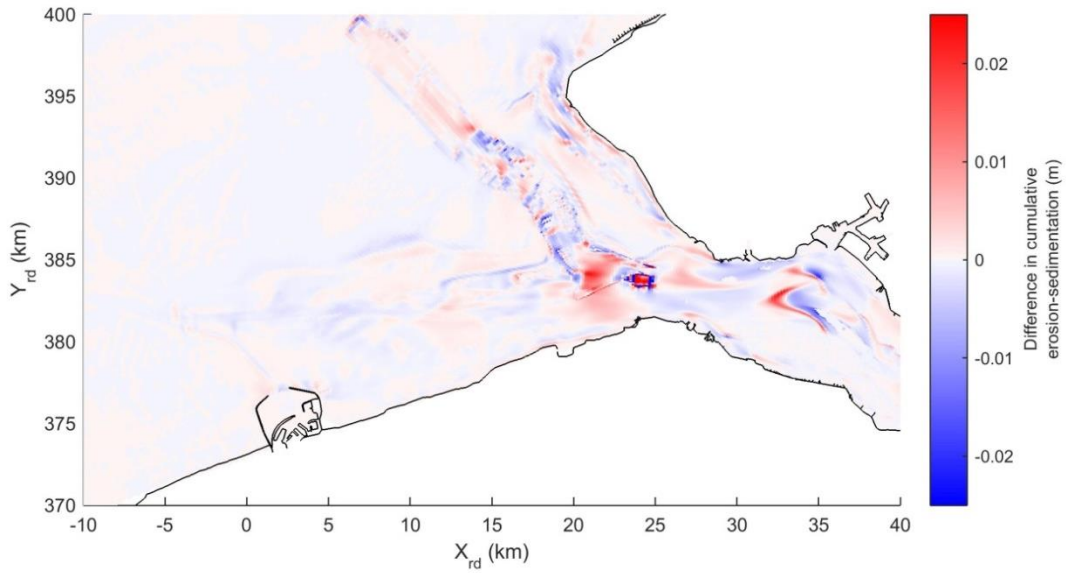


*Figure C.33 Difference between the erosion/sedimentation of cases 1 and 3. Red colors indicate relatively more (less) sedimentation (erosion) in case 3. Blue colors indicate less (more) erosion (sedimentation).*

# D Appendix of Chapter 6 - Sediment transport pathways in the mouth of the Scheldt estuary

## D.1 Acceleration coefficient

The spatial variation in the acceleration coefficient is shown Figure D.1. This coefficient is calculated following the method discussed in Section 3.3.3 (with n=5, reference height of 1 cm) and is based on the total sediment transports within the spring-neap cycle. Following the methodology discussed in the main report, the visualisation tool has to be based on a single acceleration coefficient that is used for the entire study domain and simulation period. For the mouth of the Scheldt, the maximum transport velocities are found near the inlet of the Western Scheldt. Based on this representative area (grey area in the subplot of Figure D.1), an acceleration coefficient of 1600 $m^{-1}$ is seems to be legitimate for the application of the visualisation tool for the mouth area.

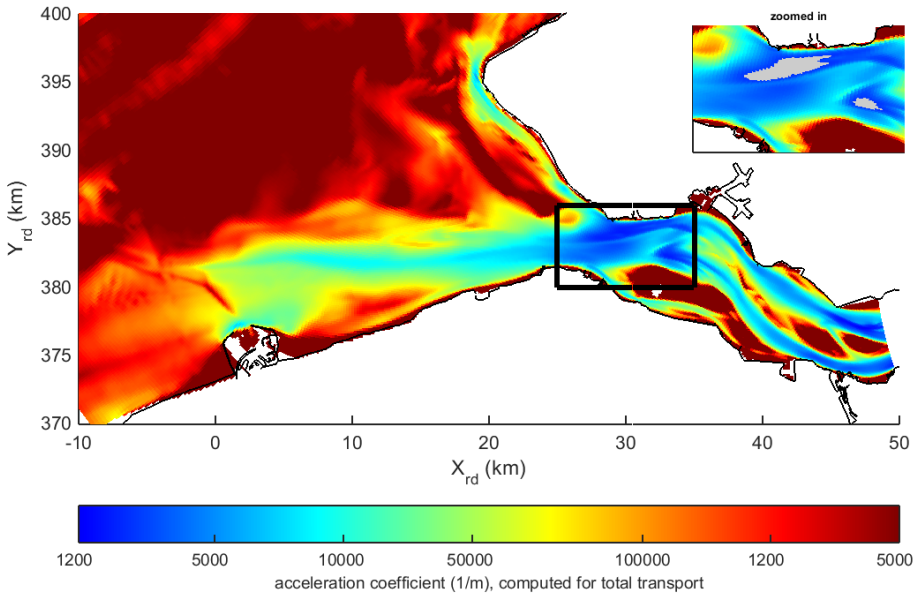


*Figure D.1 Calculated acceleration coefficient, based on the peak bed and suspended load sediment transports detected within the spring-neap cycle. The upper right corner zooms in on the area near the inlet of the Western Scheldt. The grey area describes the grid cells with an acceleration coefficient between 1200 and 1600 $m^{-1}$. See Section 3.3.3 for more information about the derivation of the acceleration coefficient.*

## D.2 Time step for particle movement calculations

As stated in Section 3.3.2, $\Delta t_{pm}$ has to be smaller than $\Delta t_{d3d-output}$ (15 min). Looking to the entire study area, the SN number indicates a maximum time step of 37 seconds. Depending on the location of the particles, the time step could be smaller or larger. When choosing the time step, one has to take into account both the numerical error of the RK4 method and the computational time of the tool.

In this appendix, the time step will be analysed for two areas: the inlet (near Vlissingen-Breskens) and the Wielingen-Scheur. The inlet contains the highest transport velocities and largest spatial gradients. For both cases, the particles are released from group of start locations (divided over the cross-section). For each of these locations, 1 particle is released every 45 minutes for a period of 1 spring-neap cycle. After this, no more particles are added. The total simulation period is 3 spring-neap cycles (~43 days).

D.2.1 Time step for particle movement calculations in the inlet of the mouth

9 start locations are divided over the cross-section of the inlet (green dots in Figure D.2). With the statistics mentioned above, this results in a total 4158 numerical particles that are followed. Assume that the simulation with a $\Delta t_{pm}$ = 1 second contains no numerical error and can be used as reference case. Compared to the time step of the Delft3D model (7.5 seconds), this quite small. With this time step, the particle displacement that is detected within the simulation period is about 2 metres.

Figure D.2 shows the maps of the tracer concentrations after 3 spring neap cycles computed with time steps of 1 and 150 second(s). An analysis of this spatial pattern in relation to the hydrodynamics and configuration of the different channels and shoals is discussed in 6.1.1.5. Here, the analysis focuses on the effect of $\Delta t_{pm}$ on the dispersal of numerical tracers. A visual comparison of the maps indicates that the effect of $\Delta t_{pm}$ is limited. They are almost identical.

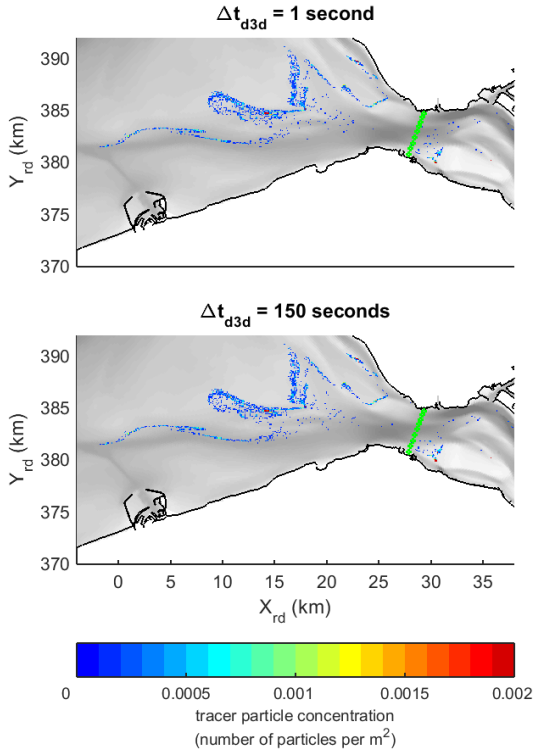


*Figure D.2 Maps of tracer particle concentrations after 3 spring neap cycles, computed with different time steps for the particle movement calculations. The green dots indicate the start locations in the inlet (9 locations).*

However, an analysis of the individual pathways results in different conclusions. The left subplot of Figure D.3 shows the percentage of particles that deviated less than a distance X (referred to as error E) from the reference pathway somewhere during the simulation. This is done for different time steps. For each of the 4158 particles, the pathway is compared with pathway of the identical twin in the reference case (similar release time and release location). Subsequently, the maximum deviation of this particle is compared with the error E. Summarized, the different lines in figure Figure D.3 describe the percentage of particles that have an error in the pathway that is smaller than error E.

At first, consider the case of $\Delta t_{pm}$ = 2.5 seconds. The subplot shows that more than 80% of the particles have an error smaller than 10 metres. In other words, they always stay within 10 metres from the reference pathway. With a large error E (e.g. 5000 m) this is percentage is of course higher. However, the results show that the percentage is never higher than about 98.4%. In other words, the pathways of some particles are very sensitive for changes in $\Delta t_{pm}$.

Although the increase in the time step compared to the reference case is very small, the pathways of some particles deviate a lot.

If we now look to the differences between the cases, it is clear that the errors in the pathways (deviations compared to the reference case) increase with larger time steps. With these larger steps, the translation of the spatial variations in the transport fields into the transport pathways is worse and the prediction of the tracer dispersal becomes less accurate. To give an example: with a time step of 2.5 seconds, 92% of the particles always stay always within 100 meters from the reference pathway. With a time step of time step of 30 seconds, this is reduced to 82%. With a time step of 150 seconds, only 68% of the particles have an error smaller than 100 metres. For this large time step, even 19% of the particles are able to deviate more than 1000 metres from the reference path somewhere during the simulation.

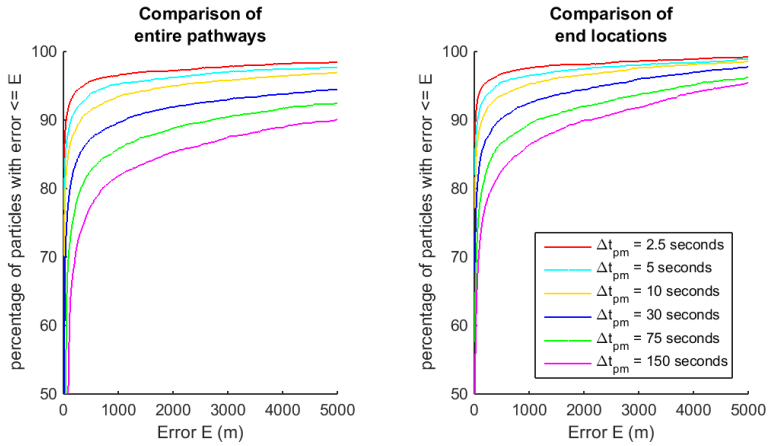


*Figure D.3 Left: Percentage of the particles' pathways with an error (compared to the reference case) larger than error E. Right: Percentage of the particles' end locations with an error (compared to the reference case) larger than error E. See the text for a more extensive description of the axes*

The right subplot describes a similar analysis, but now only based on the error in the end locations. In other words, it shows the percentage of particles that has an end location that lies within a certain distance from the reference end location. Again, it becomes clear that the percentage is always lower than 100%. For each of the selected time steps, there are particles that have an end location that is located more than 5000 metres away from the location that is found in the reference scenario. Moreover, the subplot shows that the percentages are higher compared to the left subplot. Thus, there are particles for which the maximum deviation detected in the simulation period is a lot smaller than the deviation of the end locations. There are particles for which the deviation from the reference pathway decreases for a certain part of the simulation period. Stated differently, the deviations that emerge during the first period of the simulation (particles start at the same location), sometimes reduce later on. These particles are redirected towards the reference path.

It would be desirable to use a very small time step for the particle calculations. However, the time step size also influences the computational time. Figure D.4 demonstrates that the total simulation time of the visualisation tool is strongly influenced by the time step size. The simulations are performed on a node of the Windows Computational Facility (16Gb RAM, 2.6 GHz). The simulations with a time step of 1 second took 4000 minutes, 2.7 days. As the tool is meant as tool to get quick insights with minimum computational time, a shorter calculation time is required.

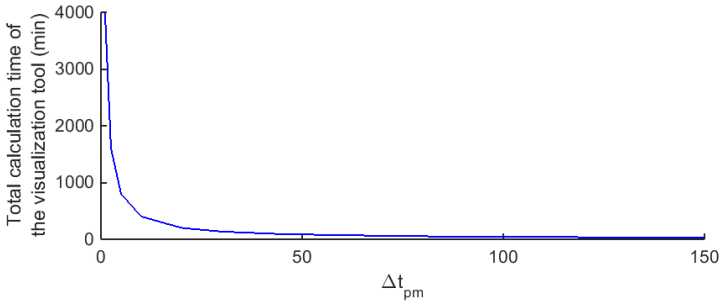


*Figure D.4 Total calculation time of the visualisation tool in case of model settings as presented in Section D.2.1*

The selection of the time step is based on the user's preferences. For this group of start locations, a time step of 30 seconds seems to be acceptable. The simulation time with these model settings (e.g. 4158 particles) is about 2 hours. For 78% of the particles, the error in the pathways (for the entire simulation) is at least smaller than 100 metres (approximately the grid resolution). If we only look to the end locations, 83% of the particles' end locations lies within a range of 100 m of the reference locations. For an interval of 1000 metres, these percentages are respectively 92% and 95%.

### D.2.2 Time step for particle movement calculations in the Wielingen-Scheur

Particles are released from 6 start locations that are spread over the cross-section of the channel. Over the first spring neap cycle, 2722 are released. Again, the scenario with $\Delta t_{pm}$=1 second is taken as reference. Again, Figure D.5 first shows the dispersal patterns of the tracer particles (at of the simulation) computed with time steps of 1 and 150 second(s). There seem to be no differences in the concentration maps.

Also here, the pathways are analysed. The left subplot of Figure D.6 describes the percentage of pathways with errors in the pathways smaller than error E (certain distance). The right subplot again shows a similar analysis, but only considers the particles' end locations. When reading and comparing the different subplots, it is important to notice that the axes describe different ranges.

Because of the lower transport velocities and gradients, the errors in the pathways are much lower. With a time step of 2.5 seconds, even 100% of the particles always stays within 2 metres from the reference pathway. With a time step of about 30 seconds and higher, none of the particles has a pathway with a maximum an error smaller than 2 metres. However, 100% of the particles stay within a distance of 40 metres from the reference pathways.

A save option could be to apply the time step of 30 seconds, that was derived in the inlet, for the entire study domain. However, the transport velocities are much lower elsewhere in the study domain. To still obtain large-scale transport pathways, longer simulation periods are needed for these areas. With a time step of 30 seconds, this would result in very long computational times. Moreover, the spatial gradients are much smaller outside the inlet. Concluding, the simulations with these model settings can be based on larger time steps.

Looking to the results, a time step of 300 seconds is still acceptable. This is much higher compared to the previous case and the maximum time step computed with the SN number for the entire area. However, still 98% of the particles have an error in the pathways smaller than 100 metres. 99,8% of the particles have an end location that lie not further 100 metres away from the reference end locations.

The SN number can also be computed solely for the grid cells (i.e. resolutions) and transport velocities the particles really come across. With a time step of 300 seconds, the maximum SN

number is 1.38. In other words, the particle displacement is always equal or lower than 1.38 times the grid resolution.

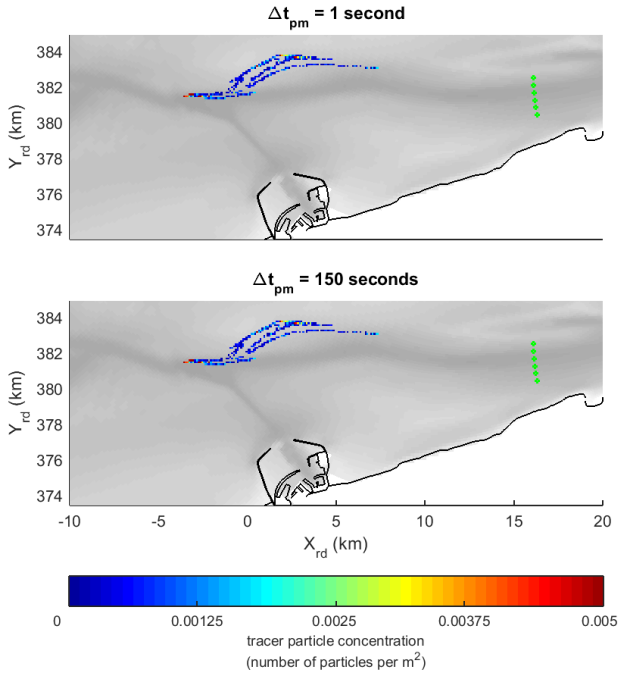


*Figure D.5 Maps of tracer particle concentrations after 3 spring neap cycles, computed with different time steps for the particle movement calculations. The green dots indicate the start locations in the Scheur (6 locations).*

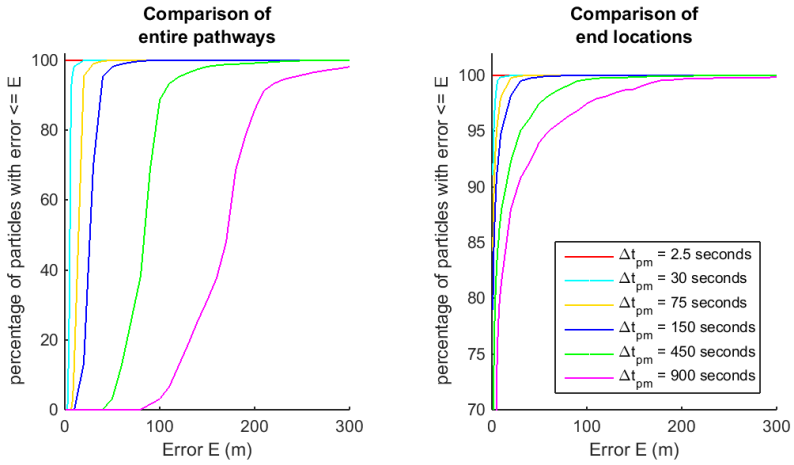


*Figure D.6 Left: Percentage of the particles' pathways with an error (compared to the reference case) larger than error E. Right: Percentage of the particles' end locations with an error (compared to the reference case) larger than error E. See the text for a more extensive description of the axes*

## D.3 Analyse temporal variations in sediment transports

Chapter 5 already discussed how the transport patterns can be used to provide more insights about the spatial variation in the sediment transports. The text below describes the usage of the visualisation tool to study temporal variations in the sediment transport conditions.

### D.3.1 Wielingen

| | | |
|---|---|---|
| T = 58 days | $\Delta t_{pm}$= 100 s | β = 0 |
| Release of particles = entire simulation | Interval of release = 1 particle per 15 min | Movie D.1 |

We consider a continuous release of particles within the middle of the Wielingen (Figure 9.1). The start location is the middle point of the group of start locations that was studied in Section 6.1.2.2.One particle is released every 15 minutes for the entire simulation period. Again, the sediment transport conditions of one spring-neap cycles a number of times to simulate the dispersal of particles over a longer period (in this case 58 days)

As shown before, the numerical particles are transported further into the Scheur and onto Vlakte van de Raan. Figure 9.2 shows the number of numerical particles that move through the cross-section shown in Figure 9.1. The results demonstrate the variations in the sediment transport during the spring neap cycle. Particles move through the cross-section from the left or right, depending whether it is ebb or flood. Moreover, the results show that the net transport of particles through the cross-section is the largest around spring tide. During neap, the particles movements are a lot smaller. In other words, the number of particles that pass through the cross-section is a lot lower.

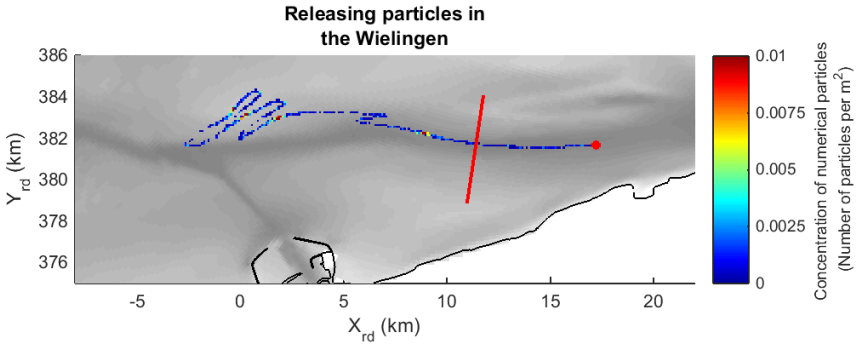


*Figure 9.1 Particle concentration after 58 days when releasing in the middle of the Wielingen (red dot). Red line represents the cross-section over which the particle movements are measured. Case 1.*

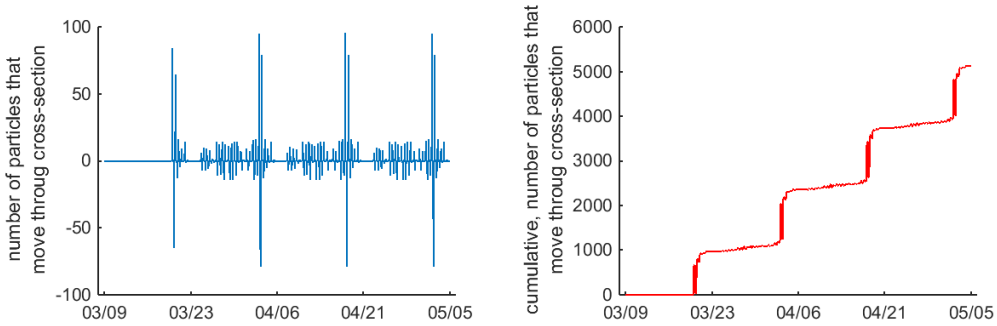


*Figure 9.2 Left: number of particles that moves through the cross-section (Figure 9.2), measured per 15 min. Positive values indicates that the particles move towards the west (during ebb). Negative values represent movements of particles towards the east (during flood). Right: cumulative number of particles that is located west of the cross-section.*

D.3.2 Inlet

| | | |
|---|---|---|
| T = 7 days (start at spring and neap) | $\Delta t_{pm}$= 30 s | β = 0 |
| Release of particles = 7 days | Interval of release = 1 particle per 45 min | Movie D.2 |

The temporal variation can also be visualised by comparing groups of particles that are released during spring tide or neap tide. As the transport velocities and spatial gradients are the highest in the inlet, this is the best location to test this.

The two subplots of Figure 9.3 describe the pathways of the particles after 7 days when they are released in the inlet during spring tide or neap tide. The periods are defined based on the tidal amplitude ranges and are both about 7 days long. In this way, the left subplot shows the pathways (over 1 spring period) of the particles that are released during spring. The right subplot demonstrates the pathways (over 1 neap period) of particles when they are released during neap. The figures look very much alike. However, compared to the right subplot, the pathways in the left subplot are longer. The pathways confirm that the sediment transports are highest during spring tide. These result in higher transport velocities and larger oscillating motions. Other tests have shown that the differences that are found in the first 7 days almost disappear for longer simulation periods. In other words, the initial deviations do not have a significant impact on the dispersal patterns for later times. Similar analyses for other locations lead to the same conclusions.

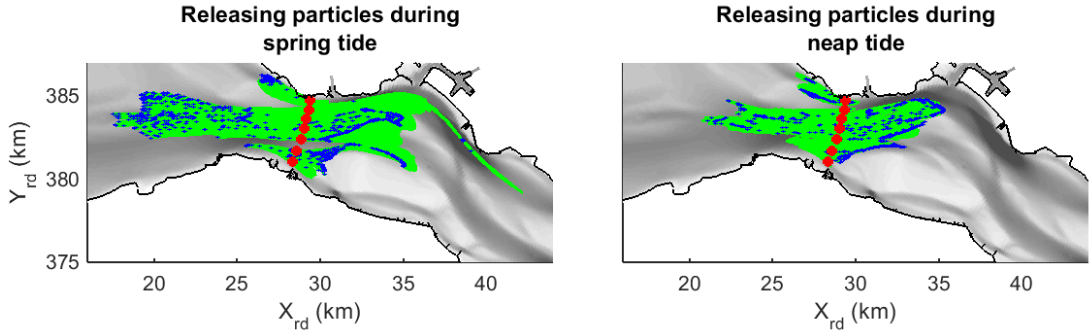


*Figure 9.3 Pathways of particles when they are released in the inlet during spring tide (left) and neap tide (right). For both subplots, the simulation period is 7 days. Case 1*

D.3.3 Conclusion

The analysis that was described above, confirms what is currently known and what can be expected when looking to the general Delft3D model output. The numerical particles have a to and fro motion that follows the ebb and flood variation in the tidal currents. Moreover, the results of the visualisation tool show that the higher flow velocities and sediment transports during spring tide compared to neap tide, result in larger oscillating motions and larger particle displacements. The current study did not reveal surprising/new insights about large temporal variations in the sediment transport conditions (e.g. a certain channel is ebb-dominant during neap tide and flood-dominant during spring tide).

## D.4 Transport pathways at Vlakte van de Raan

D.4.1 Convergence of pathways at the northern end of the Deurloo West

By releasing particles at the Vlakte van de Raan, Section 6.1.2.6 showed that the different pathways convergence and at the end of the simulation period (8 years) end within the northern part of the Deurloo West. Figure D.7 shows this location on a map of the residual

sediment transports. An explanation of the map itself can be found in Section 5.3.1.2. The transport pathways on the Vlakte van de Raan are discussed in Section 6.1.2.6.

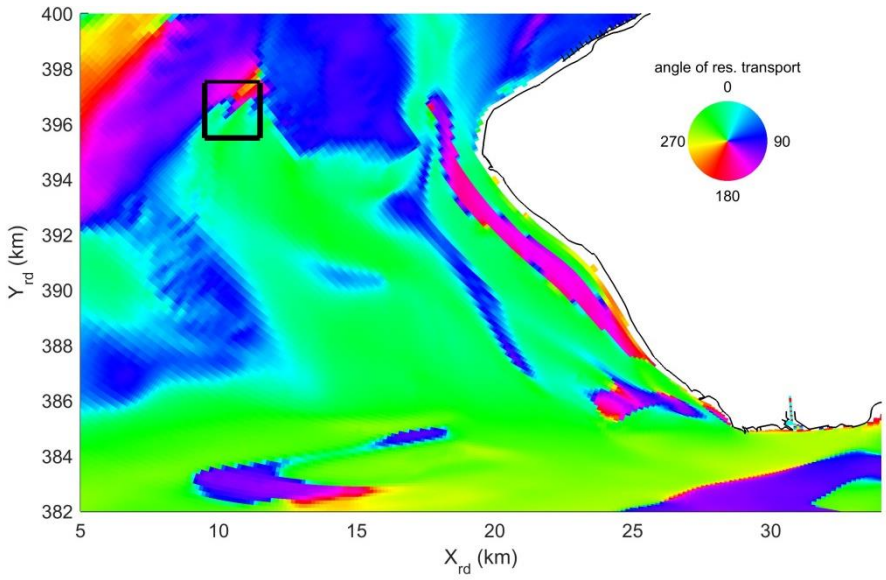


*Figure D.7 Direction of the residual sediment transport (computed for one spring-neap cycle) for case 1. The map describes the same dataset as Figure 5.11, but just uses colorscale to visualize the directions of the vectors. The black box shows the location where the different transport pathways from the Vlakte van de Raan seem to end (Section 6.1.2.6).*

D.4.2 Transport pathways at Vlakte van de Raan with locally derived acceleration coefficient

As stated in Section 6.1.2.6, the Vlakte van de Raan is a good case to test whether a locally derived acceleration coefficient leads to the same results as computing the acceleration coefficient for the area with maximum transport velocities (the inlet) and applying it to the entire study domain. If we follow the same method as presented in 3.3.3 and appendix D.1, the locally derived acceleration coefficient for the Vlakte van de Raan and the surrounding area is 16000 $m^{-1}$ (Figure D.8) This acceleration coefficient is based on the maximum transport velocities that are found at the southern boundary of the Vlakte van de Raan and the connection between the Geul van de Walvischstaart and Deurloo Oost.

| | | |
|---|---|---|
| T = 288 days | $\Delta t_{pm}$= 150 s | $\beta$ = 0 |
| Release of particles = first 14.4 days | Interval of release = 1 particle per 1 h | Movie D.3 |

As stated in appendix D.1, the acceleration coefficient that is used in the remaining part of this study is 1600 m-1. To be able to compare the transport pathways, the simulation period has to be adjusted for the differences in the acceleration coefficients (Eq. 3.24, section 3.3.3). In Section 6.1.2.6, the pathways were computed with for a period of 2881 days. For the scenario that is considered in this appendix, the simulation period is 288.1 days. Because of the larger transport velocities, the time step is reduced to 150 seconds. The other model settings are exactly the same as the ones presented in Section 6.1.2.6. Figure D.9 shows the transport pathways. The maximum particle displacement is now 70 metres. With a time step of 150, this is equal to a velocity of 0.47 m/s. This is more or less equal to the maximum modelled flow velocities (Figure 5.3). Although this simulation is based on a higher acceleration coefficient, the transport pathways are similar compared to the ones shown in Section 6.1.2.6. The pathways still converge and end up at the northern part of the Deurloo West. However, the larger transport velocities result in larger orbital velocities and transport pathways that are less clustered/stacked together.

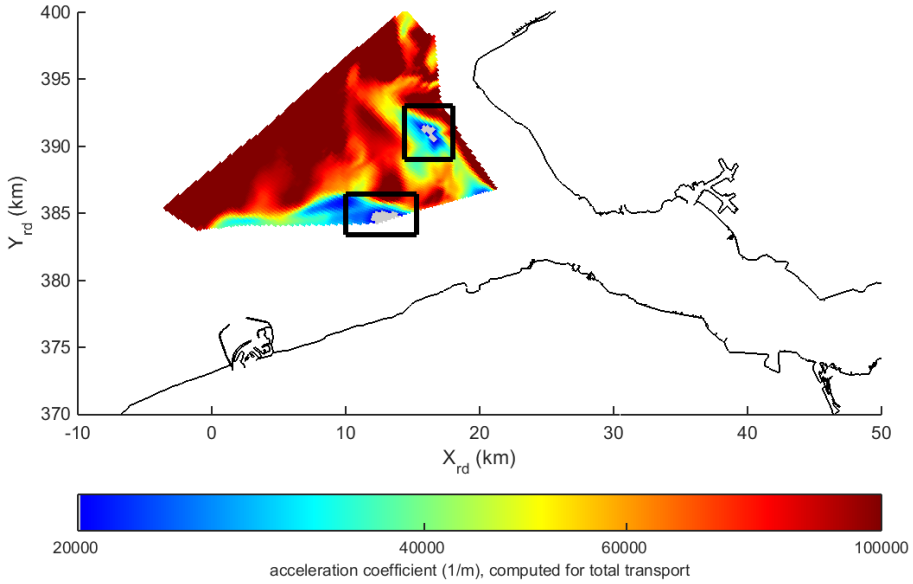


*Figure D.8 Calculated acceleration coefficient, based on the peak bed and suspended load sediment transports detected within the spring-neap cycle. The acceleration coefficient is only computed for the Vlakte van de Raan. The grey areas describe the grid cells with an acceleration coefficient between 15000 and 16000 $m^{-1}$. See Section 3.3.3 for more information about the derivation of the acceleration coefficient.*

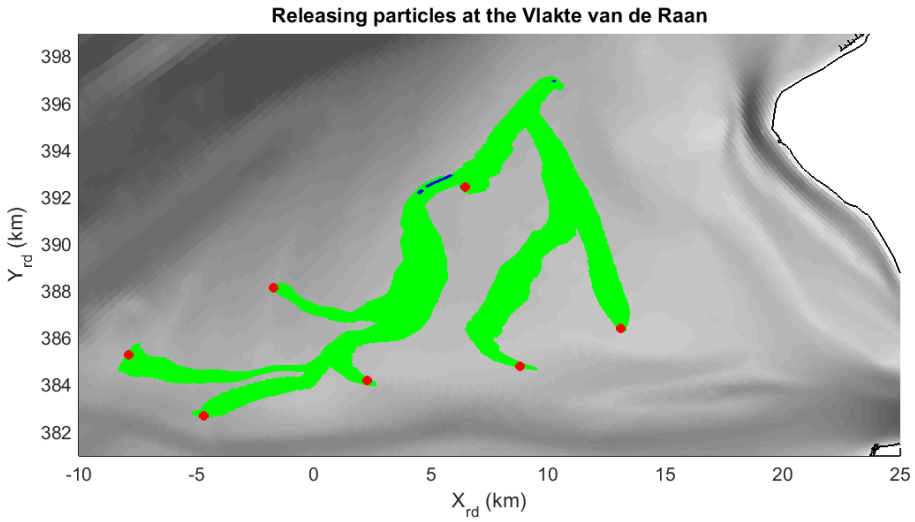


*Figure D.9 Pathways (period of 288 days) of particles that are released at the Vlakte van de Raan. Computed with an acceleration coefficient of 16000 $m^{-1}$. Case 1.*